Study of many-body dynamics in ion-ion/atom collisions : a joint experimental and theoretical investigation

Mariette Jolly

École doctorale Physique en Île-de-France

Thèse de Doctorat Sorbonne Université

Réalisée à l'Institut des NanoSciences de Paris (UMR 7588) et au Laboratoire de Chimie Physique - Matière et Rayonnement (UMR 7614)

présentée par

Mariette Jolly

Pour obtenir le grade de docteur délivré par Sorbonne Université

Dynamique à N-corps dans les collisions ion-ion/atome : étude expérimentale et théorique

Study of many-body dynamics in ion-ion/atom collisions : a joint experimental and theoretical investigation

Discipline : Physique

Dirigée par Alain DUBOIS (LCPMR) et Emily LAMOUR (INSP) et co-encadrée par Christophe PRIGENT (INSP)

Soutenue le 10 octobre 2024 devant un jury composé de :

Sophie TRINCAZ-DUVOID	PR Sorbonne Université, LPNHE	Présidente / Examinatrice
Alicja DOMARACKA	DR CNRS Univ Caen, CIMAP	Rapporteuse
Bernard PONS	PR Univ Bordeaux, CELIA	Rapporteur
Ugo ANCARANI	PR Université de Lorraine, LPCT	Examinateur
Alexandre GUMBERIDZE	Dr and associated member of GSI Darmstadt	Examinateur
Emily LAMOUR	PR Sorbonne Université, INSP	Directrice de thèse
Alain DUBOIS	PR Sorbonne Université, LCPMR	Directeur de thèse

À Dadère et Nainnain

Acknowledgements

I would like to express my gratitude to everyone at INSP and LCPMR, especially their directors, Massimiliano Marangolo and Richard Taieb, for warmly welcoming me into their labs. I extend these thanks to all the members of these labs, who have been nothing but kind to me. A special thank you goes to the INSP doctoral representatives — Benoit, Carlos, and Eliane — whose unwavering support has been a constant source of motivation for me, and to David Massot at LCPMR whose kindness and good humour throughout these three years has always been a source of comfort.

I also wish to acknowledge the EDPIF Doctoral School and the Plas@par Research Federation for their funding, which made this research possible.

I am profoundly grateful to the esteemed members of my thesis committee : Alicja Domaracka, Bernard Pons, Sophie Trincaz-Duvoid, Ugo Ancarani, and Alexandre Gumberidze. Thank you for agreeing to be part of this jury and for your genuine interest in my work.

My heartfelt thanks go to the team at CIMAP — Alain, Jimmy, and all those I had the pleasure of meeting during my stays at GANIL — as well as the dedicated team at Pantechnik.

To the wonderful team at INSP and LCPMR : Emily, Christophe, Alain, Martino, Stephane, Sebastien, Dominique, Lune, Perla, and Vikar, who shared an office with me — I will always treasure the memories we made together. I also want to express my gratitude to the interns I had the privilege of working with during this thesis: Spyros, Anatole, Marleen, Julien, Elena, Lea, and Amelie, for your invaluable help and support.

To my thesis directors, Emily, Alain, and Christophe — thank you for your guidance over these three years. Your feedback and advice have been vital to my progress, and I am deeply appreciative of your unwavering support. No words can give justice to what I felt during these three years, and can truly express the experience of working with all of you on this subject.

A special note of thanks to Mathieu and Laurent from my thesis committee for the confidence you gave me. Your feedback and support has meant a great deal. I would also like to extend my appreciation to all the teachers and staff at Sorbonne with whom I've had the pleasure of sharing this journey, from my undergraduate days to this day.

Now, for the most personal and heartfelt acknowledgments :
To my childhood teacher and dear friend Caro, and to my family friends who are like family to me — Thierry, Celestine, Sidonie, Arnaud, Helene, Titouan, Manon, Olivier, Jérémie, Bayonne, and Martine — I am forever grateful for your presence in my life.

A very personal thank you to Jean-Claude, without whom I might never have pursued studies in atomic physics.

To my beloved family — my parents, first and foremost, and Nath, Jacques,

Annette, Bernard, Daniel, Antonin, Nathalie and Sylviane — thank you from the bottom of my heart for your love and encouragement, for the curiosity and interest you showed in my subject, and for the safety and warmth you made me feel all my life. I particularly want to thank my amazing grandparents who aren't here anymore - without you I wouldn't be who I am today.

I would like to thank the CurieOsity student association for the strength it gave me, for the courage it instilled, and for the opportunities it provided. During my time as President, I met many remarkable people from Sorbonne and beyond — teachers, researchers, alumni — whose impact on my life has been immeasurable.

And last but not least, to all my friends — Leo, Maxime, Delfina, Young, Chloe, Enya, Foxwill, Yohan, Brendon (a special thanks to both of you for your help when computers refused to cooperate), LJF, Ivan, Alex, Etienne, Fivos, Hugo, Thomas, Aurane, Remi, JB, Guillaume, Isaac, Tamara, Bruno, Joachim, Garance ... — you all know what you mean to me. I could never have done it without you. Thank your for your friendship, your continued support, thank you for the laughs and the fun, thank you again.

Table of Contents

Abstract

Studying ion-atom and ion-ion collisions allows us to understand the probabilities of electronic processes such as capture, ionization, and/or excitation by controlling the number of electrons initially bound to each collision partner. By progressing from the study of a three-body system (the two nuclei with a single electron) to more complex systems involving additional electrons, we can examine the effects on the overall electron dynamics and consequently on the cross sections of elementary processes. In the theoretical section of the thesis, cross section calculations are performed for ion-atom and ion-ion systems containing up to two electrons. Carbon, hydrogen, nitrogen, helium and their respective ions have been chosen as collision partners. This is achieved using a semi-classical non-perturbative approach: the relative motion of the partners is treated classically, while the electron dynamics is described quantumly. The collisions are simulated using a "collision solver" program, from which cross sections for different processes can be extracted. The experimental part of the thesis is dedicated to the technical development, rigorous testing, and thorough characterization of various instruments critical for conducting precise ion-atom and ion-ion collision experiments. Two ion sources and their respective beamlines were set up to perform ion-ion collisions, ensuring that a large range of possible experimental conditions and collision systems can be explored. A collision chamber, a gaseous jet, an ion spectrometer and its associated detector, as well as an X-ray detection system were developed and characterized to perform the preliminary experiments. Overall, this thesis combines new theoretical calculations for ion-atom and ion-ion collisions with experimental advancements towards a setup capable of exploring a wide range of collision systems. The dual approach is very beneficial for enhancing the understanding of electron dynamics in ion-matter collisions. This knowledge is essential for both fundamental research and practical applications in various scientific and technological fields, such as astrophysical plasma, inertial confinement fusion research or hadrontherapy.

Résumé

L'étude des processus électroniques induits au cours de collisions ion-aatome ou ion-ion, en jouant et maîtrisant le nombre d'électrons sur chaque centre atomique, est un réel challenge dans le domaine des énergies intermédiaires. En allant de l'étude d'un système à trois corps (les deux noyaux avec un seul électron) vers des systèmes plus complexes impliquant des électrons supplémentaires permet d'examiner des effets sur la dynamique globale des électrons et par conséquent sur les sections efficaces des processus élémentaires. Dans la section théorique de la thèse, des calculs de sections efficaces sont effectués pour des systèmes ion-atome et ion-ion contenant jusqu'à deux électrons. Le carbone, l'hydrogène, l'azote et l'hélium neutre ou chargé ont été choisis comme partenaires de collision. Cela est réalisé en utilisant une approximation semi-classique non perturbative, qui consiste à traiter le mouvement des particules lourdes de manière classique, tandis que la dynamique des électrons est décrite en utilisant la mécanique quantique. Les collisions sont simulées à l'aide d'un programme "collision solver", à partir duquel des sections efficaces pour différents processus peuvent être extraites. La partie expérimentale de la thèse est dédiée au développement technique, aux tests et à la caractérisation de divers instruments essentiels pour la réalisation d'expériences précises de collision ion-atome et ion-ion. Deux sources d'ions et les lignes de faisceau correspondantes ont été installées pour réaliser des collisions ion-ion garantissant qu'une large gamme de conditions expérimentales et de types de collisions. Une chambre de collision, un jet gazeux, un spectromètre d'ions et son détecteur associé, un système de détection de rayons X ont été développés et caractérisées pour réaliser les premières études. Dans l'ensemble, cette thèse combine de nouveaux calculs théoriques pour les collisions ion-atome et ion-ion avec des avancées expérimentales vers une configuration capable d'explorer une large gamme de systèmes de collision. Cette double approche est très bénéfique pour améliorer la compréhension de la dynamique des électrons dans les collisions ion-matière. Ces connaissances sont essentielles tant pour la recherche fondamentale que pour les applications pratiques dans divers domaines scientifiques et technologiques, tels que les plasmas astrophysiques, la recherche sur la fusion par confinement inertiel ou encore l'hadronthérapie.

List of Figures

List of Tables

Introduction

Electronic processes that happen during ion-ion and ion-atom collisions play a crucial role in a variety of research fields. Besides their fundamental interest in atomic and molecular physics, understanding the electronic dynamics in such collisions helps for applications ranging from astrophysics—where they help explain stellar and interstellar phenomena—to material science, where they are used in techniques like surface modification and ion implantation and to medicine, where they are central in the method of cancer treatment called hadrontherapy. Additionally, an improved knowledge of these interactions is required in developing technologies such as inertial confinement fusion.

My work is divided into a theoretical part, conducted at LCPMR, and an experimental one at INSP. On the theoretical side the study utilizes a computer code developed over many years by the team, employing a semi-classical non-perturbative method known as the impact parameter approximation to investigate ion-ion and ion-atom collisions. Three collision systems, involving up to two electrons, are studied : C^{6+} - H, as a preliminary work in the project, N^{6+} - He^{+} and N^{7+} - He. These systems differ from those previously examined, as they involve much higher-charged ions and are more asymmetric in terms of charge state between target and projectile than earlier collision systems studied by the LCPMR team. They were also selected based on their feasibility for both theoretical and experimental studies. The major part of this work involved extracting cross sections for capture, excitation, and ionization processes and interpreting these results.

On the experimental side, at the start of the thesis, only one ion source (SIMPA) and a single beamline were operational at INSP. A second ion source (FISIC) was delivered at the end of 2022. A significant portion of my work involved the development and characterization of various parts of the experimental setup, including

- Modifying the setup configuration to connect the FISIC source to its beamline and reassemble the SIMPA beamline with its source in a configuration that allows 90-degree cross beam collisions. Figure 1 shows pictures of the experimental room before and after delivery of the FISIC source and reorganization of the full setup.
- Characterizing the new FISIC source in terms of current, charge state distribution and beam optic quality.
- Characterizing the ion spectrometer and its ability to separate the charge states of the ion products. Characterizing the count rate of its associated detector through two test campaigns at ARIBE (GANIL, Caen).
- Testing the beam purifier (previously characterized at ARIBE in 2018) to ensure its proper functioning in its final position in the collision zone and in connection with the ion spectrometer to ensure good beam quality.
- Implementing a new fully numerical signal processing system (FASTER), necessary for achieving coincidences between ion spectrometry and the X-rays emitted during collisions, using a low-resolution X-ray detector.

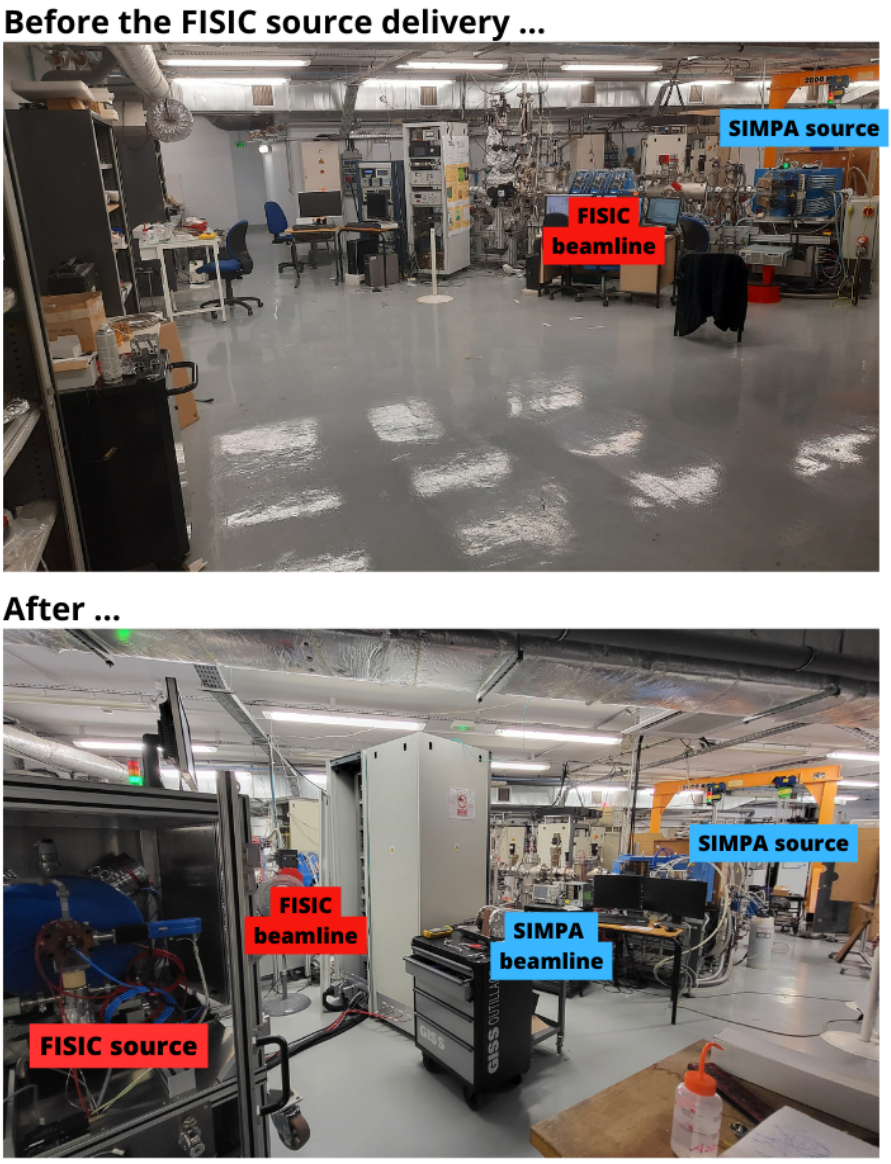

Figure 1: Pictures of the experimental room with the setup composed only of the SIMPA source and FISIC beamline (top) and of the experimental room with the full setup after delivery of the FISIC source in November 2022 (bottom).

This unique set-up newly installed in the campus was used in July 2024 for first ion-ion/atom collisions probed only by a X-ray spectroscopy method. Those preliminary studies are the first steps toward absolute cross section measurements.

My thesis manuscript is structured as follows

- **Chapter 1** provides a general introduction to the field of ion-ion and ion-atom collisions, detailing the electronic processes and energy domains of interest. Background for theoretical methods and experimental techniques as well as empirical approaches are presented.

- **Chapter 2** presents a detailed description of the semi-classical non-perturbative approach used in the theoretical study.

- **Chapter 3** discusses the theoretical results obtained for the three collision systems studied, C^{6+} - H, N^{6+} - He^{+}, N^{7+} - He.
- **Chapter 4** gives a detailed description of the various components as mentioned above.
- **Chapter 5** is dedicated to presenting tests conducted on the different components of the experimental setup : production of multicharged ions of carbon and oxygen, conclusions from the ARIBE test campaigns on the ion spectrometer and beam purifier and characterization of the X-ray detection system.
- **Chapter 6** presents the results and conclusions from the first-ever ion-ion and ion-atom collision experiments involving both ion sources conducted at INSP in July 2024 during a three-week campaign.
- The manuscript ends up with a section on **Conclusions and Perspectives** that summarizes the main findings and the conclusions reached in the research. It also discusses possible developments and areas for further study, offering insights for ongoing scientific advancement.

1 A theoretical and experimental introduction to ion-ion/atom collisions

1.1 General considerations

We present here the general motivations for the study of atomic and molecular collisions, and then we give details about the different electronic processes and energy regimes that are mentioned all along this work.

1.1.1 Motivations for the study of atomic and molecular collisions

Atomic and molecular collisions hold significant interest across multiple domains, providing essential insights and practical applications that are crucial for advancing both theoretical and technological development.

Collisions between ions and atoms play a critical role in various astrophysical plasmas. The study of these interactions is essential for understanding and modeling the behavior of astrophysical objects [1]. As an example, interactions between atoms of the cometary comae and ions of the solar wind give rise to charge exchanges in collisions between hydrogen- and helium-like C, N and O ions and atomic hydrogen at energies of the order of 1 keV/u. These processes play a significant role in the X-ray emissions from comets [2, 3]. Ions from the solar wind also interact with atoms, molecules and ions from Earth's geocorona and exosphere (for instance charge exchange processes between bare neon ions and helium or hydrogen atoms at a few keV/u), producing X-rays that constitute a problematic background for ground based astronomical X-ray observations [4]. Laboratory experiments studying those interactions provide crucial data necessary to the understanding of these astronomical X-rays observations. Molecular growth may be also induced by collisions of ions with complex molecules such as polycyclic aromatic hydrocarbons (PAHs) [5]. The study of those collisions provides insights into the physical chemistry of planetary atmospheres.

Another research domain in which atomic collisions are fundamental is inertial confinement fusion (ICF). Figure 2, shows the main steps of ICF : intense laser or ion beams irradiate a small pellet of fusion fuel (Deuterium and Tritium), ionizing its outer layer through collisions and creating a plasma. The ablation of the outer layer generates a shock wave that compresses the fuel inwards. Additionally, alpha particles (with 3.5 MeV energy) produced from fusion reactions further heat the fuel through collisional interactions, facilitating ignition [6–8]. Heavy Ion Beam (HIB)-driven Magnetized Inertial Fusion (MIF) is a promising candidate for achieving the goal of fusion energy by introducing an external magnetic field into the fusion fuel during ICF. The impact ionization process of light target atoms/ions (H, D, T, ^{3}He, ^{3}He$^+$) by heavy projectile ions (Xe^{q+}, Bi^{q+}, U^{q+}) in the 1–100 MeV/u energy range is a crucial issue in the study of HIB-MIF. These systems are promising candidate reactions for fusion power, and their collision dynamics need to be extensively studied [10].

Medical applications, particularly in cancer treatment, also benefit greatly from the study of atomic collisions. Hadrontherapy [11–13], which involves irradiating tumors with protons or light nuclei (e.g., helium, carbon ions) with energies of a few 100 MeV/u, relies on a comprehensive understanding of collision dynamics. Hadrontherapy exploits the Bragg peak [14] phenomenon, which corresponds to a maximum energy deposition at a specific depth. Heavy-ion therapy offers distinct advantages

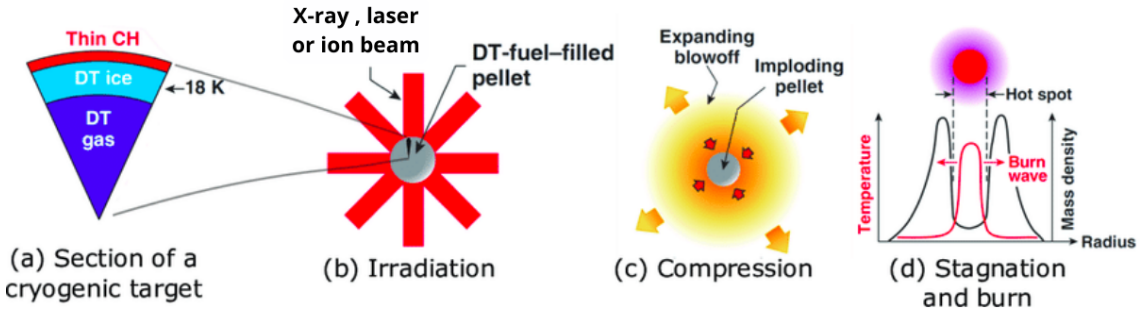

Figure 2: The four stages of inertial confinement fusion : (a) and (b) intense laser or ion beams irradiate a small pellet of fusion fuel. (c) Due to the momentum conservation during the ablation of the outer layer a radial shock-wave compresses the fuel capsule and the core of the fuel reaches the required density and temperature for ignition. (d) Fusion reactions spread rapidly through the compressed fuel. Figure taken from [9].

over conventional proton and X-ray therapy, particularly in terms of precision and effectiveness in targeting tumors as illustrated in Figure 3. In this figure the relative deposited dose of 21 MeV photons, 148 MeV/u protons and 270 MeV/u fully stripped carbon as a function of the penetration depth in water is shown. One can see that the photons deposit energy all along their path, with a maximum at a depth of about 40 mm. Protons and carbon ions, on the other hand, exhibit a Bragg peak at a depth of 140 mm, with carbon ions having a much sharper peak than protons. This enables highly localized treatment, sparing surrounding healthy tissues from significant radiation exposure, which is particularly beneficial for treating tumors that are near critical organs like the brain or spinal cord. Reduced radiation exposure to healthy tissues also significantly decreases side effects from cancer treatments. To improve the effectiveness of treatments, a better knowledge of the collision dynamics between heavy ions and organic matter atoms and molecules is highly beneficial.

Technological applications also depend on the understanding of ion-matter collisions, which is paramount for studying material damage mechanisms such as radiation damage, material fatigue, wear, and corrosion. Ion irradiation may also generate interesting modifications. For instance, decrease up to suppression of the thermal hysteresis in magnetocaloric MnAs films induced by keV-MeV ion bombardment has been observed by our team [16], opening new perspective for applications.
During processes like ion implantation, used for instance for the manufacturing of photovoltaics cells, various ions (from C to Au) with energies ranging from 10 keV to 1 MeV are used to modify the surface properties of the materials without changing their bulk properties by producing intermediate energy levels in the bandgap of a semiconductor [17]. Collisions at these energy levels are also crucial in material fatigue, where repeated atomic interactions lead to microstructural changes and crack propagation under cyclic stresses [18].

In summary, the study of ion-matter collisions is essential across a wide range of fields, from fundamental quantum mechanics to practical applications in medicine, astrophysics, plasma physics, chemical engineering, and technology. Since the energy ranges and systems at play for the collisions in these domains are varied, a lot of them have been seldom or even never studied. The insights and data that are gained from studying these processes could not only enhance our theoretical understanding but also drive innovation

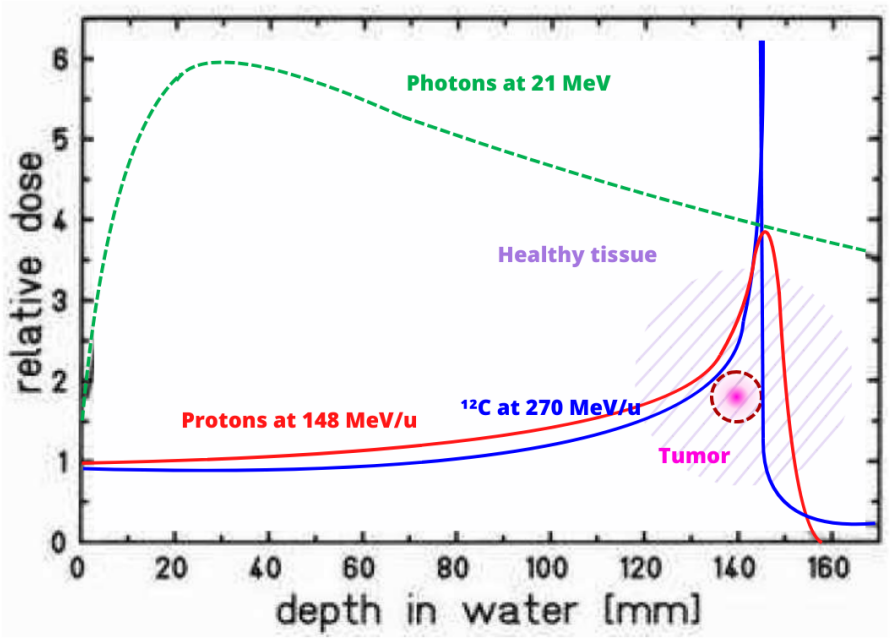

Figure 3: The Bragg Peak is associated with a lower entrance dose and no exit dose when compared to X-ray therapy. In the case of protons and heavy ions, a precise control of the area where the dose is deposited is possible via the energy of the incoming beam. Figure modified from [15].

and development in various technological and industrial sectors.

1.1.2 Description of the electronic processes at play

Atomic and molecular collisions involve several key electronic processes that can be categorized into elastic scattering and inelastic processes. The latter comprise electron transfer, excitation, and ionization, as shown in Figure 4 and described in more detail below. It is important to note that the projectile P and target T are arbitrarily defined.

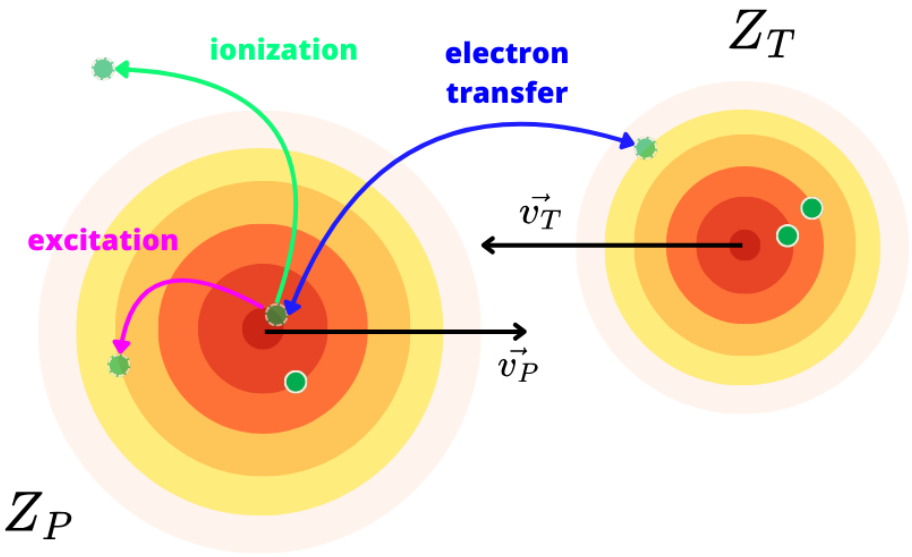

Figure 4: Possible electronic processes at play during a collision between a projectile (P) and a target (T).

As a consequence, their role could be interchanged in the equations below, without changing the generality of the description :

- *Elastic scattering* occurs when the initial and final electronic states of the target (T) and projectile (P) are the same before and after the collision. This can be represented by the equation

$$P + T \rightarrow P + T \tag{1}$$

- *Electron transfer* (also called *electron capture* or *charge exchange*) processes involve the exchange of one or several electrons between the collision partners. This is written as

$$P^{q+} + T \rightarrow P^{(q-n)+} + T^{n+} \tag{2}$$

  where n is the number of involved electrons in the process.

- *Excitation* processes promote electrons to higher energy states within the same center, e.g.

$$P + T \rightarrow P + T^{*} \tag{3}$$

- *Ionization* processes result in the ejection of electrons

$$P + T \rightarrow P^{n+} + T + ne^{-} \tag{4}$$

The behavior of atomic and molecular collisions varies significantly across different energy domains, categorized as *low*, *intermediate* and *high velocity*. These energy domains are defined by the ratio between v the relative velocity between the target and projectile and v_e the classical velocity of the active electron in the collision

- $v << v_e$: at low energies, electron capture processes are predominant. In this regime, the slow relative motion allows for the formation of transient quasi-molecules, facilitating the transfer of electrons between collision partners.

- $v \approx v_e$: in the intermediate velocity regime, a complex mix of inelastic processes such as electron capture, excitation, and ionization occurs with cross sections of the same order of magnitude.

- $v >> v_e$: at high energies, ionization and excitation processes dominate. The interaction time in this regime is very short, allowing the projectile to act as a small perturbation to the target.

As an example, Figure 5 shows schematically the cross sections for electron capture, ionization and excitation as a function of the impact energy for the H^+-H collision system. The electron capture process presents a "plateau" and dominates below 10 keV/u, then its cross section diminishes very rapidly. Excitation and ionization cross sections reach a maximum in the intermediate regime around 25 keV/u. In fact, at this energy the three processes have comparable cross sections in terms of magnitude. At energies above 100 keV/u, the excitation and ionization processes are dominant and their cross sections decrease less rapidly than the electron capture cross section. The stopping power of protons in aluminium is also plotted as a function of the impact energy. The

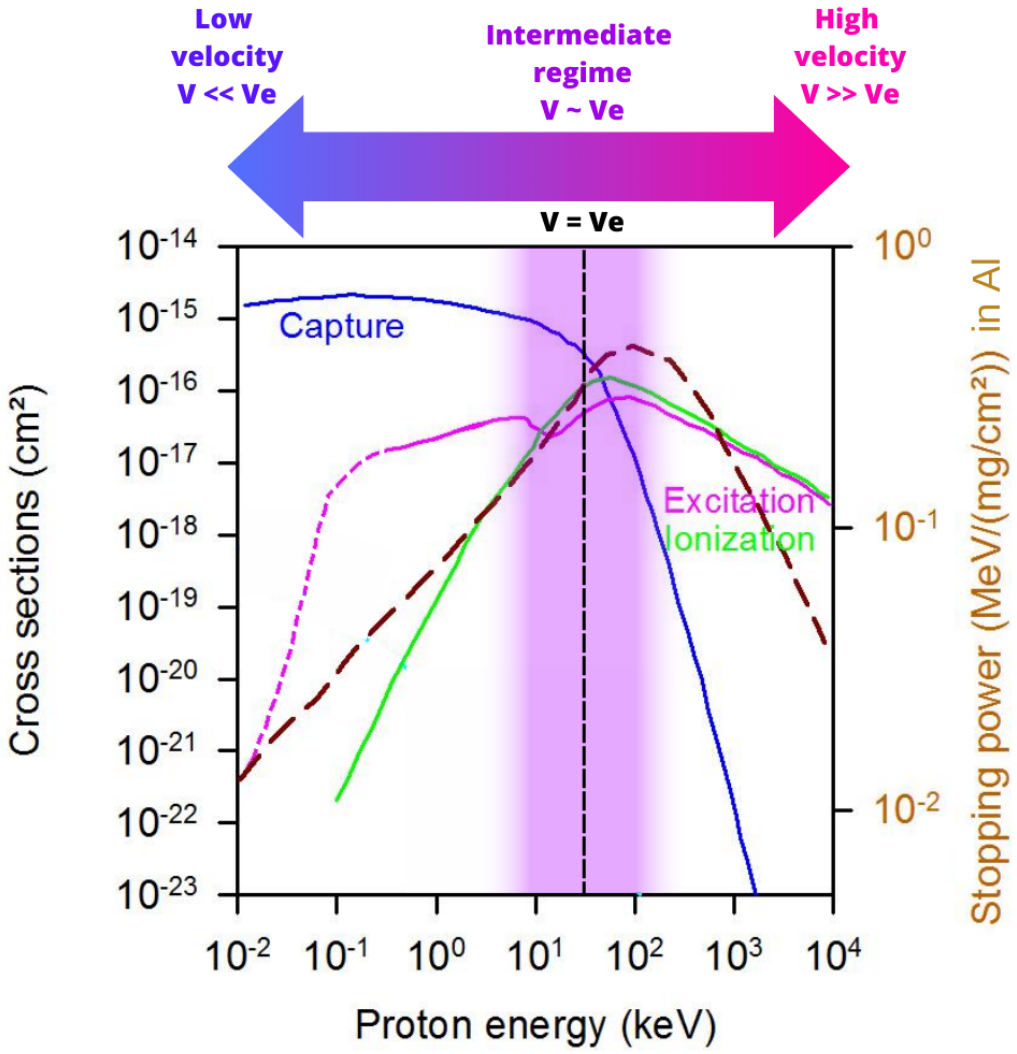

Figure 5: Cross sections for electron capture, ionization and excitation as a function of the impact energy, for H^+-H collisions. The stopping power of protons in aluminium is also indicated with the brown dashed line as a function of the impact energy. The corresponding energy domains are indicated above, and the purple band indicated the approximate extent of the so-called *intermediate velocity regime*. Figure modified from [19].

maximum of the stopping power is located in the intermediate regime, and gives rise to the so-called Bragg peak [14].

For hydrogen-like systems, the classical velocity v_e of the active electron in the collision is expressed in atomic units (see Appendix A) by

$$v_e = \frac{Z}{n} \tag{5}$$

where Z is the atomic number and n the principal quantum number of the electron. For non-hydrogenic systems, v_e is estimated using the ionization energy E_I of the electron

$$v_e = \sqrt{2 \times E_I} \tag{6}$$

For the collision system presented in Figure 5, H^++H, $v_e \approx 1$ a.u. This means that in order to be in the intermediate velocity regime for this collision system, the relative

velocity v must be of the order of 1 a.u, corresponding to a collision energy of 25 keV/u. As a second example, let us consider a collision system with highly charged heavier species : O^{7+}+O^{5+}. The active electron in this case is in the 2s shell of the O^{5+} ion, that has a velocity $v_e \approx 3.19$ a.u. To be in the intermediate velocity regime for this system, the collision energy must be of the order of 250 keV/u. This illustrates that the so-called intermediate velocity regime is situated at very different energy ranges depending on the collision system considered.
In the following, the theoretical, numerical and experimental methods used to obtain cross sections that are the most relevant for our study are presented and discussed.

1.2 Theoretical approaches in ion-ion/atom collisions

The study of atomic and molecular collisions encompasses various energy regimes, each necessitating different methodological approaches. Each regime — low, intermediate, and high velocities — presents unique challenges and requires specific theoretical approaches and computational techniques to accurately model the interactions and capture the nuances of the processes involved. For the high-energy regime the collision times are extremely short, and electronic transitions involve the initial and final states with negligible coupling to other states. Therefore perturbative methods are suitable in this regime. The first-order Born approximation was the first developed with success and has been further refined into various approaches like the Continuum Distorted Wave (CDW) methods [20, 21], where the electronic wave functions include the Coulomb field of the other collision partner leading to distorted functions. These approaches have proven successful in modeling data for electron capture and ionization in high energy ion-atom collisions as reported in [22–24] in the energy range 80 - 200 keV/u. However, this energy regime is out of the scope of this manuscript and will not be developed further.
For the low and intermediate energy domain, several methods can be employed. They

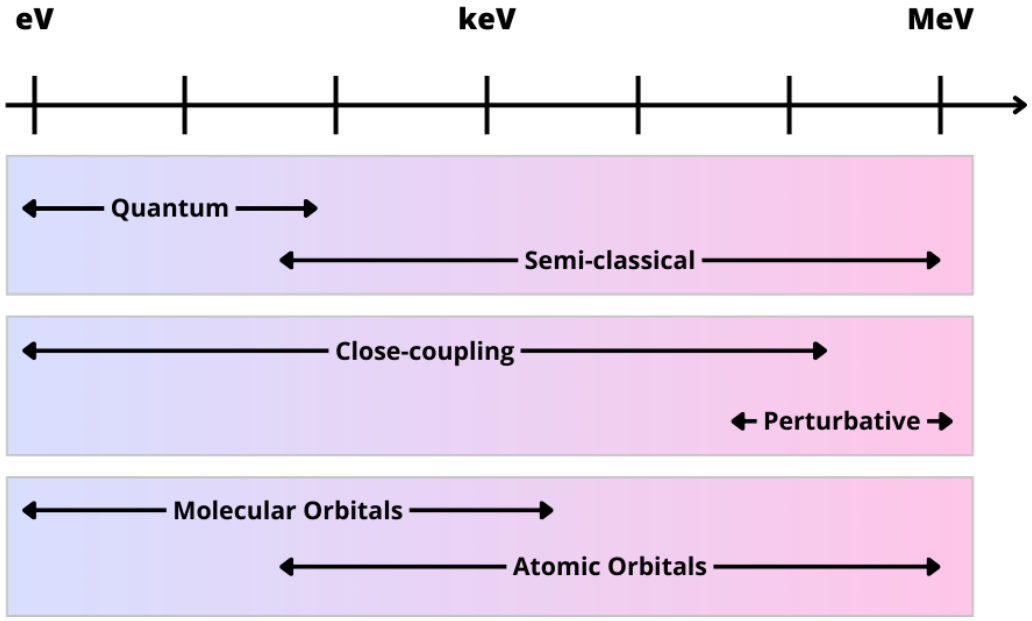

Figure 6: Different theoretical methods applicable in a large energy range, for the case of H^+-H collisions.

are often valid for a large impact energy range, as shown in Figure 6. In this figure are

represented schematically the different theoretical methods applicable for impact energies ranging from 1 eV/u to 1 MeV/u in the case of proton - hydrogen collisions. For collisions involving electrons of heavier atoms, as explained in the previous section, the energy range has to be shifted towards higher impact energies for this representation to remain correct. As an example, the validity of quantum and semi-classical approaches over a large energy range is discussed in [25], where the authors use both approaches to compute cross sections for Be^{4+} - H collisions in the 2.5 eV/u - 25 keV/u energy range. A good agreement is found between both methods for E $>$ 22.5 eV/u. This shows that both methods are valid over a large energy range. Quantum and semi-classical approaches, as well as the Classical Trajectory Monte-Carlo (CTMC) method are presented in the following sections.

1.2.1 Quantum approaches

At very small impact energies, the electronic transitions primarily occur at points where the energy variation of the system is minimal, specifically at avoided crossings between molecular states. This principle is central to methods such as the Perturbed Stationary States (PSS) method [26]. In this close-coupling approach, the kinetic energy of the relative motion is treated as the "perturbation" responsible for the transitions [27, 28]. In its original form, it has the drawback to not be Galilean invariant. The method called QMOCC (quantum-mechanical molecular orbital close-coupling) is derived from the PSS method, and is very robust for treating low-energy ion-atom and ion-molecule collisions [29, 30].

As an example, in Figure 7, the charge transfer cross sections in He^{+}-Li collisions

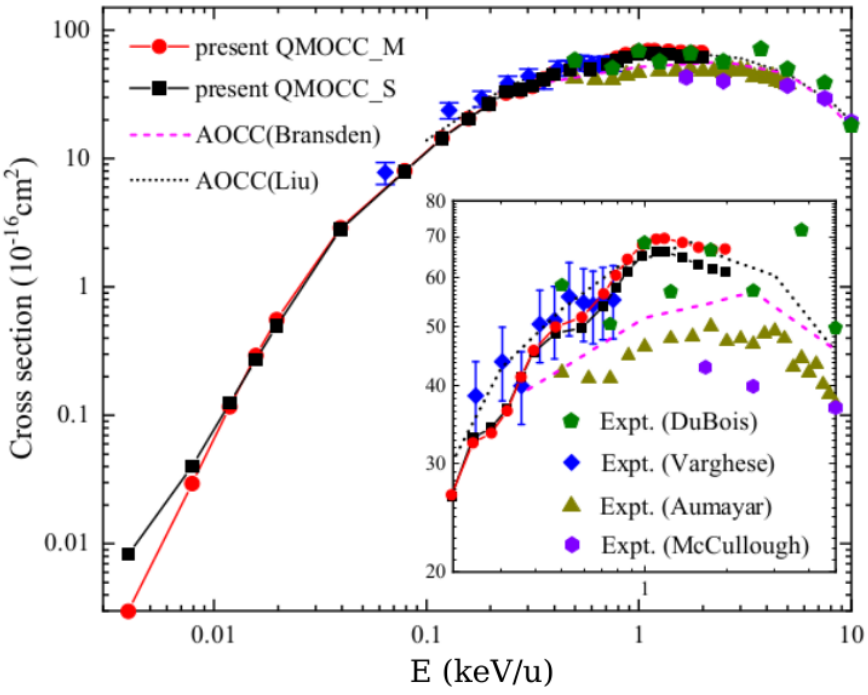

Figure 7: Spin-average total charge transfer cross sections in He^{+} -Li collisions computed with two variations of the QMOCC method in [29], compared with other AOCC theoretical [31, 32] and experimental [33–36] results as a function of collision energies. Figure taken from [29].

predicted by QMOCC calculations [29] are compared with experimental and other theoretical results in the 0.003 to 10 keV/u energy range. The QMOCC results agree well with measurements for impact energies below 0.7 keV/u. For energies between 0.7 and 2 keV/u, the QMOCC results are consistent with Atomic Orbital Close Coupling (AOCC) calculations and experimental results. Some discrepancies may be due to experimental limitations, and the smaller values of AOCC calculations [31] likely result from a limited expansion basis in their calculations. Overall the authors in [29] conclude that the QMOCC method provides very reliable results.

1.2.2 Semi-classical approaches

The highest energy range of the low-velocity domain and the intermediate velocity regime are characterized by a broader range of possible couplings between a large number of states of the system, necessitating specialized non-perturbative methods for accurate resolution. These methods involve using a mix of classical mechanics for the relative motion of the interacting nuclei, while the dynamics of the electrons are treated using quantum mechanics [37, 38]. This approach is particularly useful in the intermediate energy domain, where the de Broglie wavelength λ_d of the relative motion between target and projectile is very small compared to the collision zone. The semi-analytical methods, among them the one used in this study, as well as fully numerical methods are mentioned below.

- *Semi-analytical methods*: The electronic wave function is expanded in a basis of analytically defined functions [39]. This method is highly accurate, contingent on the thorough coverage of the Hilbert space by the chosen basis functions. Developed rigorously by Bates and McCarroll [40, 41], the AOCC (Atomic Orbital Close Coupling) method involves the use of atomic orbitals of the collision partners, with electronic wavefunctions modeled for example by hydrogenic Slater [42], Gaussian orbitals [43] or Sturmian functions [44]. The same principle can be applied by using an expansion on molecular orbitals (MOCC) rather than atomic ones, see for example [45]. For multi-electronic systems, the AOCC methods have been refined mainly by the LCPMR team and are called ASCC (Asymptotic State Close-Coupling). The resulting set of coupled differential equations that describe the time evolution of the electronic states during the collision is solved non-perturbatively, accounting for strong couplings between various open channels and electronic correlation effects. The two-center basis generator method (TC-BGM) [46] adapts the basis set used in the solution of the time-dependent Schrödinger equation as the collisional system evolves. In practice, the TC-BGM method is similar to the two-center AOCC approach, using traveling bound orbitals on collision centers A (target) and B (projectile) to represent the time-dependent wave function. However, it differs in its construction of pseudostates, which are added to atomic orbitals to describe quasimolecular couplings at low collision energies and interactions with the continuum. This method was applied in the study of [47] electron state-selective capture probabilities for Ar^{17+}–Ar collisions at v = 0.53 a.u. performed by the INSP team. These results are compared in section 1.3.2.3 with experimental data.

- *Numerical methods*: These techniques solve the time-dependent Schrödinger equation for electrons on a discrete space-time grid while the nuclei follow clas-

sical trajectories. It effectively handles various collision scenarios, including non-adiabatic processes, and is useful for calculating electron capture and excitation cross sections at intermediate energies. However, the computational cost and current limitations of computer performance constrain the precision of these approaches (for example, to represent the electron capture into highly-excited orbitals) [48–52].

1.2.3 Classical Trajectory Monte Carlo (CTMC) method

CTMC approaches are commonly employed when particles are treated using Newtonian mechanics, with the probabilistic aspects of quantum mechanics introduced via Monte Carlo methods. Initially developed by Abrines and Percival [53], these methods have been extended to multi-electronic and complex polyatomic systems, albeit with many approximations and models [54, 55]. An example from [55] is given in Figure 8. In this

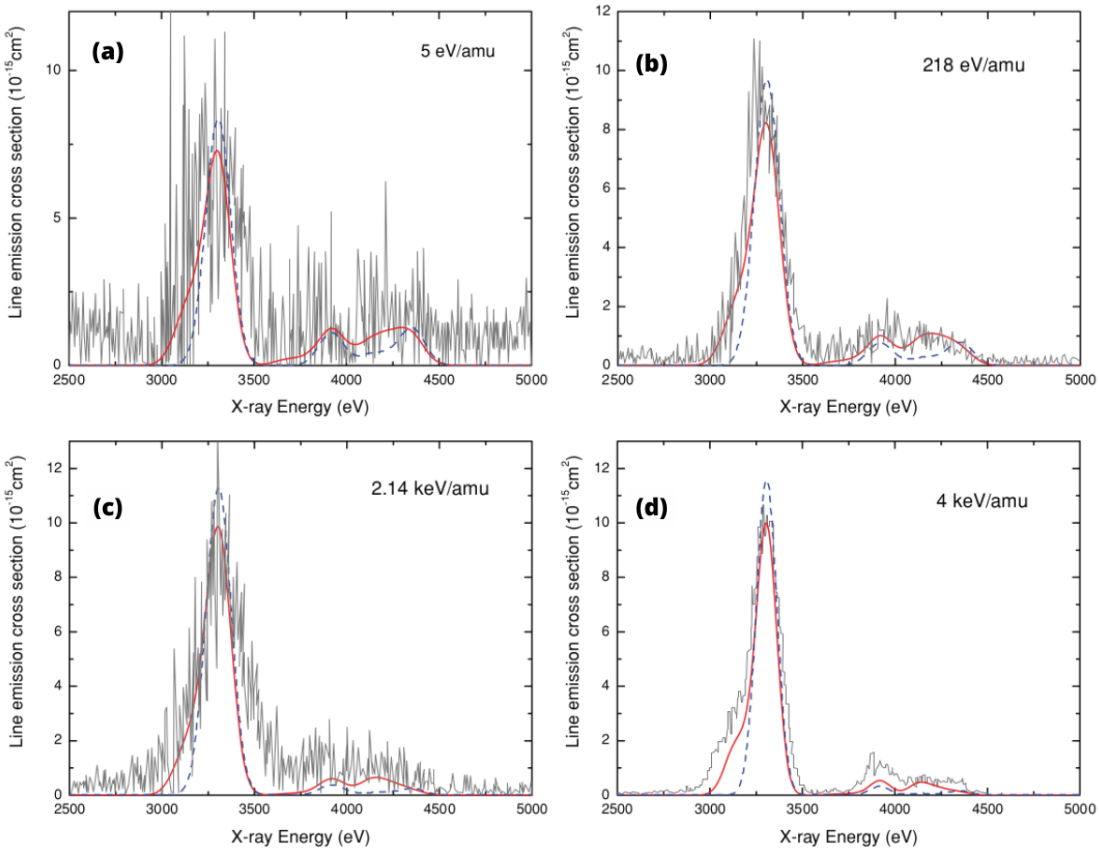

Figure 8: Line emission cross sections (solid black lines) for 5 eV/u (a), 218 eV/u (b), 2.14 keV/u (c), and 4 keV/u (d) Ar^{18+} + Ar collisions. In red, 5-electron CTMC results and in blue dashed line 3-electron CTMC results. Figure taken from [55].

article, the authors obtained line emission and charge-exchange cross sections based on CTMC calculations for collisions between Ar^{18+} and neutral argon at impact energies of 5–4000 eV/u and compared them to the experimental data. More precisely, the experimental Lyman series cross sections are compared with two versions of CTMC calculations (differing by the number of active electrons under consideration). The model using five electrons (red lines) reproduces the experimental data with good accuracy, while the model with three electrons (blue dashed lines) underestimates the

higher-energy lines and fails to reproduce the shoulder of the Lyman-α line. This highlights the fact that even though CTMC methods are straightforward to implement, they can be relatively imprecise and are not the best suited to reproduce purely quantum effects.

In our study, an ASCC semi-classical method is used to model total and partial cross sections for electron capture, excitation and ionization processes in one- and two-electron collision systems in the intermediate energy regime. This approach is detailed in Chapter 2 and applied to different collision systems in Chapter 3.

1.3 Experimental approaches for ion-ion/atom collisions

In this section we present first the principle of the experimental measurements of cross sections in cross-beam experiments. Then we describe a few tools to perform ion-atom and ion-ion experiments previously used in selected papers and reviews. Finally, we present two empirical approaches used by experimentalists for cross section calculations.

1.3.1 Cross beam experiments : extraction of cross sections

In this section we describe how to extract cross sections from cross-beam experiments. Firstly we give the method for the case of two charged particle beams crossing each other at an angle for ion-ion collisions [56–58]. After we discuss the case of a charged particle beam crossing an effusive gas jet [59]. Lastly we define the so-called "single collision condition" that is needed to be reached to extract the cross sections.

1.3.1.1 Case of two charged particle beams

Figure 9 gives the definition of the coordinates used in this section. The z axis is taken along the direction of beam 1 and z' along beam 2. y is perpendicular to z and z' and x & x' are in the plane of (z, z'), respectively perpendicular to z and z'. θ is the angle between the two beams.
Let us now consider the case of a collision between two particle beams, i.e. two flux of particles $\vec{j_1} = n_1\vec{v_1}$ and $\vec{j_2} = n_2\vec{v_2}$, with n_1 and n_2 the number of particles per unit volume. The expression of the number of physical events per second in the elementary volume dV is given by

$$dN = \sigma n_1 n_2 v dV \tag{7}$$

where σ is the cross section and $v = |\vec{v_2} - \vec{v_1}| = \sqrt{v_1^2 + v_2^2 - 2v_1v_2\cos\theta}$ the relative velocity.
From equation (7), we get the number of events per second

$$N = \sigma v \int n_1 n_2 dV \tag{8}$$

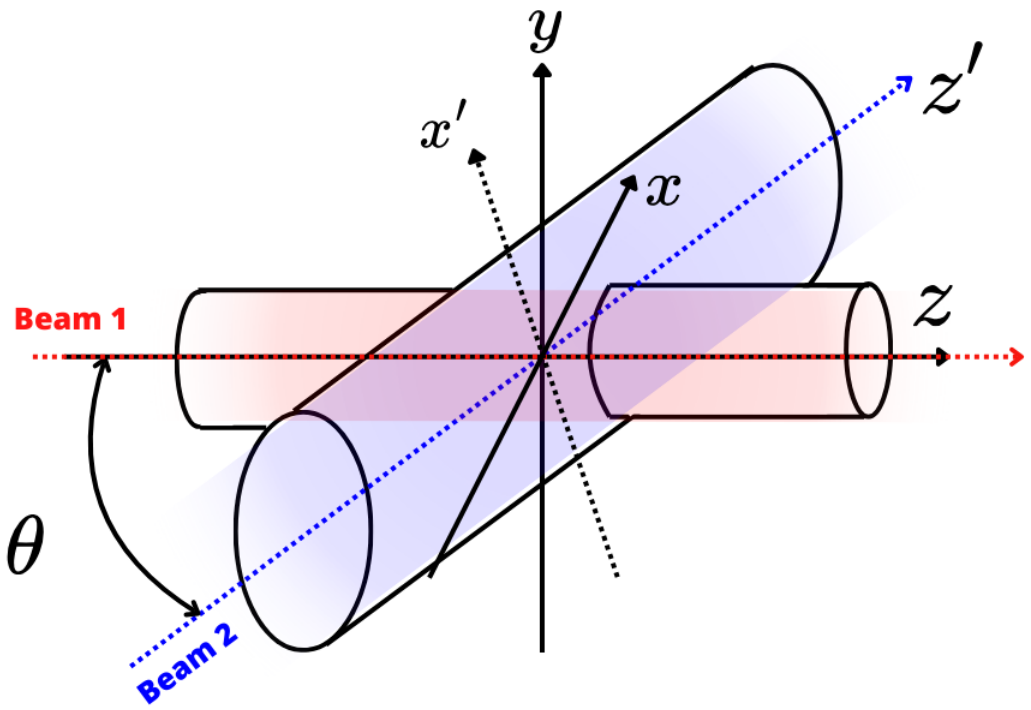

Figure 9: Coordinates used for the case of intersecting beams. Both beams are considered to be in the x, z plane. Beam 1 is along the z direction and crosses beam 2 at an angle θ.

In beams 1 and 2, the density of particles and flux are independent of coordinates z and z', respectively, meaning that

$$n_1 = \frac{j_1(x,y)}{v_1} \tag{9}$$

$$n_2 = \frac{j_2(x',y)}{v_2} \tag{10}$$

Therefore, given the volume element $dV = dydzdz'\sin\theta$, the number of events per second can be written

$$N = \sigma \frac{1}{v_1 v_2} \sin\theta \int dy F_1(y) F_2(y) \tag{11}$$

where

$$F_1(y) = \int j_1(x,y)dz' = \frac{1}{\sin\theta}\int j_1(x,y)dx = \frac{J_1(y)}{\sin\theta} \tag{12}$$

and:

$$F_2(y) = \int j_2(x',y)dz = \frac{1}{\sin\theta}\int j_2(x',y)dx' = \frac{J_2(y)}{\sin\theta} \tag{13}$$

where the one-dimensional densities along y in beams 1 and 2 are given by $J_i = dI_i/dy$ with $i = 1$, 2 and I_i the total intensity of beam i. The number of events per second is then given by the relation

$$N = \frac{\sigma v}{v_1 v_2 \sin\theta} \int dy J_1(y) J_2(y) \tag{14}$$

By introducing the so-called "form factor" F, the number of events per second is

$$N = \frac{\sigma v}{F v_1 v_2 \sin\theta} I_1 I_2 \tag{15}$$

with F (which has the dimension of a length) given by

$$F = \frac{(\int J_1(y)dy)(\int J_2(y)dy)}{\int J_1(y)J_2(y)dy} \tag{16}$$

Since it is necessary to account for the detection efficiency, the cross section for a given process is written as

$$\sigma = \frac{N}{\varepsilon_1 \varepsilon_2} \times \frac{1}{I_1 I_2} \times \frac{v_1 v_2 \sin\theta}{v} \times F \tag{17}$$

with $\varepsilon_{1,2}$ the detection efficiencies for the products of the reaction. This shows that in order to correctly extract a cross section from experimental data, a number of parameters have to be known. Aside from careful measurement of the reaction rate N, it is necessary to measure the density profiles of both beams along the vertical axis simultaneously at the crossing of the beams. This can be done when moving a slit across both beams and measuring the transmitted currents as in [57, 58]. As an example, Figure 10 taken from [58] shows the intensity profiles of two ion beams (10 keV He^+ and 66 keV H^+) at the intersection, leading to a calculated form factor $F = 2.44$ mm. In our case, beam profiles have been observed via fluorescence measurement when ions hit solid targets. This measurement is always a tricky one since it cannot be done

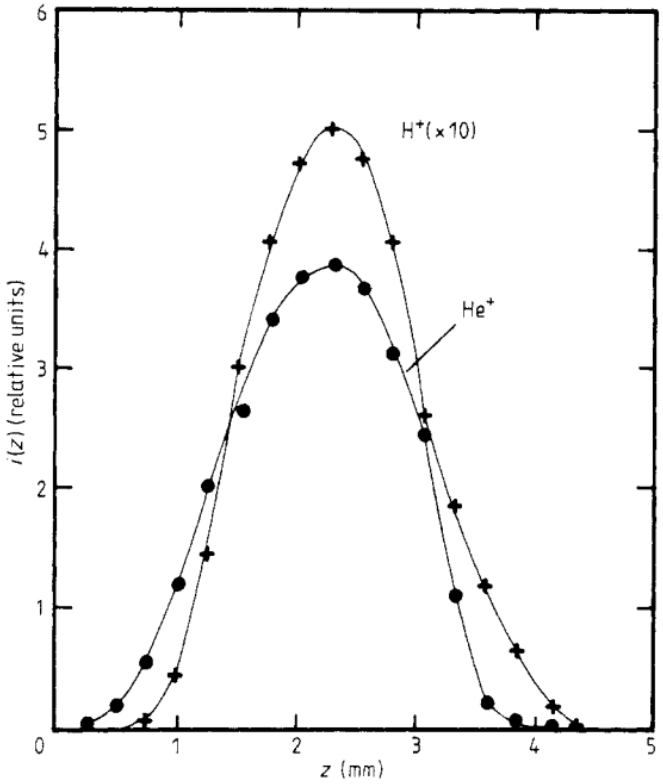

Figure 10: Intensity profiles at the intersection of two ion beams : 10 keV He^+ and 66 keV H^+ (E_{cm} = 40.3 keV). Calculated form factor F = 2.44 mm. Figure taken from [58].

simultaneously with the collision measurement, and therefore corrections have to be

made to account for fluctuations of beam density that can happen between density profiles measurements. These fluctuations are part of the uncertainties in the final cross section estimations.

1.3.1.2 Case of a charged particle beam and an effusive gas jet

Experiments involving collisions between an ion beam and atoms can be conducted using various techniques, including the use of a gas jet or merged-beam methods [60]. Gas jets are classified into two types: effusive jet [59] and supersonic jet [61]. The type of jet is determined by the Knudsen number K, defined by $K = \frac{\lambda}{d}$, where λ is the mean free path between two collisions and d the diameter of the orifice of the gas jet nozzle.

- **Effusive Jet:** When $K \geq 1$. In this scenario, the mean free path in the reservoir chamber is larger than the diameter of the orifice. As a result, atoms near the orifice have a high probability of crossing from the reservoir to the collision chamber without interacting with other atoms or the orifice itself. Consequently, the atoms escape the reservoir through simple thermal effusion. However, this non-collision condition results in low source flow and a wide dispersion of atomic velocities in both magnitude and direction.

- **Supersonic Jet:** When K « 1. A supersonic jet is produced by increasing the pressure upstream of the orifice (called in this case a sonic nozzle), so that the mean free path becomes much smaller than the nozzle diameter. This leads to a reversible adiabatic expansion of the gas, where atoms undergo numerous collisions, resulting in a highly supersonic and orderly flow. The collisions align the atomic motion along the jet axis, creating a uniform velocity distribution. Supersonic jets allow for the production of atomic beams with very small momentum spread compared to effusive sources, necessary for instance when momentum spectroscopy detection methods are used.

- **Merged-beams techniques** are more complex compared to the use of gaseous jets. General details about these techniques are found in Phaneuf *et al* [60]. For ion-atom collisions of the type $X^{q+} + Y \rightarrow X^{(q-1)+} + Y^{+}$, multicharged X^{q+} ions are produced by an ion source, and singly charged Y^{+} ions by another one. The Y^{+} ion beam is then neutralized by passing through a charge-exchange cell, allowing it to maintain its velocity. Magnetic or electrostatic analyzers are used to merge the ion beam with this neutral beam, aligning them along the same path. As the merged beams travel together over lengths of a few tens of cm, collisions between the ions and neutral particles occur. The products of these collisions are then separated from the reactants using another charge-state analyzer, and subsequently detected. An example of this technique can be found in [62].

In our experiment, an effusive gas jet for ion-atom collisions is used since our detection method does not necessitate small momentum spread of the jet atoms.

The method for the determination of the overlap between an ion beam and an effusive gas jet and by extension for extracting cross sections is given in [59]. The relevant quantities and axis are given in Figure 11. We consider a projectile beam along the x axis that traverses an effusive jet at the distance z_0 from the exit of the capillary and at a lateral position y_0 from the vertical axis z. This capillary has a diameter d and length

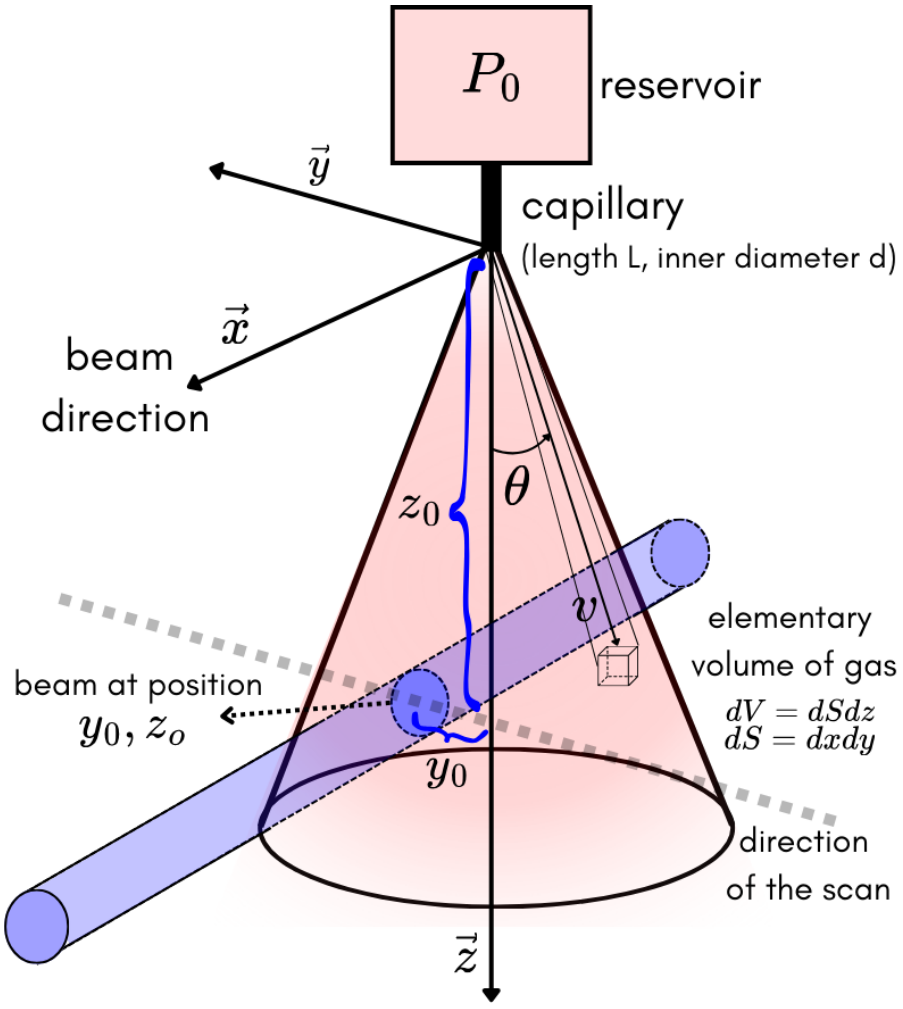

Figure 11: Schematic illustration of the geometry of the interaction zone between an ion beam and an effusive gas jet.

L, and is connected to a reservoir of gas kept at an input pressure P_0. The cross section σ of a given process happening between the ion projectile beam and the atomic targets of the jet is given by

$$\sigma = \frac{\mathsf{P}(y_0, z_0)}{B_{\text{jet}}(y_0, z_0)} \tag{18}$$

where $\mathsf{P}(y_0, z_0)$ is the inelastic event probability and and $B_{\text{jet}}(y_0, z_0)$ the beam-jet overlap. We can express $\mathsf{P}(y_0, z_0)$ as

$$\mathsf{P}(y_0, z_0) = \frac{N_{ev}(y_0, z_0)}{N_0} \cdot \frac{1}{\varepsilon} \tag{19}$$

where N_0 is the number of incident projectiles per second, N_{ev} the rate of detected events per second, and ε the detection efficiency. $B_{\text{jet}}(y_0, z_0)$ can be expressed as

$$B_{\text{jet}}(y_0, z_0) = \int\int\int \frac{j(x, y, z)}{N_0} n(x, y, z)\, dx\, dy\, dz \tag{20}$$

with $j(x, y, z)$ the ion flux and $n(x, y, z)$ the jet density.
To determine the beam-jet overlap and the probability $\mathsf{P}(y_0, z_0)$, the usual method consists in scanning laterally the jet along y. The integral $\int \mathsf{P}(y_0, z_0)\, dy_0$ is then extracted.

We define $R_{\text{exp}}(y_0, z_0)$ the experimental normalized beam-jet overlap profile as

$$R_{\text{exp}}(y_0, z_0) = \frac{\mathsf{P}(y_0, z_0)}{\int \mathsf{P}(y_0, z_0)\, dy_0} = \frac{B_{\text{jet}}(y_0, z_0)}{\int B_{\text{jet}}(y_0, z_0)\, dy_0} \tag{21}$$

Since $R_{\text{exp}}(y_0, z_0)$ is a ratio, the detection efficiency ε disappears and does not contribute to the beam-jet overlap determination.

- The **beam-jet overlap integral** $\int B_{\text{jet}}(y_0, z_0)\, dy_0$ can be determined as follows. The jet density $n(x, y, z)$ is expressed with the help of $\frac{d^3N}{dx\, dy\, dt}$, the number of atoms entering the elementary surface $(dx\, dy)$ per second at the position (x, y, z)

$$n(x, y, z) = \frac{d^3N}{dx\, dy\, dt} \cdot \frac{1}{v_z(x, y, z)} \tag{22}$$

where $v_z(x, y, z)$ is the gas velocity along z. We introduce a mean velocity $\langle v_z \rangle$ along z

$$\int\int n(x, y, z)\, dx\, dy = \frac{dN}{dt} \cdot \frac{1}{\langle v_z \rangle} \tag{23}$$

with

$$\langle v_z \rangle = \frac{\int\int dx\, dy\, n(x, y, z) v_z(x, y, z)}{\int\int dx\, dy\, n(x, y, z)} \tag{24}$$

It can be shown that $\langle v_z \rangle$ does not depend on z. Then we may write :

$$\int B_{\text{jet}}(y_0, z_0)\, dy_0 = \frac{dN}{dt} \cdot \frac{1}{\langle v_z \rangle} \tag{25}$$

This means that the beam-jet overlap integral does not depend on the beam intensity distributions along y and z.

- The **mean velocity** $\langle v_z \rangle$ is expressed as (in the case of a single emission point)

$$\frac{1}{\langle v_z \rangle} = \int_0^{\pi/2} p(\theta) \cdot \frac{1}{v \cos\theta}\, d\theta \tag{26}$$

where v is the modulus of the velocity and $p(\theta)$ the probability of flux emission θ expressed as

$$p(\theta) = \frac{2\pi}{dN/dt} \cdot \frac{dN}{d\Omega\, dt}(\theta) \sin\theta \tag{27}$$

where $dN/d\Omega\, dt(\theta)$ is the angular flux. The modulus of the atom velocity v is distributed along a $p(v)$ function having its mean value $\bar{v}$ given by

$$\bar{v} = \int p(v) v\, dv = v_{\text{th}}(1 + \alpha_l) \tag{28}$$

where α_l is a deviation factor depending on the flow regime. v_{th} is the mean thermal velocity of the atoms at temperature T, given by the well-known Maxwell-Boltzmann formula $v_{th} = \sqrt{\frac{8kT}{\pi m}}$ where k is the Boltzmann constant and m the atom mass.

Since our method integrates the interaction of many projectiles with many gas atoms, we can use the mean value $\bar{v}$ and get the final relation for $B_{\text{jet}}(y_0, z_0)$

$$B_{\text{jet}}(y_0, z_0) = R_{\text{exp}}(y_0, z_0) \cdot \frac{dN}{dt} \cdot \frac{f_\lambda}{v_{\text{th}}} \tag{29}$$

where we introduce the f_λ factor

$$f_\lambda = \frac{1}{1+\alpha_l} \int_0^{\pi/2} p(\theta) \cdot \frac{1}{\cos\theta}\, d\theta \tag{30}$$

Since $\frac{dN}{dt}$ and R_{exp} are measured and v_{th} known, the only theoretical part of this expression of the beam-jet overlap is f_λ, a factor that varies between 1.2 and 1.4 depending on the flow regime (pure molecular regime, intermediate and pure viscous regime). The flow regime can be determined by comparing the values of L, d, and λ_0 (mean free path of the atoms in the reservoir). More details on the experimental determination of f_λ are given in [59]. Once the beam-jet overlap is evaluated and the inelastic event probability for a given process is measured, the cross section given by the equation (18) can be extracted. In section 4.3.2, we give more details in the case of He and Ar effusive jets.

1.3.1.3 The single collision condition

Another important remark is that in order to correctly measure cross sections of a given process, we need to be in the single collision regime. This means that during the time of the interaction between the particles of the two beams, each particle undergoes at most one collision. The probability dP that a given process occurs is

$$dP = n\sigma dx \tag{31}$$

where σ is the reaction cross section, n the target density and dx the elementary length of the target. After integrating equation (31) we get

$$P = 1 - e^{-n\sigma\ell} \tag{32}$$

where ℓ is the thickness of the target, in this case the width of the target beam traversed by the projectile ions. When the "single collision condition" is satisfied, $P \ll 1$. The probability of double events (P^2) is negligible therefore $P \approx n\sigma\ell$. The dependence of the cross section on the target density (or any related parameter like the width or thickness of the target beam) is then linear. It is important to note that the single collision condition depends on the process considered and therefore this condition is not necessarily the same whether the process of interest is capture or excitation.

1.3.2 Selection of previous ion-atom studies

Numerous ion-atom collision experiments have been conducted across a wide range of velocities, utilizing various techniques such as ion spectroscopy, COLTRIMS, X-ray spectroscopy... This sub-section focuses on a few studies conducted at low velocities where electron capture is the main process:

- The group of C.L. Cocke at the Kansas State University performed extensive measurements. In Ali *et al* [63], they investigated multielectron reactions in 10 keV/u

Ar^{q+} + Ar collisions using ion spectroscopy, and more precisely time of flight coincidence techniques to measure absolute cross sections. The results were compared to the molecular classical over barrier model (M-COBM) [64]. A description of the COBM is given in [65,66]. The technique used and some results are presented below in section 1.3.2.1.

- Other experiments rely on the COLTRIMS (COLd Target Recoil Ion Momentum Spectroscopy) technique developed by the group of Schmidt-Böcking *et al* [67–69] as well as by our colleagues at CIMAP [70,71]. In a recent article, Zhang *et al* [72] studied state-selective charge exchange processes in Ar^{8+}-He collisions at 1 and 3 keV/u. This study was motivated by research on fusion and astrophysical plasma. Their work is briefly presented below in section 1.3.2.2.

- Another method used to study ion-atom collisions is the analysis of the X-rays emitted as a result of charge-changing processes when heavy ions are used. In fact, the captured target electrons occupy excited states of the ion that de-excites through Auger and/or radiative decays. At the end of the cascade X-rays are emitted, giving information on the dynamics. X-ray spectroscopy has been used by several research teams to study ion-atom collisions :

  - At the NIST (Maryland, USA), Tawara *et al* [73,74] studied the production of K-shell X-rays from multiple electron transfer in 4 keV/u Kr^{36+}, Ar^{18+} and Ne^{10+} - Ar collisions and hydrogen-like Si, S and Ar collisions with various atom and molecule gas targets at energies of 1-70 keV/u. The collisions involving bare ions are in the low-velocity regime ($v \approx 0.4$ a.u. and $v_e \approx 1.1$ a.u.) and those with H-like ions range from the low velocity ($v \approx 0.2$ a.u. and $v_e \approx 1.1 - 1.4$ a.u.) to intermediate regime ($v \approx 1.7$ a.u. and $v_e \approx 1.1 - 1.4$ a.u.). Low-resolution solid-state X-ray detectors were used (Ge detector with a resolution of 130 eV at 4.5 keV for bare ions and Si(Li) detector with a resolution of 200 eV at 5.9 keV for H-like ions). In the experiments with bare ions, it was found that multiple-electron transfer processes play a significant role in shaping the X-ray spectra. The experiments with H-like ions showed that at low energies ($<$ 10 keV/u) the cross sections for the production of K X-rays are nearly constant, and decrease slowly when the collision energy is increased. It was also noted that the Kα/Kβ intensity ratios increase slightly as the ionization energy of the target increases, suggesting that an electron is captured in different (n, ℓ) states when different targets are used. The study of these collisions was motivated by their role in astrophysical observations of X-rays from the tail of comets and in Tokamak fusion reactors. The results suggested that exact knowledge of the initial and final principal and angular momentum quantum numbers (n, ℓ) in electron transfer are the most essential missing information for understanding the entire X-ray emission process in plasmas.
  - At the Lawrence Livermore National Laboratory (California, USA), Beiersfdorfer *et al* [75] investigated also K-shell X-ray emission from collisions between bare oxygen ions and N_2 and CH_4 gas as well as bare neon ions on neutral neon, at much lower energies than Tawara *et al* (typically less than 20 eV/u). This corresponds to a velocity $v \approx 0.03$ a.u., and a velocity of the active electron $v_e \approx 1.3$ a.u. Therefore these collisions belong to the

low velocity regime. For detection they used a microcalorimeter with high resolution of 10 eV, sensitive to X-rays between 200 and 12000 eV. These systems have been studied to simulate the cometary X-ray emission. Their results showed that the emission from high-n levels depend on the ionization potential of the interaction gas, with electrons being captured in higher n levels if the ionization potential of the donor electron is lower.

– Our team at INSP [76] studied the X-rays produced during the collisions between 7 keV/u Ar^{17+} ions and gaseous Ar and N_2 targets from an effusive gas jet at the ARIBE facility (Caen, France) by combining low- and high-resolution detection techniques. In our experimental setup, the effusive gas jet used has the same characteristics as those described in this article. Details are given in section 1.3.2.3.

1.3.2.1 Using ion spectroscopy

The study by Ali *et al* [63] explored multielectron processes in 10-keV/u Ar^{q+} ($5 \leq q \leq 17$) on Ar collisions using time-of-flight coincidence between a channel-plate detector for recoil ions and a position sensitive detector for projectile ions, as illustrated in Figure 12.

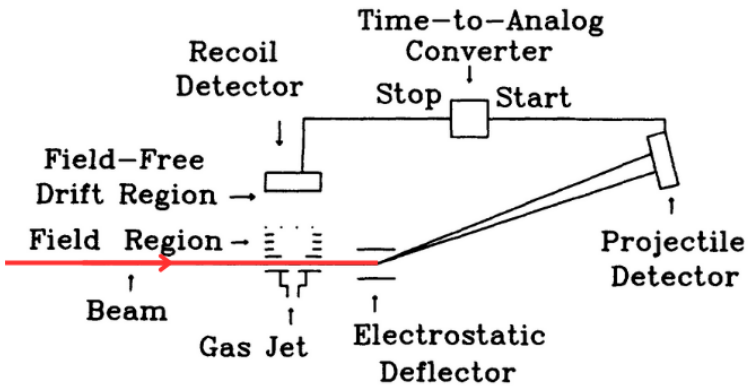

Figure 12: Schematic of the experimental setup used by Ali *et al* [63].

Absolute cross sections for total charge-transfer (σ_q) and projectile charge-change ($\sigma_{q,q'}$) were obtained by normalizing to cross sections reported in the literature in [77]. The experimental setup involved a 10-keV/u Ar^{q+} ion beam provided by the Kansas State University Cryogenic EBIS. This corresponds to the low-velocity regime since $v \approx 0.6$ a.u. and $v_e \approx 1.1$ a.u. The Ar gas target was supplied by a molecular jet, and the gas flow was adjusted to be in the single collision regime with an estimated pressure of 0.2-0.5 $\times$ 10^{-3} mbar. Figure 13 gives the experimental cross sections for projectile charge-change ($\sigma_{q,q-k}$) from reaction

$$Ar^{q+} + Ar \rightarrow Ar^{(q-k)+} + Ar^{i+} + (i-k)e^- \quad (33)$$

and total charge transfer ($\sigma_q = \sum_k \sigma_{q,q-k}$) as a function of q. The cross sections for projectile charge change decrease with k and cross sections for total and one-electron charge change exhibit nearly linear dependence on the projectile charge state (q). This observation is in reasonable agreement with the molecular classical overbarrier model (MCBM) predictions. This allowed for a detailed interpretation of the experimental

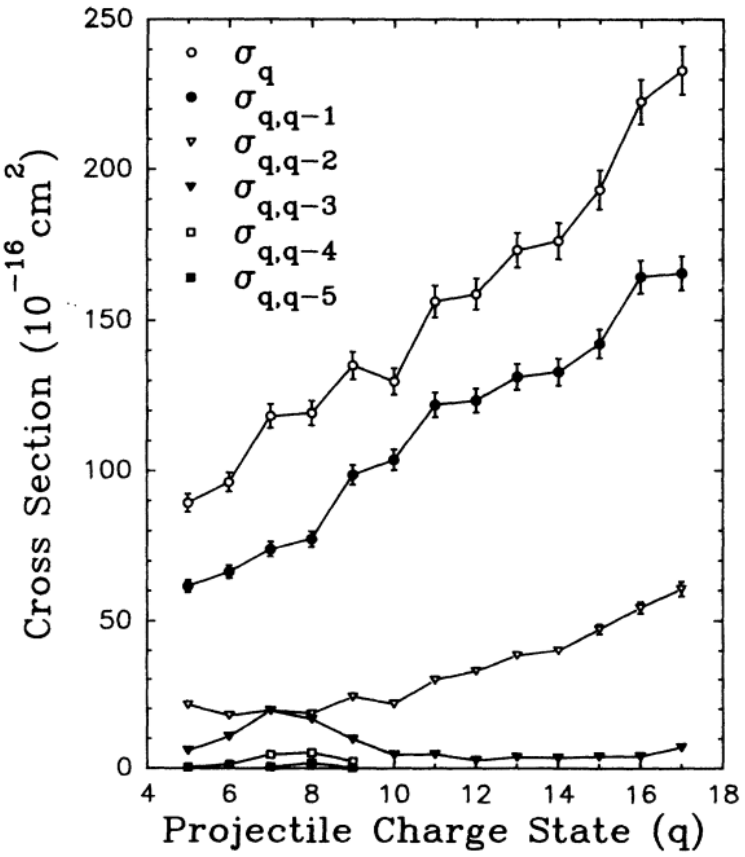

Figure 13: Projectile charge-change cross sections ($\sigma_{q,q-k}$) and total charge transfer cross section (σ_q) for 10 keV/u Ar^{q+} or Ar. Figure taken from [63].

data, indicating that the MCBM reasonably predicts the cascade stabilization of multiply excited projectiles, especially when including autoionization processes. This important work underscored the need for a more extensive experimental database on multielectron processes in slow ion-atom collisions to better understand the dynamics leading to the stabilization of multiply excited ionic species.

1.3.2.2 Using COLTRIMS

The study by Zhang *et al* [72] explored $Ar^{8+} + He \rightarrow Ar^{7+} + He^+$ charge exchange process at a collision energy of 1 and 3 keV/u, and only 1 keV/u result is presented here. This corresponds to the low-velocity regime since $v \approx 0.2$ a.u. and $v_e \approx 1.3$ a.u. They use the COLTRIMS technique, which allowed a state-selective study of the capture process. Their setup involves intersecting a beam of Ar^{8+} ions produced from an electron beam ion source (EBIS) with a supersonic He gas jet within a time-of-flight (TOF) spectrometer. The spectrometer measures the longitudinal and transverse momentum of the recoil ions, enabling the resolution of quantum-state selectivity for one 1s electron of He captured into the 4s, 4p, 4d + 4f, and 5s states of Ar^{7+}, see Figure 14. The experimental resolution was not capable of discerning between 4d and 4f capture processes. Capture is dominant in the n = 4 channel, and especially in the 4d+4f channel. Differential and absolute cross sections were measured and were found to be in good agreement with calculations performed using a semiclassical Asymptotic

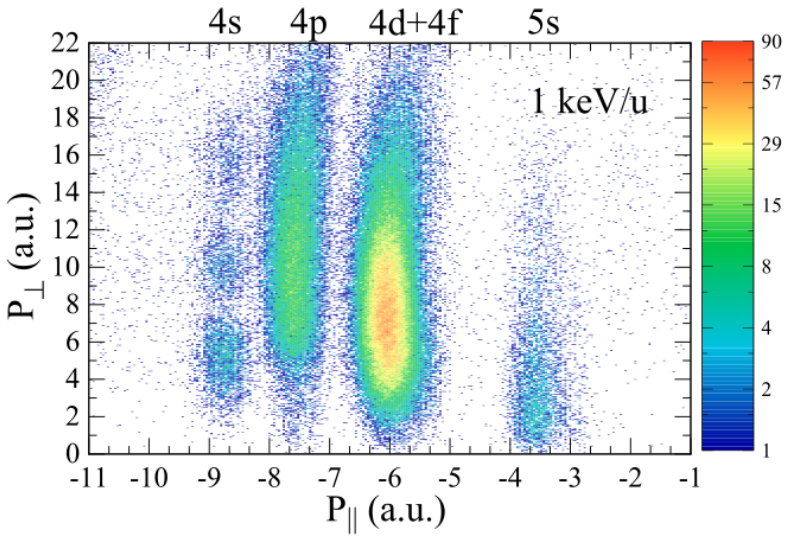

Figure 14: Two-dimensional momentum distributions in the 1 keV/u Ar^{8+} charge-exchange with He. The horizontal axis and the vertical axis represent the longitudinal recoil ion momentum $P_{\parallel}$ and the transversal recoil ion momentum $P_{\perp}$, respectively. Figure taken from [72].

State Close Coupling (SCASCC) approach with two active electrons (the electrons from Ar^{8+} are frozen and only those from He are taken into account) in collaboration with the LCPMR team [72]. Table 1 gives the comparison between experimentally determined and calculated relative capture cross sections into different $n\ell$ states of Ar^{7+}. In fact, the best agreement that was found is between experimental results and SCASCC calculations among other comparison with theoretical and experimental data from [78, 79].

$n\ell$	Exp.	SCASCC
4s	3.5	3.6
4p	22.5	22.6
4d + 4f	70.7	70.4
5s	3.3	3.5

Table 1: Relative state-selective capture cross sections for charge exchange between Ar^{8+} and He at 1 keV/u. Table extracted from [72].

Overall this study demonstrates the need for systematic state-selective charge exchange studies in ion-atom collisions, to further improve the knowledge of highly excited quantum state-selective dynamics.

1.3.2.3 Using X-ray spectroscopy

The study by our team at INSP [76] focused on collisions involving Ar^{17+} ions with gaseous Ar and N_2 targets. These interactions were investigated with 7 keV/u argon beams ($v \approx 0.53$ a.u., and the velocity of the active electron $v_e \approx 1.1$ a.u., corresponding to the low-velocity regime) produced by an Electron Cyclotron Resonance (ECR) ion source at the ARIBE facility in Caen. These ions were directed towards the target gases in a controlled environment, ensuring precise interactions by carefully overlapping the ion beam with an effusive jet.

The experimental setup shown in Figure 15 included two types of X-ray detectors: a

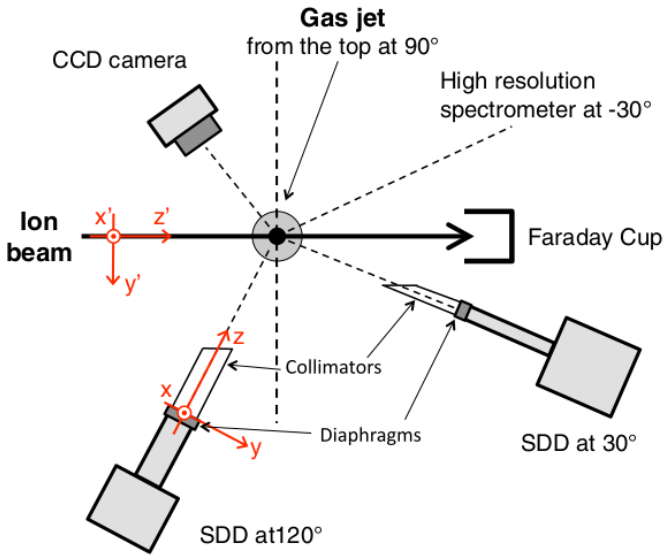

Figure 15: Schematic view of the experimental setup used by our team in [76].

SDD detector for low-resolution (190-210 eV at 3 keV) spectroscopy and a high-resolution (3.2 eV at 3.1 keV) Bragg Crystal Spectrometer. This detection setup allowed to resolve He-like Ar^{16+} Lyman series and enabled the precise determination of the distribution of the $n\ell$ electron capture probability. The low-resolution and high-resolution spectra are shown in Figure 16. For fitting the low-resolution spectrum, gaussian profiles were used, with relative intensities derived from the analysis of the high-resolution spectrum. On the high-resolution spectrum, the Ar^{16+} 1snp $\rightarrow$ $1s^2$ (with n up to 10) transitions are visible. The transitions from n = 2 are partially resolved, as well as transitions from Li-like Ar. These latter originate from de-excitation of the 1s2s2p state. This state is formed by multiple-electron capture from the primary 1s Ar^{17+}. It can also originate from single capture on 1s2s $^3S_1$ Ar^{16+} metastable ions formed by collision with the residual gas in the beamline (maintained at a pressure of 10^{-7} mbar) or present in the interaction chamber (10^{-6} mbar with the gas jet). A 10 % contribution from metastable states was determined. Taking this into account, the hardness ratio H (ratio between the unresolved n $>$ 2 $\rightarrow$ 1 and the 2 $\rightarrow$ 1 transitions) was reduced by a factor of 2 compared to other studies with different setups, showing the importance to know the metastable states proportion. From the X-ray spectra, the total and partial X-ray emission cross sections are extracted. The total one was found to be 11.4×10^{-15} cm^2 $\pm$ 15 %, showing good agreement with previous studies but with improved precision.
The (P_n) distribution of the single electron capture probability was measured with populations from $n = 7$ to $n = 10$. Multielectron capture has been highlighted as well. They populate preferentially excited states lying in lower ℓ values than single-electron capture. The sensitivity to the ℓ-distribution of n levels populated has been tested with two extreme cases, i.e. flat and statistical distribution. This enabled the extraction of the absolute value of the single-electron capture cross section occurring in $n = 7 - 10$. The extracted cross section value ranges from σ_s = 4.6 $\times$ 10^{-15} cm^2 (flat) to σ_s = 12.8 $\times$ 10^{-15} cm^2 (statistical). This result was found to be satisfactory compared to the value of about 8 $\times$ 10^{-15} cm^2 obtained by Ali *et al* [63]. Note that those values are also in good agreement with the Classical Over Barrier (COB) model [65, 66] that predicts σ_s = 6.6 $\times$ 10^{-15} cm^2.

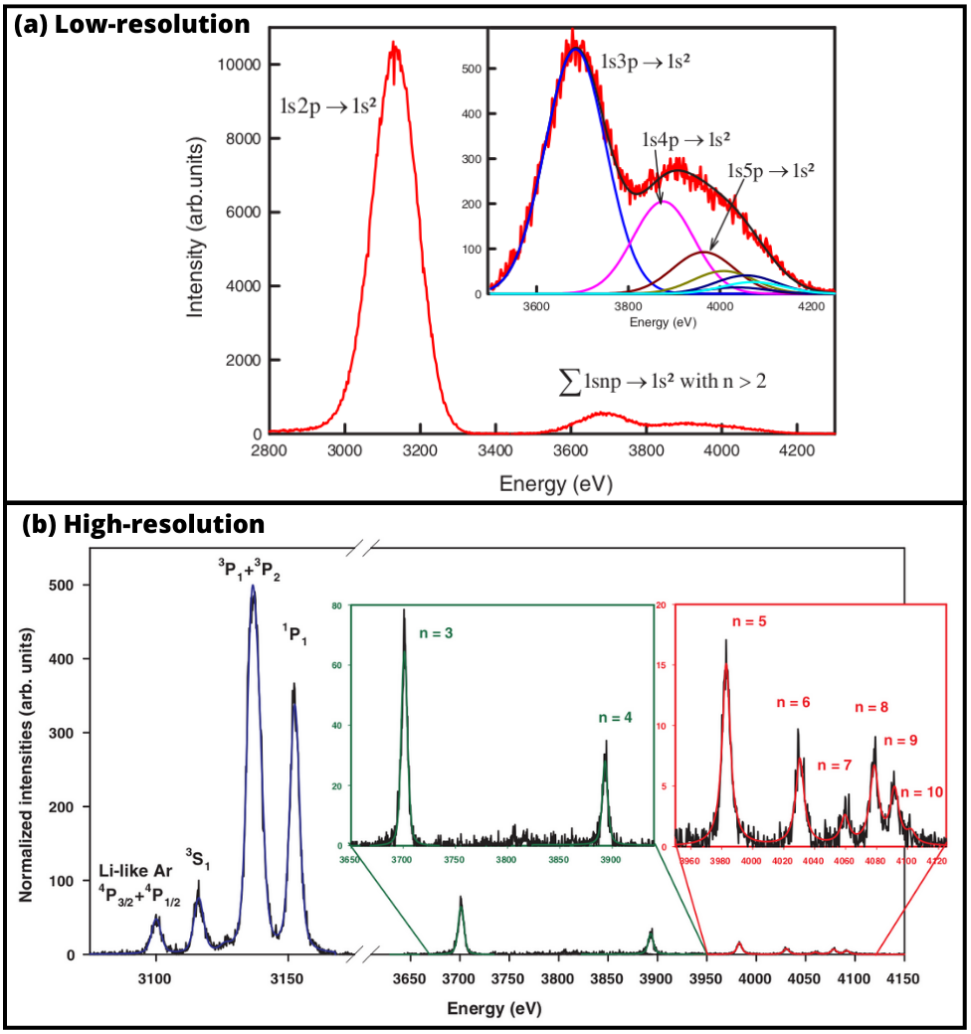

Figure 16: X-ray spectra after background subtraction exhibiting transitions from Ar^{16+} ions produced by collisions of 7 keV/u Ar^{17+} ions with the argon gaseous target (p = 1.5 mbar). (a) Low-resolution spectrum with experimental data in red and gaussian fit results for different n > 3 → 1 transitions in the zoom inset. (b) High resolution spectrum where the He-like Ar 1snp → $1s^2$ (with n up to 10) transitions are visible and fitted with Voigt profiles. Figures taken from [76].

Additionally, Figure 17 shows the comparison of the measured X-ray intensities from $n = 2$ to 10 with the intensities obtained from TC-BGM calculations [47], a semi-classical approach mentioned in section 1.2.2, for single capture and cumulative single and double capture (the term "cumulative capture" is used to designate the sum of the actual capture in a given shell and the apparent capture into the same shell, resulting from Auger decay). When multiple capture is not considered, the results differ greatly from experimental data. The agreement between the experimental data and the cumulative single and single + double calculations is very good between $n = 3$ and $n = 7$. For correctly modelling results for $n > 7$, the authors state that a larger basis including higher n shells may be useful.

Overall, the findings emphasize the importance of combining X-ray spectroscopy with other diagnostic techniques, such as ion spectroscopy, for ion charge state detection to obtain a more comprehensive understanding of the dynamics of ion-atom collisions. Accounting for metastable states for accurate measurements is also an important

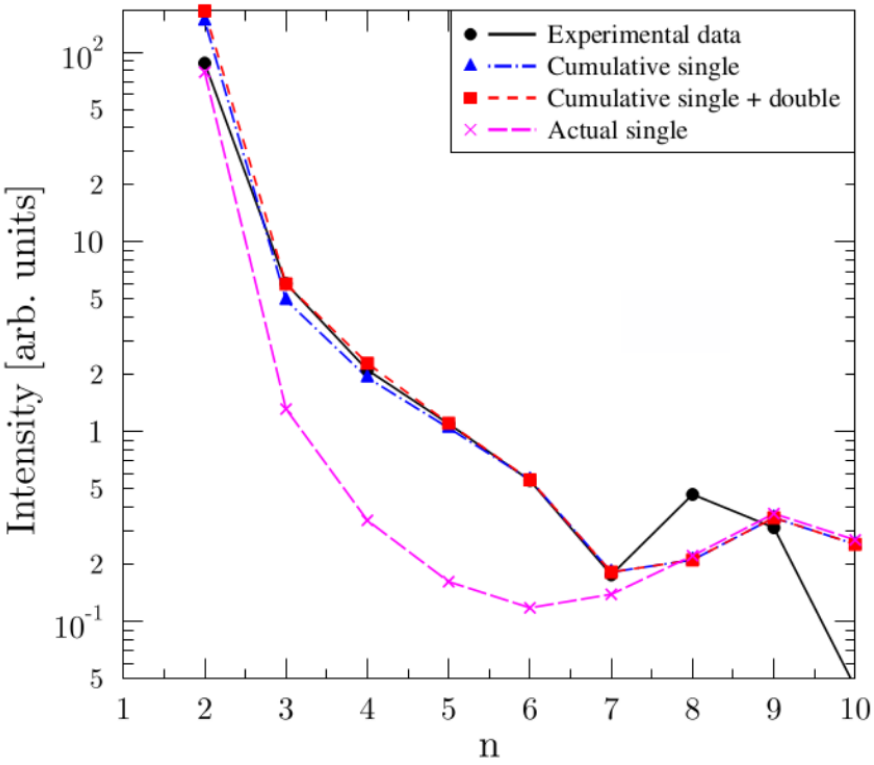

Figure 17: Comparison of experimental X-ray intensities from [76] with the intensities obtained from the single, the cumulative single as well as the sum of the cumulative single and double capture cross sections for each shell. Figure taken from [47].

aspect. Our collision setup at INSP has been designed with these considerations in mind, and aims to propose ion and X-ray spectroscopy coincidence measurements for ion-ion and ion-atom collisions.
The cross sections for ion-atom charge exchange need to be known in our experiments since collisions between the ion beams and residual gas are a main source of pollution in our measurements. The proportion of metastable ions in the beams produced by our ECR sources needs also to be determined.

1.3.3 Selection of previous ion-ion studies

Ion-atom studies offer great insight into the electron dynamics during collisions, but they often involve a lot of electrons, so to gain an even better understanding, ion-ion studies are necessary. Experimental studies on ion-ion collisions are less common compared to those on ion-atom collisions when gas jets are used. This is primarily due to the increased complexity of conducting ion-ion experiments. These experiments require the creation of not one, but two ion beams, each necessitating a precise control of their charge state before the collision, their shape and overlap at the collision point and the capability to perform measurements on the ion products, making the experimental setup significantly heavier. Vacuum conditions required are also extremely stringent, necessitating an ultra-high vacuum (UHV) environment, typically around 10^{-10}-10^{-11} mbar. Several teams have already conducted ion-ion collision experiments in the low velocity regime. The collision energy used in the works presented below is the center-of-mass energy E_{CM}

given in the specific case of a cross beam experiment by

$$E_{\mathrm{CM}} = \mu \left(\frac{E_1}{m_1} + \frac{E_2}{m_2} - 2\sqrt{\frac{E_1 E_2}{m_1 m_2}} \cos\theta \right) \tag{34}$$

where θ is the intersection angle and $\mu = m_1 m_2/(m_1 + m_2)$ the reduced mass.

- At Newcastle University (UK), Peart *et al* [80–82] measured cross sections for the formation of X^{2+} in X^{+}+X^{+} collisions (where X^{2+} can be formed by electron capture but also by ionization of one of the X^{+}) between singly charged alkaline ions from lithium to cesium at interaction energies between 20 and 90 keV. The experimental apparatus involved crossing the beams from two ion sources at 160°. One of the beams has a higher energy than the other by a factor 1 to 4 approximately. The energies of each beam varied between 10 keV to 80 keV (corresponding to velocities v between 0.05 a.u. for 10 keV Cs^{+} and 0.7 a.u. for 80 keV Li^{+}). The corresponding electron velocities v_e go from 1.3 a.u. for Cs^{+} to 2.4 a.u. for Li^{+}, therefore these collisions are in the low-velocity regime. Cross sections for the production of X^{2+} range from the order of 10^{-18} cm^2 for Li^{+} to 10^{-17} cm^2 for Cs^{+} at 20 keV and from 10^{-17} cm^2 for Li^{+} to 10^{-16} cm^2 for Cs^{+} at 80 keV. The authors concluded that no simple empirical scaling laws for cross sections could be found. These collision systems were chosen for their relevance in heavy ion fusion (HIF) research.

- At Oak Ridge University (Tennessee, USA), Kim and Janev [83] carried out X^{3+}+X^{3+} collisions (where X = Ar and Kr) at a center-of-mass energy of 60 keV to measure electron-loss cross sections, i.e. the formation of X^{4+}. A folded-beam ion-ion collider was used. It works by mirroring and folding onto itself a 30 keV beam that is produced by an ion source. The velocities of the beams were $v \approx 0.1 - 0.2$ a.u. and the electron velocities $v_e \approx 1.9 - 2.1$ a.u., making these collisions belonging to the low velocity domain. The cross sections obtained for electron loss $\sigma(3 \rightarrow 4)$ are $(6.1 \pm 1.7) \times 10^{-16}$ cm^2 and $(2.9 \pm 0.8) \times 10^{-16}$ cm^2 for argon and krypton, respectively.

- At Kansas State University, the team of C.L. Cocke [84] investigated single charge exchange in collisions of the type X^{2+}+X^{+} (where X = He, Ne, Ar) with center-of-mass energies between 2 an 15 keV using a 90° intersecting beam technique. In order to separate the ion–ion collision products from ions coming from background collisions, the collision region was maintained at a high retarding voltage. These collisions are in the low-velocity regime since the velocities of the beams were $v \approx 0.1 - 0.4$ a.u. and the electron velocities $v_e \approx 1.7 - 2$ a.u. The data showed that the charge transfer cross section for helium collisions is about the same as that for the nitrogen collision ($\approx 7\times$ 10^{-16} cm^2), while the cross section for the argon collision in the same energy range is about a factor of two larger. The origin of this result was demonstrated to be due to the size of the atomic orbital of the active electron involved in the collision.

- The team from Giessen (Germany) studied various types of ion-ion collisions like Li-like ions on bare helium ions [85] at center-of-mass energies between 10 and 256 keV and symmetrical collisions between multiply charged heavy ions [86–88] at energies between 10 an 90 keV using a setup that we drew inspiration from

for our own experiments. The study of single charge exchange and ionization in symmetrical ion-ion collisions is motivated by the need to better predict and understand intensity loss in ion storage rings due to interactions between the ions of the beam. The method and results of the Giessen group for the multiply charged heavy ions collisions are presented in more details below.

The experimental setup used at the University of Giessen to perform collisions between multiply charged ions is presented in details in [89] and shown in Figure 18. The

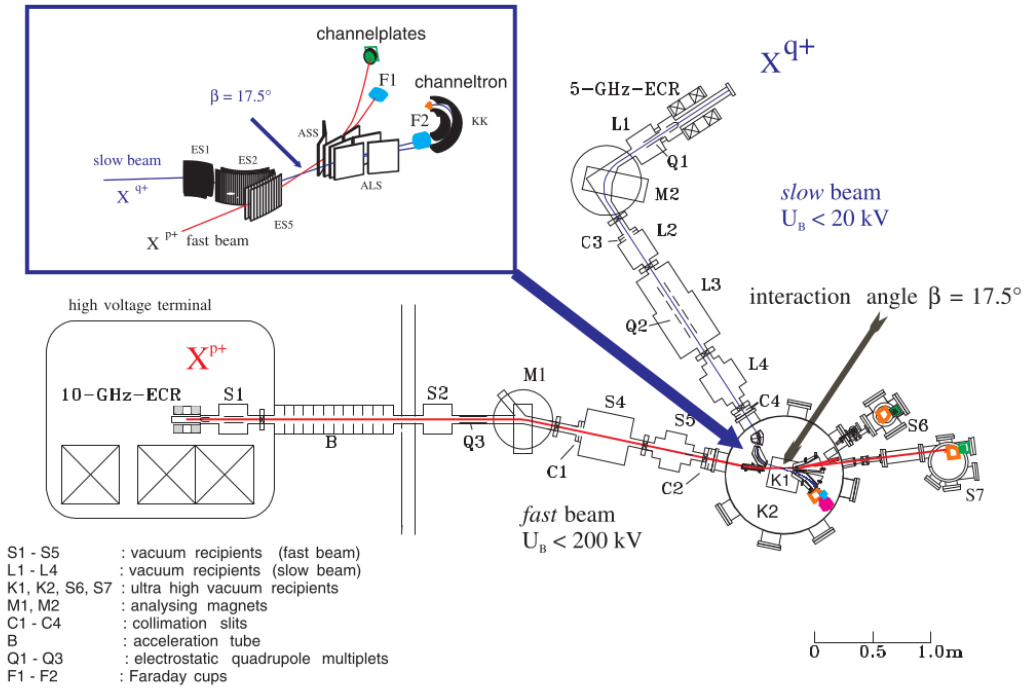

Figure 18: Setup for ion-ion collisions at Giessen university. Figure taken from [87].

high-energy beam line provides ions produced in a 10 GHz ECR ion source on a high-voltage terminal with potentials up to 200 kV. The ion beam (with current of a few hundred nA) is focused using electrostatic quadrupoles and collimated by two four-jaw slits before entering the UHV chamber. The low-energy beam line delivers ions generated by a 5 GHz ECR ion source and extracted at voltages up to 20 kV with currents of a few tens of nA [87]. The beam is focused by electrostatic quadrupoles, and the parameters can be adjusted by modifying the quadrupole voltages. The beam path intersects at angles of 17.5° (as shown on Figure 18) or 137.5°, if the geometry of the interaction chamber is inverted. Electrostatic sectors (ES1, ES2, ES5) are used prior to the collision for beam focusing, and electrostatic analyzers (ASS, ALS, KK) for product separation after the collision. The collision environment for these experiments is maintained in UHV conditions, with a background pressure measured at 7×10^{-11} mbar [88]. The detection system includes Faraday cups (F1 and F2) and single-particle detectors (channeltron and channelplates). F1 collects the primary slow ion beam, and F2 the fast primary ion beam. A channeltron detects ions from ion-ion or residual gas collisions. A chevron array of microchannel plates and a resistive anode, providing position sensitivity, detect product ions from the fast beam. Coincidence measurements use a Time-to-Amplitude Converter (TAC).

The studies [86–88] involve symmetrical collisions of the type $X^{q+} + X^{q+}$ with q = 2,3,4 and X = Ar, Kr, Xe, Pb and Bi for center of mass energies in the range of 10-90 keV. The electron velocities v_e are between 0.7 and 1.1 a.u. and the ion velocities $v \approx 0.05 - 0.5$ a.u. The crossed-beams technique used in these studies is effective for measuring absolute total cross sections for both total charge transfer ($X^{q+} + X^{q+} \rightarrow X^{(q-1)+} + X^{(q+1)+}$) and ionization reactions ($X^{4+} + X^{4+} \rightarrow X^{4+} + X^{5+} + e^-$). The cross sections extracted by the Giessen group for these processes for the different ion species are all of the order of 10^{-16} cm^2 and are presented in Figure 19. As can be

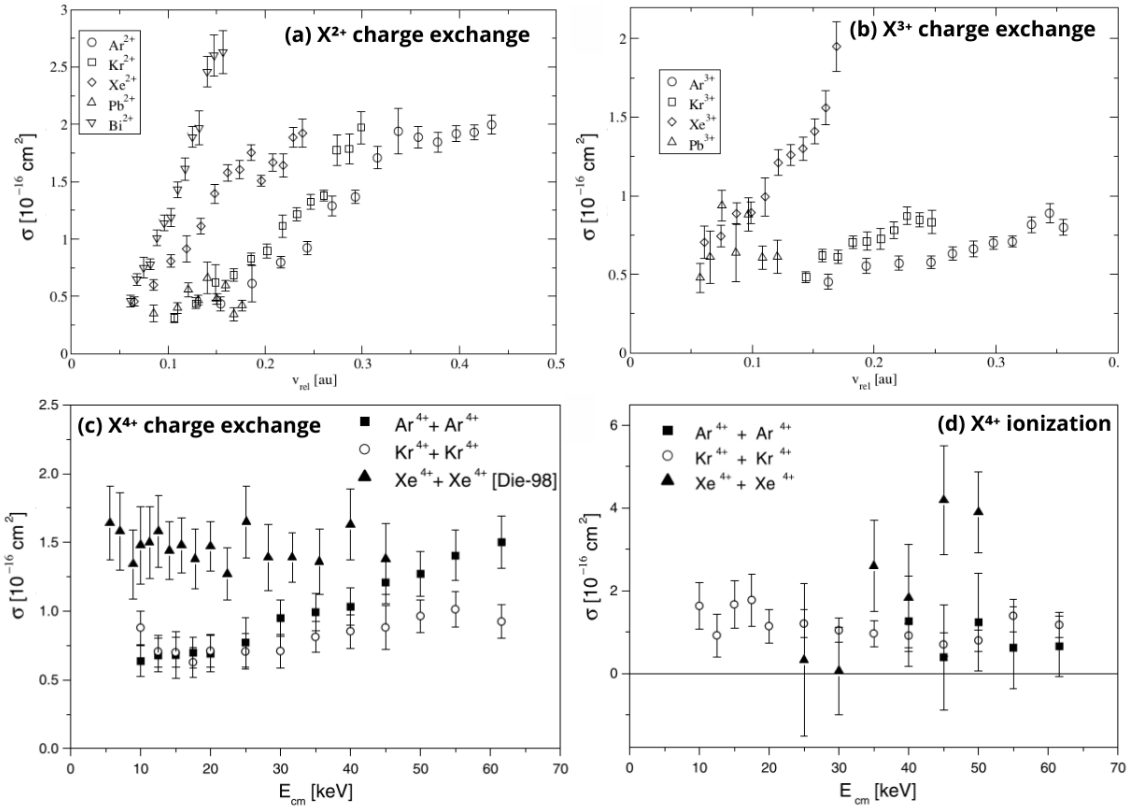

Figure 19: Cross section measurements for charge exchange and ionization : (a) charge exchange cross section for X^{2+} + X^{2+} as a function of the relative velocity [88], (b) charge exchange cross section for X^{3+} + X^{3+} as a function of the relative velocity [88], (c) charge exchange cross section for X^{4+} + X^{4+} as a function of the center-of-mass energy [87], and (d) ionization cross section for X^{4+} + X^{4+} as a function of the center-of-mass energy [87].

seen, ionization cross sections (d) are comparable to or slightly lower than the electron transfer cross sections (c) for the same systems [87], with no significant variation observed with the energy. However, for Xe^{4+}, the ionization cross section increases with energy and surpassed the transfer cross section at higher energies, exhibiting a threshold behavior that remains not fully understood [86].

The cross sections for charge transfer (Figure 19 (a), (b) and (c)) depend on the relative velocity of the ions and the charge state. For lower charge states ($q = 2$ and 3), the cross sections increase with the collision energy, however for higher charge states ($q = 4$) the cross sections show less dependence on energy. The cross sections are influenced by the presence of metastable ions in the beams. Especially for X^{4+} collision systems, charge transfer from an excited state leads to larger cross sections and less dependance on the collision energy [88]. These metastable ions also complicate the treatment of the experimental data since more possible channels are available for charge

transfer. This emphasizes the necessity for systematic measures of the percentage of metastable ions in beams when performing collision experiments.
In conclusion, the Giessen group measured absolute charge transfer and ionization cross sections. Their study also highlighted the need for further studies, especially in the determination of the role of metastable states in ion beams. Their experiments used ions with low charge states and therefore a lot of electrons may be involved in the collision dynamics. To fully understand the electronic processes and how additional electrons play a role in the collision dynamics, systematic studies with highly charged ions involving one electron at first, then adding more electrons one by one into the system are necessary. Our setup, largely inspired by the Giessen setup, aims at performing such experiments.

1.3.4 Empirical methods to estimate cross sections

To plan experimental studies, assess their feasibility, and assess the compatibility of results, the experimenter must be able to estimate, even in a very approximate way (at the order of magnitude level), the expected outcomes. When no data is available in the literature for comparison, relying on simple models is the only solution: this is referred to as an experimental approach to theory. For this reason, two models are presented below, which have been used to compare results (such as the extraction of cross sections) obtained during tests of the experimental setup (discussed in Chapter 5). The first one is a scaling law for capture cross sections developed by Müller and Salzborn [90], and the second one is a method for estimating capture cross sections based on the evolution of the populations of the different charge states in ion-atom interactions, called growth-rate method [91].

1.3.4.1 Müller-Salzborn scaling model

Alfred Müller and Erhard Salzborn developed in 1977 [90] a scaling law for cross sections in multiple electron transfer during collisions between highly charged ions and neutral atoms or molecules. This law was derived through a systematic process involving experimental data collection, empirical modeling, and theoretical insights. Initially, they conducted experiments measuring cross sections for electron capture of up to four electrons in collisions involving rare gas ions (such as $Ne^{q+}, Ar^{q+}, Kr^{q+}, Xe^{q+}$ with charge states ranging from 2 to 8) and various neutral targets including rare gases (He, Ne, Ar, Kr, Xe) and molecular gases (H_2, N_2, O_2, CH_4, CO_2). These experiments focused on collision energies between a few keV and 100 keV.
To establish an empirical relationship describing these measurements, they considered factors such as the initial charge state of the projectile, the number of electrons transferred, and the ionization potential of the target. The empirical scaling law for the transfer of k electrons that they proposed is

$$\sigma_{q,q-k}(\text{cm}^2) = A_k \times q^{\alpha_k} \times (I(\text{eV}))^{\beta_k}, \quad k = 1, 2, 3, 4 \tag{35}$$

where I is the first ionization potential of the target and A_k, α_k and β_k are free parameters. They performed a regression analysis to fit the measured cross sections to this empirical formula, optimizing the parameters A_k, α_k, and β_k for different numbers of transferred electrons (k ranging from 1 to 4). These parameters are given in Table

k	A_k	α_k	β_k
1	$(1.43 \pm 0.76) \times 10^{-12}$	1.17 ± 0.09	-2.76 ± 0.19
2	$(1.08 \pm 0.95) \times 10^{-12}$	0.71 ± 0.14	-2.80 ± 0.32
3	$(5.50 \pm 5.8) \times 10^{-14}$	2.10 ± 0.24	-2.89 ± 0.39
4	$(3.57 \pm 8.9) \times 10^{-16}$	4.20 ± 0.79	-3.03 ± 0.86

Table 2: Fit parameters for the Müller and Salzborn cross section scaling law given by equation (35).

2. The fit quality was validated by comparing the calculated cross sections with experimental data for specific collision systems and iteratively adjusting the empirical formula to improve the fit. Figure 20 (taken from [90]) shows experimental cross sections for charge transfer of 1 to 4 electrons as a function of the projectile charge state for 30 keV Ar^{i+} incident ions on Xe (a) and 30 keV Xe^{i+} incident ions on Kr (b). The solid lines represent the fits made with equation (35) using parameters from Table 2. One can see that for both collision systems, the evolution of cross sections with the initial projectile charge state have very similar shapes and values of the same order of magnitude. All cross sections increase with the initial charge state. The dominant process in both cases is single electron capture, followed in order by two- three- and four-electron capture. The agreement between the experimental data points and the empirical scaling law can be seen to be fairly good.

To objectively assess the scaling law applicability, they analyzed the frequency distri-

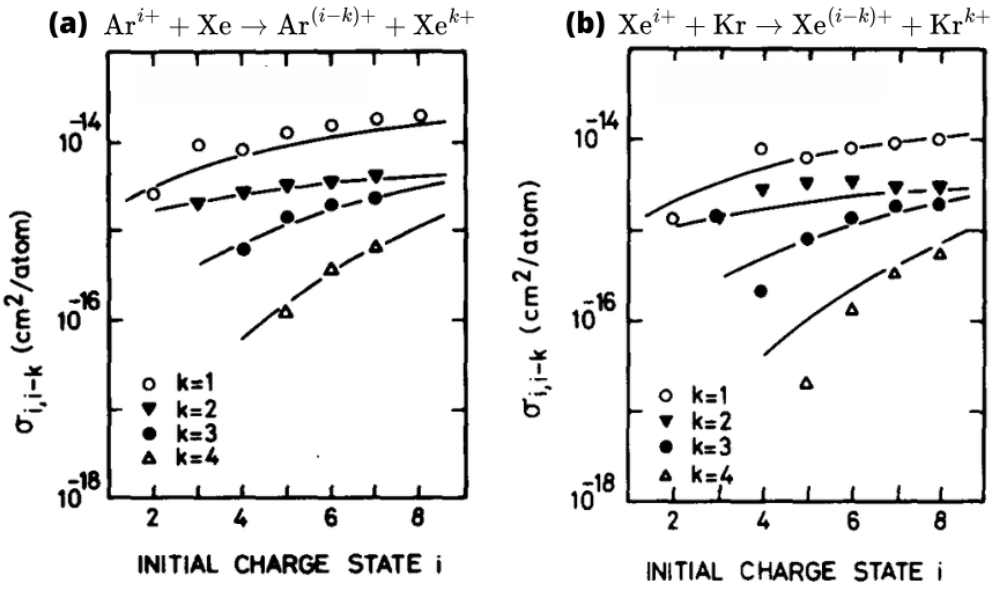

Figure 20: Electron capture cross sections for 30 keV Ar^{i+} ions on incident on Xe (a) and 30 keV Xe^{i+} ions incident on Kr (b). The solid lines are computed with equation (35) using the parameters of Table 2. Figures taken from [90].

bution of the ratios of experimental to predicted cross sections. This analysis showed that about two-thirds of the measured cross sections fell within a $\pm 35\%$ error margin around the predicted values, demonstrating the law's reliability across different condi-

tions. Further studies have proven that this scaling law is applicable for projectile charge states up to q = 40 [92]. Even though this empirical model does not pretend to give an exact value for electron capture cross sections, it can provide a very good basis for an estimation of cross sections, especially in collisions where no direct comparative data is available. This scaling law is used in our study for comparing cross section for one- and two- electron capture on residual gas from argon ions, in the framework of the tests performed on different parts of the experimental setup. This work is detailed in section 5.3.

1.3.4.2 Growth-rate method

The growth rate method was first used by Tawara and Russek in [93] and in the article of Vancura *et al* [91]. These measurements involve evaluating the evolution of different charge states of ions as they pass through a gas cell to infer the cross sections for various charge-changing collisions. In this method, a beam of ions with an initial charge state q traverses a gas cell of length l and of density n, leading to a target thickness denoted by $\rho = nl$. Due to charge-changing collisions, new charge state fractions are produced, and the growth of these different ion charge states is recorded as a function of the pressure in the gas cell, directly linked to ρ. Figure 21 shows the pathways that can lead to a

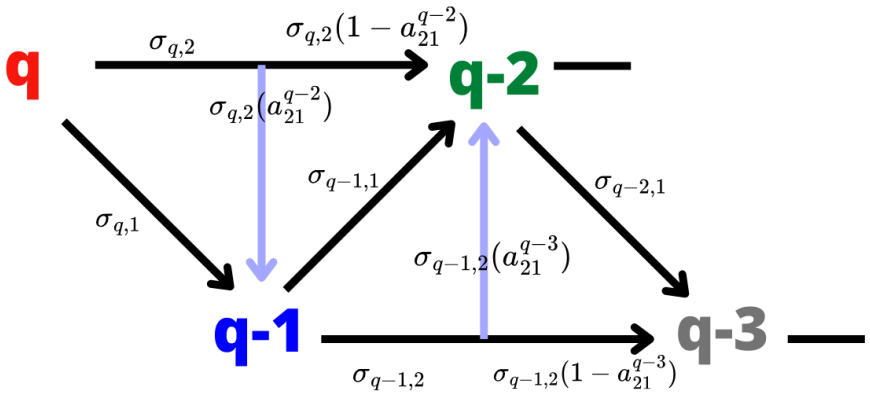

Figure 21: Pathways that can lead to a given charge state of a projectile of initial charge state q. Only direct one- and two-electron capture, and autoionization of excited states of the projectile are represented.

given charge state of a projectile of initial charge state q. The charge state q can change directly to $q-1$ or $q-2$ following collisions, with effective cross sections denoted by $\sigma_{q,1}$ and $\sigma_{q,2}$. It is also possible that the charge state q changes to $q-1$ by two-electron capture followed by autoionization with a cross section $\sigma_{q,2}a_{21}^{q-2}$.The effective charge transfer cross section is given by

$$\sigma_{qq-1} = \sigma_{q,1} + a_{21}^{q-2}\sigma_{q,2} \tag{36}$$

The set of differential equations describing the evolution of the charge state distribution with gas-target thickness ρ for the q, $q-1$ and $q-2$ charge states are

$$\begin{aligned}
\frac{dN_q}{d\rho} &= -N_q(\sigma_{q,1}+\sigma_{q,2}) \\
\frac{dN_{q-1}}{d\rho} &= N_q(\sigma_{q,1}+\sigma_{q,2}a_{21}^{q-2}) - N_{q-1}(\sigma_{q-1,1}+\sigma_{q-1,2}) \\
\frac{dN_{q-2}}{d\rho} &= N_q\sigma_{q,2}(1-a_{21}^{q-2}) + N_{q-1}(\sigma_{q-1,1}+\sigma_{q-1,2}a_{21}^{q-3}) - N_{q-2}(\sigma_{q-2,1}+\sigma_{q-2,3})
\end{aligned} \tag{37}$$

From equation (37) and Figure 21, the equations for the evolution of the other charge states can be easily determined.

The system of equations can be solved using Laplace transforms to yield the ratios between the final number of ions of different charge states ($N_q(\rho)$, $N_{q-1}(\rho)$...) and the initial number of ions $N_q(0)$. For data analysis, the recorded data from collisions between the ion beam and the gas jet are fitted by a second-order polynomial. The coefficients of the fit are directly related to the cross section of interest.

More precisely, the growth rate method enables the determination of cross sections through the following steps: measuring the fraction of ions in each charge state $N_q(\rho)$, $N_{q-1}(\rho)$, and $N_{q-2}(\rho)$ as a function of gas-target thickness ρ; fitting the measured fractions to the equations derived from the growth rate model; and extracting cross sections from the fitting process. As an example, Figure 22 gives the evolution of the ratio between the one- and two-electron transfer populations and the initial population, as a function of the gas target thickness, for a 0.7 keV/u Ar^{13+} on H_2 collision. The experimental points as well as a polynomial fit are represented. From the fit parameters, the cross section were extracted and are $\sigma_{13,12} = 46.2 \pm 6.1 \times 10^{-16}$ cm^2 and $\sigma_{13,11} = 0.9 \pm 0.7 \times 10^{-16}$ cm^2. By analyzing how the charge state fractions evolve with increasing ρ, it is possible to characterize the interaction dynamics between the ions and the target gas. In the case of a linear evolution like for one-electron transfer in Figure 22, it means that the system is in a "single collision regime" as described in section 1.3.1. In the case of the two-electron capture in Figure 22, which shows a second-degree polynomial evolution, the system is in a "multi collision regime". In that case, the cross section $\sigma_{13,12}$ includes the formation of the $q-2$ charge state from single two-electron capture processes and from two single-electron capture processes. In our work, we extended the growth-rate method to interactions between an ion beam and residual gas, as explained in section 5.3.2.2. In this case, the density of atoms is derived from the residual gas pressure, and the varying parameter is the length l of residual gas traveled. This method is used in our studies with cross sections obtained with the Müller-Salzborn scaling law [90] to simulate the evolution of populations and check the consistency of our experimental data.

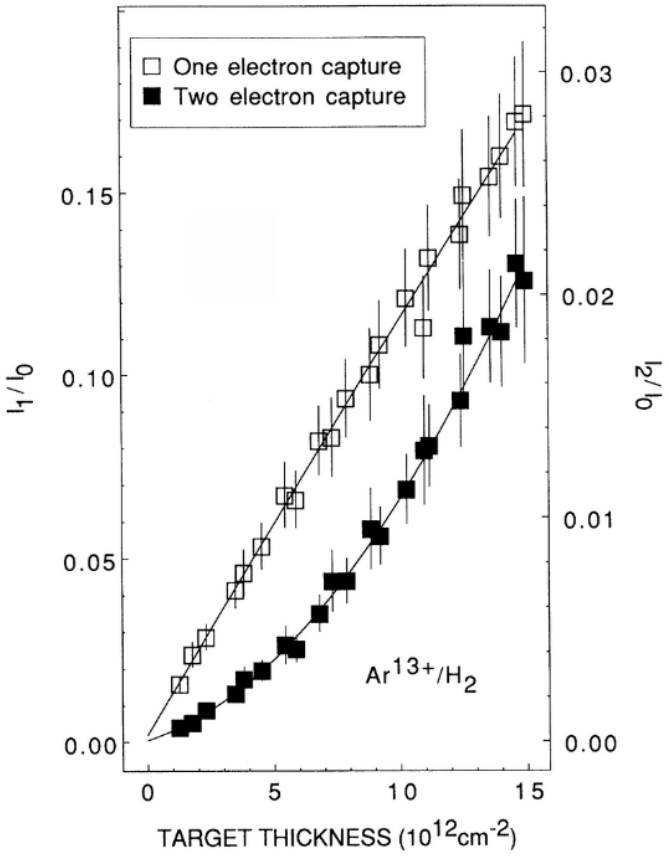

Figure 22: One- and two-electron transfer charge fraction I_k/I_0 growth with target thickness for Ar^{13+} on H_2 at 0.7 keV/u. The left y-axis corresponds to one-electron charge transfer ($k = 1$) and the right y-axis corresponds to two-electron charge transfer ($k = 2$). Figure taken from [91].

2 Theoretical approach to atomic collisions

This work is devoted to investigating electronic processes occurring in atomic collisions within the intermediate energy range. This encompasses the study of collision systems involving atoms in their neutral or charged states, as targets and/or projectiles. Our methodology consists in establishing a semiclassical description suitable for scenarios where the kinetic energy of the colliding nuclei significantly exceeds the electronic energy of the system under investigation. This approach consists in separating the overall dynamics into two subsystems : the atomic nuclei, whose relative motion is treated classically, and the electrons, governed by quantum mechanics. Within this semiclassical impact parameter approximation, the problem reduces to solving the time-dependent Schrödinger equation for the electronic wave function, which describes the evolution of electrons during the collision. Since exact solutions are non-existent, we rely on semi-analytical or numerical methods to achieve precision without introducing additional approximations. In the 1950s, Bates and McCarroll pioneered a non-perturbative method for representing the wave function of the collisional system using atomic orbitals centered on each moving collision partner, and this method has been used extensively since, e.g. [39–41, 94]. Originally limited to the description of one-active electron as in this pioneer work, our approach was called semiclassical atomic orbital close-coupling (AOCC) since many open channels are taken into account through the non perturbative treatment. Now our approach and codes are extended to describe multielectronic systems and it is called ASCC for Asymptotic State Close Coupling. In the following chapter, we detail the theoretical framework of the impact parameter approximation, as well as the development of the calculation method.

2.1 Impact parameter approximation

The validity of the approximations in atomic collision studies is dependent on the relative velocity of the colliding partners and their charge. The semiclassical approximation holds true provided that the de Broglie wavelength associated with the relative motion of the target and projectile remains considerably smaller than the typical zone where the interactions happen effectively during the collision. As an example the de Broglie wavelength for a proton moving with velocity v relative to a stationary target is given in atomic units

$$\lambda_d = \frac{2\pi}{1836\, v} \tag{38}$$

At an impact energy of $E = 25\,\text{keV/u}$, the projectile impact velocity is $v = 1\,\text{a.u.}$ since the correspondence between the energy E and velocity v is given in atomic units by

$$v = \sqrt{\frac{E(\text{keV/u})}{25}} \tag{39}$$

This results in a de Broglie wavelength of

$$\lambda_d = 3.4 \times 10^{-3}\,\text{a.u.} \tag{40}$$

Typically, the electronic processes are effective when the target and projectile are separated by few atomic units, which is significantly larger than the de Broglie wavelength. In our project, we focus on collision energies larger than 0.1 keV/u, i.e. $v > 0.06\,\text{a.u.}$, ensuring the validity of the semiclassical approximation. The relevant quantities are shown

in Figure 23 for a collision system with two active electrons. The vectors $\vec{v}$ and $\vec{b}$ are the relative velocity between T and P and impact parameter, respectively, with $\vec{b} \perp \vec{v}$, these two vectors defining the collision plane. The vectors between the two nuclei and between the target nucleus and the electrons are given by $\vec{R}(t)$, $\vec{r_1}$ and $\vec{r_2}$ respectively.

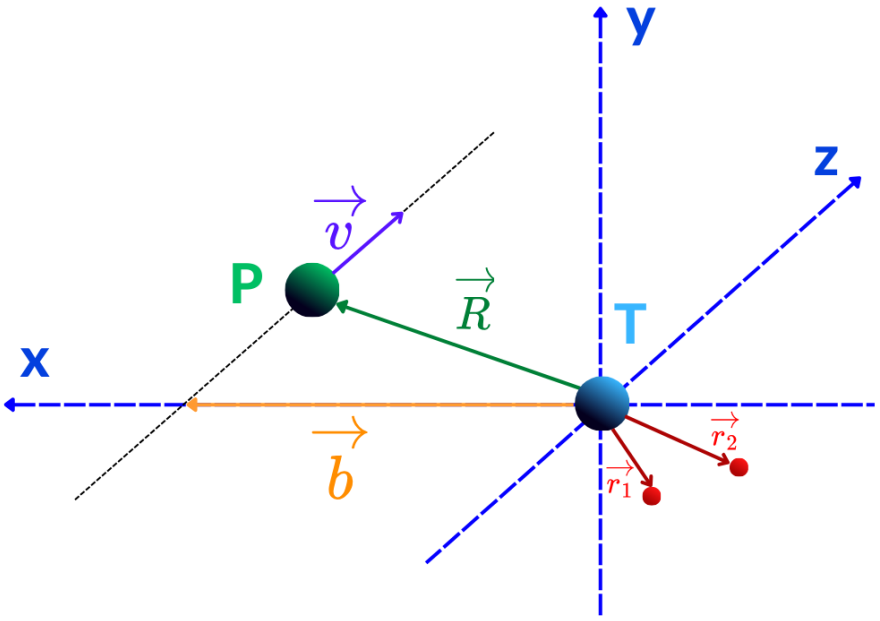

Figure 23: Sketch of an atomic collision for a system with two active electrons. T and P represent respectively the target and projectile nuclei (including frozen core electrons, if necessary). The target is placed at the origin for simplicity.

2.1.1 The eikonal equation

For a collision system composed of a projectile ion P and an atomic or ionic target T, the general treatment involves solving the time-independent Schrödinger equation

$$\hat{H}_{\text{tot}}\Psi_{\text{sys}} = E_{\text{tot}}\Psi_{\text{sys}} \tag{41}$$

where $\hat{H}_{\text{tot}}$ is the Hamiltonian operator and E_{tot} the corresponding energy of the complete system in the laboratory reference frame. The Hamiltonian operator can be decomposed into the kinetic and potential energies operators (in atomic units)

$$\hat{H}_{\text{tot}} = \hat{T}_{\text{tot}} + \hat{V}_{\text{tot}} \tag{42}$$

$$\hat{T}_{\text{tot}} = \sum_{I=T}^{P} -\frac{1}{2M_I}\nabla_R^2 + \sum_{i=1}^{2} -\frac{1}{2}\nabla_{r_i}^2 \tag{43}$$

$$\hat{V}_{\text{tot}} = \sum_{i=1}^{2} V^T(r_i) + \sum_{i=1}^{2} V^P(|\vec{r_i} - \vec{R}|) + V^{TP}(R) + V^{e_1e_2}(|\vec{r_1} - \vec{r_2}|) \tag{44}$$

where M_I are the masses of the target or projectile nuclei. The potential energy operator is the sum of the Coulomb potentials for the nucleus-electron (V^T and V^P), internuclear

(V^{TP}) and interelectronic interactions ($V^{e_1e_2}$). The equations that will be derived are galilean invariant, and therefore the projectile and target could be inverted without any change of the equations.
Since the potential energy depends only on the relative coordinates between the particles, the Hamiltonian can be written as

$$\hat{H}_{\text{int}} = \hat{H}_{\text{tot}} + \frac{1}{2M_{\text{tot}}}\nabla^2_{R_G} \tag{45}$$

with $M_{\text{tot}} = M_T + M_P$ the total mass and $\vec{R_G}$ the position of the centre of mass in the laboratory reference frame. The internal Hamiltonian $\hat{H}_{\text{int}}$ can be expressed in terms of the electronic Hamiltonian $\hat{H}_{\text{el}}$ as

$$\hat{H}_{\text{int}} = \hat{H}_{\text{el}} - \frac{1}{2\mu_{TP}}\nabla^2_R \quad \text{with} \quad \hat{H}_{\text{el}} = -\frac{1}{2}\nabla^2_{r_1} - \frac{1}{2}\nabla^2_{r_2} + \hat{V}_{\text{tot}} \tag{46}$$

with μ_{TP} the reduced mass

$$\mu_{TP} = \frac{M_T M_P}{M_T + M_P} \tag{47}$$

By separating the center of mass coordinates, the total wave function and the energy of the system are written respectively as

$$\Psi_{\text{sys}} = \Psi_{\text{int}}\Psi_G \quad \text{and} \quad E_{\text{tot}} = E_{\text{int}} + E_G \tag{48}$$

where $\Psi_G = e^{i\vec{k}_G\cdot\vec{R}_G}$ and $E_G = \frac{k^2_G}{2M_{\text{tot}}}$ are the wave function and the kinetic energy of the center of mass. $\vec{k}_G$ is a vector in the same direction as the relative velocity $\vec{v}$ of P with respect to the target T and its electrons. The internal wave function Ψ_{int}, which depends only on the internal coordinates, is the solution of the equation

$$\hat{H}_{\text{int}}\Psi_{\text{int}} = E_{\text{int}}\Psi_{\text{int}} \tag{49}$$

and can be approximately written as a product of an electronic function $\Psi(\vec{r}_1, \vec{r}_2, \vec{R})$ and a nuclear function $\Xi(\vec{R})$

$$\Psi_{\text{int}} = \Psi(\vec{r}_1, \vec{r}_2, \vec{R})\Xi(\vec{R}) \tag{50}$$

This approximation is valid considering that the nuclei are much more massive than the electrons. Therefore the kinetic energy associated with the relative motion of the collision partners T and P is much greater than the internal (electronic) energy of the system in the impact energy domain considered. It is then natural to treat the movement of the nuclei independently of that of the electrons. The dependence on $\vec{R}$ is mainly included in $\Xi(\vec{R})$, so it is possible to neglect the term $\nabla^2_R\Psi(\vec{r}_1, \vec{r}_2, \vec{R})$ in the treatment. Since in the impact energy domain considered, the scattering happens predominantely in the forward direction, the wavefunction $\Xi(\vec{R})$ can be approximated by a plane wave [40]

$$\Xi(\vec{R}) = e^{i\vec{k}\cdot\vec{R}} \tag{51}$$

where $\vec{k}$ is the wave vector of magnitude $k = \sqrt{2\mu_{TP}E_{\text{int}}}$. By using equations (46), (50), and (51), the Schrödinger equation for the internal wave function (49) becomes

$$\left[\hat{H}_{\text{el}} - \frac{i}{\mu_{TP}}\vec{k}\cdot\vec{\nabla}_R\right]\Psi = 0 \tag{52}$$

Since the spread of the projectile is mainly forward and the kinetic energy related to the relative motion of T and P is much larger than any change of the electronic energy during the collision, the relative motion of the nuclei is approximated classically by a straight line, constant velocity trajectory

$$\vec{R}(t) = \vec{b} + \vec{v}t \tag{53}$$

with

$$\vec{v} = \frac{1}{\mu_{TP}}\vec{k} \tag{54}$$

Thus, we can write

$$\frac{1}{\mu_{TP}}\vec{k}\cdot\vec{\nabla}_R = \vec{v}\cdot\vec{\nabla}_R = v\frac{\partial}{\partial Z} = \frac{\partial}{\partial t} \tag{55}$$

By inserting this last expression into equation (52), we finally obtain the so-called eikonal equation

$$\left[\hat{H}_{\text{el}} - i\frac{\partial}{\partial t}\right]\Psi(\vec{r}_1,\vec{r}_2,t) = 0 \tag{56}$$

which is equivalent to the time-dependent Schrödinger equation in this approach. Numerical solution of this equation is necessary to determine probabilities of the electronic processes induced in the collision and to compute the related cross sections. We adopt a semi-analytical method to solve the eikonal equation, describing the wave function on a set of states of the isolated (asymptotic) collision partners. This method is well-suited for describing transitions between bound-states and can be applied to systems with one or multiple active electrons [95–97]. In the following section we detail how this method has been developed in the case of two-electron systems.

2.1.2 Solving the eikonal equation

During a collision between a projectile ion and an atomic target with two active electrons, three different asymptotic states are possible for the collision system

- Before or after the collision, the two collision partners are at an infinite distance from each other, rendering their mutual interaction negligible. The two electrons are bound to the target while the projectile P is outside of the ($T + 2e^-$) system described by the Schrödinger equation

$$\hat{H}_{\text{el}}^{TT}\Phi_i^{TT}(\vec{r}_1,\vec{r}_2) = E_i^T\Phi_i^{TT}(\vec{r}_1,\vec{r}_2) \tag{57}$$

  with

$$\hat{H}_{\text{el}}^{TT} = -\frac{1}{2}\nabla_{r_1}^2 + V^T(r_1) - \frac{1}{2}\nabla_{r_2}^2 + V^T(r_2) + V^{e_1e_2}(|\vec{r_1}-\vec{r_2}|) \tag{58}$$

  and $\Phi_i^{TT}(\vec{r}_1,\vec{r}_2)$ describes the states of the target, when the two electrons are bound to it with energy E_i^T.

- After the collision, two electrons can be captured by the projectile. The Hamiltonian of the system ($P + 2e^-$) is expressed by equation

$$\hat{H}_{\text{el}}^{PP} = -\frac{1}{2}\nabla_{r_1^P}^2 + V^P(r_1^P) - \frac{1}{2}\nabla_{r_2^P}^2 + V^P(r_2^P) + V^{e_1e_2}(|\vec{r_1}-\vec{r_2}|) \tag{59}$$

with $\vec{r}_i^{\,P} = \vec{r}_i - \vec{R}$ $(i = 1, 2)$ and $\vec{\nabla}_{r_i^P} = \vec{\nabla}_{r_i}$ since the three independent variables are $\vec{r}_1$, $\vec{r}_2$ and t. The wave functions $\Phi_i^{PP}(\vec{r}_1^{\,P}, \vec{r}_2^{\,P})$ describe the states of the projectile, when the two electrons are bound to it with the energies E_i^P. They are described by the Schrödinger equation

$$\hat{H}_{\text{el}}^{PP}\Phi_i^{PP}(\vec{r}_1^{\,P}, \vec{r}_2^{\,P}) = E_i^P\Phi_i^{PP}(\vec{r}_1^{\,P}, \vec{r}_2^{\,P}) \tag{60}$$

- If one of the electrons is captured by the projectile while the other remains bound to the target, we asymptotically have two one-electron systems with each electron on a different center, each of them satisfying the Schrödinger equation given in equation

$$h_i^{T(P)}\Phi_i^{T(P)} = \varepsilon_i^{T(P)}\Phi_i^{T(P)} \tag{61}$$

where

$$h_i^T = -\frac{1}{2}\nabla_{r_i}^2 + V^T(r_i), \quad h_i^P = -\frac{1}{2}\nabla_{r_i^P}^2 + V^P(r_i^P) \tag{62}$$

and ε_i^T and ε_i^P are the energies associated respectively with the one-electron states of the target, Φ_i^T, and of the projectile, Φ_i^P.

These three types of asymptotic states are used in the development of the electronic wave function $\Psi(\vec{r}_1, \vec{r}_2, t)$ in the eikonal equation (56) and can describe any collision system with two active electrons (for example N^{6+} + He^+, N^{7+} + He, as investigated in the next chapter.)
In the following, for readability purposes, we express the equations by taking the target T as the origin of the reference frame as shown in Figure 23. In this reference frame, the projectile P is in translational motion relative to the target T, and we have to apply an appropriate phase to the states of the moving projectile. This is to take into account the displacement of each electron bound to the projectile relative to the target and to ensure the Galilean invariance of the results. This phase is called the electronic translation factor $f(\vec{r}_i, t)$ [40] and is defined by

$$f(\vec{r}_i, t) = e^{i\vec{v}\cdot\vec{r}_i - i\frac{1}{2}v^2 t} \quad (\vec{r}_i \equiv \vec{r}_1, \vec{r}_2). \tag{63}$$

Then, to describe the collision we develop the total wave function over the set of one- and two-electronic states centered on the target and on the projectile as follows :

$$\begin{aligned}\Psi(\vec{r}_1, \vec{r}_2, t) = &\sum_{i=1}^{N^{TT}} a_i^{TT}(t)\Phi_i^{TT}(\vec{r}_1, \vec{r}_2)e^{-iE_i^T t} \\ &+ \sum_{k=1}^{N^T}\sum_{l=1}^{N^P} a_{kl}^{TP}(t)\left[\Phi_k^T(\vec{r}_1)\Phi_l^P(\vec{r}_2)e^{i\vec{v}\cdot\vec{r}_2} \pm \Phi_l^P(\vec{r}_1)\Phi_k^T(\vec{r}_2)e^{i\vec{v}\cdot\vec{r}_1}\right] e^{-i\left(\frac{1}{2}v^2 + \varepsilon_k^T + \varepsilon_l^P\right)t} \\ &+ \sum_{j=1}^{N^{PP}} a_j^{PP}(t)\Phi_j^{PP}(\vec{r}_1^{\,P}, \vec{r}_2^{\,P})e^{-i(E_j^P + v^2)t}e^{i\vec{v}\cdot(\vec{r}_1 + \vec{r}_2)}\end{aligned} \tag{64}$$

The sign $\pm$ appearing in the expression of the wave function is related to the spin state for the collision system considered (singlet corresponding to $+$ and triplet to -). This spin symmetry, imposed by the initial conditions, is retained during the collision, since our model does not include spin-orbit couplings. ϕ^{TT} and ϕ^{PP} must describe the corresponding spin state. Inserting equation (64) into the eikonal equation (56), we obtain a system of coupled equations for the expansion coefficients $a(t)$ that can be written in matrix form

$$iS\dot{a} = Ma \tag{65}$$

The overlap matrix S is defined as

$$S = \begin{pmatrix} S_{f,i}^{TT,TT} & S_{f,kl}^{TT,TP} & S_{f,j}^{TT,PP} \\ S_{mn,i}^{TP,TT} & S_{mn,kl}^{TP,TP} & S_{mn,j}^{TP,PP} \\ S_{f,i}^{PP,TT} & S_{f,kl}^{PP,TP} & S_{f,j}^{PP,PP} \end{pmatrix} \tag{66}$$

with the different terms being partial matrices for which the elements are defined as follows

$$S_{f,i}^{TT,TT} = \delta_{f,i} \tag{67}$$

$$S_{f,kl}^{TT,TP} = \left[\langle \Phi_f^{TT} | e^{i\vec{v}\cdot\vec{r}_2} | \Phi_k^T \Phi_l^P \rangle \pm \langle \Phi_f^{TT} | e^{i\vec{v}\cdot\vec{r}_1} | \Phi_l^P \Phi_k^T \rangle \right] e^{-i\left[\frac{v^2}{2} + (\varepsilon_k^T + \varepsilon_l^P) - E_f^T\right]t} \tag{68}$$

$$S_{f,j}^{TT,PP} = \langle \Phi_f^{TT} | e^{i\vec{v}\cdot(\vec{r}_1+\vec{r}_2)} | \Phi_j^{PP} \rangle e^{-i\left[E_j^P - E_f^T + v^2\right]t} \tag{69}$$

$$S_{mn,i}^{TP,TT} = \left[\langle \Phi_m^T \Phi_n^P | e^{-i\vec{v}\cdot\vec{r}_2} | \Phi_i^{TT} \rangle \pm \langle \Phi_n^P \Phi_m^T | e^{-i\vec{v}\cdot\vec{r}_1} | \Phi_i^{TT} \rangle \right] e^{-i\left[E_i^T - (\varepsilon_m^T + \varepsilon_n^P) - \frac{v^2}{2}\right]t} \tag{70}$$

$$S_{mn,kl}^{TP,TP} = \left[2\delta_{mk}\delta_{nl} \pm 2\langle \Phi_m^T \Phi_n^P | e^{i\vec{v}\cdot(\vec{r}_1-\vec{r}_2)} | \Phi_l^P \Phi_k^T \rangle \right] \tag{71}$$

$$S_{mn,j}^{TP,PP} = \left[\langle \Phi_m^T \Phi_n^P | e^{i\vec{v}\cdot\vec{r}_1} | \Phi_j^{PP} \rangle \pm \langle \Phi_n^P \Phi_m^T | e^{i\vec{v}\cdot\vec{r}_2} | \Phi_j^{PP} \rangle \right] e^{-i\left[E_j^P - (\varepsilon_m^T + \varepsilon_n^P) - \frac{v^2}{2}\right]t} \tag{72}$$

$$S_{f,i}^{PP,TT} = \langle \Phi_f^{PP} | e^{-i\vec{v}\cdot(\vec{r}_1+\vec{r}_2)} | \Phi_i^{TT} \rangle e^{-i\left[E_i^T - E_f^P - v^2\right]t} \tag{73}$$

$$S_{f,kl}^{PP,TP} = \left[\langle \Phi_f^{PP} | e^{-i\vec{v}\cdot\vec{r}_1} | \Phi_k^T \Phi_l^P \rangle \pm \langle \Phi_f^{PP} | e^{-i\vec{v}\cdot\vec{r}_2} | \Phi_l^P \Phi_k^T \rangle \right] e^{-i\left[\varepsilon_k^T + \varepsilon_l^P - E_f^P - \frac{v^2}{2}\right]t} \tag{74}$$

$$S_{f,j}^{PP,PP} = \delta_{f,j} \tag{75}$$

Similarly, the coupling matrix M is a global matrix defined as

$$M = \begin{pmatrix} M_{f,i}^{TT,TT} & M_{f,kl}^{TT,TP} & M_{f,j}^{TT,PP} \\ M_{mn,i}^{TP,TT} & M_{mn,kl}^{TP,TP} & M_{mn,j}^{TP,PP} \\ M_{f,i}^{PP,TT} & M_{f,kl}^{PP,TP} & M_{f,j}^{PP,PP} \end{pmatrix} \tag{76}$$

in which the different types of matrix elements can be written in a more complex form than the ones of the overlap matrix. The column vectors $\dot{a}$ and a can be expressed schematically as

$$\dot{a} = \begin{pmatrix} \dot{a}^{TT} \\ \dot{a}^{TP} \\ \dot{a}^{PP} \end{pmatrix}, \quad a = \begin{pmatrix} a^{TT} \\ a^{TP} \\ a^{PP} \end{pmatrix} \tag{77}$$

with elements of the forms

$$\begin{cases} \dot{a}^{TT} = (\dot{a}_i^{TT})_{1 \le i \le N_{TT}} \\ \dot{a}^{TP} = (\dot{a}_{kl}^{TP})_{1 \le k \le N_T, 1 \le l \le N_P} \\ \dot{a}^{PP} = (\dot{a}_j^{PP})_{1 \le j \le N_{PP}} \end{cases}, \quad \begin{cases} a^{TT} = (a_i^{TT})_{1 \le i \le N_{TT}} \\ a^{TP} = (a_{kl}^{TP})_{1 \le k \le N_T, 1 \le l \le N_P} \\ a^{PP} = (a_j^{PP})_{1 \le j \le N_{PP}} \end{cases} \tag{78}$$

where $\dot{a}^I \equiv \frac{\partial a^I}{\partial t}$. The determination of the development coefficients a is done by solving the differential equations (65) for the coefficients $a(t)$ with initial conditions at $t \to -\infty$ given by an initial state i, velocity v, and impact parameter b. This is done by using a predictor-corrector time-step method developed by Shampine and Gordon [98]. The probability of a transition from an initial state i to a final state f is given by the coefficients $a_f^{(i)}$ when the two partners are far apart after the collision :

$$P_{fi}(v,b) = \lim_{t \to \infty} |a_f^{(i)}(t)|^2 \tag{79}$$

From that, the evaluation of the total cross section for this transition is given by :

$$\sigma_{fi}(v) = 2\pi \int_0^{+\infty} b P_{fi}(v,b) db \tag{80}$$

2.2 Development of the calculation method

2.2.1 Gaussian Type Orbitals (GTO)

The one- and two-electron asymptotic states described in equation (64) that may be populated during the collision are expanded on a basis of Gaussian Type Orbitals (GTO), and spin-adapted products of the same GTO set. The GTOs are described in spherical coordinates by

$$G_{\alpha,\ell,m}(\vec{r}) = Y_{\ell,m}(\theta,\phi) r^\ell e^{-\alpha r^2} \tag{81}$$

where r, θ, ϕ are spherical coordinates, $Y_{\ell,m}$ the spherical harmonics and ℓ, m the azimutal and magnetic quantum numbers. The use of GTOs is motivated by their ability to yield analytical forms for the integrals necessary for solving the eikonal equation (56).
Note that in the earliest treatments of this kind, Slater-type orbitals (STOs) of the form

$$\chi_{n,\ell,m}(r,\theta,\phi) = Nr^n e^{-\zeta r} Y_{\ell,m}(\theta,\phi) \tag{82}$$

with N a normalization constant, n an integer and ζ the orbital exponent were used. STOs exhibit correct asymptotic behavior and have a direct physical interpretation, but introduce computational complexity in evaluating two-centre and two-electron integrals which limits their practical use. To overcome this, Boys proposed using GTOs [99], which simplify integral evaluation and speed up computations, making them widely adopted in quantum chemistry. The code developed by our team uses GTOs for the same reasons. The one-electron states of the target and the projectile are described by linear combinations of GTOs

$$\Phi_i^I(\vec{r}) = \sum_{i=1}^{N_I} c_i^I G_{\alpha_i,\ell_i,m_i}(\vec{r}) \quad (I \equiv T, P \text{ and } \vec{r} \equiv \vec{r}_1, \vec{r}_2, \vec{r}_1^P, \vec{r}_2^P) \tag{83}$$

while the two-electron states are expressed as a sum of products of GTOs for each of the electrons

$$\Phi_i^I(\vec{r},\vec{r'}) = \sum_{i=1}^{N_I}\sum_{j=1}^{N_I} C_{ij}^I \left[G_{\alpha_i,\ell_i,m_i}(\vec{r})G_{\alpha_j,\ell_j,m_j}(\vec{r'}) \pm G_{\alpha_j,\ell_j,m_j}(\vec{r})G_{\alpha_i,\ell_i,m_i}(\vec{r'})\right] \tag{84}$$

with $I \equiv TT$ or PP, $\vec{r} \equiv \vec{r}_1, \vec{r}_1^P$ and $\vec{r'} \equiv \vec{r}_2, \vec{r}_2^P$.The coefficients c_i^I and C_{ij}^I in equations (83) and (84) are obtained through the diagonalization of the isolated target (or projectile) Hamiltonian on these sets of one- and two-electron functions.

2.2.2 GTO basis optimization method

The optimization procedure for Gaussian-type orbitals (GTOs) in the Fortran collision solver program is designed to enhance computational efficiency and accuracy. To accurately describe the states of collision systems, GTOs are optimized by adjusting their number and exponents. The exponents are fine-tuned to provide a good description of eigenstates of interest. A basis can be deemed good if the states and their energies included in the dynamics are accurately described, and the number of GTOs is kept low enough to minimize computation time and memory usage while maintaining precision. A different basis is therefore used for each collision partner. Within a basis for one-electron states, the states with different quantum number ℓ are described by a distinct set of GTOs, or *sub-basis*. This means that states 1s,2s,3s have to be described by the same sub-basis, same goes for states 2p,3p,4p,5p etc.
In practice, the exponents of the GTOs are optimized in geometric progressions. Even-tempered GTOs were proposed by Reeves and Harrison [100] and Raffenetti [101] who observed that optimized exponents for a basis form an almost straight line on a logarithmic scale. An even-tempered set of exponents $\{\alpha_k\}$ is defined such that:

$$\alpha_k = \alpha_1 \beta^{k-1} \quad \text{for} \quad k = 2, 3, \ldots, N \tag{85}$$

where α_1 is the smallest exponent, β is a constant ratio greater than one and N is the number of GTOs in a basis for a given ℓ. This optimization is time-consuming as it requires multiple diagonalizations of the Hamiltonians. However until a correct basis

is selected, only the diagonalization part of the collision solver is run, the code being stopped before the computation of the coupling and overlap matrix elements, saving therefore a lot of time in the optimization process.
For the optimization of the basis of GTO, a custom made Python algorithm was written to try and somewhat automate the process. First, the states to optimize in priority are chosen, as well as the number N_ℓ of GTOs for each sub-basis. It is important to note that optimizing a sub-basis for higher ℓ requires significantly more computing time than for a lower ℓ. Therefore, the higher the ℓ, the lower the number of GTOs in the corresponding sub-basis. Once the number of GTOs N_ℓ is decided on, the set of exponents α can be entirely defined by an $\{\alpha_{\text{min}};\alpha_{\text{max}}\}$ combination. To find an adequate sub-basis set, a first algorithm loops over a range of α_{min} and α_{max} to find the optimal $\{\alpha_{\text{min}};\alpha_{\text{max}}\}$. This is done by diagonalizing the Hamiltonians to check the energy levels of the electronic states. Since a sub-basis must describe several states with the same ℓ at once, the energy that the program tries to match is actually a weighted sum $\langle E\rangle$ of the energies of a selection of states with the same ℓ :

$$\langle E\rangle = \sum k_i E_i \tag{86}$$

The weight k_i on each state is determined by the user based on the systems in likelihood of that state being populated. For example in a very asymmetrical collision, the higher states are more likely to be populated than the lower after electron capture on the projectile, so the energies of the higher states of the projectile will have a bigger weight in the energy to be optimized. For example in $C^{6+} - H$ collisions, the n = 4 and 5 are the main shells to be populated by capture so the weight k of the corresponding states needs to be the highest among the other states. This ensures that the best described states are the ones which are more likely to be populated. Once $\{\alpha_{\text{min}};\alpha_{\text{max}}\}$ is determined, a second algorithm loops over the α coefficients and adjusts them slightly to better fit the electronic states energies, using a gradient-based descent minimization. This procedure allows to create well described bound states, but also pseudo-states both under and above the ionization threshold. The latter are used to describe approximately the ionization process.
In the case of a two-electron collision partner, the program finds a GTO basis that optimizes simultaneously the one- and two-electron states. As an example, for the N^{7+}+He collisions for which single and double capture are likely, the GTO basis are optimized both for N^{6+} and N^{5+} states simultaneously, the latter correlating the different ℓ-sub basis found for the one-electron states.
The biggest basis that was optimized during the project was composed of 141 GTOs up to $\ell = 5$ (so a total of 6 sub-basis) for C^{5+}, taking an average of 10 hours of computation time per sub-basis. The working principle of the optimization algorithm can be outlined as shown in Figure 24.

2.2.3 The collision solver program

The collision solver program is a sophisticated tool developed by the group and their collaborators over decades to evaluate probabilities and cross sections characterizing electronic processes in ion-atom and ion-molecule collisions. Initially, the program was designed to handle one-active-electron collisions [102, 103], but it has been expanded to accommodate up to four-active-electron collisions [95–97, 104]. The operation of the program is divided into four main stages:

```
Initialize N, alpha_min array, alpha max array
Initialize weighted energy E_tot =(a*E(1s)+a1*E(2s)...)
Initialize E_best = 0
for each alpha_min :
    for each alpha max :
        create geometric sequence {alpha_min, alpha_max, N}
        diagonalize hamiltonian
        get E_calc
        new_E_best = min |E_tot- E_calc|
        if new_E_best better than E_best :
            E_best = new_E_best
return E_best, {alpha_min, alpha_max}
```

Figure 24: Outline of the Python algorithm for the optimization of the basis α coefficients.

- In the *initialization stage*, the exponents of Gaussian Type Orbitals (GTOs, see equation (81)) are selected and optimized to accurately describe the electronic states of each isolated collision partner. The criteria used to determine whether a state is accurately described or not is its energy (in a.u.).
- Next, the *diagonalization stage* uses the optimized GTOs from the initialization stage to determine the one- and two-electron states of the isolated collision partners. A large number of these states are included in the dynamic stage, when solving numerically the coupled differential equations (65).
- The *matrices evaluation stage* follows, where the overlap matrix $\mathbf{S}$ and coupling matrix $\mathbf{M}$ elements along the projectile trajectory are evaluated at numerous grid points within the collision zone [43]. To ensure efficient and accurate computation when solving the differential equations, these matrix elements are interpolated between points, significantly reducing CPU time.
- During the *dynamics stage*, the system of first-order coupled differential equations is integrated over time, based on initial conditions given in the initialization stage and the predefined grid along the collision trajectory.

Finally, let's state that throughout the process, the program is designed to balance the inclusion of a comprehensive basis set of states with the need to maintain reasonable computation times. The basis set is carefully optimized to describe with the best possible precision the most likely populated states and those of experimental interest, ensuring the convergence and accuracy of the results. This optimization ensures that the computational resources are used effectively.
Once an adequate basis is found for each collision partner, the cross sections can be computed. The collision solver is designed to work for one collision energy at a time, so the code must run as many times as necessary to cover the energy range of interest. The input parameters for the collision solver are as follows :

- *Impact parameter* b : all the values for the impact parameter for a collision must be specified.
- *Impact velocity* v

- *Initial state of the system* : after the optimization stage, a file called "sta" is produced with the states' energies, on which the states are numbered. In the case of a one-electron system, states T and P are given, and for a two-electron system, states TT, PP and TP are given. The input file takes the number of the state given in "sta" that corresponds to the initial configuration of the system (for example in the N^{7+} + He($1s^2$) system, it is the ground state of He, labelled 1)

- *Target and Projectile states* : in practice, the input is the name of the file containing the basis information for the target or projectile, and the number of states to be used (taken from the "sta" file). Choosing the number of states wisely is important because if it is too small then the convergence of the cross sections is impacted. One might think that to avoid this problem we can choose a very large number of states that is sure to cover all possible final states of the interaction, but if we do so the problem of computation time arises. So a balance must be reached in order to keep enough states to have an accurate final states description, but keeping the computation time reasonable.

It is important to note that the collision solver does not take the parity (singlet or triplet) as input. Indeed there are actually two slightly different versions of the collision solver made for singlet and triplet states. In the case of a two-electron collision system where the total spin of the system can be either singlet or triplet (e.g. N^{6+}(1s) + He^{+}(1s)), the collision solver must be run twice for each collision energy, to account for singlet and triplet states. However, in the N^{7+} + He($1s^2$) collision system, the total spin of the initial state is singlet, and the collision solver must only be run once for each collision energy for singlet states.
The output for the collision solver is a file where the final states are listed (in the same order as the "sta" file) with their respective probability $P(b)$, for each impact parameter b. A Python program is then used to sort through the impact parameters and extract the $bP(b)$ values for each state, which are then converted into cross sections with the equation (80).

3 Theoretical results

3.1 Choice of systems

The collision systems studied in the following were carefully chosen based on different criteria, such as feasibility, comparability, and general interest. To gain a better understanding of the workings of the program itself and to test the running time of the different components, a benchmark system with one electron, C^{6+} - H(1s), was first considered. Interactions between fully stripped ions, particularly carbon, and atomic hydrogen have been the subject of numerous studies in the past [45, 105–108]. Carbon ions are highly prevalent in various environments, including astrophysical and fusion plasmas. Understanding their interactions with hydrogen is essential for improving diagnostic techniques and modeling the behavior of these plasmas. Charge exchange and ionization phenomena during these carbon-hydrogen collisions are investigated to enhance the understanding of the mechanisms occurring within magnetically confined fusion plasmas. On the other hand, the study of systems with two active electrons represents a challenge since it is more demanding in computing resources and more complex to describe, with mono- and bi-electronic processes being likely and competing. The basis must be optimized to accurately describe both one-electron states for each partner but also two-electron states. In the following, two different two-electron systems are studied: $N^{6+}(1s)+He^{+}(1s)$ and $N^{7+}+He(1s^2)$. To the extent of our knowledge, the $N^{6+}(1s)+He^{+}(1s)$ system has not been studied before, and no reference could be found in the literature. In contrast, the $N^{7+}+He(1s^2)$ system has been the subject of several studies [109–111]. One of the main reasons for the study of this system is the nitrogen autoionizing states that arise from double electron capture into doubly excited states. Autoionizing states play an important role in collisions between highly charged ions and atoms or surfaces and in plasma physics. Another motivation for the initial choice of these two-electron systems was the anticipation that they would be best suited to be studied experimentally with the setup at INSP, which is presented in section 4.3.

3.2 One-electron system : C^{6+}+ H(1s)

This system is a one-electron system where the electron is located initially on an atomic target and the projectile is a bare ion. Electron capture and ionization processes, respectively

$$C^{6+} + H(1s) \rightarrow C^{5+}(n\ell) + H^{+} \tag{87}$$

$$C^{6+} + H(1s) \rightarrow C^{6+} + H^{+} + e^{-} \tag{88}$$

have been investigated, and the results are compared with those previously reported in the literature [45, 105–108]. Additionally, target excitation

$$C^{6+} + H(1s) \rightarrow C^{6+} + H(n'\ell'), n' > 1 \tag{89}$$

is also discussed.

3.2.1 Implementation

Cross sections are computed for 11 impact energies ranging from 0.1 to 100 keV/u, with 200 values of the impact parameter each. Since $v_e = 1$ a.u. (corresponding to

E = 25 keV/u) for H(1s), the energy range chosen for this study corresponds to the intermediate energy range as defined in section 1.1.2. In average, the calculations for one impact energy takes 50 hours.
For this collision system, two GTO sets are used, one for the hydrogen atom and one for the C^{5+} ion. The GTO set for hydrogen is composed of 64 GTO total (10 for s states, 8×3 for p states and 6×5 for d states), and the GTO set for C^{5+} is composed of a total of 141 GTO (10 for s states, 8×3 for p states, 6×5 for d states, 4×7 for f states, 3×9 for g states and 2×11 for h states). After diagonalization, 24 states for hydrogen and 140 states for C^{5+} are selected for the description of electron capture to C^{5+} and excitation of hydrogen. Pseudo states (39 for H and 37 for C^{5+}) with energy above the ionization threshold are also included to model ionization of hydrogen. Not all of the states created by diagonalization of the basis are used, since pseudostates with positive energy corresponding to high energy ionization are not likely to be populated and may induce numerical instabilities. For this reason, a cut-off at 2.5 a.u. is decided to limit the number of states while conserving a description of ionization states. In table 3, a selection of the energies of most important states of C^{5+} and H are presented. The values obtained with our GTO set are compared with the theoretical values calculated with equation

$$E(a.u.) = -\frac{Z^2}{2n^2} \tag{90}$$

which is the well-known Bohr energy formula for hydrogen-like ions. It gives the energy of electrons in the level n of an atom of atomic number Z. Our calculated eigenvalues

State	E_{Calc}	E_{GTO}	Δ(%)	State	E_{Calc}	E_{GTO}	Δ(%)
H(1s)	-0.5	-0.4998	0.04	**C^{5+}(4p)**	-1.125	-1.1240	0.08
H(2s)	-0.125	-0.1249	0.08	**C^{5+}(4d)**	-1.125	-1.1241	0.07
H(2p)	-0.125	-0.1249	0.08	**C^{5+}(4f)**	-1.125	-1.1240	0.07
H(3l)	-0.0556	-0.0555	0.18	**C^{5+}(5d)**	-0.72	-0.7195	0.07
C^{5+}(1s)	-18	-17.9564	0.24	**C^{5+}(5f)**	-0.72	-0.7178	0.3
C^{5+}(2s)	-4.5	-4.4941	0.13	**C^{5+}(5g)**	-0.72	-0.7193	0.09
C^{5+}(2p)	-4.5	-4.4985	0.03	**C^{5+}(6g)**	-0.5	-0.4964	0.7
C^{5+}(3p)	-2	-1.9991	0.05	**C^{5+}(6h)**	-0.5	-0.4980	0.4

Table 3: Comparison of energies, in a.u., for a selection of states of the H atom and the $C^{5+}(n\ell)$ ion states, calculated based on the GTO basis set and equation (90). Relative difference Δ is given by $\Delta = |(E_{\text{GTO}} - E_{\text{Calc}})/E_{\text{Calc}}| \times 100$.

are in very good agreement with the theoretical ones, with differences smaller than 1%, down to 0.4‰ for the ground state of hydrogen.
The Python optimization code described in section 2.2.2 allows for an investigation of a range of α_{min} and α_{max} values, offering an overall mapping to determine where the eigenvalues of any state of interest achieve their optimal value. This functionality is depicted in Figure 25, which illustrates the results of this optimization for three different states of C^{5+}. Each image maps the energies obtained through diagonalization as a function of α_{max} (x-axis) and α_{min} (y-axis), with the color scale indicating the proximity with the theoretical value. The closest values are in deep red and the furthest are in blue. The values highlighted by yellow crosses on the graphs show the values of $\{\alpha_{\text{min}};\alpha_{\text{max}}\}$

that optimize simultaneously all states with the same ℓ (for 3d and 4d). On the colormap for the 3d and 4d states, one could think that a better $\{\alpha_{\text{min}};\alpha_{\text{max}}\}$ combination could be found for each, since the yellow cross is not in the apparent optimal position. However as explained before, the same basis must be used for all states with the same ℓ so ,in this case, for the 3d, 4d, 5d and 6d states. This is why the basis for $\ell = 2$ does not apparently lead to an optimal description of *each* state, but rather the optimal value of a *weighted combination* of the energies of all states as in equation (86).

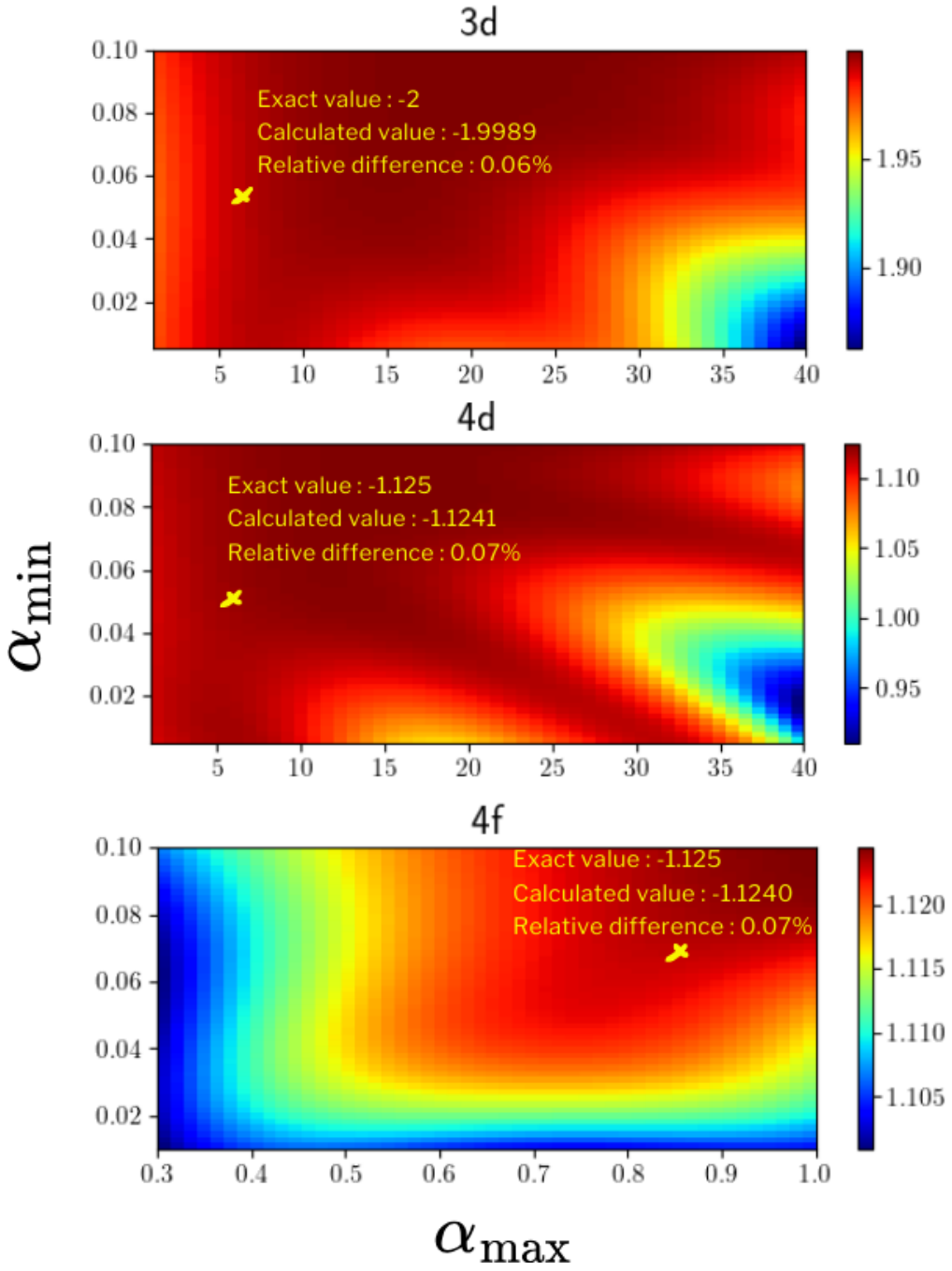

Figure 25: Optimisation of the α exponents of the GTO for the description the 3d, 4d and 4f states for C^{5+}. The investigation as a function of α_{min} and α_{max} shows the values of the exponents that can optimise three excited states of C^{5+}, represented on the colormaps by yellow crosses. The corresponding calculated values and relative difference with the values from equation (90). The colorbar corresponds to -E $(a.u.)$

3.2.2 Results and discussion

In Figure 26 the cross sections for total capture, ionization and excitation are presented, (equations (87), (88) and (89) respectively) as a function of the impact energy, between 0.1 and 100 keV/u. Capture and ionization cross sections will be compared with previous values from the literature in this section. No cross section data for excitation of hydrogen was found in the literature, therefore no comparison is provided. In Figure 26, it is clear that for the majority of the energy range studied, the electron capture cross sections are larger by up to three orders of magnitude than the excitation ones, and by up to 4 orders of magnitude than the ionization ones. One can see that capture cross sections show a smooth dependence on energy with a maximum around 10 keV/u. On the other hand, for the two other processes, the cross sections increase by about five orders of magnitude since, as expected, their maximum is located at energies above 100 keV/u. On Figure 27,

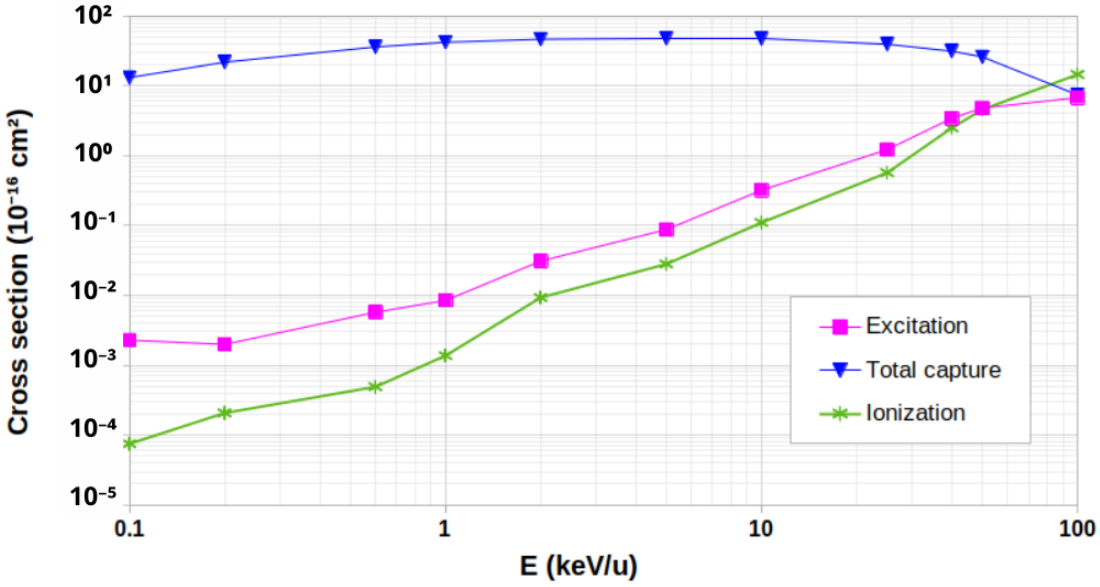

Figure 26: Cross sections obtained for total electron capture, ionization and excitation processes (equations (87) – (89)) for the C^{6+}+ H(1s) collision system.

the cross sections for total electron capture (a) and partial electron capture to n=4 (b) and n=5 (c) are presented along with other theoretical results from previous studies by Harel *et al* [45], Caillat *et al* [105], Igenbergs *et al* [107] and Abdurakhmanov *et al* [106], as well as a fit by Suno et al [108] derived from previous experimental and theoretical data. These data have been chosen since they use different approaches, and therefore could serve as comparison material to test the accuracy of our calculations and the robustness of the GTO basis chosen. The studies mentioned previously employ different methods and encompass different processes in their calculations. The particularities of each are summarized below :

- Harel *et al* [45] employs a molecular approach to atomic collisions to calculate electron capture cross sections. Using the impact parameter approximation, these authors solve the time-dependent Schrödinger equation with an expansion over the eigenfunctions of the full electronic Hamiltonian, referred to as one-electron diatomic molecule (OEDM) orbitals. This approach is especially efficient in the

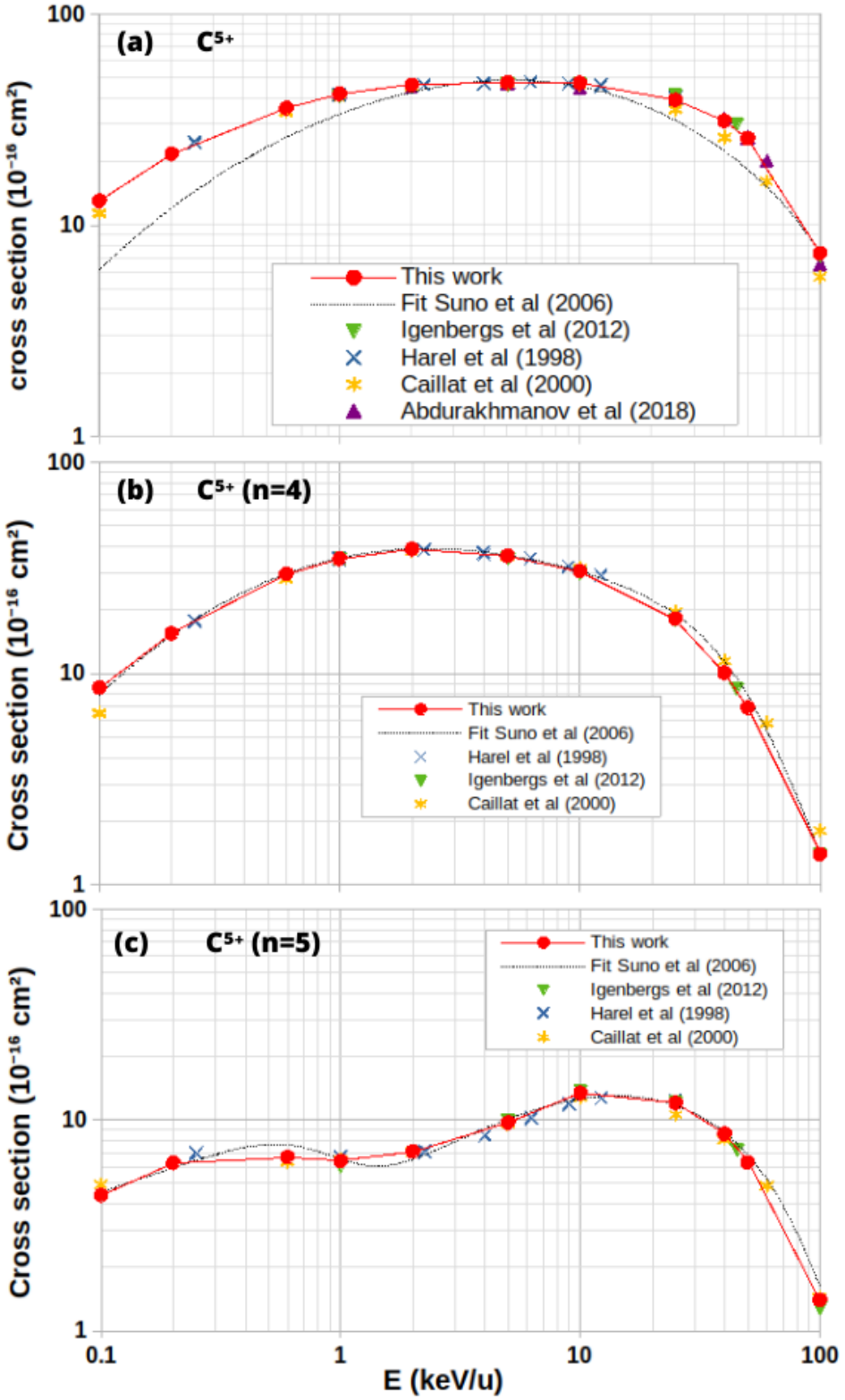

Figure 27: Total (a) and partial electron capture cross sections to n = 4 (b) and n = 5 (c) for the C^{6+} + H(1s) collision, with comparison between this work (in red) and the previous results by Harel *et al* [45], Caillat *et al* [105], Igenbergs *et al* [107] and Abdurakhmanov *et al* [106]. Cross sections fitted by an analytical function from Suno *et al* [108].

low energy part of the intermediate energy domain. For C^{6+} - H(1s) collisions, they utilize a molecular basis set that includes states correlating asymptotically to

capture channels up to $n = 8$, totaling 121 states.

- Caillat *et al* [105] uses the same impact parameter semiclassical method, with an atomic-state close-coupling approach, as ours. However their calculations are focused on electron capture and do not take into account ionization and hydrogen excitation. The study employs a comprehensive basis set of 92 states, spanning C^{5+}(n = 1–6) shells.

- Igenbergs *et al* [107] applies the Atomic-Orbital Close-Coupling (AOCC) method as in [105] and our study. They calculate inelastic cross sections for C^{6+} + H collisions, using basis sets of up to 286 states on the ion center and 54 states on the hydrogen center, including pure hydrogen states and unbound pseudostates representing the ionization continuum. This approach allows for calculations of charge exchange and ionization cross sections.

- In their very recent investigations, Abdurakhmanov *et al* [106] use a wave-packet convergent close-coupling (WP-CCC) approach tailored for ionization calculations, to study both ionization and electron capture. This method is also semi-classical and expands the scattering wave function into target and projectile pseudostates and solves the resulting differential equations for time-dependent coefficients using GPU-accelerated Runge-Kutta methods. The extensive basis of 2534 states ensures accurate convergence across a wide range of collision energies. Their approach is therefore similar to ours, except in the representation of the scattering wave function, but represents the most converged calculations with respect to the size of the basis set used.

- Finally, Suno *et al* [108] compiles cross section data for charge exchange processes between C^{6+} ions and hydrogen atoms from various theoretical and experimental sources to derive recommended data. The recommended cross sections are expressed as simple analytic functions with fitting parameters for each charge exchange process. The fitting function used is:

$$\sigma[\mathrm{cm}^2] = 10^{-16}\left(\frac{a_1\exp\left[-\left(\frac{a_2}{E}\right)^{a_3}\right]}{1+\left(\frac{E}{a_4}\right)^{a_5}+\left(\frac{E}{a_6}\right)^{a_7}+\left(\frac{E}{a_8}\right)^{a_9}}+\frac{a_{10}\exp\left[-\left(\frac{a_{11}}{E}\right)^{a_{12}}\right]}{1+\left(\frac{E}{a_{13}}\right)^{a_{14}}}\right) \tag{91}$$

where E is the collision energy in eV/amu, and a_i are fitting parameters which can be found in [108].

Overall, as can be seen in Figure 27 the agreement between our data and the other data for total and partial electron capture is very good in the 0.1 to 10 keV/u range, diverging by only a few percents from other calculations. At higher energies, above 25 keV/u, discrepencies of the order of 10 to 20% can also be found with Caillat. That can be explained by the fact that our basis set is tailored to take into account ionization and excitation channels as well as capture channels, whereas Caillat only takes capture channels into account. A much better agreement is found with the results of Igenbergs and Abdurakhmanov (of the order of a few %), whose calculations also take into account the ionization channels. This agreement with the very recent and intensive calculations reported in [106] proves the convergence of our results, though obtained with a smaller

basis set.
The fit by Suno *et al* shows excellent agreement with our capture cross section data, as well as the selected data from the literature for the n = 4 and n = 5 capture channels, as shown in Figure 27 (b) and (c), respectively. However, surprisingly, the fit is not as good for the total electron capture (Figure 27 (a)). This can be explained by the difference in approach used by Suno for the calculation of the fit parameters between the partial capture (n= 4, 5) and total capture. For partial capture, only data from previous calculations by various teams were used, and, instead, a mix of experimental and theoretical data was used to derive the fit parameters for total capture. Additionally for total capture, a larger energy range was used in the lower energies (as low as 0.001 keV/u), with only one dataset between 0.001 and 0.1 keV/u. This could explain the difference in fit accuracy observed between partial and total cross sections in our energy range. In Figure 28, ionization cross sections are presented and compared with previous

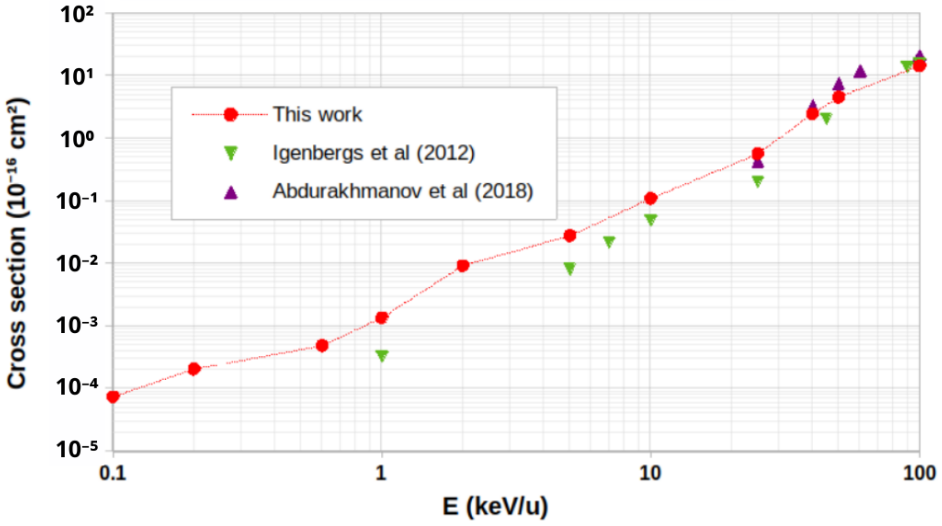

Figure 28: Cross sections for ionization compared with previous results by Igenbergs *et al* [107] and Abdurakhmanov *et al* [106].

calculations by Igenbergs *et al* [107] and Abdurakhmanov *et al* [106]. The discrepancy between our results and those from Igenbergs below 25 keV/u is of the order of 30%, and show much better agreement (less that 10 % difference) at higher energies. Since ionization at lower energies is not a dominant process, calculations are not easy to be converged and depend a lot on the basis set used. The method used by Abdurakhmanov is tailored for ionization calculations and their basis have been extensively tested for convergence, as reported in [106]. Our results at high energies only differ from theirs by a few percents, showcasing the robustness of our method for the description of both capture and ionization at energies where both processes have cross sections of the same order of magnitude. Unfortunately they did not extend their calculations at energies below 25 keV/u, certainly due to convergence issues.
The two most prevalent channels for capture cross sections are $C^{5+}(4\ell)$ and $C^{5+}(5\ell)$. The mechanism responsible for these processes at lower energies can be identified with the help of the adiabatic molecular curves presented in Figure 29 [105]. Capture to n = 4 happens through the avoided crossing around R = 8 a.u. between the $5g\sigma$ curve correlated asymptotically with the initial state of the target H(1s) and the $4f\sigma$ curve

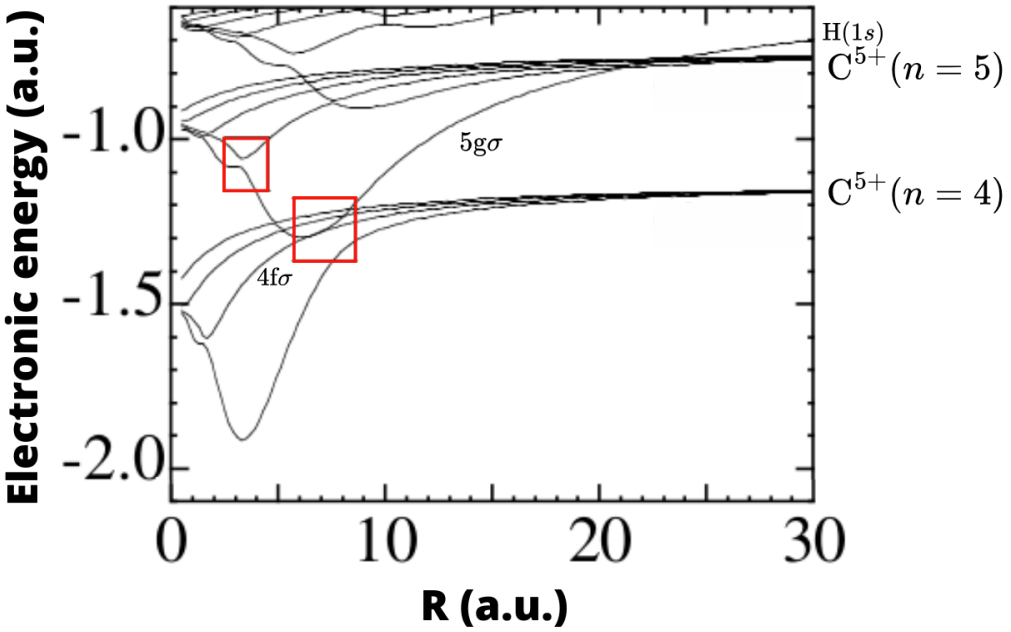

Figure 29: Adiabatic potential energy curves of the Σ states for the $(CH)^{6+}$ system : with two important avoided crossings framed. Figure modified from Caillat *et al* [105].

correlated asymptotically with the C^{5+}(n = 4) state. Capture to n = 5 happens in two steps : first the mechanism described previously for the capture to n = 4 and then the avoided crossings around R = 3 a.u. between the curves correlated to the n = 4 and n = 5 states. This prevalence of the n = 4 and n = 5 capture channels is also visible in Figure 30, which shows the reduced probability bP(b) for C^{5+}(n=3,4,5,6) and total capture, as well as total excitation and ionization, at a collision energy of 2 keV/u. The corresponding cross sections are recalled in the legend in multiples of 10^{-16} cm^2. The prevalence of the n = 4 and n = 5 capture channels is easily visible with the dominance of the n = 4 over the n = 5 channel. Figure 30 shows that capture to n = 4 is important below b = 9 a.u., in agreement with the position of the avoided crossing in Figure 29. On the other hand, the production of $C^{5+}(5\ell)$ only appears at lower impact parameters, b<5 a.u.

In conclusion, this study has significantly enhanced our understanding of the dynamics of the C^{6+}+ H(1s) collision system. Comparisons with previous results from the literature [45, 105–108] demonstrate the robustness and accuracy of our method, particularly in agreement with the data for both total and partial electron capture cross sections. The observed discrepancies in various energy levels have been attributed to differences in methodological approaches, further validating the comprehensive nature of our study. In particular the agreement with the most recent studies [107] [106], and particularly with Abdurakhmanov *et al* [106] (which appears to be the most converged and recent approach) validates with an unprecedented precision a series of reliable data for this collision system. The insights gained from this investigation laid a solid foundation for studies involving two-electron systems.

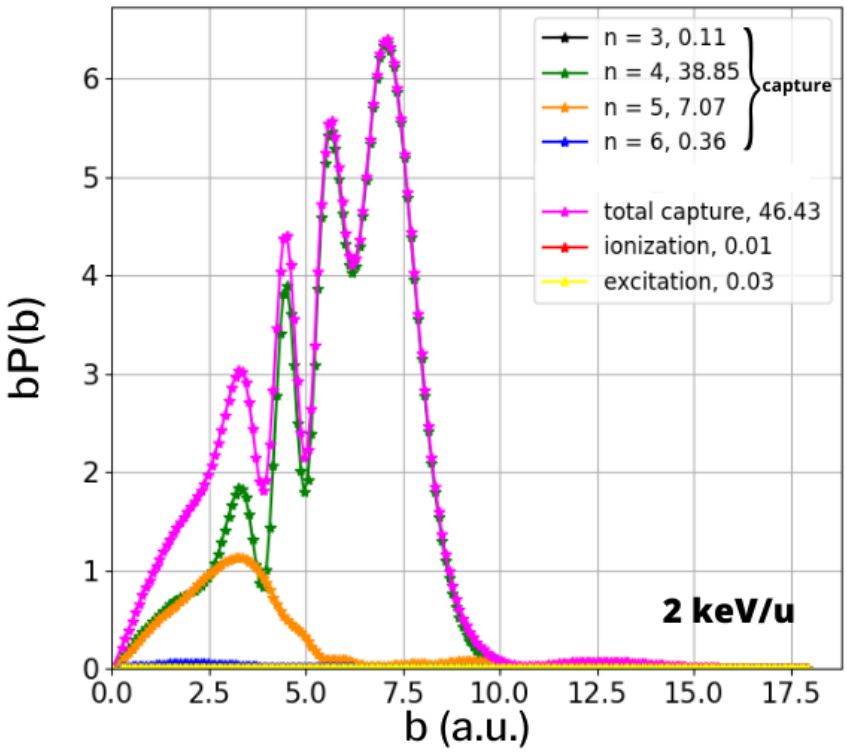

Figure 30: Reduced probabilities for different processes for the C^{6+} + H(1s) collision at a collision energy of 2 keV/u. The numbers following the channels in the captions are the cross sections in multiples of 10^{-16} cm^2

3.3 Two-electron systems

In the following, electronic processes in the collisions $N^{6+}(1s)$ + $He^{+}(1s)$ and N^{7+} + $He(1s^2)$ are investigated. Both systems concern nitrogen and helium, neutral and charged. Then one needs to obtain the states of N^{6+}, N^{5+} (produced by single or double capture) and the states of He and He^{+}. Therefore these two studies require only a unique stage of state production, this latter being very time consuming since requiring difficult optimization of GTOs. In the following, the implementation of the GTO basis sets necessary for this study is presented, followed by the results and discussion for each collision system.

3.3.1 Implementation

Two GTO sets are created, one to describe the states of the helium target, and another one to describe the nitrogen projectile. Since two electrons are at play in these collisions, the GTO sets for helium must be able to accurately describe both the states of He^{+} and He, and the GTO sets for nitrogen must describe N^{6+} and N^{5+} states. After several tests, the optimal GTO set was created and comprised for helium a total of 28 GTOs (7 for s states, 7×3 for p states), and for nitrogen, 78 GTOs (10 for s states, 8×3 for p states, 6×5 for d states, 2×7 for f states). These GTOs are listed in Appendix B.2. In Table 4, a selection of the energies of the most important one-electron states of N^{6+} and He^{+} are presented. The values obtained with our GTO sets are compared with the theoretical values calculated with the Bohr equation (90). Tables 5 and 6 give the comparison between the energies for the two-electron states of N^{5+} and He obtained

State	E_{Calc}	E_{GTO}	Δ(%)	State	E_{Calc}	E_{GTO}	Δ(%)
N^{6+}(1s)	-24.50	-24.4890	0.04	**He^{+}(1s)**	-2.00	-1.9938	0.31
N^{6+}(2s)	-6.125	-6.1236	0.02	**He^{+}(2s)**	-0.50	-0.4980	0.40
N^{6+}(2p)	-6.125	-6.1228	0.04	**He^{+}(2p)**	-0.50	-0.5000	0.01
N^{6+}(3s)	-2.722	-2.7217	0.01	**He^{+}(3s)**	-0.222	-0.2213	0.29
N^{6+}(3p)	-2.722	-2.7214	0.02	**He^{+}(3p)**	-0.222	-0.2222	0.04
N^{6+}(3d)	-2.722	-2.7218	0.01				
N^{6+}(4s)	-1.531	-1.5309	0.01				
N^{6+}(4p)	-1.531	-1.5305	0.03				
N^{6+}(4d)	-1.531	-1.5307	0.02				
N^{6+}(4f)	-1.531	-1.5218	0.61				

Table 4: Energies E_{GTO}, in a.u., of the N^{6+} (left) and He^{+} (right) ion states, compared to the values given by equation (90). Relative difference Δ is given by $\Delta = |(E_{\mathrm{GTO}} - E_{\mathrm{Calc}})/E_{\mathrm{Calc}}| \times 100$.

with the same GTO sets, and the values given in NIST [112, 113].

State	E_{NIST}	E_{GTO}	Δ(%)	State	E_{NIST}	E_{GTO}	Δ(%)
Singlet states				Triplet states			
N^{5+}($1s^2$)	-44.7881	-44.7557	0.07				
N^{5+}(1s2s)	-29.1176	-29.1026	0.05	**N^{5+}(1s2s)**	-29.3609	-29.3455	0.05
N^{5+}(1s2p)	-28.9603	-28.9453	0.05	**N^{5+}(1s2p)**	-29.1212	-29.1078	0.05
N^{5+}(1s3s)	-26.5381	-26.5232	0.06	**N^{5+}(1s3s)**	-26.5998	-26.5875	0.05
N^{5+}(1s3p)	-26.4881	-26.4775	0.04	**N^{5+}(1s3p)**	-26.5347	-26.5230	0.04
N^{5+}(1s3d)	-26.5000	-26.4888	0.04	**N^{5+}(1s3d)**	-26.5014	-26.4901	0.04
N^{5+}(1s4s)	-25.6400	-25.6248	0.06	**N^{5+}(1s4s)**	-25.6661	-25.6519	0.06
N^{5+}(1s4p)	-25.6205	-25.6040	0.06	**N^{5+}(1s4p)**	-25.6396	-25.6237	0.06
N^{5+}(1s4d)	-25.6249	-25.6099	0.06	**N^{5+}(1s4d)**	-25.6250	-25.6108	0.06

Table 5: Energies E_{GTO}, in a.u., of the N^{5+} singlet (left) and triplet (right) states, compared to NIST values. Relative difference Δ is given by $\Delta = |(E_{\mathrm{GTO}} - E_{\mathrm{NIST}})/E_{\mathrm{NIST}}| \times 100$.

One observes that, for the different atomic species, our calculated energies are in very good agreement with the tabulated ones, with differences no larger than a few ‰, except for the N^{6+}(4f) states for which the difference reaches 0.6%, due to the limited number of GTO used to describe the $\ell = 3$ states (to avoid an unaffordable CPU consumption). Note that the diagonalization of the different atomic Hamiltonian for these GTO sets produces a large number of one- and two- electron states. A selection of them is included in the dynamical stage of the calculations and depends on the system considered.

State	E_{NIST}	E_{GTO}	Δ(%)	State	E_{NIST}	E_{GTO}	Δ(%)
Singlet states				Triplet states			
He ($1s^2$)	-2.9036	-2.8937	0.34				
He (1s2s)	-2.1459	-2.1385	0.04	**He (1s2s)**	-2.1752	-2.1675	0.35
He (1s2p)	-2.1238	-2.1162	0.35	**He (1s2p)**	-2.1331	-2.1263	0.32
He (1s3s)	-2.0575	-2.0540	0.17	**He (1s3s)**	-2.0601	-2.0650	0.24
He (1s3p)	-2.0514	-2.0587	0.35	**He (1s3p)**	-2.0286	-2.0544	1.27

Table 6: Energies E_{GTO}, in a.u., of the He singlet (left) and triplet (right) states, compared to NIST values. Relative difference Δ is given by $\Delta = |(E_{\mathrm{GTO}} - E_{\mathrm{NIST}})/E_{\mathrm{NIST}}| \times 100$.

3.3.2 N^{6+}(1s) + He^{+}(1s) collisions

For this collision system, two different processes are considered in the 0.25-25 keV/u energy range, namely charge transfer to the nitrogen ion and excitation of the helium ion

$$N^{6+}(1s) + He^{+}(1s) \rightarrow N^{5+}(1sn\ell) + He^{2+} \quad (92)$$

$$N^{6+}(1s) + He^{+}(1s) \rightarrow N^{6+}(1s) + He^{+}(n\ell) \quad (93)$$

Indeed, during the first stages of our study, the capture to helium, the nitrogen and helium ionization processes and the excitation of N^{6+} have been found to have extremely small cross sections in the energy range considered. Therefore it was decided not to include the states where the two electrons are on the target (He, corresponding to capture to helium). Moreover, after several tests, no noticeable difference in the cross sections for capture to nitrogen and helium excitation could be found whether states describing helium capture were included or not in the basis set, meaning that these channels were hardly coupled to the ones under consideration. These preliminary tests validate the state basis that we finally selected, without requiring large CPU consumption to include channels of very little importance.

For the description of the (N^{6+}(1s), He^{+}(nℓ)) final state, 27 states are used, spanning up to He^{+}(3p) and pseudostates. For the N^{5+}(1snℓ) final states, 79 singlet states or 75 triplet states are used, spanning up to N^{5+}(1s4d). Only 5 energies between 0.25 keV/u and 25 keV/u were computed, with 50 values of the impact parameter for each to compute accurately the cross sections. This restricted number of impact energies is due to the very high computation time required for this system, and the energy range has been chosen as a function of what is experimentally accessible at INSP. In average, the calculations for one energy takes 80 hours per spin state, meaning that completing a calculation for both singlet and triplet states for one energy value takes no less than 160 hours. For this reason we limit ourselves to a few energy values.

Second, for this two-electron system the calculations are two-folded : even though the initial states are well defined (N^{6+}(1s) and He^{+}(1s)), the total spin state can be singlet or triplet. Experiments where the ion beams are polarized do not exist for this system and, in fact, are very scarce in general. Moreover the set up at INSP does not allow for the production of polarized beams. Therefore the initial total spin state remains undefined, and the calculations for singlet and triplet total spin have to be performed separately. The *collision solver* program only allows calculations for one spin state at a time, as two separate versions of the code are used for singlet and triplet states. The

total capture and excitation cross sections for a specific channel χ are spin averaged as follows

$$\sigma(\chi) = \frac{\sigma_\chi^S + 3\sigma_\chi^T}{4} \tag{94}$$

where σ_χ^S and σ_χ^T are the cross sections for the channel χ calculated for singlet and triplet total spin states, respectively. Figure 31 shows the spin averaged cross sections

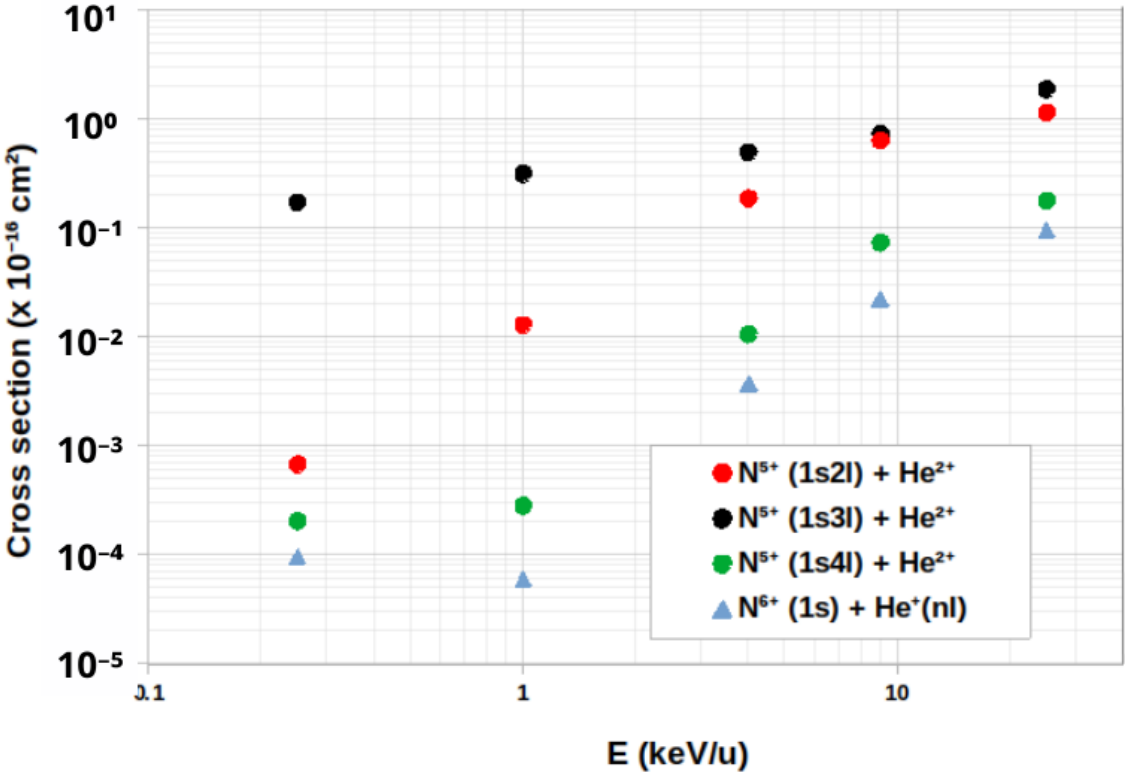

Figure 31: Spin averaged cross sections for single capture to $N^{5+}(1sn\ell)$ (n = 2, 3, 4) and excitation $N^{6+}(1s) + He^{+}(n\ell)$.

for single capture to $N^{5+}(1sn\ell)$ (n = 2, 3, 4) and total excitation of He^+. In the energy range considered, the dominant process by several orders of magnitude is electron capture, and the important channels for this process are mainly the ones to n = 3 and also to n = 2, especially at the highest energies considered. These capture cross sections show a continuous increase, their maximum being therefore located at energies higher than 25 keV/u. On the other hand, for He^+ excitation, the cross section seems to present a minimum at 1 keV/u, followed by a fast increase, as expected. However, this minimum should be tested further since in this energy region the cross sections are very low ($\approx 10^{-20}$ cm^2), so that convergence may not have been reached for these channels. Figure 32 presents a comparison between the singlet and triplet states reduced partial probabilities for electron capture to $N^{5+}(1s2s)$ and $N^{5+}(1s2p)$. At the two lowest energies we can notice that the reduced partial probabilities exhibit an oscillating behaviour. Such oscillations are a well-known phenomenon in ion-atom collisions, when a process is induced both through an avoided crossing and interference effects between the two corresponding molecular states (expressed as phase accumulation of

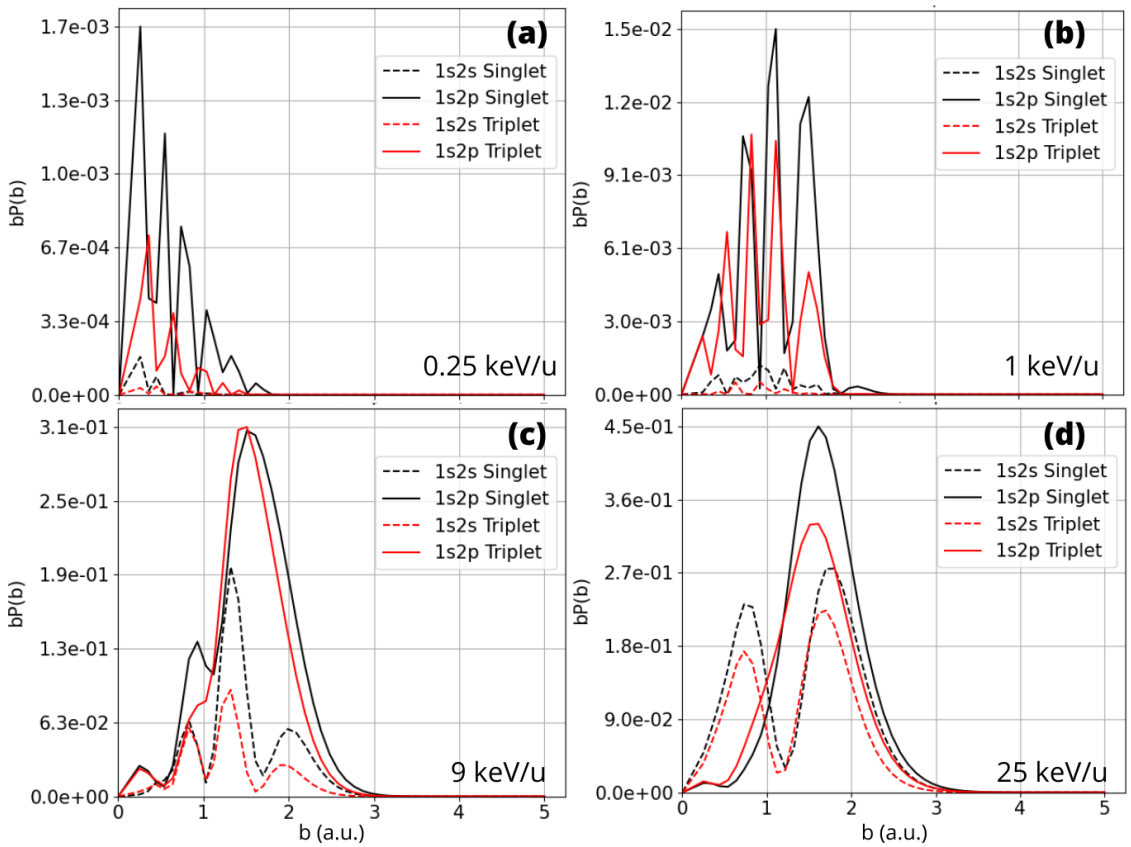

Figure 32: Comparison between the singlet and triplet states reduced partial probabilities for electron capture to $N^{6+}(1s2s)$ and $N^{6+}(1s2p)$, for four typical energies.

their scattering amplitudes during the relative motion of target and projectile [114]). We observe in these figures a clear dominance of the 1s2p capture over the 1s2s one. Moreover, in both cases, capture to the singlet states show the largest probabilities (and therefore cross sections) except at 9 keV/u for capture to 1s2p where singlet and triplet spin states are about equiprobable. These results are commented in the following.

To better understand the mechanisms at play during electron capture, calculations of the potential energy curves for the singlet and triplet Σ states of the $(NHe)^{7+}$ pseudo-molecule have been performed. These curves are presented in Figure 33 and a zoom on an important avoided crossing is presented in Figure 34. This avoided crossing between the curves correlated asymptotically to the initial channel and to the production of $N^{5+}(1s2\ell)$ at around R = 2 a.u. is responsible for the capture into n = 2 at low energies. Indeed in Figure 32, one can see that below 1 keV/u there is a cut-off at b = 2 a.u. whereas at higher energies the capture happens also at higher impact parameters. That is because at higher energies, capture takes place via direct coupling working at higher internuclear distances, and not just at avoided crossings. As mentioned before, capture to 2p is more important than capture to 2s. The potential energy curves (Figure 34) show indeed that the avoided crossing to 2s presents a larger gap than the one to 2p, explaining the predominance of the 2p capture channel over the 2s. The 2s and 2p singlet states have overall larger cross sections than the triplet states ones, which is easily explained by the potential energy curves : for the avoided crossing that gives rise to the 2ℓ capture, the curves are further apart in energy for the triplet

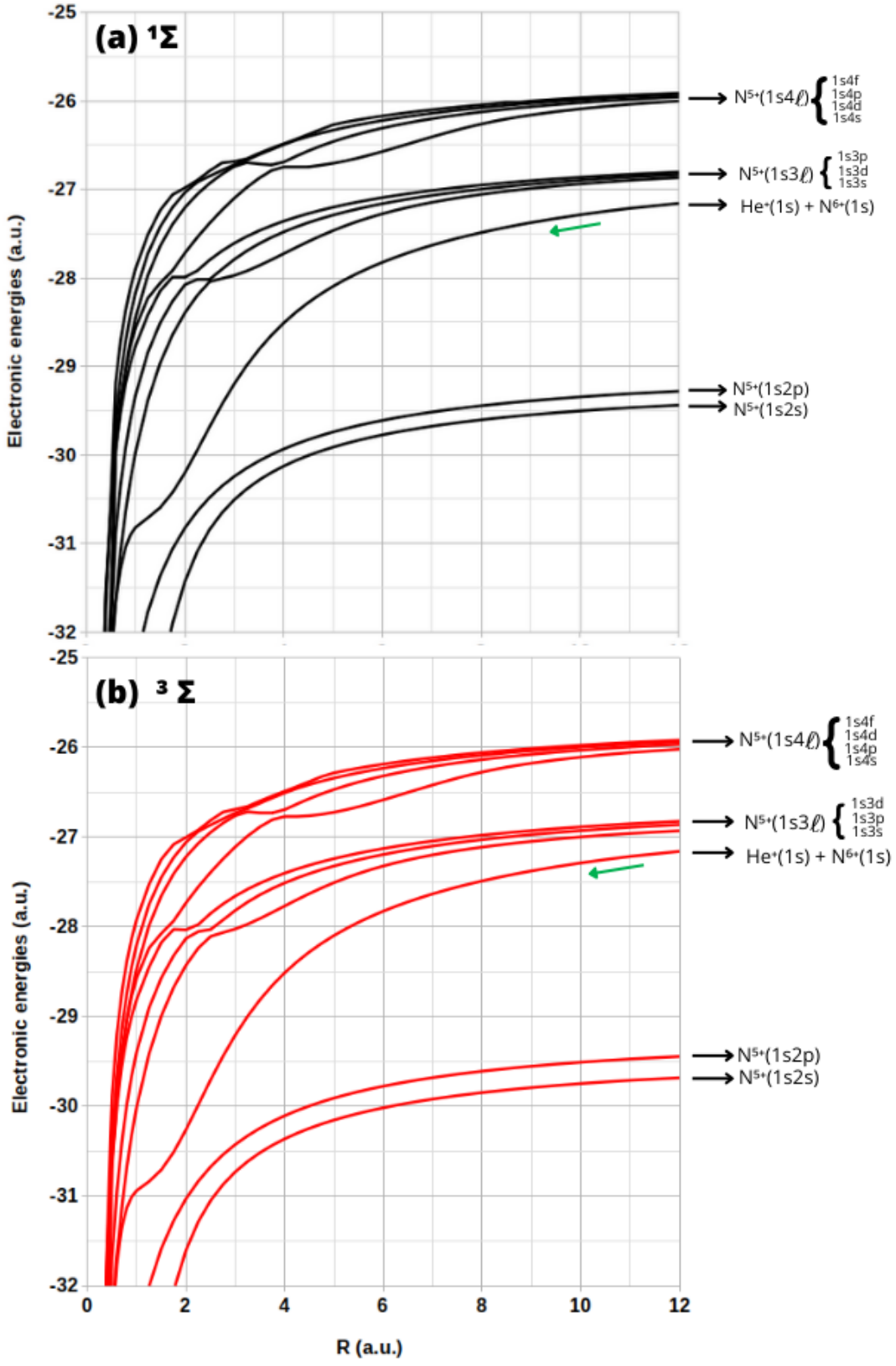

Figure 33: Potential energy curves of the singlet (a) and triplet (b) Σ states for the $(NHe)^{7+}$ system. Asymptotic states of N^{5+} are given by black arrows and the states are energy ordered from lowest to highest after the brackets. The green arrow indicates the curve that is correlated asymptotically to the initial channel $N^{6+}(1s) + He^{+}(1s)$.

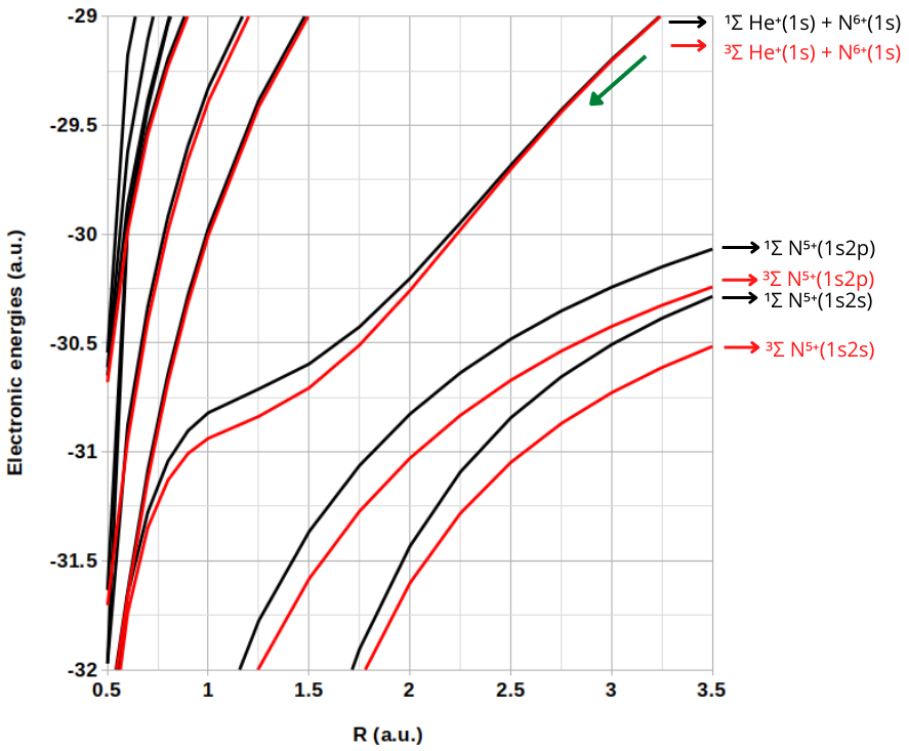

Figure 34: Zoom on an important avoided crossing in the potential energy curves of the singlet (black) and triplet (red) Σ states for the $(NHe)^{7+}$ system. The green arrow indicates the curve that can be asymptotically identified as the initial state $N^{6+}(1s)$ +$He^{+}(1s)$.

states than for the singlet states, leading to lower probabilities of capture and smaller cross sections. In Figure 34, one can also observe that the avoided crossing seems to appear at somewhat larger internuclear distance for the singlet states, explaining the largest probabilities for these spin states around the cut-off at b = 3 a.u. on Figure 32. In Figure 35, the reduced partial probabilities for electron capture to $N^{5+}(1s3\ell)$ for 1 and 4 keV/u energies are presented. We can notice that these capture processes arise at lower impact parameter compared to the capture to n = 2, and the avoided crossing(s) responsible for this mechanism are not visible in the potential energy curves of figures 33 and 34. However an interesting remark is that between the singlet states ((a) and (c) on the left) and the triplet states ((b) and (d) on the right) we can notice an inversion in terms of probability between the 1s3p and 1s3d states. In the singlet case, capture to 1s3d is more probable than capture to 1s3p, and it is the contrary for triplet states. Indeed from Table 5 it is clear that the s and p states are inverted in terms of energy for n = 3 (and also for n = 4) between singlet and triplet spin states. This is reflected in the cross sections for capture into these states. It would be interesting, in the future, to probe experimentally this inversion.

In this section, a large number of results on capture for the $N^{6+}(1s)$ + $He^{+}(1s)$ collision system have been presented. No data was found in the literature to compare with our results, even for the most probable processes. It was possible to evaluate the cross sections for other less important channels (not shown in this work). It would now be particularly interesting to have experimental results on this collision system, not only to compare with the data presented in this section but also due to the originality that this collision system presents. However, since capture cross sections are of the order of

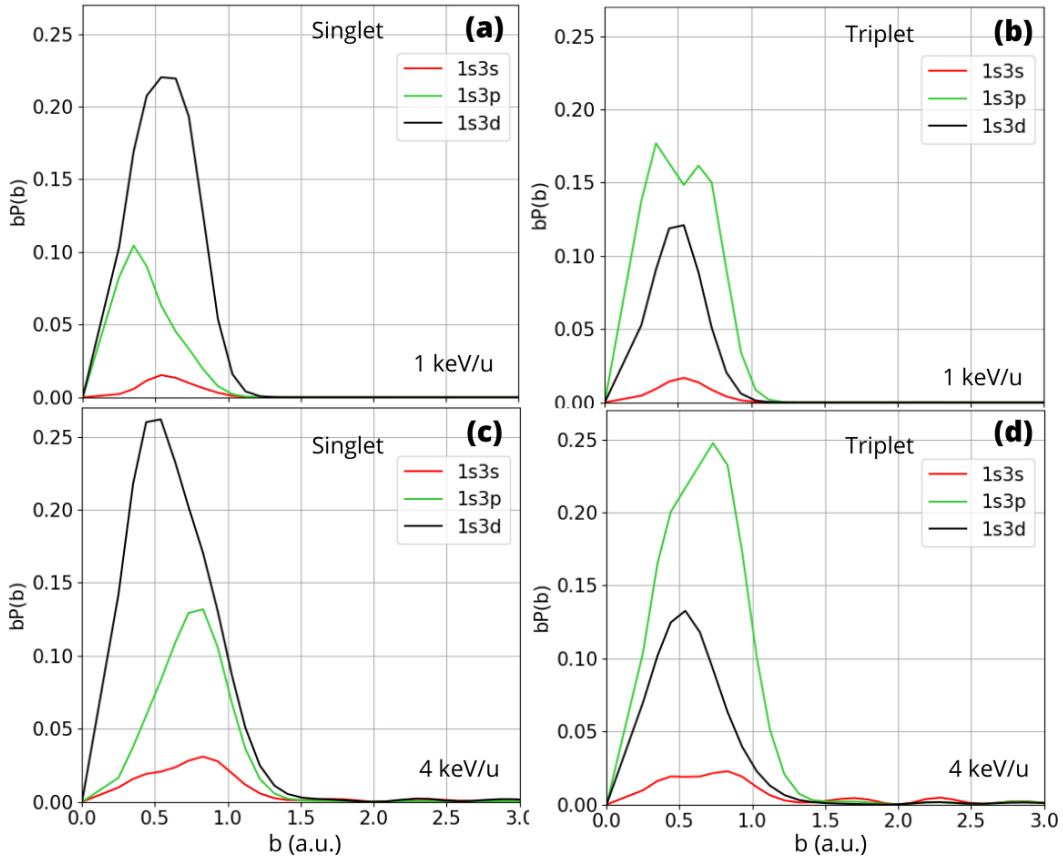

Figure 35: Reduced partial probabilities for electron capture to $N^{5+}(1s3\ell)$ for energies of 1 and 4 keV/u, singlet states (left) and triplet states (right).

10^{-17} cm^2, this system would be difficult to study at INSP given the current sensitivity of our setup.

3.3.3 N^{7+} + He($1s^2$) collisions

The same GTO set was used for this system as for the $N^{6+}(1s)$ + $He^+(1s)$ collision system. It is important to note that unlike the case of $N^{6+}(1s)$ + $He^+(1s)$, we consider here the initial total spin state to be singlet since the initial state of the target atom with both electrons is a singlet state, He($1s^2$). This, combined with the fact that the computation time was less important for this system (an average of 50 hours per energy value), has allowed us to compute a larger number of energy values (16) within the 0.25 - 100 keV/u energy range. For these calculations we use a basis comprising 75 states for the description of He, 600 states for (N^{6+}(nℓ), He^+(nℓ)), and 691 states for N^{5+}(nℓn'ℓ'), this latter allowing a thorough and accurate description of doubly excited states of N^{5+}. For this collision system, six possible processes have been considered

- Simple capture to nitrogen (SC):
$$N^{7+} + He(1s^2) \rightarrow N^{6+}(n\ell) + He^+(1s) \quad (95)$$
- Double capture to autoionizing states of N^{5+} (ADC) :
$$N^{7+} + He(1s^2) \rightarrow N^{5+}(n\ell n'\ell') + He^{2+} \quad (n, n' > 1) \quad (96)$$
- Double capture (DC) to bound states of N^{5+}:
$$N^{7+} + He(1s^2) \rightarrow N^{5+}(1sn'\ell') + He^{2+} \quad (97)$$

- Transfer excitation (TE) combining electron capture to N^{6+} and excitation of He^{+}:

$$N^{7+} + He(1s^2) \rightarrow N^{6+}(n\ell) + He^{+}(n'\ell, n' > 1) \quad (98)$$

- Transfer ionization (TI) combining electron capture to N^{6+} and ionization of He^{+} to He^{2+}:

$$N^{7+} + He(1s^2) \rightarrow N^{6+}(n\ell) + He^{2+} + e^{-} \quad (99)$$

- Simple and double excitation of helium (EXC) :

$$N^{7+} + He(1s^2) \rightarrow N^{7+} + He(n\ell n'\ell') \quad (100)$$

The energies of the doubly excited states of N^{5+} used in our calculations for ADC are given in Table 7, and compared to calculations made by Van der Hart *et al* [109]. In this article, the authors employ a B-spline basis set to calculate energy levels and autoionization widths of doubly excited states in the N^{5+} ion. The truncated diagonalization method (TDM) is extended to account for open channels, improving the accuracy of the calculations. In Table 7, the agreement between our values and values from [109] is seen to be very good, of the order of a few ‰, validating the quality of our GTO basis set.

LS	$\mathbf{E_{Calc}}$	$\mathbf{E_{GTO}}$	**Δ(%)**
$^1\mathbf{S}^e$ **(3,3)**	-5.1079	-5.1024	0.11
$^1\mathbf{S}^e$ **(3,4)**	-4.0019	-4.0012	0.02
$^1\mathbf{P}^o$ **(3,3)**	-5.0205	-5.0114	0.18
$^1\mathbf{P}^o$ **(3,4)**	-4.0280	-4.0263	0.04
$^1\mathbf{D}^o$ **(3,3)**	-5.0040	-5.0029	0.02
$^1\mathbf{D}^o$ **(3,4)**	-3.9568	-3.9527	0.10
$^1\mathbf{D}^e$ **(3,3)**	-5.0608	-5.0588	0.04
$^1\mathbf{D}^e$ **(3,4)**	-3.9759	-3.9745	0.04
$^1\mathbf{F}^o$ **(3,3)**	-4.8510	-4.8548	0.08
$^1\mathbf{F}^o$ **(3,4)**	-3.9891	-3.9857	0.09
$^1\mathbf{G}^e$ **(3,3)**	-4.8629	-4.8499	0.27
$^1\mathbf{G}^e$ **(3,4)**	-3.8963	-3.9010	0.12

Table 7: Energies of autoionizing states N^{5+}(nℓn'ℓ') (marked as $^{2S+1}$L(n,n')) given in [109], E_{calc}, compared to our values, E_{GTO}, with relative differences.

In Figure 36 the cross sections are represented for all the processes described by equations (95) to (100), except for DC. Indeed, double capture as defined in equation (97) (double capture to bound states) is very unlikely, the cross sections being about 4 orders of magnitude smaller than the ones presented in Figure 36. Numerical problems often arise when dealing with such small cross sections (of the order of 10^{-21} cm^2) and it is hard to separate the real values from numerical instabilities. Therefore they are not presented along with the others and the process are not discussed further. The two main capture channels are SC and ADC, with SC being the dominant process. SC, ADC and TE exhibit weak dependence upon energy. However, the TI cross sections

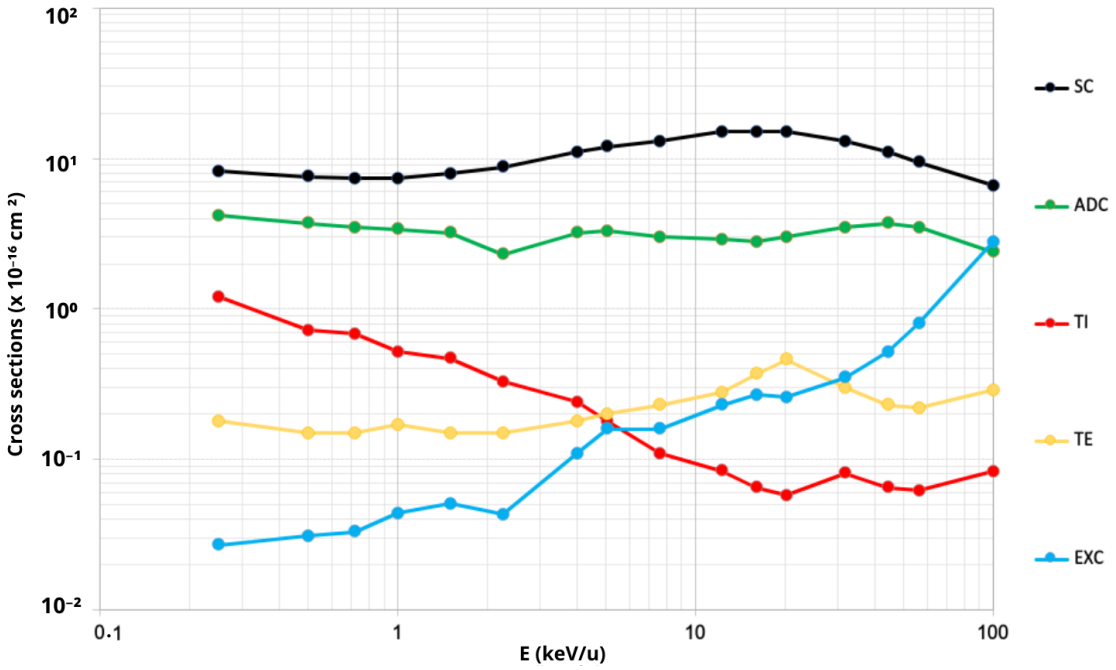

Figure 36: Cross sections for the SC, ADC, TI, TE, EXC processes as a function of the collision energy.

decrease by more than one order of magnitude between 0.25 and 100 keV/u while the EXC cross sections increase by nearly 2 orders of magnitude. At lower energies (below 10 keV), TE and TI have cross sections larger than EXC. However at larger energies, above 30 keV/u, EXC becomes significant, with cross sections larger than TE or TI. Contrarily to SC and ADC, no data for TI, TE and EXC were found in the literature, and therefore no comparison is possible. In the following, our results for SC and ADC will be compared with data from Harel *et al* [110], Wu *et al* [111] and Iwai *et al* [115] :

- Wu *et al* [111] measure experimentally SC and ADC processes using coincident recoil momentum spectroscopy. It is important to note that in this article, the authors call "transfer ionization" the process called ADC in our work.
- Iwai *et al* [115] measure experimentally one-electron transfer in N^{7+} - He collisions. Collision products are charge analyzed using a parallel plate electrostatic analyzer and subsequently detected by a microchannel plate detector.
- Harel *et al* [110] present a detailed theoretical investigation of the autoionizing double capture (ADC) process during collisions at low energies. The authors use a method involving the expansion of the total electronic wave function onto configurations built from One-Electron Diatomic Molecule (OEDM) orbitals. These configurations account for both single-electron and double-electron capture channels.

Figure 37 shows the comparison between our results and the cross sections obtained by Wu *et al* [111] for ADC and SC as a function of the collision energy. Also included are three SC experimental points from Iwai *et al* [115]. Even though our SC and ADC results differ significantly from all experimental data at low energies (< 8 keV/u), we

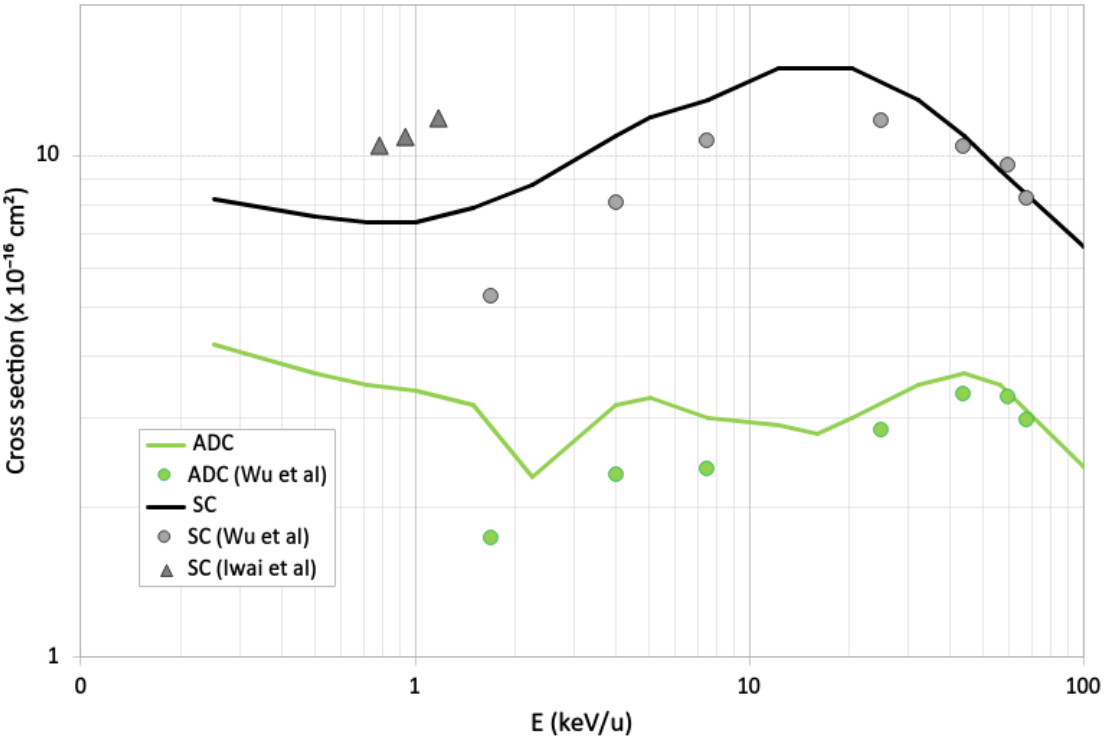

Figure 37: Comparison between our results and the cross sections measures by Wu *et al* [111] and Iwai *et al* [115] for ADC and SC as a function of the collision energy.

can however see that both sets of experimental results do not agree with each other and that our results lie in-between them. The evolution of the cross sections with the collision energy is the same in our results and the data of Wu *et al*, showing a maximum at about 20 keV/u for SC and at about 40 keV/u for ADC. At higher energies (above 40 keV/u), our SC and ADC results only differ by a few percents from the experimental data of Wu *et al*. Given the possibility that some processes may or may not be included into SC and ADC depending on the authors and the method used, particularly in the case of experimental data, our agreement with results from [111] and [115] is rather good.

Figure 38 shows the comparison between our results and the results from Harel *et al* [110], for total capture cross section, SC to n = 3, 4 and ADC to N^{5+}(3,3) and N^{5+}(3,4). The single capture to n = 4 emerges as the dominant process, showing minimal energy dependence below 10 keV/u, with a peak followed by a sharp decline around 20 keV/u. In contrast, cross sections for single capture to n = 3 exhibit a distinct behavior, rapidly increasing by over an order of magnitude between 0.25 and 10 keV/u, peaking around 20 keV/u, and then decreasing. At 0.25 keV/u, single capture to n = 3 has the lowest cross section among the processes presented, but it takes over ADC to N^{5+}(3,4) around 1 keV/u and ADC to N^{5+}(3,3) around 4 keV/u. ADC to N^{5+}(3,3) is the strongest ADC channel and exhibits an overall low dependence on energy, with a decrease above 20 keV/u. Cross sections for ADC to N^{5+}(3,4) shows a slight increase up to 20 keV/u, followed by a decrease. Although only three energy points of [110] are available for comparison, the overall order of magnitude and energy dependence of the results are consistent.

Figure 39 shows the reduced probabilities bP(b) for SC transitions to n = 3,4 and

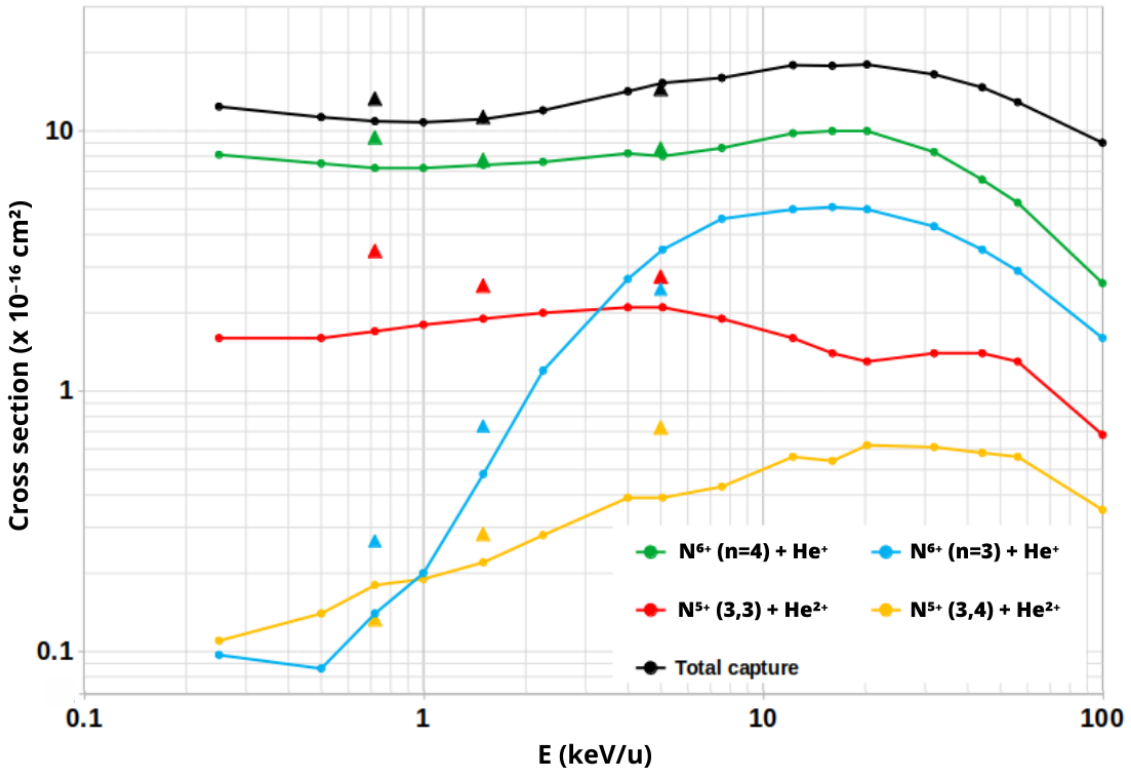

Figure 38: Comparison between our results and the ones obtained by Harel *et al* [110] for ADC, SC and total capture as a function of the collision energy. Our results are represented by the full curves and the results of Harel by triangles of the same colour.

ADC transitions to n = 3, n' = 3,4 at 1 and 7.6 keV/u collision energies. At both energies, as expected from Figure 38, the most prominent process is SC to n = 4, which shows two main peaks at impact parameters b ≈ 2 and 6 a.u., with a cut-off around b = 10 a.u. For single capture to n = 3, the reduced probabilities are hardly noticeable at the scale of our figure for 1 keV/u. For the highest energy (Figure 39 (b)), the reduced probability extends to b ≈ 5 a.u. and presents a peak at about 3 a.u. This illustrates the important increase of the cross sections observed in Figure 38. The reduced probabilities for ADC to N^{5+}(3,3) exhibit for both energies a maximum around 3 a.u., with a cut-off at b = 4 a.u., maintaining a similar amplitude at both energies. The reduced probabilities for ADC to N^{5+}(3,4) have a very small magnitude compared to other processes (in Figure 39 the reduced probabilities for N^{5+}(3,4) have been multiplied by a factor 10 (a) and 4 (b) in order to improve readability) and show a maximum at very small impact parameters for both collision energies. While the reduced probabilities for ADC to N^{5+}(3,4) retain a similar magnitude at 1 and 7.6 keV/u, the ones for SC to n = 3 show a significantly increase at 7.6 keV/u, with magnitude comparable to the other two processes, showing a cut-off around 4 a.u. The inversion in the probabilities of N^{5+}(3,3) and N^{6+}(n = 3) is depicted in Figure 38, where their cross section curves intersect at an energy of approximately 4 keV/u.
Another interesting discussion of the results for this collision system can be made by analyzing the diabatic molecular energy curves in Figure 40 obtained by Harel *et al* [110] and the partial reduced probabilities in Figure 39. One observes in Figure 40 that the curve correlated to the initial state crosses the curves correlated to SC N^{6+}(n = 4) and ADC N^{5+}(3,4) at internuclear distance R ≈ 10 a.u. and then SC N^{6+}(n = 3) and ADC

$N^{5+}(3,3)$ at R ≈ 4 a.u. For the $N^{6+}(n = 4)$ final states in Figure 39, a cut off indeed

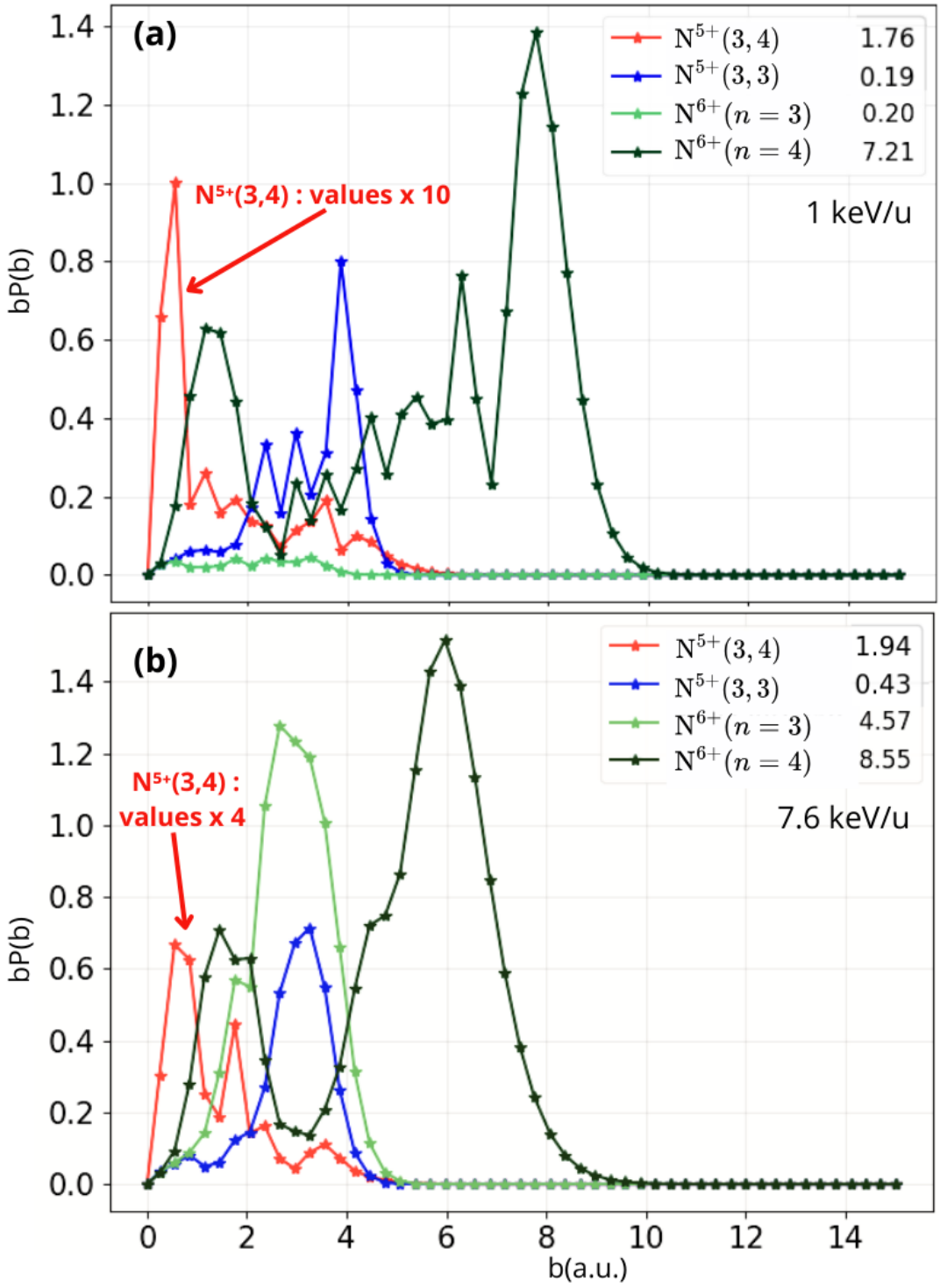

Figure 39: Partial reduced probabilities for ADC to n = 3 and n' = 3,4 and SC for n = 3 and 4, for collision energies of 1 kev/u (a) and 7.6 keV/u (b). The cross sections are given in the caption in multiples of 10^{-16} cm^2. The reduced probabilities for N^{5+}(3,4) have been multiplied by a factor 10 (a) and 4 (b) in order to improve readability.

happens near b = 10 a.u., in accordance with the crossing mentioned just above. This region of crossings seems to be inactive to induce ADC to N^{5+}(3,4), largely dominated

by the SC channels. The position of the inner crossings for SC to n = 3 and ADC to N^{5+}(3,3) is consistent with the peak of reduced probability around b = 3 a.u., followed by a fast decrease. However it is important to note that these considerations are only qualitative since from Figure 40 one cannot deduce any information on the strength to induce the transition among molecular curves. Indeed, in Figure 39, one can observe a very different, quantitative, difference for, e.g., the reduced probability for SC to n = 3 between the two energies considered. This demonstrates also the importance of using non perturbative approach to model this complex system.

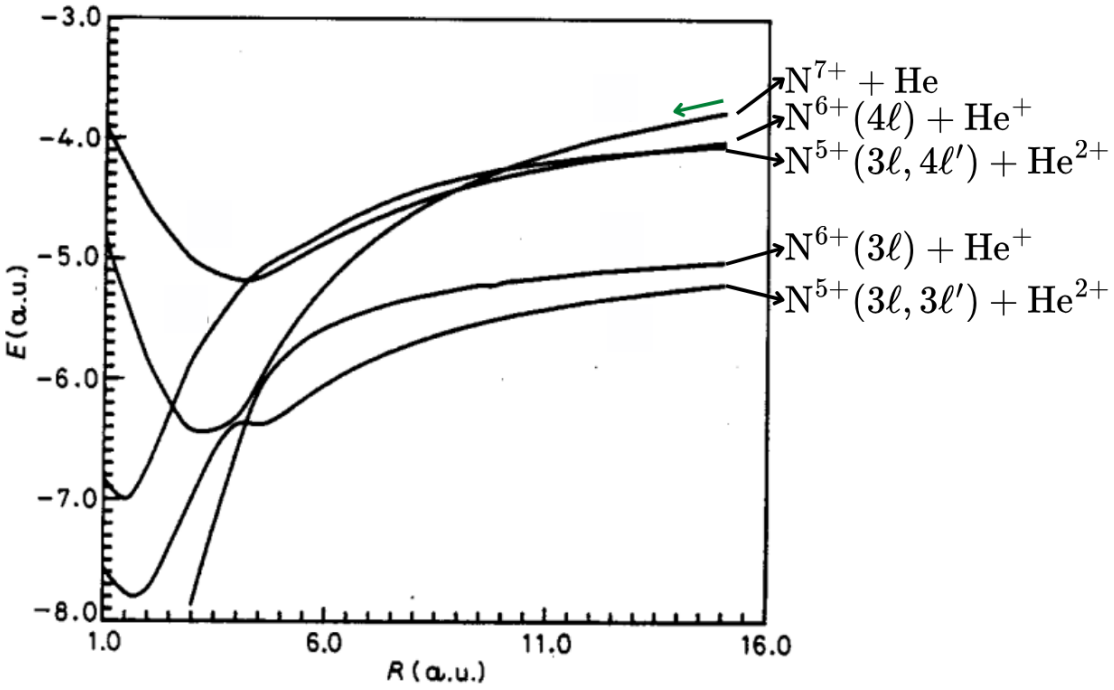

Figure 40: Diabatic correlation diagram for the $(NHe)^{7+}$ quasimolecule. Asymptotic states are given by arrows and the green arrow indicates the curve that can be identified as the initial state N^{7+}(1s) + He($1s^2$). Graph modified from [110].

In conclusion, the study of the collision system involving N^{7+} and He has provided significant insights into various electron capture processes. It was observed that direct double capture is highly unlikely due to its extremely low cross section values. The most dominant processes identified are Simple Capture and Double Capture to autoionizing states. This is in line with the findings of previous studies from Harel *et al* [110] and Wu *et al* [111], who also noted the significance of SC and ADC in similar collision systems. The discrepancies between our results and results by these authors (30% at low energies and only a few percents at higher energies) could in part stem from differences in methodologies and the definition of processes. Furthermore, our study highlights the importance of using a comprehensive basis set to accurately describe doubly excited states of N^{5+}. The comparison of calculated energy levels with those obtained by Van der Hart *et al* [109] confirms the reliability of our approach. The detailed investigation into the diabatic molecular energy curves provides additional understanding of the electron capture dynamics, revealing several key molecular mechanics that significantly influence the capture probabilities. The study of autoionizing states highlights the importance of a thorough and precise definition of the different processes to avoid confusion when comparing data, especially with regard to future experimental results, where some processes may not be easily distinguishable from others (ADC from SC for instance).

4 Description of experimental devices and acquisition systems

This chapter is dedicated to the description of the various experimental devices used. Firstly, it covers the ion sources from the INSP and ARIBE at GANIL, along with their respective beamlines. Secondly, it details the different instruments in the collision zone. Finally, the instruments dedicated to the detection of ions and X-rays, as well as the data processing systems are presented.

4.1 Sources for ion production

4.1.1 Existing types of ion sources

For investigating the interaction between ions and matter, and more specifically ion-ion interactions, the production of multicharged ion beams is necessary. Various types of specialized ion sources are used in different fields of research and applications. Some of the most common types of ion sources are listed below.

- *Laser ion sources (LIS)* : LIS work by using intense laser beams to ionize target materials. These lasers interact with the target, causing ionization through processes like multiphoton and tunneling ionization. This creates ions that are then extracted. Laser Ion Sources (LIS) are used in applications such as cancer therapy, ion-driven fast ignition, material science, and fusion research. They generate high-energy proton and light ion beams with energies ranging from tens of MeV to hundreds of MeV or GeV necessary for these fields of research. However, LIS face limitations in achieving high repetition rates, high average power, and stable beam production, which are crucial for industrial and medical applications [116].

- *Electron Beam Ion Sources (EBIS)* : EBIS utilize an electron beam to ionize neutral atoms or molecules. These sources are known for their ability to produce highly charged ions for atomic physics, synchrotrons and colliders. They offer precise control over ion extraction times and are valuable for studying ion-electron collisions. Their limitations include restricted ion yield, instabilities at high currents, and the need for sophisticated cooling techniques. Typical ion species produced include highly charged ions like N^{7+}, Ar^{14+}, Xe^{28+}, and even U^{92+}, with the use of electron beam energies ranging from a few keV to around 198 keV [117].

- *Penning Ion Sources (PIS)* : PIS use a combination of magnetic and electric fields to generate ions from a gas discharge. They are known for their ability to produce intense beams of singly charged ions and are widely used in ion thrusters for spacecraft propulsion, as well as in mass spectrometry and ion beam applications. Typical ion species generated are hydrogen and helium, with beam intensities of the order of the mA. Limitations include poor beam quality, high power requirements, and a short lifetime of some of the components when heavy ions are used [118].

- *Electron Cyclotron Resonance Ion Sources (ECRIS)* : ECRIS utilize strong magnetic fields and microwave radiation to confine electrons in a resonance condition, leading to efficient ionization of gas atoms. They are known for their high ionization efficiency, stable and continuous operation, and can produce highly charged

ions across a wide range of elements from gases like hydrogen and helium to heavy metals. However, they are complex, costly, require significant power and infrastructure, and demand precise tuning and effective cooling systems, which can limit their accessibility and ease of use. They are commonly used in ion implantation, accelerator injection, ion beam analysis and hadrontherapy [11–13, 119–123].

Each type of ion source has its unique advantages and limitations, and the choice of ion source depends on factors such as the desired ion species, beam intensity, energy, degree of ionization and application requirements. For the production of low-energy (in the keV/u range) highly charged ion beams, ECRIS are the most widely used type. For all experiments performed and described in this work, three different ECRIS have been used, called SIMPA (Source d'Ions Multichargés de PAris) & FISIC (Fast Ion-Slow Ion Collisions) at INSP in Paris (which are two commercial ion sources from the Pantechnik company [124]), and GTS (Grenoble Test Source) at ARIBE (GANIL, Caen). The working principle and the specificities of the three aforementioned sources are presented in the following sections.

4.1.2 Principle of ECRIS

The historical development of ECRIS began in the mid-20th century, propelled by advancements in plasma physics and ion source technology. The concept saw practical implementation in the late 1960s and early 1970s, with the construction of the first operational prototypes by physicists like Richard Geller [120]. Early experiments demonstrated the feasibility of using microwave heating to achieve high degrees of ionization by electron impact in a magnetically confined plasma.

Figure 41 shows the general structure and mechanism of an ECRIS. This structure can

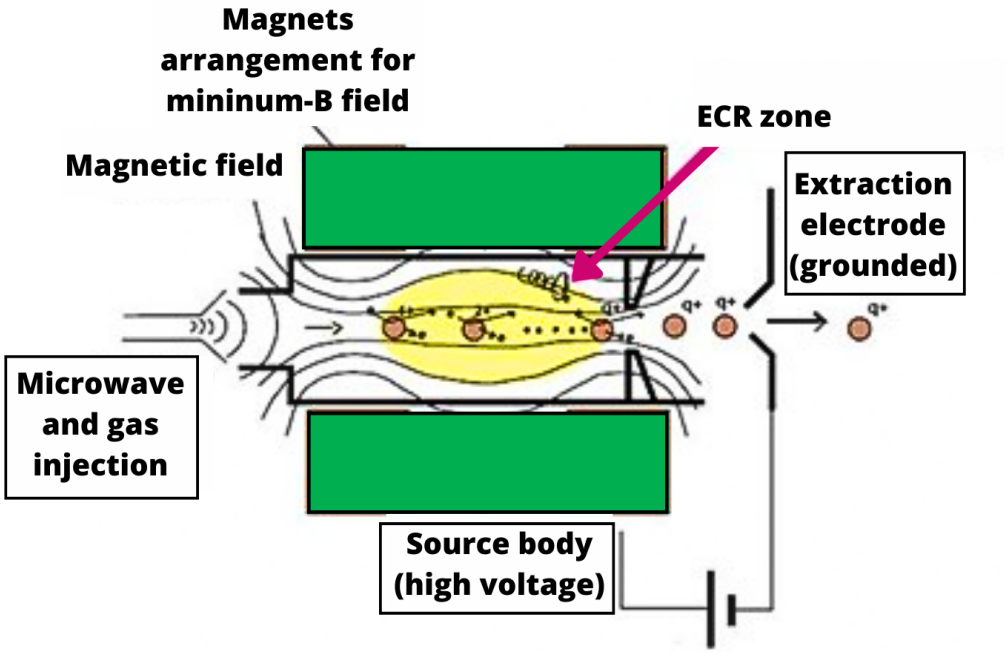

Figure 41: General structure and functioning mechanism of an ECR ion source [119].

be decomposed into three parts : the gas injection, the source body where the plasma is created, and the extraction system.

- The *gas injection system* allows for controlled injection of usually two distinct gases, called *main* and *support* gas. The role of the support gas is to provide additional electrons to the plasma, therefore increasing the ionization rate to obtain multicharged ions. Another advantage is the stabilization of the plasma resulting from a reduction in the main gas temperature subsequent to collisions with the lighter ions from the support gas. The support gas is chosen so that its ionization potential energy is lower than the ionization potential energy of the main gas. The overall gas pressure is typically maintained at a few 10^{-5} mbar to avoid electron recombination.

- The innermost part is a *vacuum chamber*, typically maintained at a pressure of approximately 10^{-5} mbar, and between 10^{-7} and 10^{-8} mbar in the extraction region during operation. This chamber is encompassed in an arrangement of magnets that produce both an axial and radial *magnetic field*. The magnetic field induced by these magnets is a minimum-B field configuration that is characterized by a minimal B intensity at the center of the chamber, and maxima in all directions from the center. This configuration allows for magnetic confinement of the plasma, which has a diameter of a few centimeters and a length of the order of 10 cm. The magnetic field B has a typical value of the order of 1T at maximum. The typical axial magnetic configuration as well as the radial shape of the plasma are shown on Figure 42. Within this field, plasma electrons undergo circular motion along magnetic field lines, oscillating at a frequency called the *cyclotron frequency* f given by equation (101) with e the elementary charge, B the magnetic field and m the electron mass.

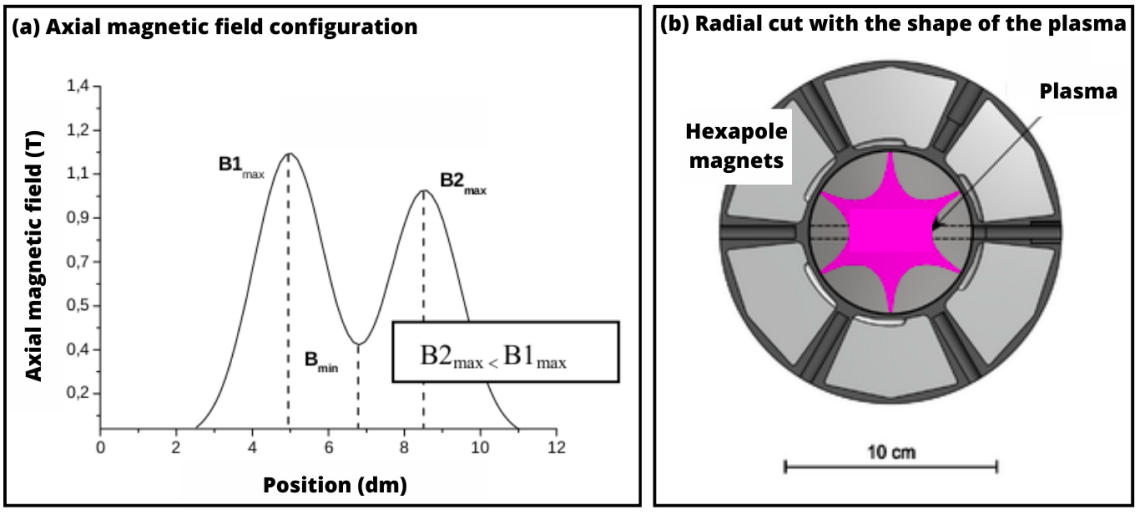

Figure 42: Typical magnetic configuration : the axial magnetic field configuration (a) and radial shape of the plasma (b).

$$\omega_{\text{cyclotron}} = 2\pi f = \frac{eB}{m} \tag{101}$$

This cyclotron motion results in the trapping of electrons within the region of minimal magnetic fields. A waveguide enables the injection of a microwave field with a frequency of a few tens of GHz. The microwaves are injected

at the cyclotron frequency f corresponding to the magnetic field B delivered by the magnets arrangement. The microwaves heat the neutral gas injected, releasing the less bounded electrons which in turn may enter in resonance with the microwave frequency. These accelerated electrons subsequently collide with atoms, molecules, and ions within the plasma, enhancing their ionization degree. The ions are confined by the combination of the space charge created by the electrons and the plasma potential (related to the electron density). Electrons are confined within the plasma region by the magnetic field, reducing contact with the plasma chamber and thereby minimizing charge loss through electronic recombination, and allowing ions to reach higher charge states [125].

- Ions are extracted by applying a *voltage difference* V between the body of the source, polarized at a few tens of kV, and an extraction electrode which is grounded [119, 122]. The specificities in extraction design of the three ECRIS at INSP and ARIBE are detailed below.

An ECRIS delivers ions with kinetic energies $E_c = q \times V$, where q is the charge of the ion. After being extracted, the beam goes through a magnetic dipole with a given deflection angle (usually 90° or 60°) that selects a given charge-over-mass (q/M) ion beam from the different ion species present in the extracted beam. The selection is made by deflecting the beam inside the dipole with a uniform magnetic field B on a circular path due to the Lorentz force. By adjusting the magnetic field, a given charge state can be selected according to

$$\frac{M}{q} = \frac{(B\rho)^2}{2V} \tag{102}$$

where ρ is the radius of curvature of the dipole.

4.1.3 Sources at INSP

The two ion sources, SIMPA and FISIC, installed on the PMC (Pierre et Marie Curie) campus and utilized by the INSP, are both 14.5 GHz SUPERNANOGAN [126] ECRIS with permanent magnets manufactured by Pantechnik in Bayeux [124]. SIMPA was integrated into the laboratory setup in 2003, while FISIC joined in 2022. Both sources have the same magnetic configuration and the same plasma chamber with a length of 128 mm. References [127] and [128] give the main parameters and performances of the SIMPA source.
Pumping is ensured by turbopumps on both sources. The location of the pressure measurement points is shown on Figures 44 and 45. The injection pressure of the main and support gases are controlled by UDV valves. Made by the Pfeiffer Vacuum company, they are all-metal regulating valves used for controlling gas inlet into vacuum systems. On SIMPA the parameter that controls the valves is a signal called $I_{opening}$ that varies between 3 mA (fully closed) and 10 mA (fully open). On FISIC the parameter for the valves is an opening rate given in percent. Figure 43 gives the pressure calibration for the valve opening for SIMPA and FISIC. Microwave and gas injection occur within a copper cube, which also houses a polarization electrode [129]. Microwave injection occurs from a klystron for SIMPA and from a solid-state amplifier for FISIC. The RF generator for FISIC is able to provide an RF frequency between 13.5 and 14.5 GHz, giving rise to

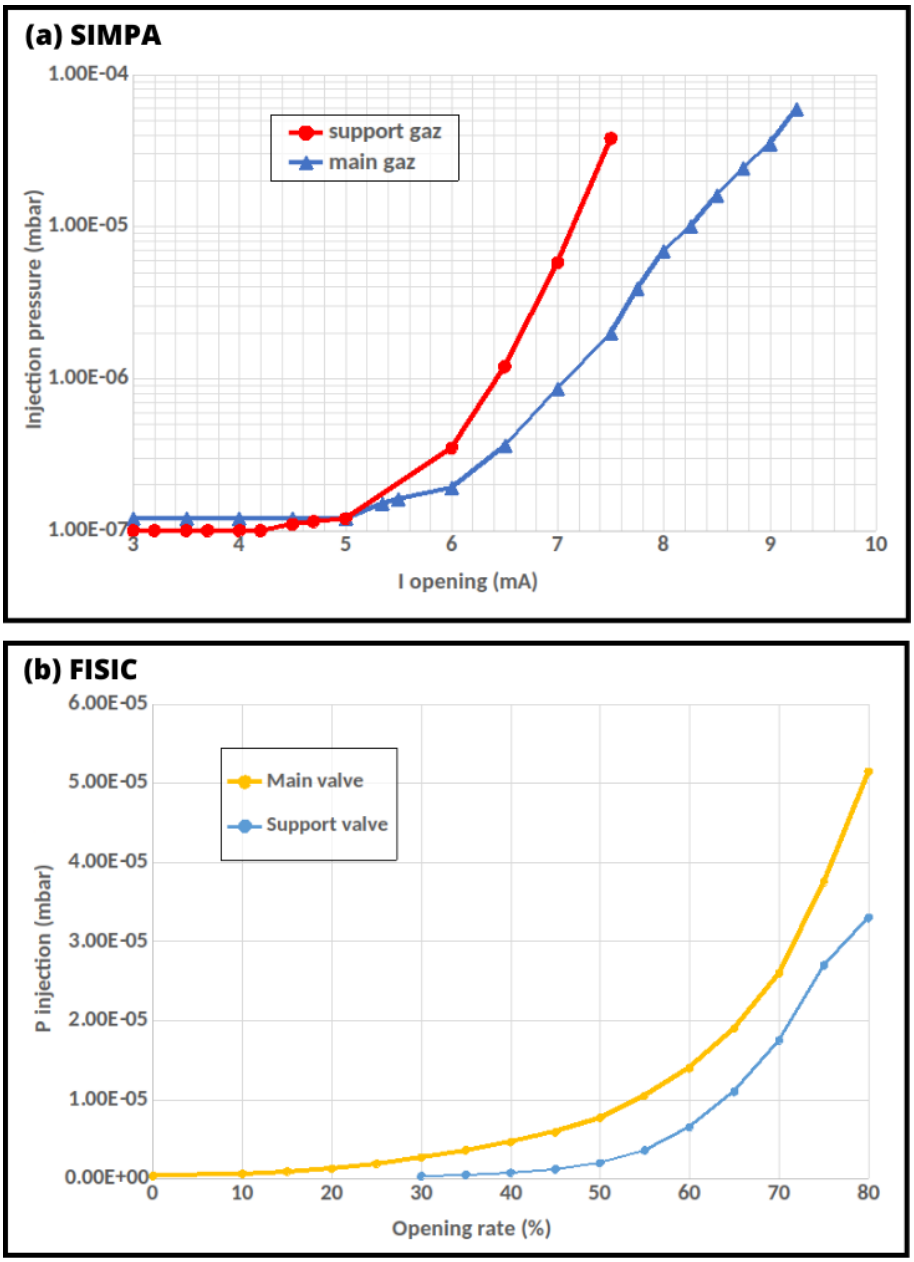

Figure 43: Variation of partial pressure of main and support gases as a function of the valve opening parameter on (a) SIMPA and (b) FISIC.

an additional parameter to control the source. Additionally, a piston called a RF tuner within the injection cube regulates its volume, allowing a better control of the microwave frequency and consequently minimizing microwave reflection. The injected RF power is almost entirely transmitted into the plasma cavity. The polarization electrode, also called DC bias electrode, set at a negative voltage marginally lower (a few hundred Volt) than the extraction voltage V, serves to emit additional electrons and also to repel all electrons towards the plasma chamber. This helps to maintain a high electron density within the main plasma chamber, and therefore a more efficient production of highly charged ions. For both sources, the magnetic field mentioned in section 4.1.2 is generated by an arrangement of hexapole magnets and cylindrical magnets. The extraction voltage V can vary between 10 and 20 kV for SIMPA and up to 35 kV for FISIC. Despite sharing the same core design, their extraction systems differ significantly.

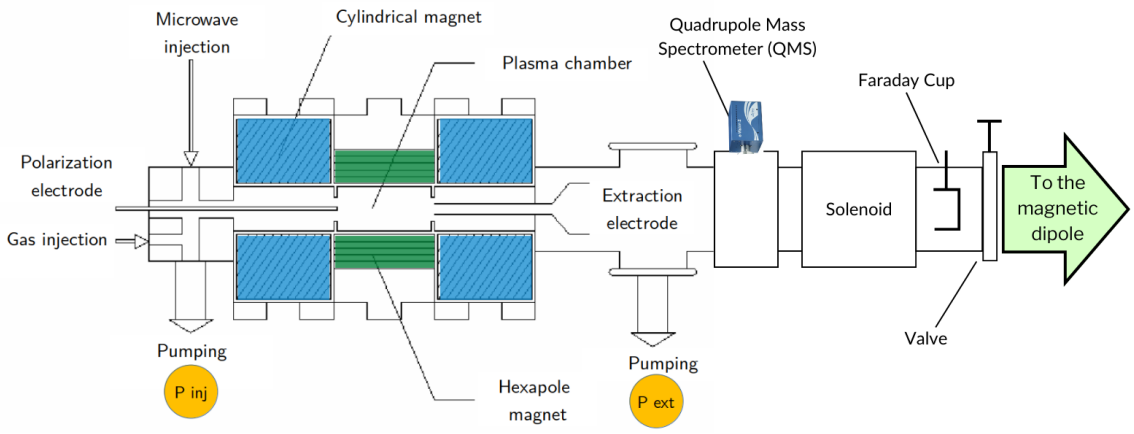

Figure 44: Structure of the SIMPA ECRIS and extraction system up to the 90° magnetic dipole. Diagram modified from [128].

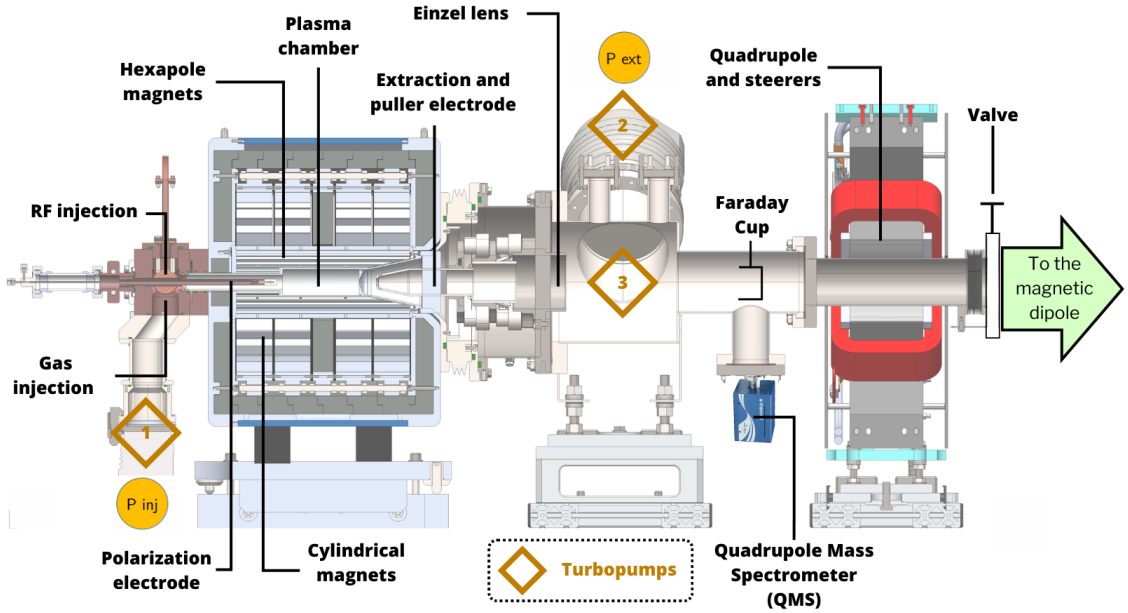

Figure 45: Structure of the FISIC ECRIS and extraction system up to the 90° magnetic dipole.

As can be seen on Figure 44, SIMPA employs a solenoid (magnetic coil) for beam focusing, allowing adjustable focusing point manipulation by controlling the magnetic field. In contrast, FISIC, Figure 45, utilizes a puller electrode and an Einzel lens followed by a quadrupole & steerer assembly for beam shaping and focusing. The extraction system for FISIC has been adapted from the extraction system of the GTS ion source at ARIBE (see section 4.1.4). Additionally, both sources feature a partial gas pressure control system at the extraction point, along with a movable Faraday cup for total extracted current measurements. The partial gas pressure system, also called a residual gas analyzer, is a Quadrupole Mass Spectrometer (QMS) [130] from the MKS company [131] in both cases. It is used to monitor inherent contaminants like nitrogen or water but also the gases of interest. The partial pressures of the contaminants must be low to ensure optimal operation, typically in the order of 1×10^{-8} mbar as seen on Figure 46. Once the extraction voltage is set, the main adjustable parameters to optimize the

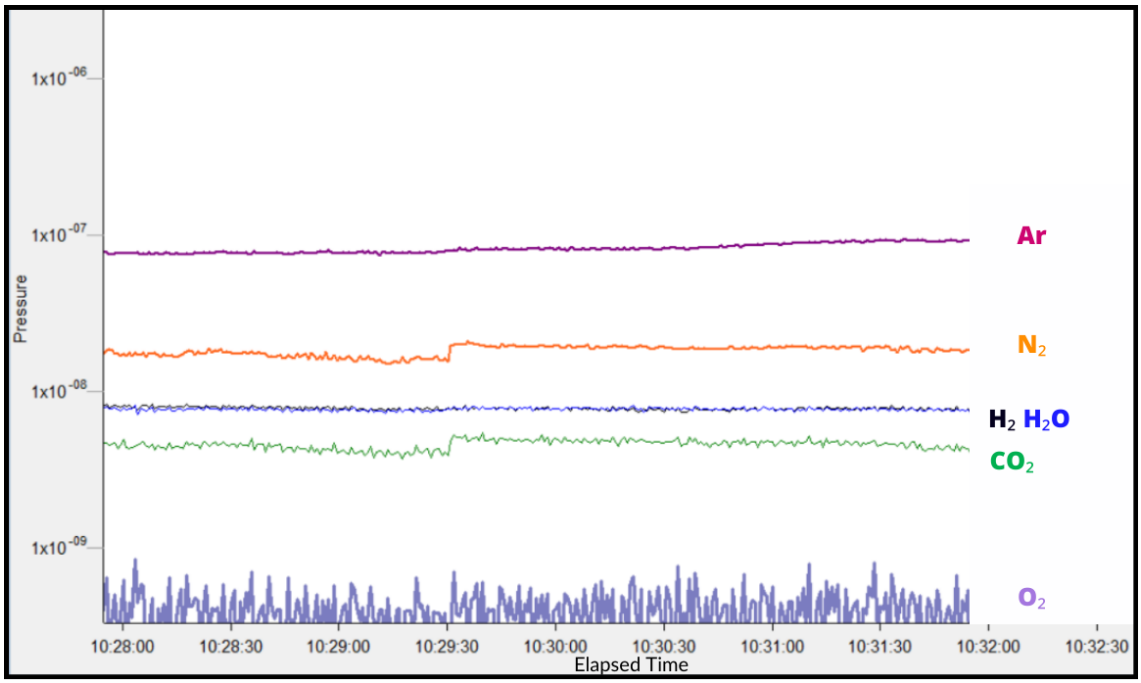

Figure 46: Partial pressures of various gases recorded by a QMS for the residual gas analyzer for a 10.2 µA extracted Ar^{8+} beam at an energy of 2 keV/u and a RF power of 70 W.

beam current of interest are the quantity & type of the injected gas (via the valve opening parameter), the RF power, the polarization electrode voltage and extraction optics parameters. Obtaining high charge states is difficult due to the kinetic energy of electrons required for ionization. For example, in the case of argon (the most commonly used gas at INSP), the highest charge state obtained was Ar^{18+} (with a current of about 100 pA). It is not possible to achieve such high charge states immediately upon source startup. Intermediate optimization steps of lower charge states are necessary, especially as transitioning from ionization of one shell to another (e.g., 3s to 2p) is a delicate procedure. Additionally, parameters such as RF power or bias electrode voltage (V_{bias}) must be gradually increased to avoid the risk of creating instabilities in the plasma [132]. Figure 47 shows the cross sections for ionization by electron impact for several charge states of argon. The curves were computed using the Lotz semi-empirical formula given in [133]

$$\sigma_{q\to q+1} = \frac{A}{(E_e E_q)} \ln\left(E_e/E_q\right) \tag{103}$$

with E_e the electron energy, E_q the effective ionization potential and A a scaling factor. Values for E_q and A for the transitions depicted in Figure 47 are given in Table 8 [133, 134]. Not only does the electron energy needed for ionization increases with the ion charge state q, but the cross sections decrease by several orders of magnitude when reaching higher charge states. This highlights the fact that in order to obtain beams of highly charged ions, both the energy and the number of the electrons in the plasma must be increased, in order to have high ionization rates. This is done in part by increasing the voltage on the bias electrode, which injects more electrons in the plasma. Figure 48 gives the ionization potentials for several charge states for two commonly used gases, argon and oxygen. The "jumps" visible on the curve correspond to a change of electronic shell. It is clearly visible from both the ionization cross sections and the ionization potential

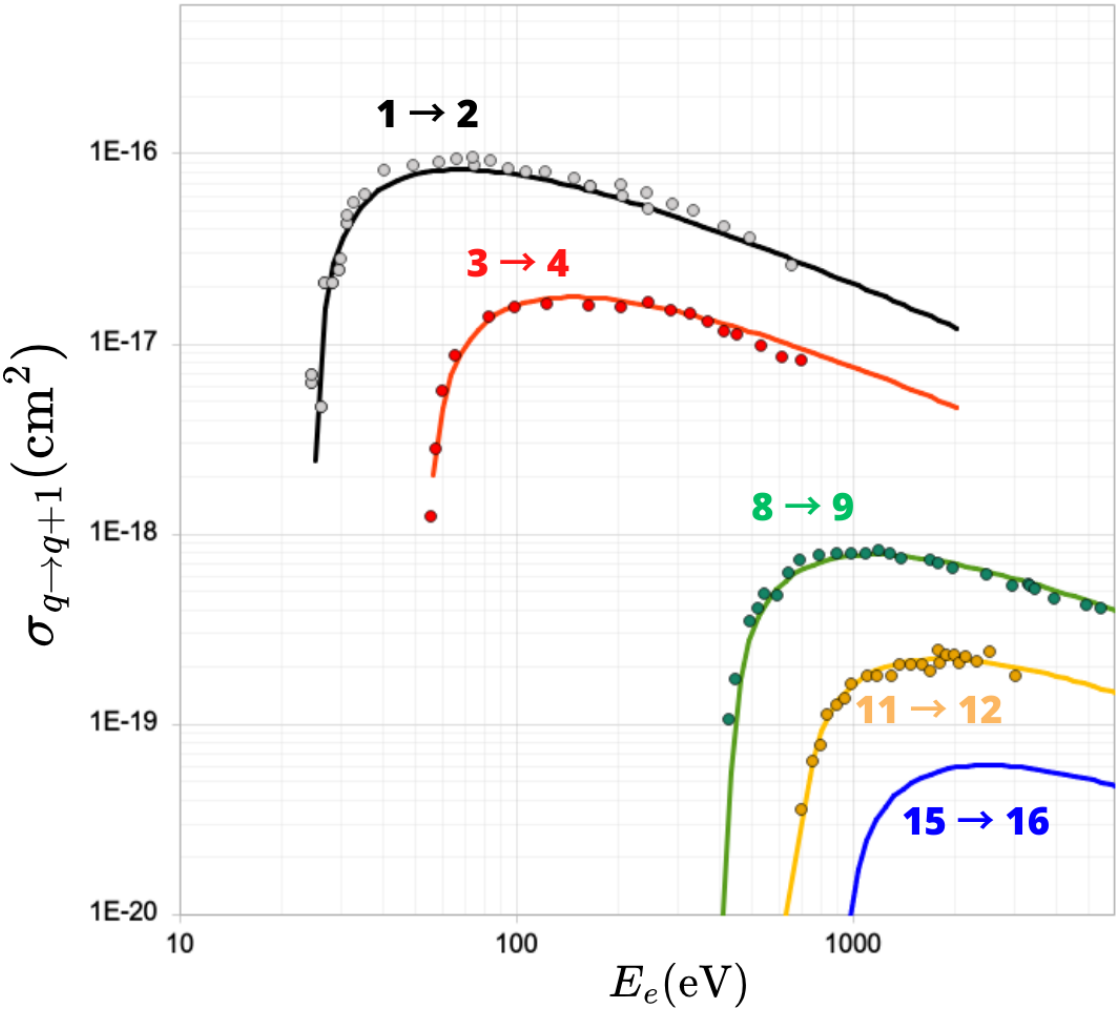

Figure 47: Cross sections for ionization by electron impact as a function of the electron energy. Curves were computed with the Lotz formula [133] and the experimental points are given in [135, 136].

$q \to q+1$	E_q (eV)	A ($\mathrm{cm}^2 \cdot \mathrm{eV}^2$)
$Ar^{1+} \to Ar^{2+}$	25 ± 1	1.4×10^{-13}
$Ar^{3+} \to Ar^{4+}$	54 ± 2	1.4×10^{-13}
$Ar^{8+} \to Ar^{9+}$	422 ± 1	3.8×10^{-13}
$Ar^{11+} \to Ar^{12+}$	670 ± 5	2.7×10^{-13}
$Ar^{15+} \to Ar^{16+}$	918 ± 2	1.4×10^{-13}

Table 8: Values of E_q and A to calculate electron impact ionization cross sections (see equation (103) for argon ions.

curves that obtaining high charge states is not easy. There is more than 3 orders of magnitude difference in cross sections between the $Ar^{1+} \to Ar^{2+}$ and $Ar^{15+} \to Ar^{16+}$ processes. Optimization may begin, for example, with Ar^{8+}, then Ar^{9+}, progressing to higher charge states as needed. Population in terms of charge states extracted in the

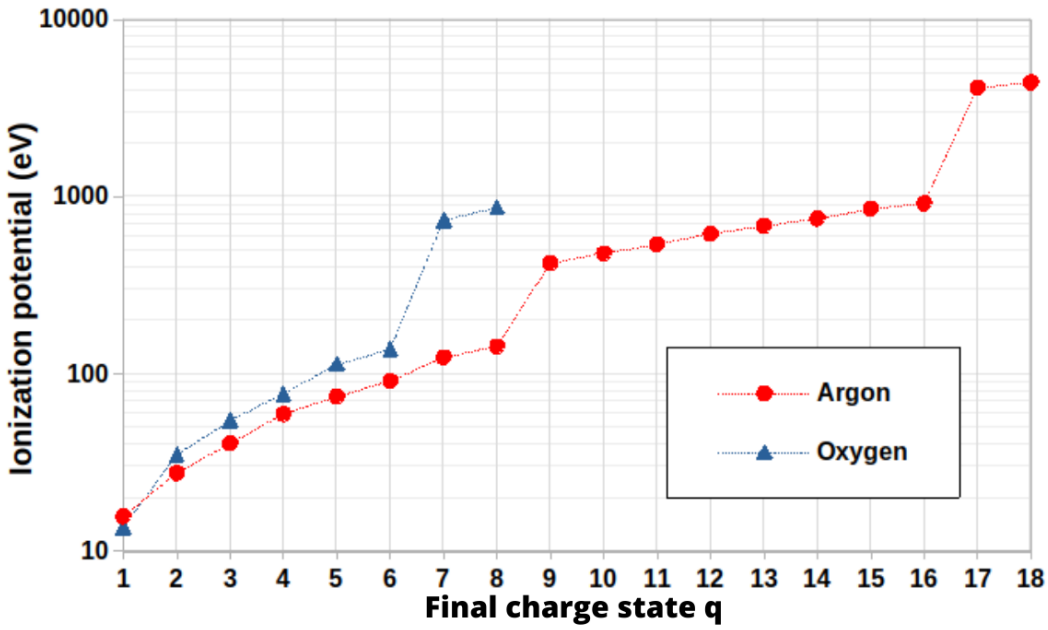

Figure 48: Ionization potential of different charge states of argon and oxygen [137]

plasma can be controlled by performing what is called a charge state spectrum. The procedure is as follows : the magnetic field of the selection dipole is changed to sweep a predefined range, and the beam current is measured with a Faraday Cup after the dipole. The result is a spectrum showing the beam current as a function of the dipole magnetic field, which is related to the ion q/M ratio according to equation (102). Each peak thus corresponds to a charge state based on this value. Unambiguous attributes of the correct charge state is performed via a complete series of all the charge states for a given M. Figure 49 shows two charge state spectra obtained with the SIMPA and FISIC sources. It is important to note that since oxygen is used as a support gas, some peaks cannot be attributed to a well given charge state, as two different charge states may have the same q/M ratio (e.g., $q/M(O^{4+})=q/M(Ar^{10+})=0.25$). Charge state spectra allow to monitor the ion intensity in the extracted beam and to determine when the current of a higher charge state becomes significant enough to be optimized without risking beam loss (typically of the order of µA, even less for very high charge states). Table 9 shows typical source and extraction parameters for obtaining an Ar^{13+} beam. It is interesting to remark that with the FISIC source, higher RF power are needed for producing beams with currents of the same order of magnitude than with SIMPA. Table 10 displays typical currents obtained with the SIMPA and FISIC sources for different ion species.

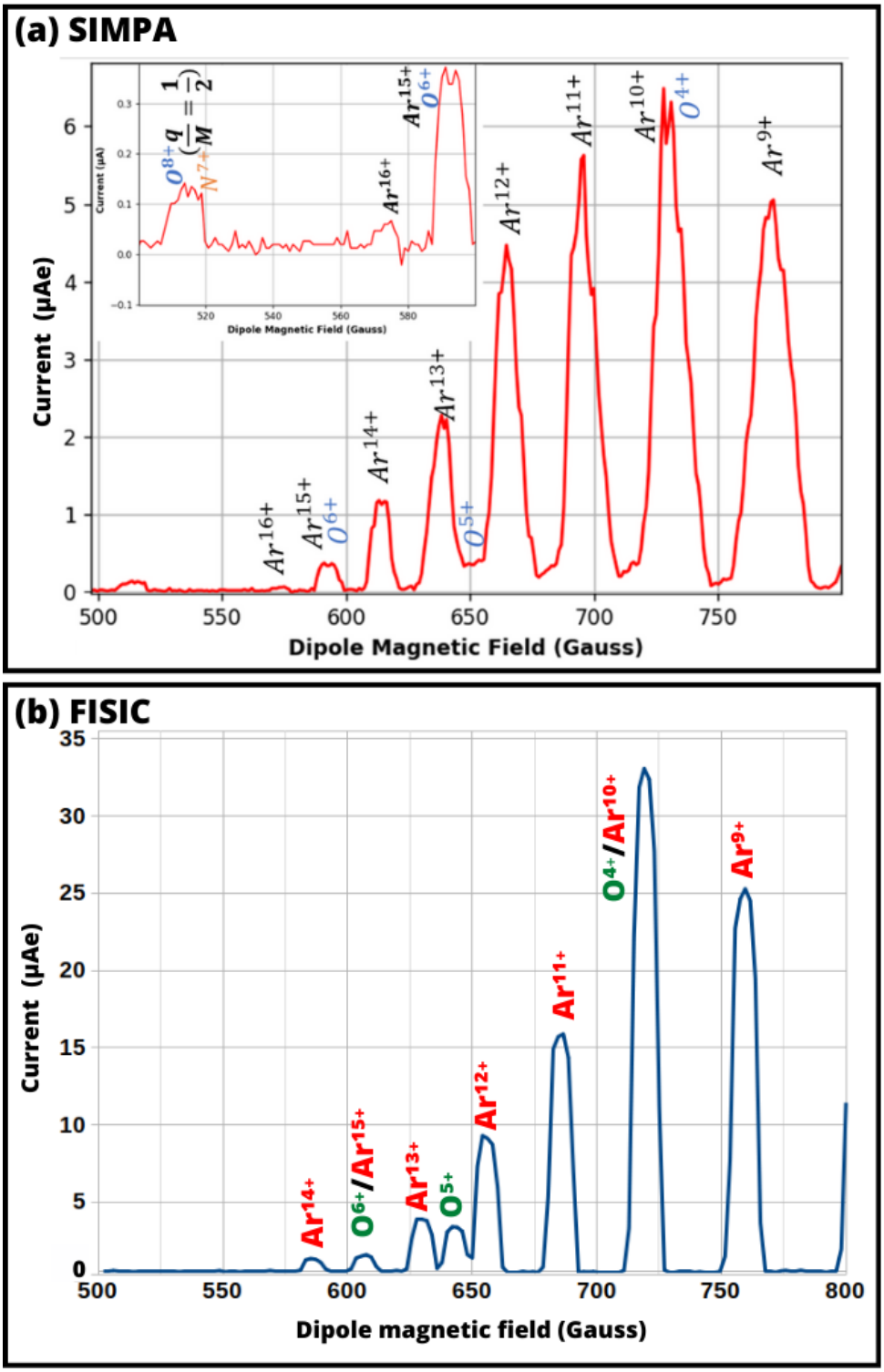

Figure 49: Currents of various ion beams as a function of the applied magnetic field of the dipole for an Ar/O mixture. Spectrum (a) was obtained with the SIMPA source when the current of Ar^{14+} is optimized [138] (I(Ar^{14+}) = 1.15 μA, $V_{ext} = 10$ kV, P_{RF} = 80 W). Spectrum (b) was obtained with the FISIC source when the current of Ar^{13+} is optimized (I(Ar^{13+}) = 3.4 μA, $V_{ext} = 10$ kV, P_{RF} = 175 W).

	SIMPA	FISIC
P_{RF}(W)	80	175
F_{RF}(GHz)	14.5	13.9
Main gas (Ar)	7.6 mA	56.2%
Support Gas (O)	5.2 mA	50.6%
Injection (mbar)	2.4×10^{-5}	2.1×10^{-5}
V_{BIAS}(V)	200	232
Puller(V)	-	-5555
Focus(V)	-	1624
Solenoid(mT)	202	-
Quadrupole(A)	-	4.1

Table 9: Optimization parameters of the ion sources for generating an Ar^{13+} beam with a 10 kV extraction voltage.

Ion	$^{40}Ar^{11+}$	$^{40}Ar^{13+}$	$^{40}Ar^{17+}$	$^{16}O^{8+}$	$^{13}C^{6+}$
I(µA) SIMPA	-	6.3	0.003	0.7	2.7
I(µA) FISIC	6.18	3.8	-	1	-

Table 10: Typical maximum currents obtained with the SIMPA and FISIC source for different ion species [128, 138]

4.1.4 Source at ARIBE

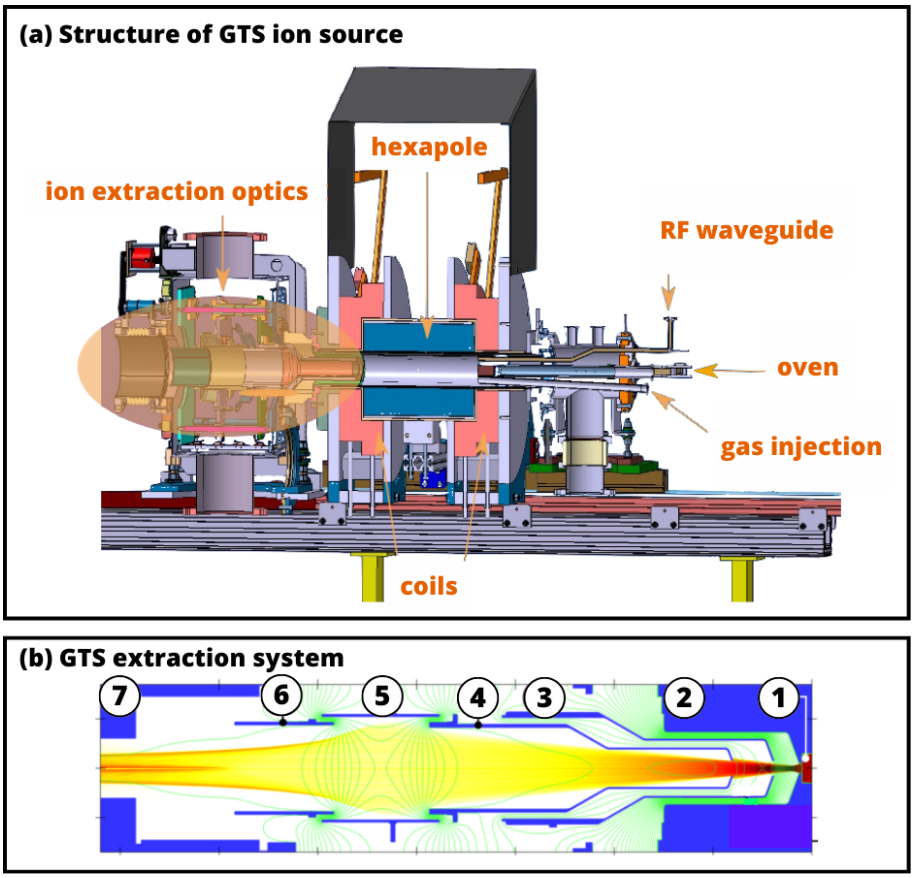

Figure 50: (a) Structure of the GTS ion source at the ARIBE facility [139]. (b) Detail of the extraction system with simulated extraction of a 1.5 µA Ar+O beam. The system consists of (1) plasma, (2) source body and plasma electrode at 15 kV, (3) puller electrode at -3.2 kV,(4) grounded electrode, (5) Einzel electrode 10.8 kV, (6) grounded electrode and (7) beam pipe entrance [140].

The ECRIS source used at ARIBE, called Grenoble Test Source (GTS), has been developed by CEA-Grenoble in 2002 [140–143]. Figure 50 presents a general view of the source structure and a more detailed view of the beam extraction optics. GTS is capable of forming intense (a few tens of µA) ion beams at energies that range from a few keV/q up to 25 keV/q. The radial magnetic field is created by a series of hexapoles placed around the 300 mm-long plasma chamber. The axial magnetic field is created by two coils placed on the injection and extraction side of the chamber. An additional coil, not pictured on Figure 50, was added in 2016 between the injection and extraction coils. Its position and polarity can be adjusted. Optimal performances have been reached when the center coil polarity is the same as the main coils and when it is located at the injection side of the source [140]. The injection system of GTS includes a vanadium cone that increases the maximum axial magnetic field at injection by 10%. Two different waveguides allow for an injection of microwaves in a 8 - 18 GHz frequency range. A biased disc is also installed. Its purpose is similar to the polarization electrode described above [129]. Thanks to an oven at injection site, metal beam production is possible with GTS. The performances of this source in terms of current are presented in Table 11 for beams extracted at 15 keV.

Ion	$^{3}He^{2+}$	$^{20}Ne^{6+}$	$^{40}Ar^{14+}$	$^{84}Kr^{23+}$	$^{129}Xe^{25+}$
I(μA)	1510	185	37	25	63

Table 11: GTS measured currents for a selection of beams with a 15 kV extraction voltage [140].

4.2 Beam transport and monitoring

4.2.1 Principles of beam transport and monitoring : general considerations

Various instruments and methods are commonly used to control and measure the properties of ion beams, such as shape, size, emittance and intensity and are exposed in this paragraph. Key components in controlling the trajectory and shape of the beam include quadrupoles, steerers, and Einzel lenses [144, 145]. Furthermore, for beam diagnostics, which involve measuring the intensity, shape, and emittance of a beam, specialized instruments are employed [146]. The instruments most commonly used for these purposes are described below.

For beam transportation and shaping :

- *Quadrupoles* : A quadrupole operates on the principle of magnetic manipulation to control charged particle beams. Composed of four magnetic poles configured strategically, its primary function lies in focusing or deflecting charged particles passing through it. This focusing action stems from the quadrupole's ability to generate a magnetic field gradient along the beam path, focusing particles in one direction while dispersing them in the perpendicular axis, as shown on Figure 51. By changing the magnetic field it is possible to gain precise control over the trajectory and shape of the ion beam within the beamline. Quadrupoles are often positioned in sets of three, with the first quadrupole focusing in a direction, the second one focusing in the perpendicular direction (and therefore defocusing in the direction of the first quadrupole) and the third one used to correct the defocusing of the second one.

- *Steerers* : Electric and magnetic steerers are devices used to manipulate the trajectory of charged particle beams. *Electric steerers* use electric fields to exert force on the particles, altering their path depending on the charge and magnitude of the field. *Magnetic steerers* use magnetic fields to change the direction of particle beams through the Lorentz force, which depends on the particle velocity, charge and on the magnetic field strength. Through meticulous calibration and coordination with beamline control systems, the steerers facilitate precise beam steering, crucial for directing ions to specific locations within experimental setups.

- *Einzel lenses* : An Einzel lens (from German: Einzellinse – single lens) is a type of electrostatic lens. It is designed to focus charged particle beams without changing their energy. The Einzel lens consists of three or more cylindrical electrodes arranged coaxially along the beam axis. These electrodes are biased with different voltages to create an electric field configuration that shapes the trajectory of the charged particles passing through it. The central electrode is typically biased at a high positive voltage (for positively charged particles) while the outer

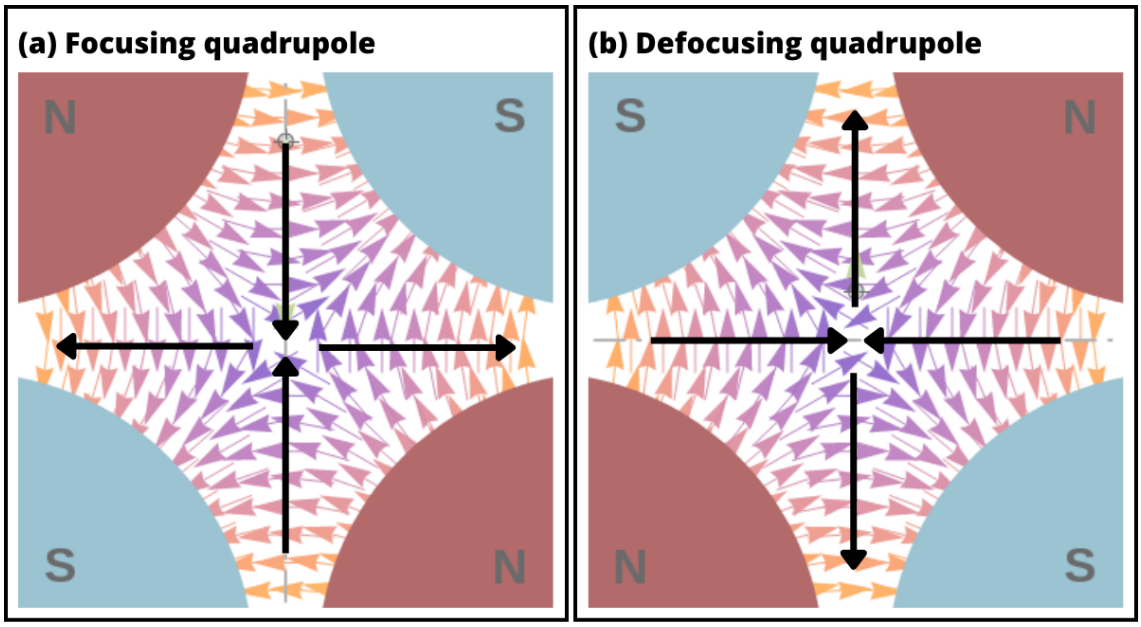

Figure 51: Direction of the magnetic field for a focusing (a) and defocusing (b) quadrupole in the vertical direction. Black arrows indicate the direction of the Lorentz force on a positive particle going into the image plane. By alternating the two types of quadrupoles, a focusing effect can be achieved in both horizontal and vertical planes [147].

electrodes are biased at lower voltages or even grounded. This voltage gradient between the central and outer electrodes creates a converging electric field that focuses the charged particles towards the optical axis of the lens as shown on Figure 52 [148–150].

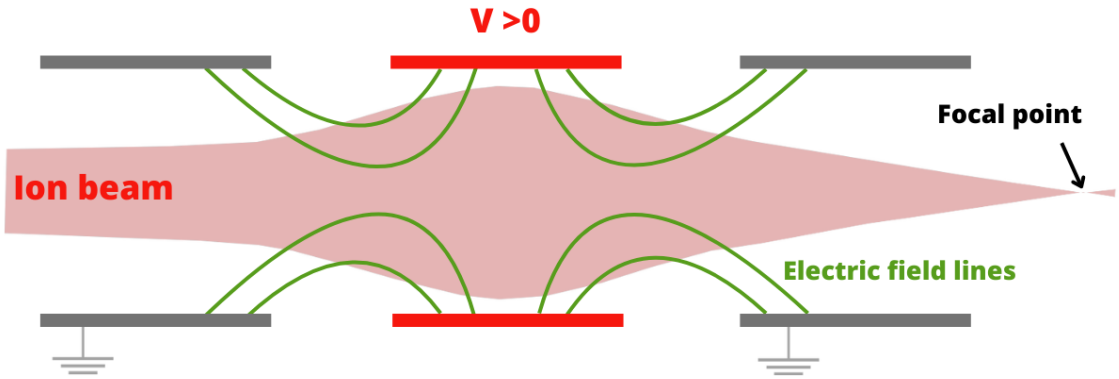

Figure 52: Longitudinal cut of an Einzel lens showing the electric lines, the electrodes potential and the ion beam path with the focusing point.

For beam diagnostics :

- *Faraday Cup* : A Faraday cup is a device used to measure the total electric charge of a charged particle beam. It consists of a metallic cylinder cup that is electrically insulated from its surroundings. When the charged particle beam enters the cup, it deposits its charge onto the cup surface. This charge induces a current in the cup circuit, which is proportional to the total charge of the beam. It is measured either via a circuit with a resistance R (the corresponding voltage is measured in this case

and converted into current value via Ohm's law) or directly with an ammeter. By measuring this current, the total charge of the beam can be determined. Usually a ring electrode, called a repeller, is polarized and placed just above the Faraday cup entrance to ensure no charged particles escape the cup, and that the total beam current is correctly measured [151].

- *Beam Profile measurement* : A multiwire beam profiler [152] is a device used to analyze the spatial profile of charged ion beams. It consists of an array of closely spaced wires arranged perpendicular to the beam direction. As the beam passes through this wire array, interactions with the metallic wires generate current which are then measured, allowing for the determination of the beam intensity distribution across the transverse plane. The spatial resolution of the profiler depends on factors such as wire spacing and diameter.

- *Emittance measurement* : The quality of a beam is not just defined by its profile at a given position in a beamline. Its emittance is a more appropriate characteristic. The emittance of an ion beam refers to a measure of its divergence or spread in

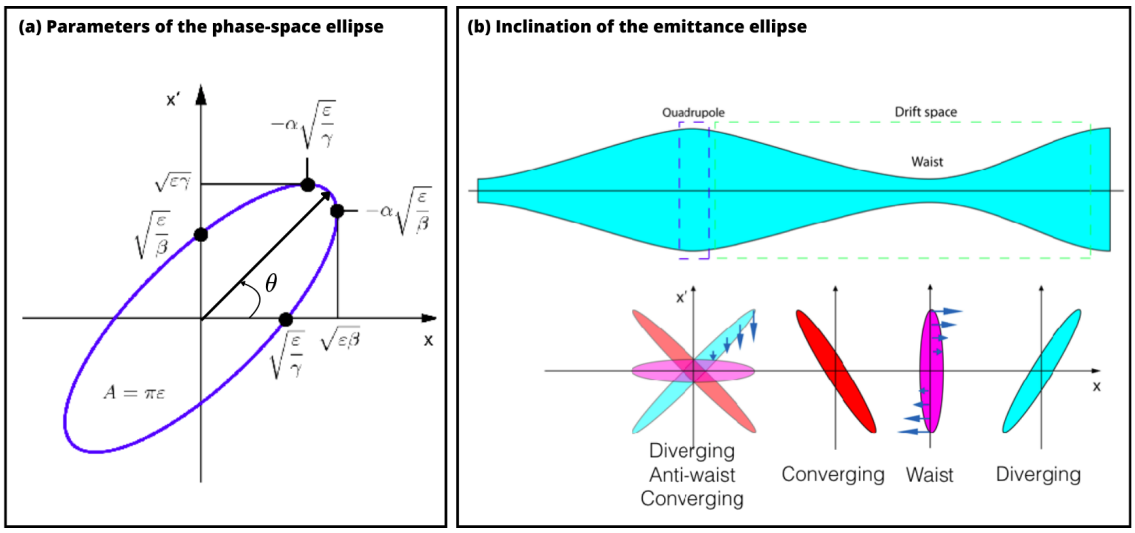

Figure 53: (a) Parameters of the phase space ellipse for emittance. (b) Evolution of the inclination of the phase-space ellipse as a function of the position of the emittance scan after a focusing element (here a quadrupole). Figures taken from [153].

both position and momentum space. It quantifies the extent to which an individual ion within the beam deviates from an ideal, perfectly collimated trajectory. The transverse emittance of a beam that propagates along the z direction is measured in the (x, y, x', y') space where $x' = \frac{P_x}{P_z}, y' = \frac{P_y}{P_z}$ are angles of divergence on the x and y direction respectively. Since there is no coupling between the (x, x') and (y, y') dimensions, transverse emittance can be simplified in two 2-dimensional spaces : (x, x') for horizontal emittance and (y, y') for vertical emittance. The beam emittance can be approximated by an ellipse, the horizontal and vertical emittances are expressed as an area of phase-space as shown on Figure 53 (a). The emittance $A = \pi\varepsilon$ is expressed in πmmmrad. The quantities α, β and γ are called the Twiss parameters. The value of the emittance does not depend on the location where the measurement is carried out. It is preserved throughout the transport of the beam if the electromagnetic forces applied to the particles are conservative,

which is the case on the FISIC beamline. A beam with low emittance has ions that are parallel to the optical axis. The focalization of an ion beam is limited by the space charge. The inclination of the phase-space ellipse, indicated by the angle θ on Figure 53 (a) changes depending on where the emittance measurement is performed after a focusing element (Figure 53 (b)).

Several types of emittance meters exist such as Pepperpot emittance meter [154] or Allisson scanner emittance meter [155] or wire-slits emittance meter [156]. The latter type is the one installed on the FISIC beamline.

4.2.2 Beam transport and monitoring for FISIC

Figure 54 shows the layout of the FISIC beamline at INSP. Four turbo pumps maintain the vacuum at around 10^{-8} mbar along the beamline when the source is in operation. Following the dipole, there is a wire-slit emittance meter located in front of a Faraday cup, followed downstream by three quadrupoles, three magnetic steerers and a multi wire beam profiler featuring a second Faraday cup. The transmission efficiency along the beamline is close to 100%.

Figure 55 shows the working principle of the FISIC wire-slit emittancemeter : it features

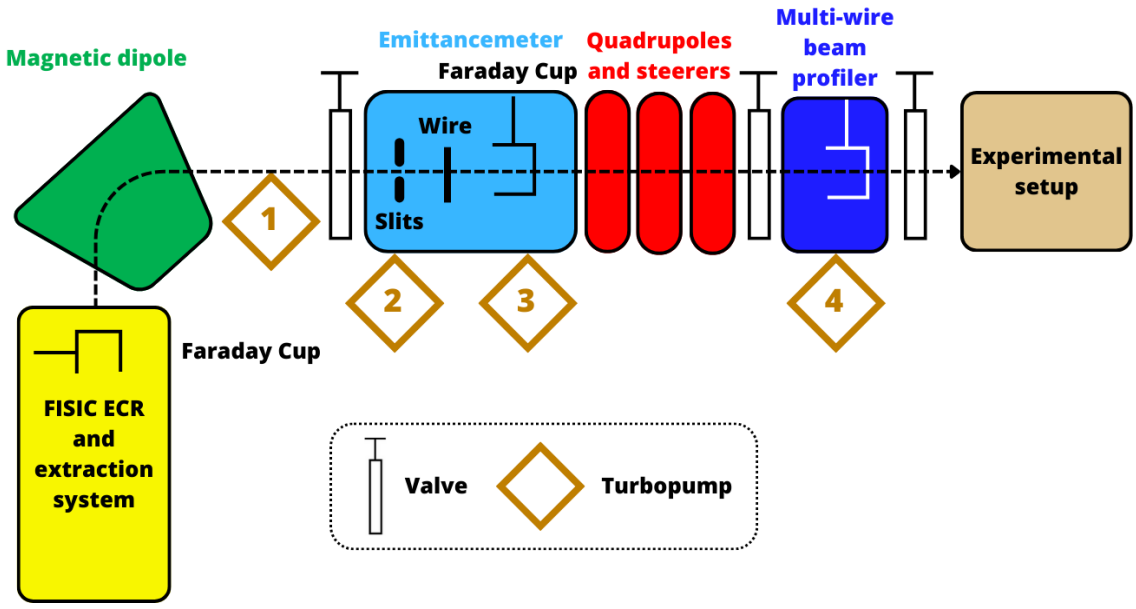

Figure 54: Schematic view of the FISIC beamline up to the experimental setup.

a set of vertical and horizontal slits placed along the beam path. A set of two wires (horizontal and vertical) is placed at a distance D behind the slits. The measurement is made separately in the vertical and horizontal directions. The slits are closed to a few millimeter gap (we mostly use a 1 mm or 2 mm gap) to restrict the spatial extent of the beam in one direction, and the corresponding wire scans the beam. The slit gap is then moved by an adjustable distance of a few millimeters (we use a 1 mm distance) and the wire scanning resumes. By scanning the entire span in this manner, a 2D image is produced, representing the divergence (in mrad) as a function of the position (in mm).

The ellipse emittance A can then be measured from these scans. We consider the ellipse emittance to be a good value for the beam emittance when 70% of the density current is inside the ellipse, as shown of Figure 56. The Figure shows the horizontal

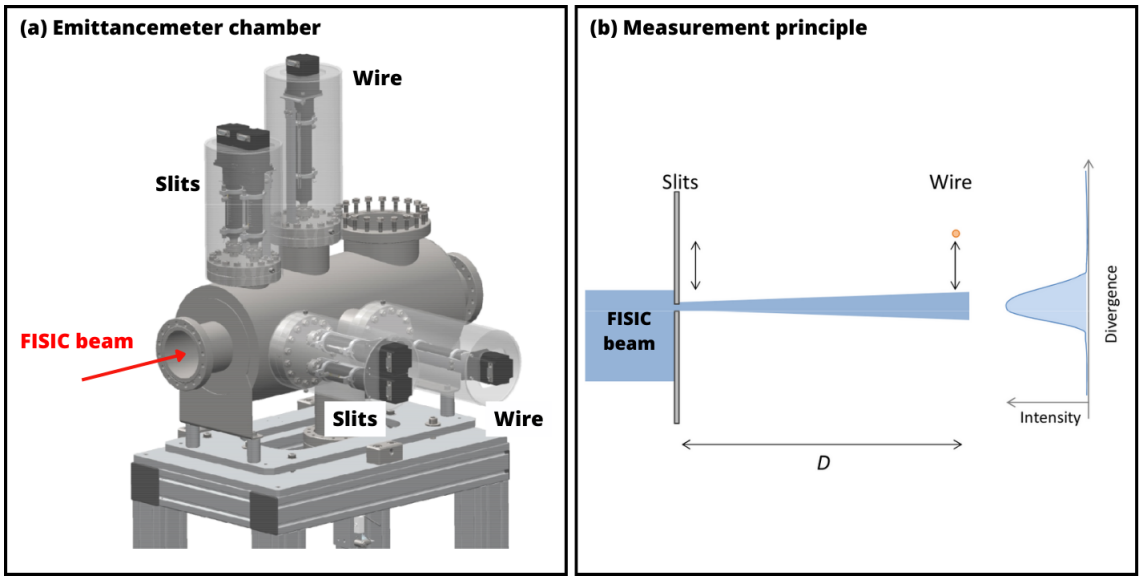

Figure 55: (a) The wire-slit emittancemeter chamber. (b) Measure principle of the wire-slit emittancemeter

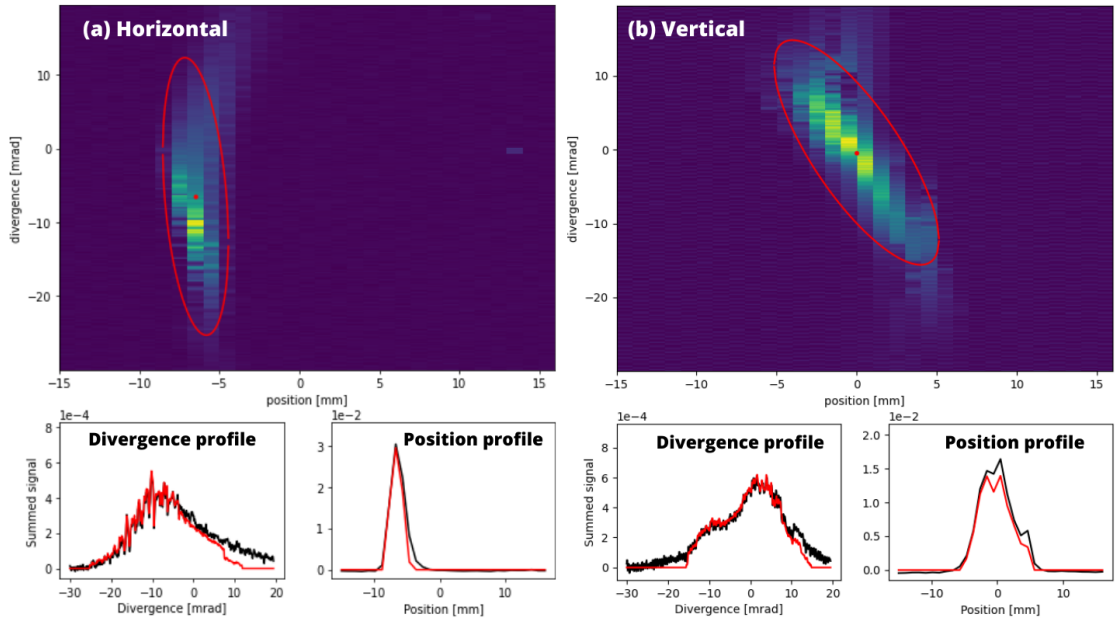

Figure 56: (a) Horizontal emittance measurement. (b) Vertical emittance measurement. For both, the position and divergence profiles are shown with in black the data profile and in red the profile of the data that is within the ellipse. This measurement was taken with a 6.2 µA Ar^{11+} beam with an energy of 2.75 keV/u, and gives a horizontal emittance of 36πmmmrad and a vertical emittance of 49πmmmrad.

and vertical emittance of a 6.2 µA Ar^{11+} beam of an energy of 110 keV, and gives a horizontal emittance of 36 πmmmrad and a vertical emittance of 49 πmmmrad. For both, the position and divergence profiles are shown with in black the data profile and in red the profile of the data that is within the ellipse. A systematic study was conducted in 2024 to measure the emittance of different beams of Ar^{q+} (q = 8, 9, 11) and O^{q+} (q = 5, 7, 8) while testing the effects of several parameters with the FISIC setup. The most significant results are reported in appendix C. It was found that for both directions, the beam emittance of the FISIC source is comprised between 28 and 54 π mmmrad. The

emittance of the SIMPA source was measured by the manufacturer prior to the source delivery in 2003 and was of the order of 100 πmmmrad.
The beam profiler (see Figure 57) is composed of an array of 47×47 wires with a 1 mm gap between the wires. An example of a beam profile taken for a 1 µA Ar^{14+} beam with an energy of 3.5 keV/u is shown on Figure 58.

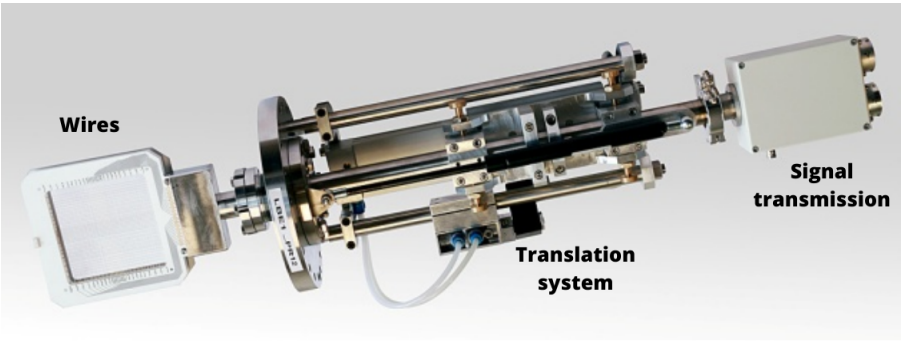

Figure 57: Image of the profiler installed on the FISIC beamline.

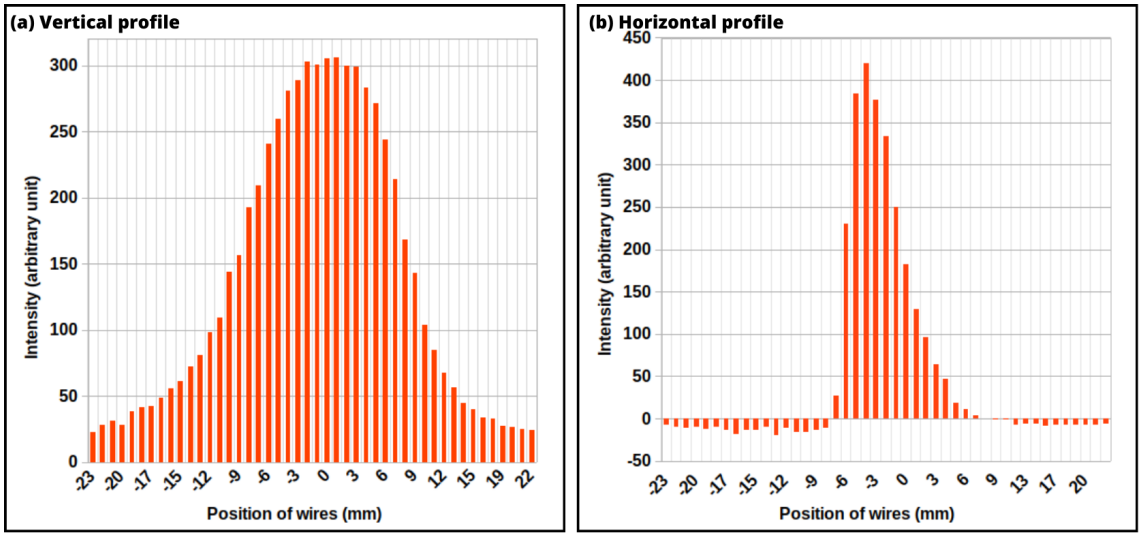

Figure 58: Beam profiles for a 1 µA Ar^{14+} beam with an energy of 3.5 keV/u. (a) Vertical orientation and (b) horizontal orientation [138].

4.2.3 Beam transport and monitoring for SIMPA

The layout of the SIMPA beamline is depicted in Figure 59. Following the dipole magnet, a pair horizontal and vertical steerers is employed to control the trajectory of the beam. These steerers are followed by four slits (two horizontal and two vertical slits) and then a Faraday cup to monitor the beam current. Immediately after, another chamber houses a Faraday Cup Array (FCA) used to image the beam profile. Downstream the FCA chamber, an Einzel lens is employed to focus the beam inside the collision chamber. A second set of four slits is located just upstream the collision chamber. These slits serve to reduce the beam intensity, and size if needed. The FCA was developed at the University of Kiel [157]. As shown on Figure 60 (a), it consists of an array of 44 small Faraday cups with a 0.3 mm diameter for measuring the beam profile. Additionally, a larger Faraday cup with a 22.8 mm diameter is placed above the FCA to measure the total beam current. To prevent the loss of secondary electrons a repeller before the cup is supplied with a negative high voltage (up to -3 kV for the large FC and -300 V for the FCA). The FCA is driven through the beam in the vertical direction perpendicular to the beam axis by a motor to create a line of measurement points for each small Faraday cup. A data point is recorded each 0.44 mm. This and the compact horizontal spacing of the cups allow for a high resolution beam profile of which an example is given in Figure 60 (b). The motor and the data acquisition are controlled with a Python script and the detector is calibrated by measuring the signal without ion beam and subtracting it. Several measurements were carried out in 2024 and are reported in appendix D. The FCA will allow to estimate the fluence (number of ions per cm^2) of the beam, since each small Faraday Cup in the array measures a current over a determined surface. Measurements of this kind have been performed previously with the SIMPA beamline as reported in [158].

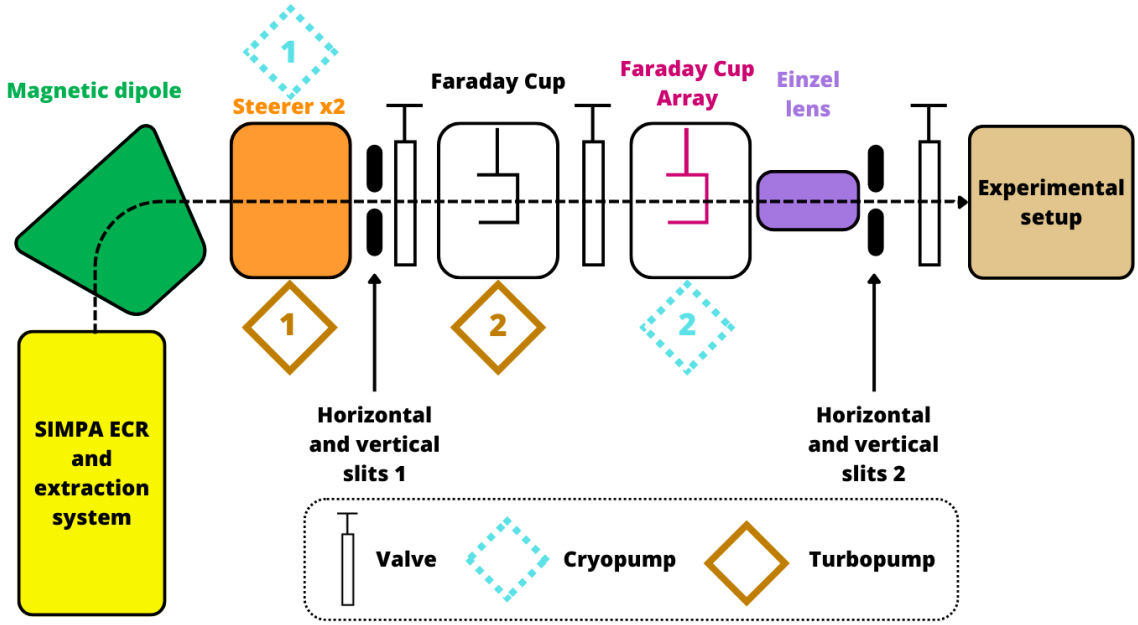

Figure 59: Schematic view of the SIMPA beamline up to the experimental setup.

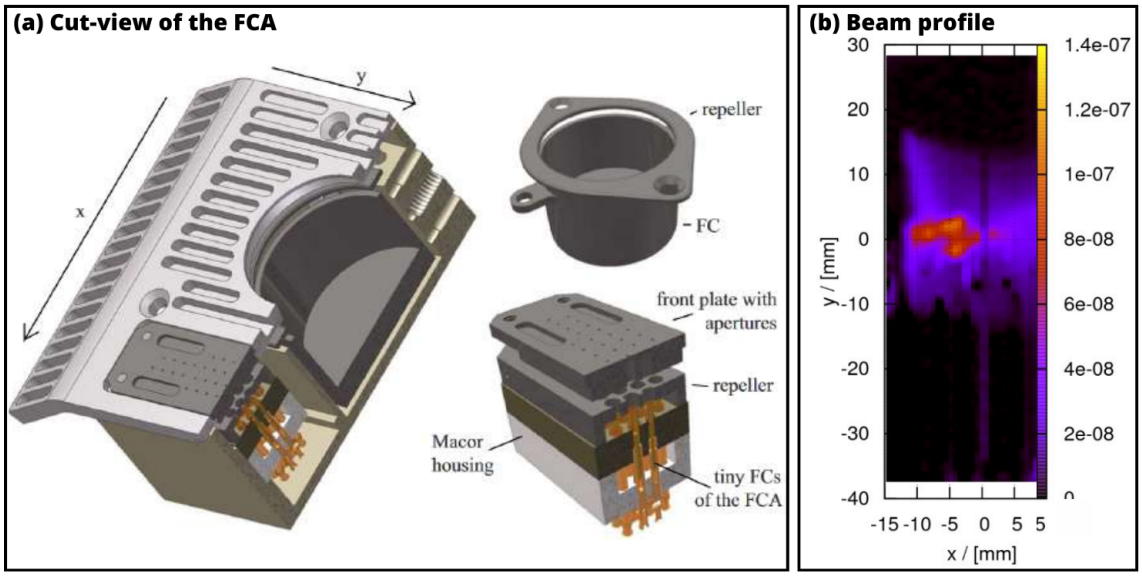

Figure 60: (a) Cut-view of the Faraday Cup Array (FCA) detector system with detailed views of the large Faraday Cup and the FCA on the right [157]. (b) Example of a beam profile obtained with the FCA for a 12 µA Ar^{8+} beam with an energy of 80 keV.

4.2.4 Beam transport and monitoring for ARIBE

There are five beamlines at ARIBE , and here we will detail the L4 beamline, which was used during tests [159, 160]. The layout is presented in Figure 61. Immediately after the

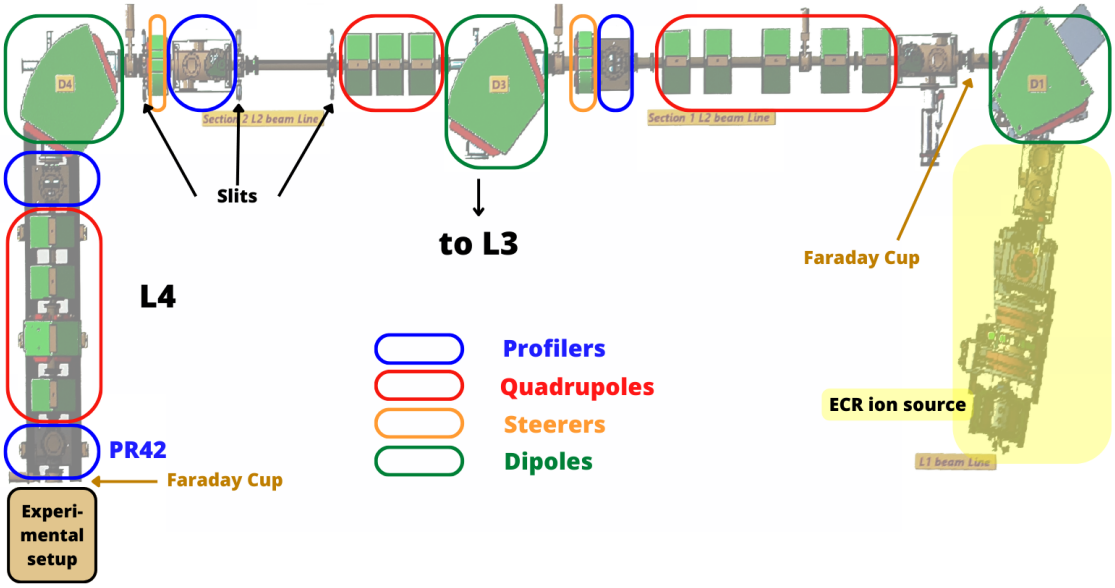

Figure 61: Schematic view of the L4 ARIBE beamline from the ECR ion source to the last Faraday Cup, after which the test chambers for OMEGA and spectrometer were placed for experiments. Image taken from the beamline control panel at ARIBE.

source, a 60° magnetic dipole directs the beam towards the main beamline. Along the beamline, sets of magnetic steerers and quadrupoles are employed to shape and steer the beam. Beam current is monitored using Faraday cups and beam shape using 47×47 multi-wire beam profilers. Two 90° selection dipoles are used to deliver the beam to the L3 and L4 beamlines. Upstream the L4 dipole, a set of three slits spaced 90 cm apart can

be used to reduce the beam emittance and intensity. The middle slit has to be placed at a focal point to ensure emittance reduction, as shown on Figure 62. Following the second dipole, which further purifies the beam, two profilers and a set of quadrupoles are used to monitor and adjust the beam shape. A beam profile for a 3 keV/u Ar^{8+} beam of 1 µA intensity taken with PR42 is shown on Figure 63. A final Faraday cup is situated at the end of the line before the experimental setup to monitor the beam current.

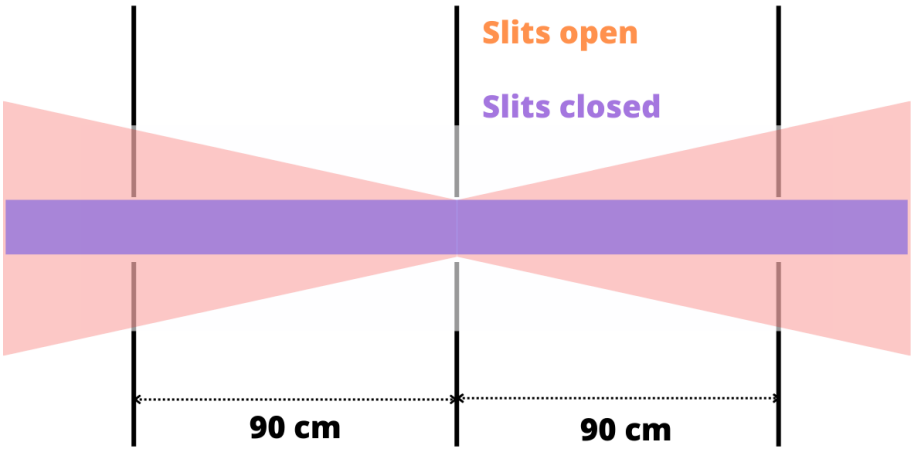

Figure 62: Principle of emittance reduction using 3 sets of slits placed 90 cm apart. The center slit is at a focal point, and when the side slits are closed the emittance of the beam is reduced, as well as its intensity.

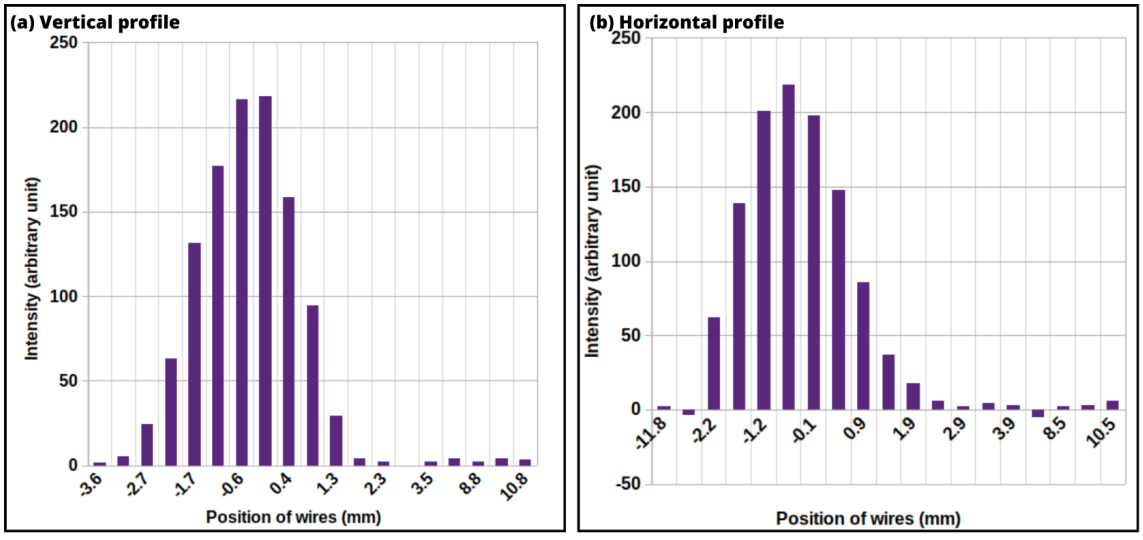

Figure 63: Typical profile for a 3 keV/u Ar^{8+} beam of 1 µA intensity taken with the multi-wire imaging profiler placed at the end of the L4 beamline (PR42) just before the experimental setup.

4.3 The collision zone

The collision zone installed as a continuation of the FISIC beamline is composed of three home-made devices. The first, an in-line charge state purificator named *OMEGA*, is situated at the end of the FISIC beamline. It is followed by an ultra-high vacuum chamber where the collision between two beams occurs. Downstream the collision chamber in the alignment of the FISIC beamline, there is an ion spectrometer and its associated detector to separate and detect the ion beams created during the collision from the FISIC primary beam. Steerers and electrostatic lenses are placed between these three devices which are described in detail in the following sections. Figure 64 shows a SIMION simulation of the ideal trajectories of a primary beam with a charge q and secondary beams with charges $q-1$ and $q+1$. The OMEGA plays the role of a beam purification system since it only lets the primary beam pass through, and the spectrometer disperses the three beams in terms of charge states.

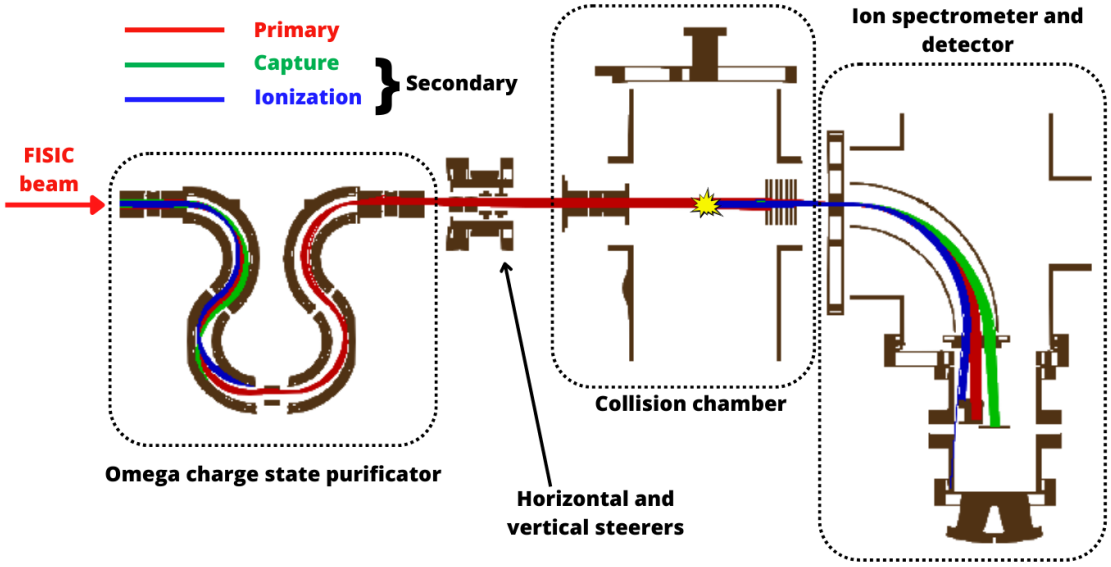

Figure 64: SIMION simulation of the trajectories of the primary (q) and secondary ((q-1) and (q+1)) ion beams in the collision zone elements.

4.3.1 The OMEGA charge-state purification system

The OMEGA charge-state purification system (so-called because of the shape of its electrodes arrangement) was developed with the aim of purifying the primary beam in terms of charge states just before the collision zone. Collision processes with the residual gas giving rise to charge state modifications (mostly capture) may occur along the beamline upstream the collision zone. To clean this beam, the simplicity of a purely electrostatic device allowing also to maintain the beam axis was chosen. The operation of the OMEGA lies on the principle of electrostatic charge state analyzers (ECSA) widely used for electron beams [161]. In an ECSA setup, the incoming charged particles beam encounters an array of electrostatic lenses or plates that generate a well defined electric field. This field deflects the charged particles from their initial trajectory. For a fixed voltage, the extent of deflection depends on the energy to charge ratio (E/q) of the ions, with higher E/q resulting in greater deflection. This leads to a spatial separation of ions

according to their charge states.
As shown on Figure 65, the OMEGA is composed of four sequential electrostatic 140° concentric cylindrical electrodes, enclosed by Matsuda electrodes [162]. These Matsuda electrodes help to focus the beam in the vertical plane. They are coupled, and therefore both are at the same voltage. At the entry and exit of the OMEGA, two Einzel lenses are placed, which focus the beam in the first half of the OMEGA, and to refocus it after its passage inside the device. A central deflector made of pair of parallel plates is situated between the second and third sections of the OMEGA. They create an electrical correction field to adjust the beam position in the vertical direction. Finally in the first and last outer plates, two holes are made in order to let the incoming beam pass in a straight trajectory if the voltages are turned off. A removable Faraday cup can be inserted between those plates to monitor the current of the beam. The voltages that have to be applied to the inner (V_i), outer (V_o) and Matsuda electrodes (V_M) in order to guide a beam of charge q_0 for an extraction voltage V and a primary beam of charge q are given by equations (104), (105) and (106) respectively. For the case of positive ions, $V_i<0$ and $V_o>0$. R_i, R and R_o are the inner, center and outer curvature radii of the electrodes, as shown in Figure 65.

$$V_i = 2 \times \ln\left(\frac{R_i}{R}\right) \times \frac{q_o V}{q} \tag{104}$$

$$V_o = 2 \times \ln\left(\frac{R_o}{R}\right) \times \frac{q_o V}{q} \tag{105}$$

$$V_M = V_i + 0.6 \times (V_o - V_i) \tag{106}$$

The resolving power of the OMEGA, as well as the presence of unwanted charge states

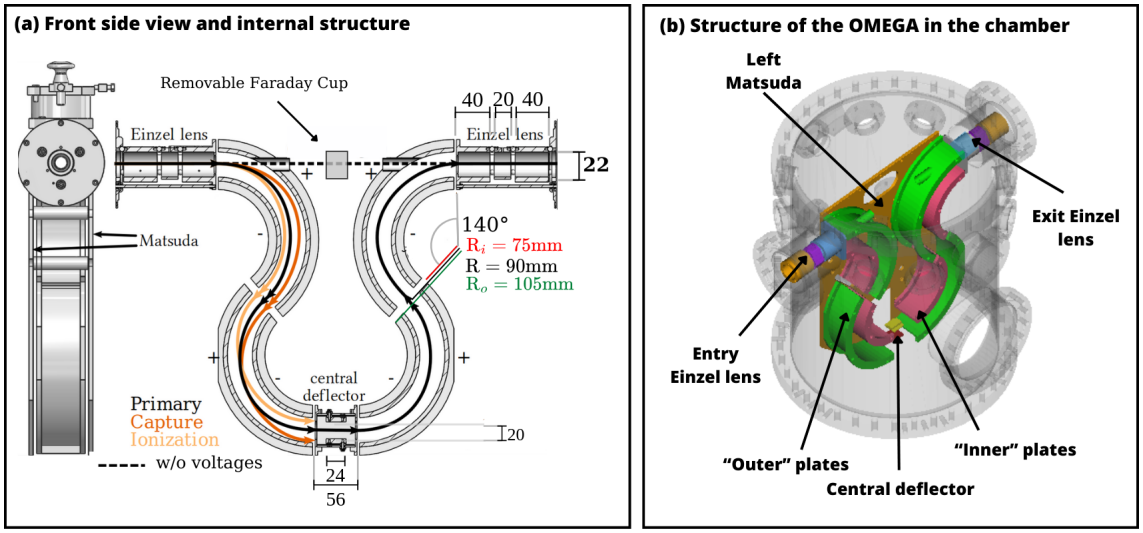

Figure 65: The OMEGA beam purification device. a : Front and side internal structure of the OMEGA with its principal dimensions, showing the typical trajectories of primary, capture and ionization beams. b : Three-dimensional image of the internal structure of the OMEGA within the chamber. Right Matsuda plate removed for clarity.

in the beam can be determined by a voltage-scan procedure. First, the voltages of the OMEGA are optimized to allow 100% transmission for the primary charge state q_0. Then the voltages on the inner and outer electrodes (V_i^q and V_o^q), and consequently the transmitted energy E_q are scaled as given by equations (107) and (108) to optimize

transmission of secondary charge states.

$$V_a^q = \frac{q_o V_a}{q} \tag{107}$$

$$E_q = \frac{E_o q_0}{q} \tag{108}$$

In the equation (107), V_a represents the voltages on either the inner or outer electrodes for which optimal transmission of a beam with energy E_0 and charge state q_0 is achieved. Therefore V_a^q is the voltage for which a beam with the same energy E_0 but charge state q is transmitted through the OMEGA.
The resulting graph gives the intensity of the transmitted beam as a function of the energy E_q/q. Figure 66 shows such energy scans for different primary charge states (O^{5+}, Ar^{9+}, Xe^{20+}) at an extraction voltage of 14 kV taken at ARIBE in 2018, and Figure 67 shows the scans made for Ar^{12+} and Ar^{8+} at an extraction voltage of 10 kV at ARIBE in 2023 (a) and at INSP in 2020 (b) and 2024 (c). The broad plateau-like appearance of the peaks is in part due to the fact that the Faraday cup (that has a diameter of 35 mm) used to measure the current is larger than the size of the focused ion beam and that the analyzer was build to have a broad acceptance range.

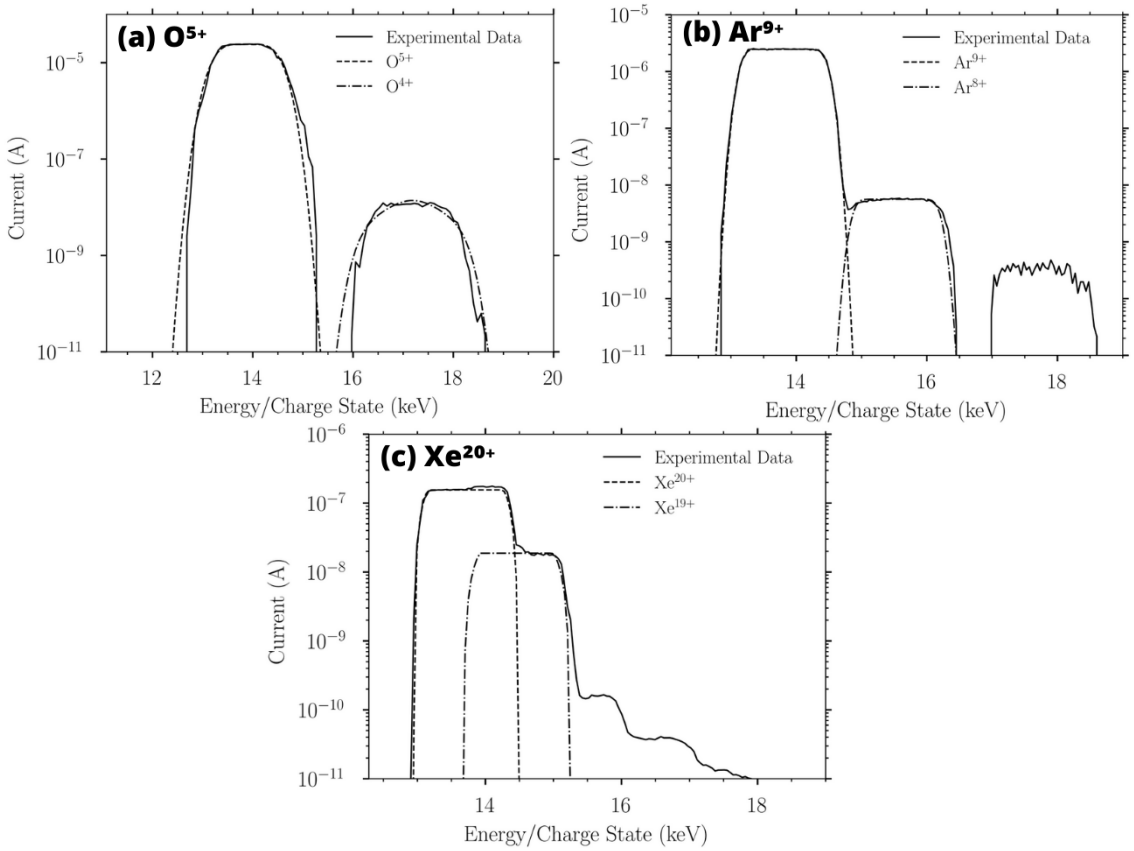

Figure 66: Energy scans of (a) 4.4 keV/u O^{5+}, (b) 3.15 keV/u Ar^{9+}, (c) 2.14 keV/u Xe^{20+} primary beams performed at ARIBE [159]. The dashed line is a fit of the primary charge state and the dotted-dashed line is a fit of the single electron capture charge state.

The OMEGA underwent several testing campaigns both at the ARIBE facility and INSP, using a variety of ion beams with 10 and 14 qkeV energies and typical beam

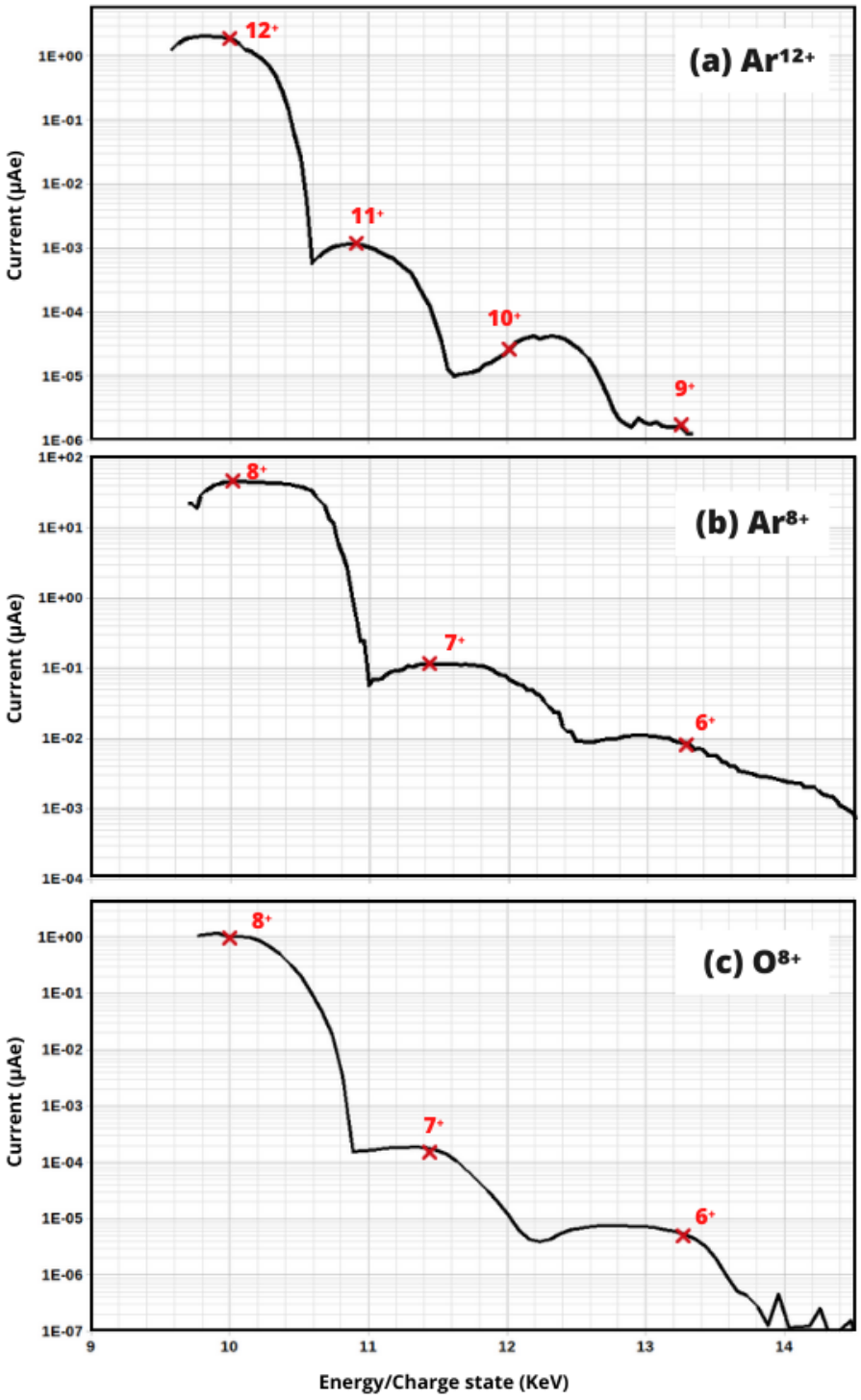

Figure 67: Energy scans of (a) 3 keV/u 11 µA Ar^{12+} primary beam performed at ARIBE, (b) 2 keV/u 44 µA Ar^{8+} primary beam with the SIMPA source and (c) 5 keV/u 1.1 µA O^{8+} primary beams with the FISIC source.

intensities between 2 and 45 µA. The results exhibit a resolving power of 10.5 and a 100% transmission rate for the intended charge state, facilitating effective purification of incoming ion beams with charge states up to 12+ and reasonably effective purification for charge states reaching at least 20+ [159]. The resolving power of the analyzer is computed in the same way as in mass spectrometry as $E/\Delta E$ where ΔE is the full width at half maximum of the measured peak. The percentage of the beam that is stopped inside the OMEGA varies between 0.01% and 0.3%. This depends mostly on the pressure inside the beamline at the moment of the measure, since a higher pressure means more ions will be produced via in-line capture, and secondary charge state will make up for a higher portion of the beam.

4.3.2 The collision Chamber

The collision chamber is supposed to operate under ultra-high vacuum conditions, between 10^{-9} mbar and 10^{-10} mbar. The chamber is preceded by two beam shaping and focusing elements, as depicted in Figure 68 (a): an electrostatic deflector to adjust the vertical and horizontal trajectory of the beam, and an Einzel lens with the central point of the chamber serving as the focal point. At the exit, there is a cross lens [163, 164] composed of 7 plates perforated with either vertical or horizontal windows and polarized as illustrated in Figure 68 (b). The design of this lens was chosen for its lower voltage requirement compared to cylindrical lenses, weakly coupled X-Y focusing, and behavior akin to a FODO (Focus (F) - Drift (O) - Defocus (D) - Drift (O)) cell [165]. These three elements were designed by a member of the INSP team before the beginning of my thesis.
Within the collision chamber, several devices are employed to monitor and analyze the collision environment 69, and a capillary is installed to produce a gas jet for collisions with atoms as shown on Figure 70 and described below.

- *Gas jet* : Mounted on the top flange of the chamber is a system comprising a retractable nozzle for gas injection. The inclusion of a gas jet provides the capability to perform collisions between ions and atoms, as well as to "scan" the SIMPA and FISIC beams by observing interactions between the beam and the jet using an X-ray detector. As shown on Figure 70, the effusive gaseous jet intersects the ion beam at a 90-degree angle and at a distance h_{jet} from the capillary exit. The effusive jet is produced by gas diffusion through the capillary into the collision chamber. The capillary has a length $L = 35$ mm and an inner diameter $d = 0.1$ cm, operating at room temperature with a backing pressure p_0 between 0.5 and 5 mbar. The jet has an angular opening θ between $\pm 10°$ and $\pm 40°$ depending on the backing pressure and is tailored to operate in the *viscous* regime, meaning that a large number of collisions take place between the gas atoms and the capillary walls.The characteristics of the jet allowed us, by moving it along the vertical axis, to maximize the interaction zone between the projectile ions and the gas targets. To ensure that the cross sections are estimated correctly from the data, we need to be in the "single-collision regime" described in section 1.3.1.3. Therefore we need to know the density of target atoms at the level of the jet-beam interaction, as a function of the backing pressure p_0. To ensure that we are in the single-collision regime, we estimate a maximum probability of events P_{max} [166]

$$P_{max} \approx \bar{n}_{jet}(\text{at.cm}^{-3})\sigma_{capt}(\text{cm}^2)\ell_{jet}(\text{mm}) \tag{109}$$

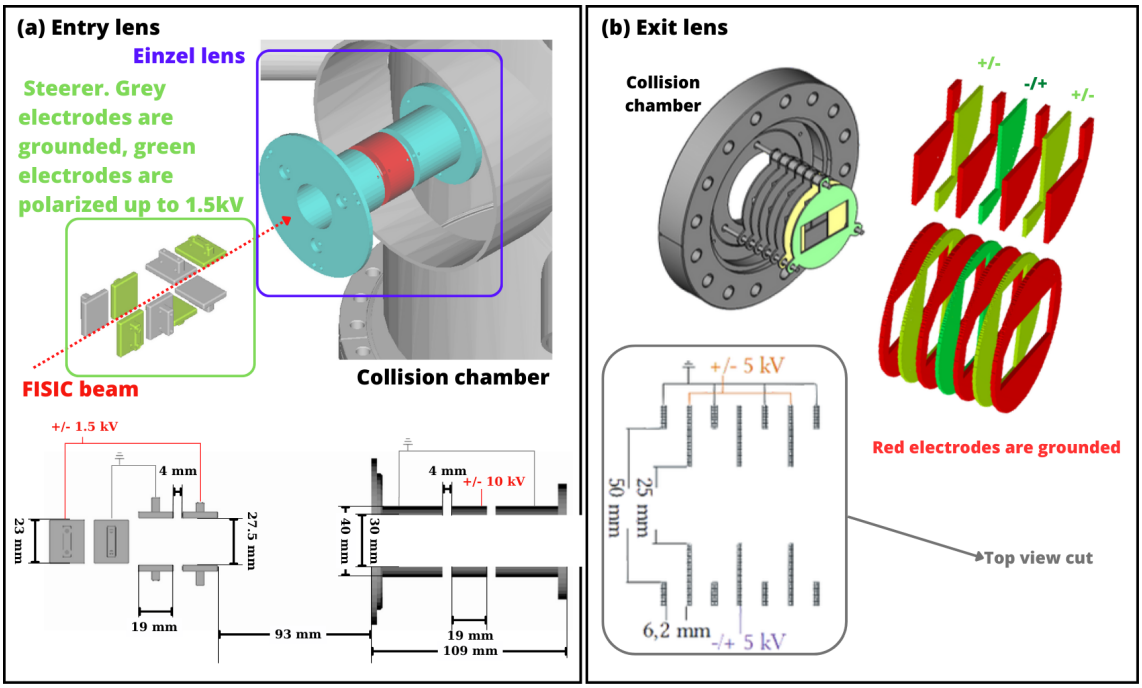

Figure 68: (a) View of the electrostatic steerers situated downstream the OMEGA chamber and the entry lens of the collision chamber. (b) View of the exit cross lens of the collision chamber.

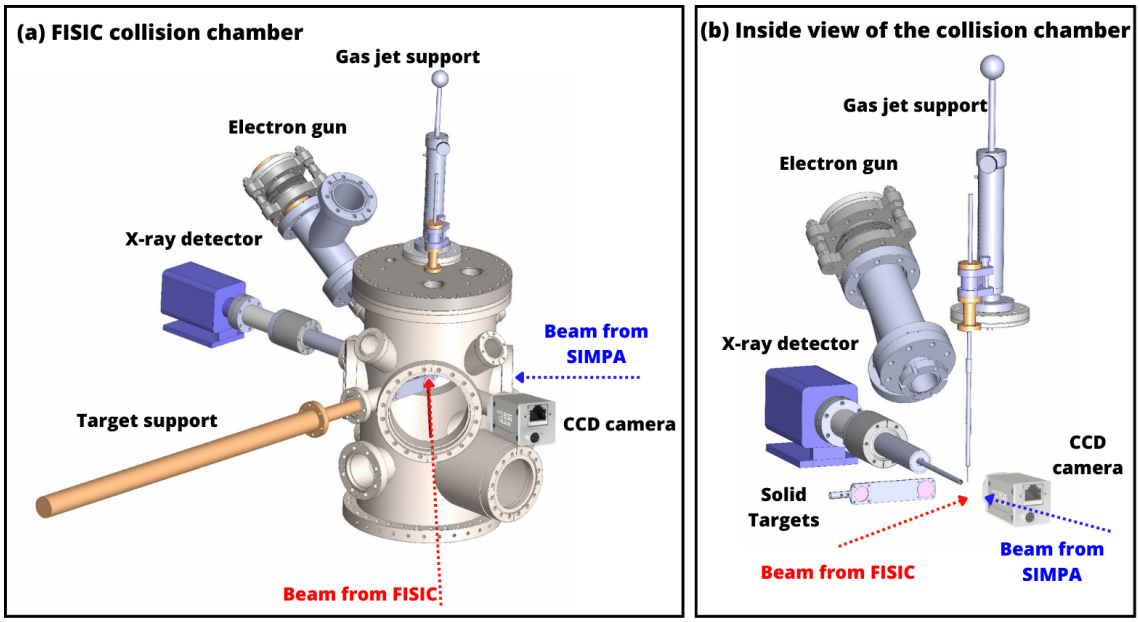

Figure 69: (a) View of the collision chamber from the FISIC beamline axis, with the different systems. (b) Inside view with the chamber removed, showing the interaction zone.

with $\bar{n}_{jet}$ the maximal density, ℓ_{jet} the minimal length of the jet and σ_{capt} the total capture cross section.
The maximal density $\bar{n}_{jet}$ can be expressed like

$$\bar{n}_{jet}(\text{at.cm}^{-3}) = \frac{dN/dt\ (\text{part.s}^{-1})}{\bar{v}\ (\text{cm.s}^{-1})\pi\frac{\ell_{jet}^2(\text{cm})}{4}} \tag{110}$$

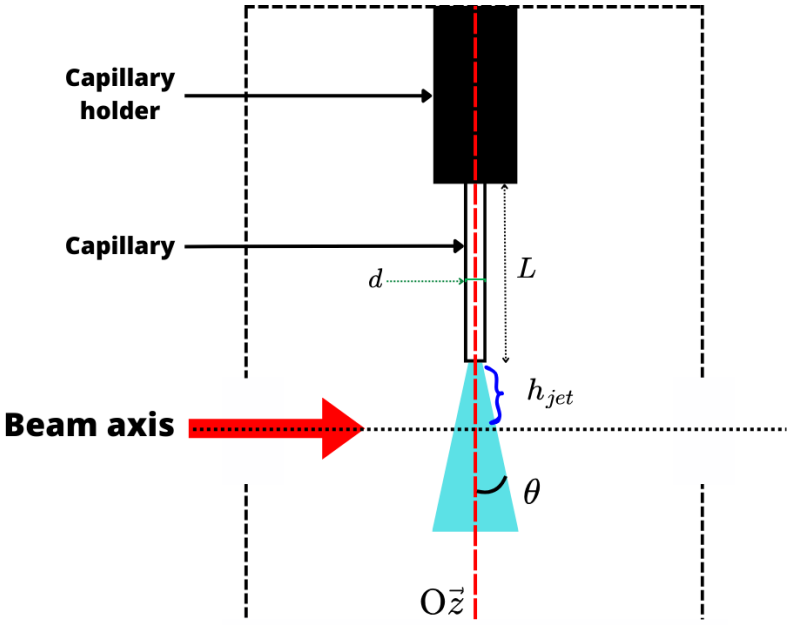

Figure 70: Schematic view of the gas injection system in the collision chamber.

where $\bar{v} = \sqrt{\frac{8RT}{\pi M}}$ is the mean velocity of the gas molecules (with M the molar mass) and dN/dt is the total flow of the gas. In the viscous regime, this flow is expressed as

$$\frac{dN}{dt}(\mathrm{s}^{-1}) = \frac{\pi^2\sqrt{\pi}}{84 \times 16} d^4(\mathrm{mm}) \frac{p_0^2(\mathrm{Pa})}{\eta(\mathrm{kg.s^{-1}.m^{-1}}) k(\mathrm{m^2.kg.s^{-2}.K^{-1}}) T(\mathrm{K}) L(\mathrm{m})} \quad (111)$$

where η is the viscosity of the gas and k the Boltzmann constant. The factor $\frac{\pi^2\sqrt{\pi}}{84\times16}$ is a dimensionless constant.
The minimal length of the jet ℓ_{jet} can be written [166]

$$\ell_{jet} = 2h_{jet} \tan \Delta\theta \quad (112)$$

where h_{jet} is the distance between the end of the capillary and the ion beam as illustrated in Figure 70 and $\Delta\theta$ is the jet directivity, both depending on experimental conditions. The capture cross section σ_{capt} is of the order of 10^{-15} cm^2 for the case of 4.4 keV/u O^{7+} ions and Ar or He atoms. The main characteristics for He and Ar gas are reported in Table 12. They have been computed for a backing pressure $p_0 = 1.6$ mbar and $h_{jet} = 6$ mm. The condition for single collision is

Gas	$\bar{v}$(m.s^{-1})	η(g.s^{-1}.cm^{-1})	$\Delta\theta(^\circ)$	dN/dt (part.s^{-1})	ℓ_{jet} (mm)	$\bar{n}$ (at.cm^{-3})	P_{max}
Ar	399	2.22$\times$ 10^{-5}	26.9	1.04$\times$ 10^{17}	6.1	8.97$\times$ 10^{12}	0.005
He	1260	1.94$\times$ 10^{-5}	16.5	1.18$\times$ 10^{17}	3.6	9.47$\times$ 10^{12}	0.003

Table 12: Main parameters for an effusive jet of Ar and He.

respected since the probability for simple capture P_{max} reported in the last column of Table 12 is very small compared to 1.

- *Solid targets* : A retractable target support capable of holding 4 targets (2 on either side of the target holder) is mounted so that the beams from FISIC and SIMPA hit the targets at a 45° angle. Two types of targets are used, one made of silicon and the other made of a special kind of fluorescent ceramics called AF995R (Al_2O_3:Cr) [167]. The part of the stainless steel support between the two targets is also used as a target itself when the intensity of the beams is a few tens of µA. The ceramic and silicon targets are used for intensities of the order of 100 nA and a few µA, respectively. When the beam hits the targets, the light emitted due to fluorescent effect can be picked up by a camera and thanks to an engraved scale on the target, the beam dimensions can be measured and the beam position adjusted.

- *CCD camera* : The CCD camera is mounted at a 90° viewing angle with respect to the solid targets and at a 45° angle with respect to each of the beams. It permits to observe precisely the shape and size of the beams at the interaction point and therefore optimize their overlap which is a key parameter to evaluate cross sections. The camera is a Basler ACE 2 Pro CCD camera [168], equipped with a CMOS sensor (Complementary Metal-Oxide-Semiconductor, a sensor that converts light into electrical signals using an array of photodiodes, amplifiers, and analog-to-digital converters on a single chip). It has a resolution of 2.3 Megapixels and a pixel size of 3.45 µm × 3.45 µm, ensuring high-quality image capture with fine details. With a dynamic range of 71.7 dB, the camera accurately depicts various lighting conditions, while its signal-to-noise ratio of 40.2 dB ensures minimal background noise. Figure 71 shows images on the stainless steel target and vertical and horizontal intensity profiles of a 7.9 µA O^{7+} beam made with the FISIC source (a) and a 5.1 µA O^{7+} beam made with the SIMPA source (b).

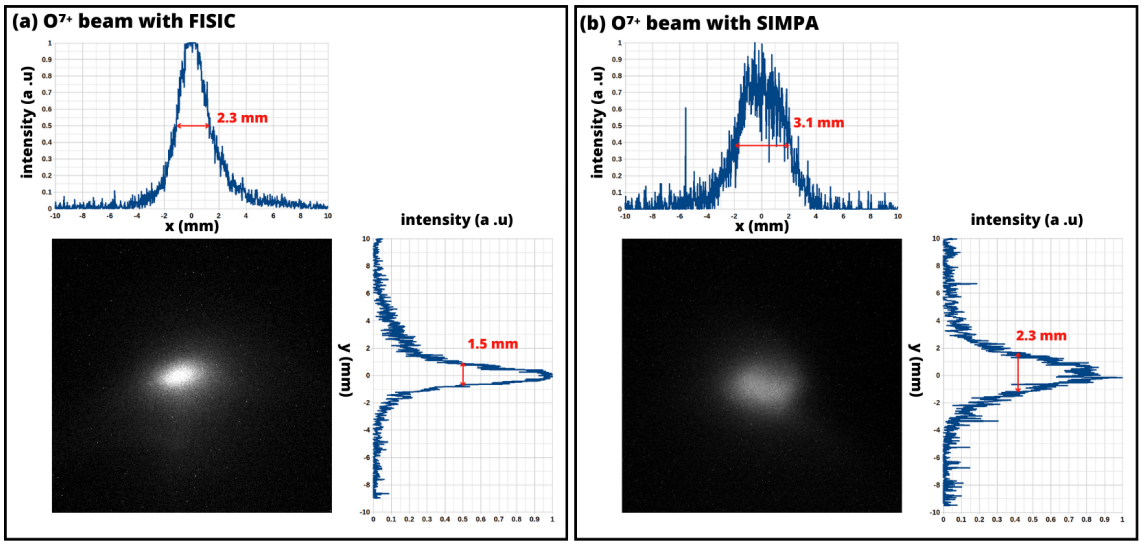

Figure 71: CCD images on the stainless steel target and intensity profiles of (a) 7.9 µA O^{7+} beam (made with the FISIC source at an RF power of 137 W and an extraction voltage of 10 kV) and (b) 5.1 µA O^{7+} beam (made with the SIMPA source at an RF power of 48 W and an extraction voltage of 10 kV).

- *Electron gun* : An electron gun is positioned at a 45° angle relative to the vertical axis of the beam propagation. It is employed to calibrate the X-ray detector in

terms of energy using the X-rays emitted by the solid targets described below. The electron gun generates an electron beam by heating a filament with a current of approximately 1.3 A. The electrons have a kinetic energy of 10 keV. The electron beam has a diameter of around 1 mm.

- *X-ray detector* : A detector for X-ray spectroscopy is installed to have a 45° view relative to both beam axes. Its purpose is to detect X-rays emitted during ion-ion or ion-atom collisions. The specifications of the X-ray detector used are given in section 4.3.4.2. The total distance from the Si crystal to the center of the chamber, where the interactions of interest occur is 207 mm. In front of the detector, a long collimator of 160 mm in length with an internal diameter of 6 mm is placed in front of the X-ray detector (see Figure 72 (a)). This collimator defines a zone viewed by the detector centered on the interaction zone between the two ion beams or between one of the ion beams and the gas jet. This reduces the detection of X-rays originating from the interaction of the beams with the residual gas or the chamber walls for instance. The collimator permits to see 100% of the interaction zone, meaning that the viewed zone could still be reduced without impacting signal detection, but that would allow for an even better reduction of background noise. On Figure 72 (b), a zoom of the interaction zone is presented, where the zone with a 100% efficiency detection and the so-called penumbra zones are indicated.

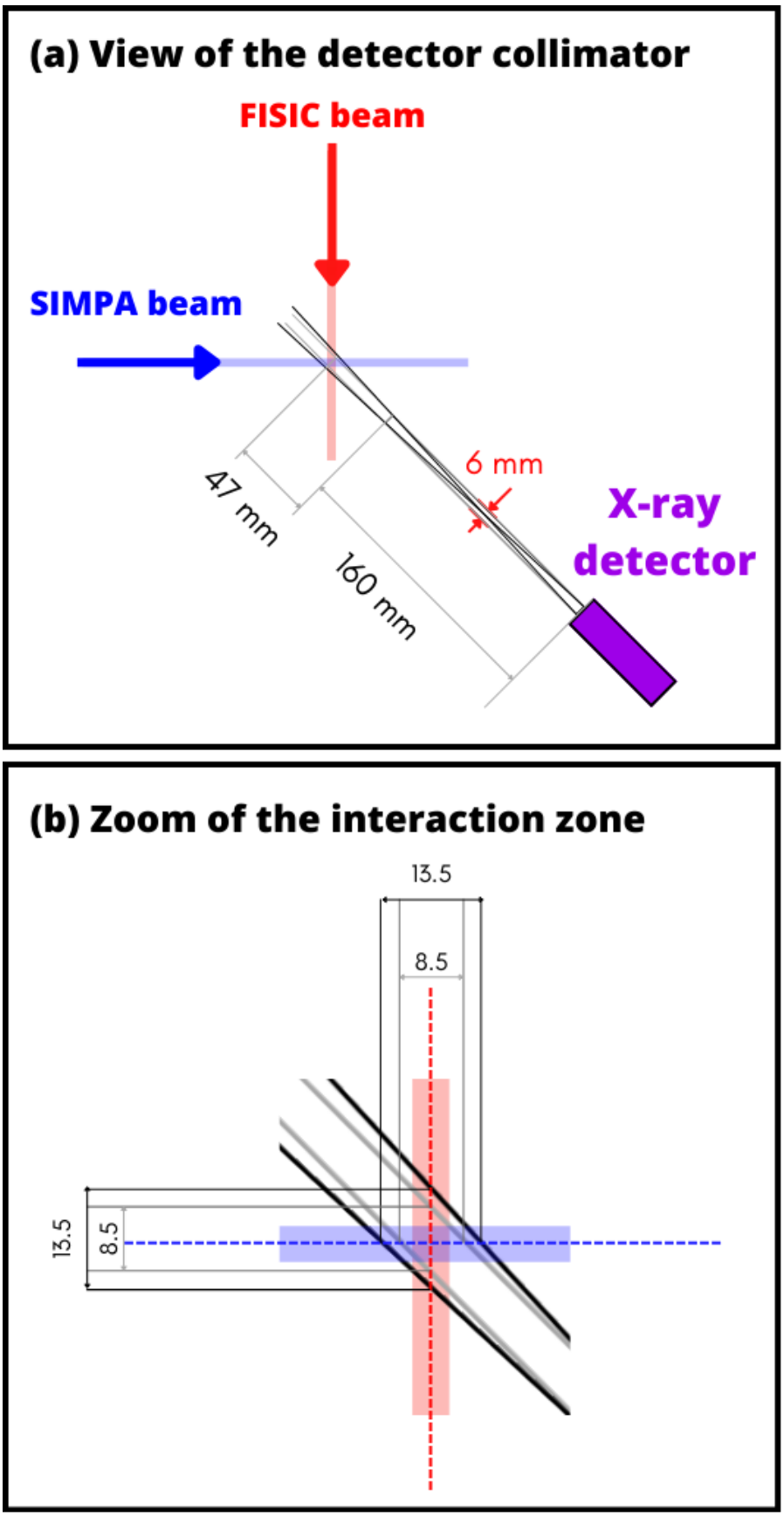

Figure 72: (a) Long collimator placed in front of the crystal X-ray detector to determine a restricted viewed zone. (b) Zoom of the interaction zone.

4.3.3 The ion spectrometer

The ion spectroscopy setup positioned after the collision chamber must exhibit charge dispersion for multicharged ions with kinetic energies in the keV/u range. Additionally, it should be capable of separating the primary charge state from the secondary charge states that could be generated during ion-ion or ion-atom interactions in the collision chamber. We have opted for a complete electrostatic system (see Figure 73) based on the principle of an electrostatic charge state analyzer, as detailed in section 4.3.1 [160]. This system comprises two 90° curved plates to separate the charge states, along with two vertically positioned Matsuda electrodes [162] for ion beam focusing and steering. This system was constructed based on a design of the CIMAP (GANIL) team. An ion detection system composed of a Faraday cup and a position-sensitive device measures the intensity of the primary beam and the intensities and positions of secondary charge states. Details about this detection system are given in section 4.3.4.1. To guide a charge state q into the Faraday cup of the detector, the voltages U applied to the curved outer and inner plates must be as given by equation (113), where q_0 is the primary charge state, V the extraction voltage of the ion source, R the curvature radius of the spectrometer, and $2d$ the distance between the outer and inner electrodes. The values of R and $2d$ are reported in Figure 73.

$$U_{outer} = -U_{inner} = \frac{2dq_0V}{Rq} \tag{113}$$

The ion spectrometer underwent testing at ARIBE in 2021 and 2023. The results of

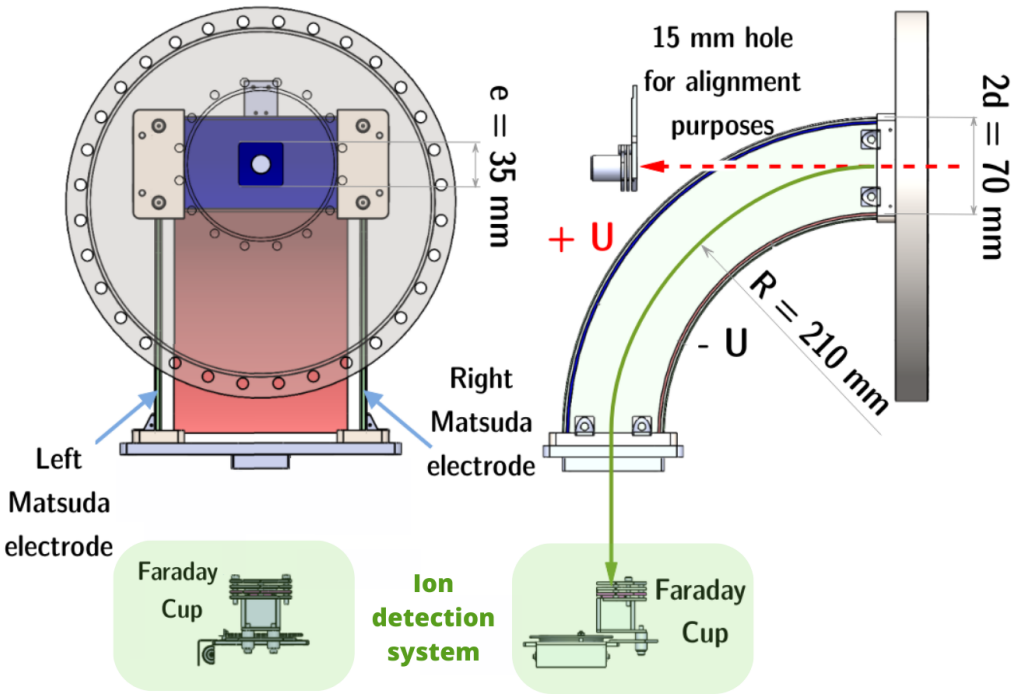

Figure 73: Left : Front view of the spectrometer showing the entrance square with side $e = 35$ mm. Right : Schematic cut through the ion spectrometer (side view). The expected ion trajectories for V = 10 kV and $q = q_0$ corresponding to $U = 3333$ V (solid line), and with $U = 0$ V for beam alignment purposes (dotted line) are shown.

these campaigns are detailed in Section 5.3. Following the initial campaign in 2021, a

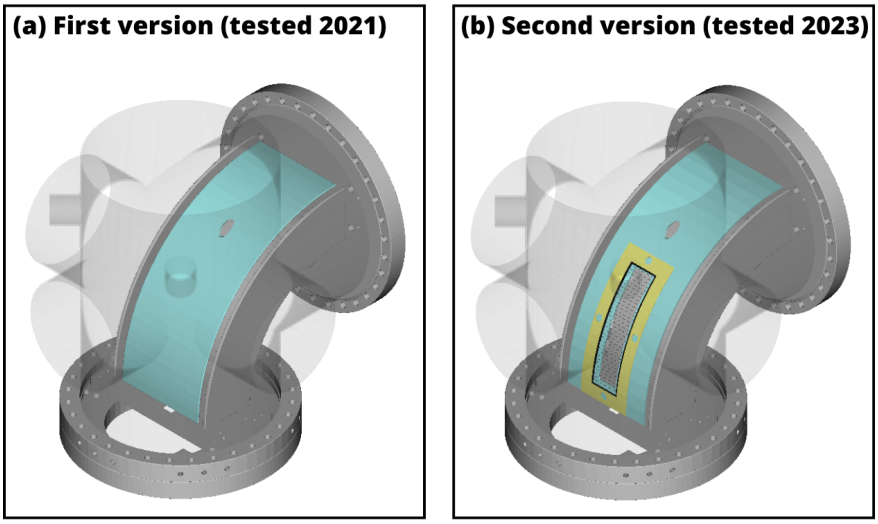

Figure 74: Views of the ion spectrometer outer plate in blue within the chamber, a) First version with a full plate and b) second version with a hole in the plate and a 15.6×3 cm grid (in black) with its support (in yellow).

modification was made to the ion spectrometer to reduce background noise contributions [160]. The outer plate of the ion spectrometer was perforated along a length of 20 cm and a width of 5 cm to allow secondary beams to pass through. Over the hole, a stainless steel grid measuring 180 mm by 50 mm with a thickness of 200 µm was placed, with holes measuring 20 mm by 5 mm wide to maintain the electric field of the plate. The dimensions of the grid were calculated to ensure a transmission rate exceeding 90%. Figure 74 depicts the outer plate of the spectrometer before and after the modification. The effects of this new design are discussed in Section 5.3.

4.3.4 Detection systems for ion and X-ray spectroscopy

4.3.4.1 Ion detection system

The detector positioned after the ion spectrometer must meet several criteria: it should be capable of detecting both the primary beam and secondary beams, it should have a high detection efficiency for ions with energies around 100 keV, exhibit good time and position resolution, and its size should be suitable for detecting one or two secondary beams simultaneously. The detector was constructed by CIMAP (GANIL), and the chosen design is depicted in Figure 75. A Faraday cup collects the primary beam to measure its intensity, while a time and position sensitive detector composed of two *microchannel plates (MCP)* [169] and *delay-line anode* detects the secondary beams. The *MCP* operates by using an array of microscopic channels or pores embedded within a thin glass or ceramic plate. When particles strike the surface of the MCP, they release secondary electrons through secondary electron emission. These secondary electrons are accelerated and focused by a potential difference applied across the MCP. They undergo cascaded multiplication as they travel through the channels, resulting in a significant amplification of the original signal. The *delay-line anode* is composed of a planar conductive surface with an array of closely spaced electrodes arranged in a specific geometric pattern (see Figure 75 (a)).

When charged particles interact with the surface, they induce electrical signals in the electrodes. The position of particle impacts is determined by measuring the arrival

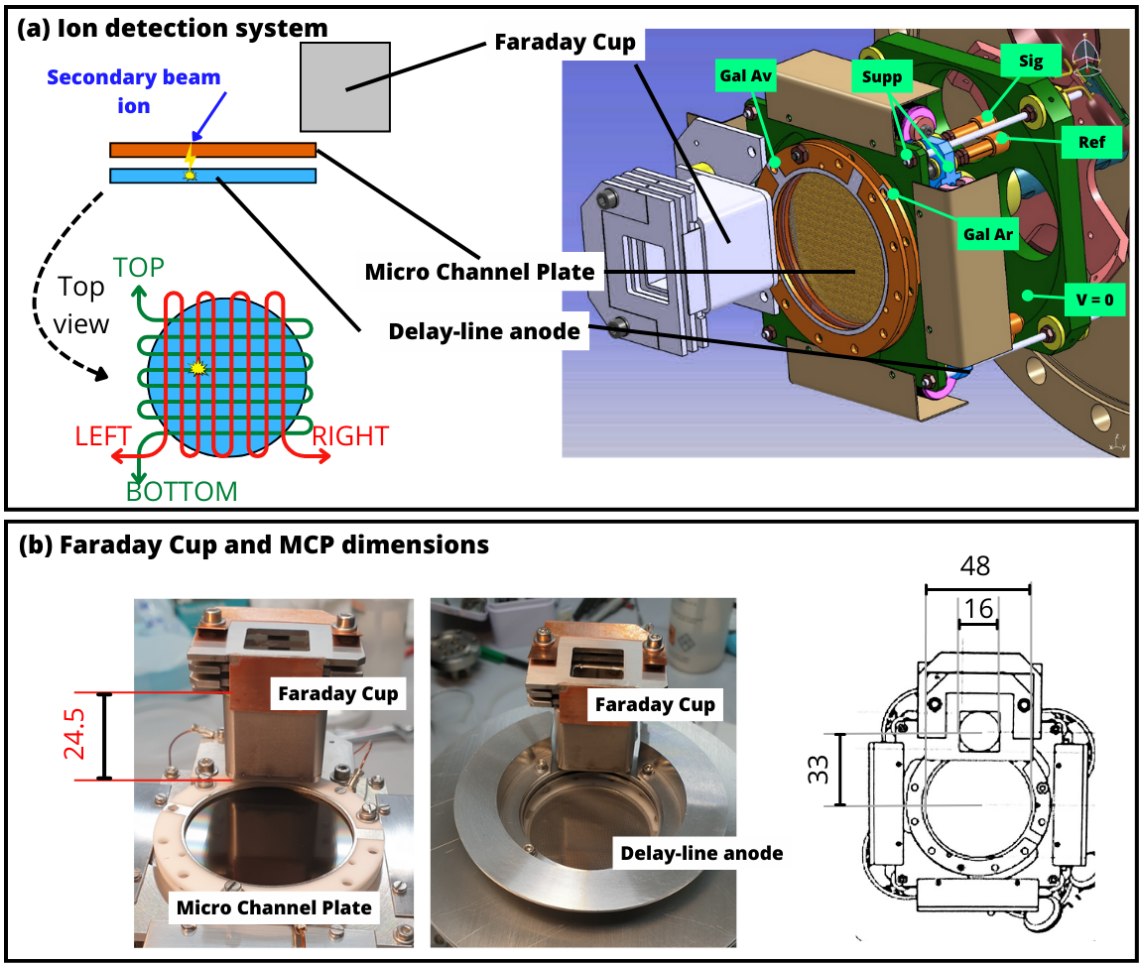

Figure 75: (a) Schematic view of the ion spectroscopy detector, with the position of the electrodes for the polarization of the detector indicated in green. (b) Pictures of the Faraday Cup and MCP (left) and Faraday cup and delay-line anode (right).

Electrode	Voltage (V)
Supp	1400
Ref	1550
Gal AV	-400
Gal AR	1300
Sig	1600

Table 13: Voltages applied on the position sensitive detector (see Figure 75 (a) for the localization.

times of these signals at different electrodes. By converting the time intervals into spatial coordinates and considering the known geometry of the electrode array, the exact position of particle impacts can be evaluated. Four signals are produced by the delay-line anode for localization purpose (*top, bottom, left and right*) whose arrival time is measured by referring to a start time coming from the rear side of the MCP, noted *Tmcp*. The Tleft and Tright pulse time are given by equations (114), where L is the total length of the anode wire and Tp the time taken by an electric signal to travel a

length L.

$$\text{Tleft} = \text{Tp} \times \frac{x}{L} + \text{Tmcp} \tag{114}$$
$$\text{Tright} = \text{Tp} \times \frac{L - x}{L} + \text{Tmcp}$$

The detector is polarized as indicated on Figure 75 (a) with the voltages given in Table 13.

4.3.4.2 X-ray detectors

For X-ray spectroscopy, a silicon crystal solid-state X-ray detector is used. The detection principle of such a device is as follows : when X-rays with a given energy hit the silicon crystal, they are converted into electron-hole pairs via photoelectric effect. As shown on Figure 76, the electrons move toward the anode and the holes toward the cathode due to an applied electric field (see [170] for details), generating current pulses measured through a charge resistor. The voltage, integrated over time, is proportional to the charge deposited in the crystal, and thus to the photon energy. To measure the photon energy spectrum, each pulse is processed and digitized using the acquisition systems described in section 4.4. In order to test the new acquisition, two different detectors were used, that differ mostly by the type of window used to seal the detector. One of them uses a beryllium window (named GALA) and the other a polymer window (named LANCELOT), allowing it to have a higher efficiency below 1 keV. Both detectors operate at low temperatures (several tens of °C below zero). they are cooled using a thermoelectric Peltier cooler. The specifications of these two detectors are given in Table 14. The resolution and efficiency of these detectors when associated with a fully analog detection system (see section 4.4.2) has been determined previously in [138], and the efficiency curves for LANCELOT and GALA are given in Figure 77.

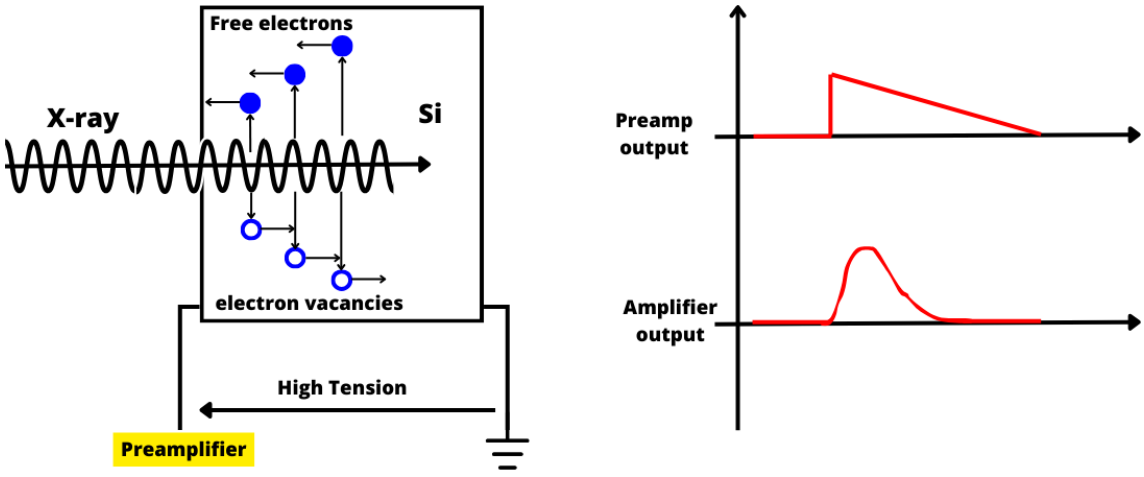

Figure 76: Working principle of the solid-state detector by migration of electron-vacancies pairs (left) and shape of the signals at the output of the preamplifier and the amplifier (right).

Detector name	Window	Active crystal	Si thickness (µm)	Si diameter (mm)
GALA	Be (15 ± 1 µm)	Si	240 ± 1	2.09 ± 0.05
LANCELOT	Polymer AP3.3	Si	450	8.74

Table 14: Geometrical characteristics of the two X-ray detectors.

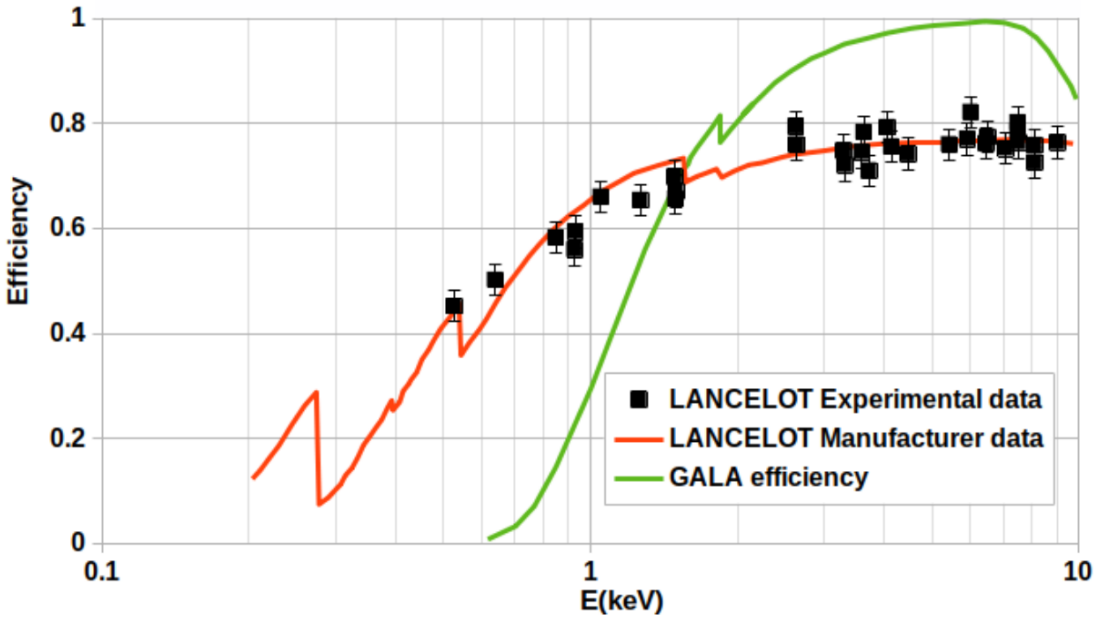

Figure 77: Efficiency curves of the LANCELOT and GALA X-ray detectors [138, 171].

4.4 Acquisition systems

4.4.1 FASTER Digital acquisition system

For the last 10 years, the LPC laboratory (Laboratoire de Physique Corpusculaire) in Caen has been developing a novel kind of digital acquisition system for nuclear physics called FASTER (Fast Acquisition System for nuclEar Research) [172]. FASTER is a modular system capable of performing high accuracy time of flight measurements and energy spectra. It is able to handle a wide variety of detectors such as solid-state detectors for photons, scintillaters, micro-channel plates and so on. FASTER is widely used by our colleagues from CIMAP, GANIL, Caen. Its main goal is to provide the user with a high accuracy acquisition system with build-in digital modules for signal treatment, and build-in trigger and coincidence modules, thereby greatly reducing the use of external analog modules and analog to digital converters. The FASTER hardware is composed of a support crate that connects to a computer via an ethernet cable. Three different kind of detection cards called daughterboards are available to be mounted on motherboards and put into the crate. In total, 6 motherboards each containing two daughterboards can be put into the crate. Figure 78 shows the crate we use at INSP, with the 4 CARAS daughterboards on their two motherboards and the two MOSAHR daughterboards on their motherboard. The specificities of each daughterboard are detailed in 4.4.1.2. Six software modules are available, among which the CRRC-4 spectroscopy module and the QDC-TDC time and charge measurement module. Their working principles are presented in section 4.4.1.3. FASTER is also paired with a visualization tool called RHB (ROOT Histogram Builder). ROOT is an object-oriented computer program associated with a library developed by CERN. It is very close in syntax to C++ and contains very powerful data analysis and histogramming tools. RHB is also developed by LPC Caen to fulfill the needs of FASTER. When using a specific module of FASTER, a RHB configuration can be created that allows the user to visualize data acquisition in real time and to monitor the signal processing. The histograms are pre-defined in a configuration file by the FASTER interface. Figure 79 shows an example of a RHB configuration for the CRRC4 spectroscopy module.

4.4.1.1 Advantages for coincidence detection

In the framework of the ion-ion collisions project, coincidence measurements need to be performed between the ion MCP detector and the X-ray detector. The FASTER acquisition system is particularly suited for this purpose, since both detectors can be easily plugged in and coincidence measurements performed either immediately or later during data analysis. For time of flight measurements with the MCP detector the so-called QDC-TDC module is used with the CARAS card whereas the CRRC4-spectro module is used for the X-ray detection with the MOSAHR card.

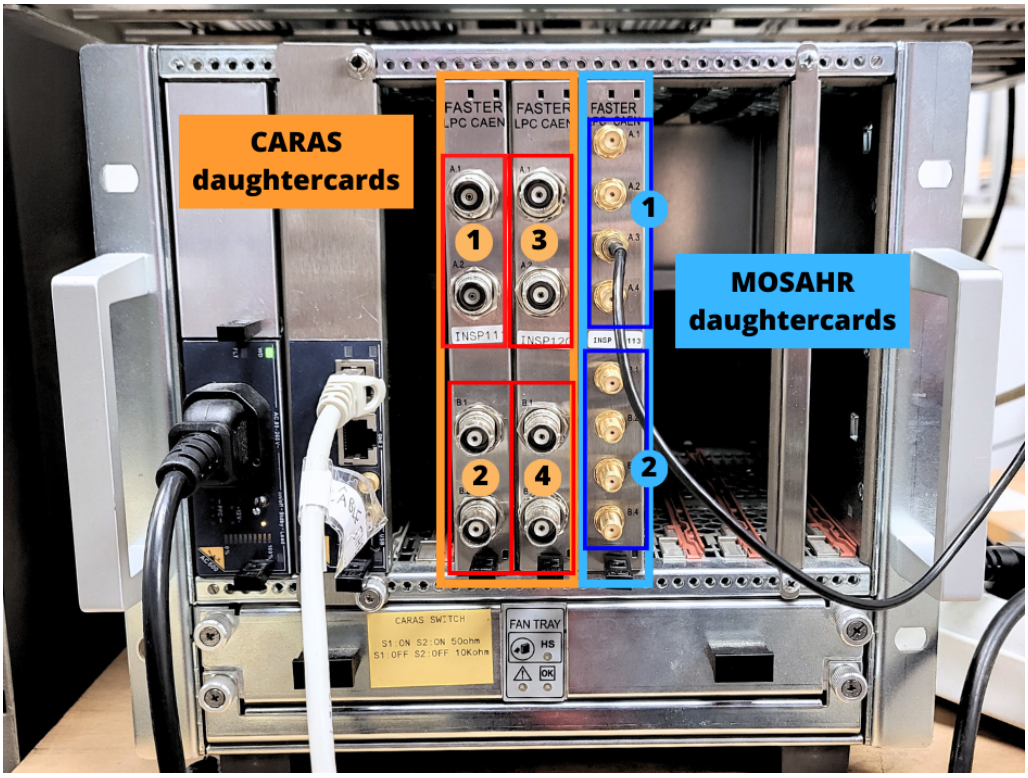

Figure 78: FASTER crate at INSP with CARAS and MOSAHR daughterboards.

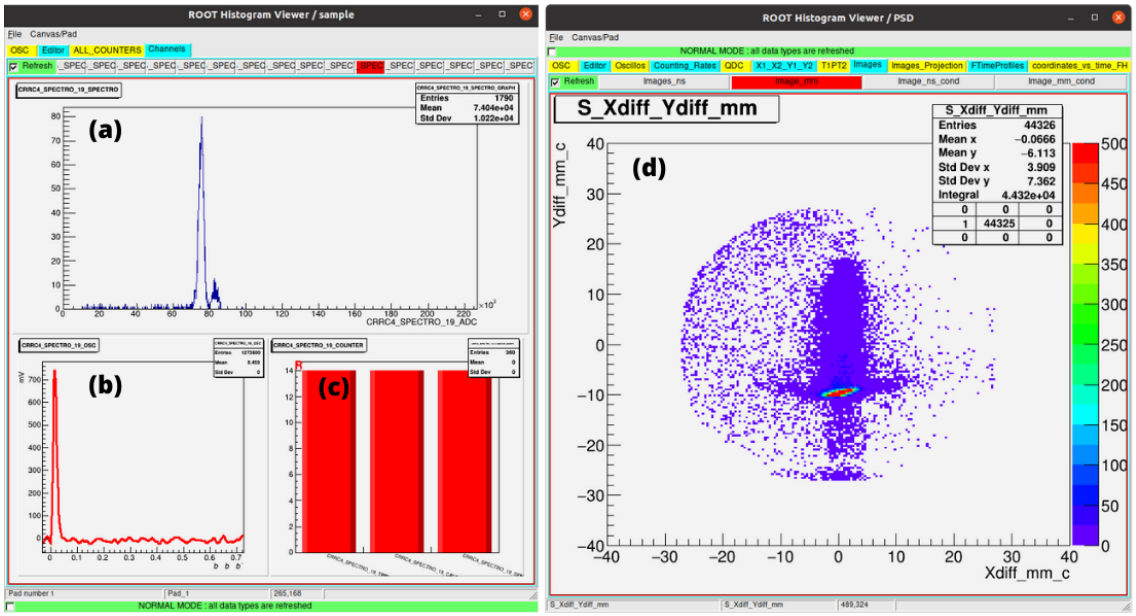

Figure 79: RHB window examples for the CRRC4 spectroscopy module with the MOSAHR card on the left. Panel (a) shows the spectrum reconstruction obtained with the LANCELOT X-ray detector, panel (b) shows the associated oscilloscope signal and panel (c) the event counter. On the right, panel (d) shows the RHB window for QDC-TDC measurements with the CARAS card obtained with the ion position sensitive detector.

4.4.1.2 CARAS and MOSAHR cards

We use two different daughter-boards :

- *CARAS :* It provides a dual channel 12-bits up to 500 Msps ADC capability. It is ideal for time of flight and charge measurements. It has a $\pm$ 1.15 V dynamic range with two impedance settings (50 Ω or 10 Ω) that are selected with an internal switch. The input offset is adjustable via the software between -1.1 V and 1.1 V. We use it with the QDC-TDC module for time and position measurements with our MCP detector for ion spectroscopy.
- *MOSAHR :* It provides a four channel 14-bits up to 125 Msps capability which is ideally suited for energy measurements. Contrary to CARAS, it has 4 input dynamic ranges ($\pm$ 1 V,$\pm$ 2 V,$\pm$ 5 V,$\pm$ 10 V) but only one impedance setting of 10 kΩ. The different ranges are only selected by manual switch and are not changeable via the software. We use it for photon energy measurements with our X-ray detectors.

The CRRC4 module provides three kinds of 8 ns-accuracy timestamped data : oscilloscope data, ADC data and event counter data. The QDC-TDC module provides three kinds of 2 ns-accuracy timestamped data : oscilloscope data, charge data (with an additional 7.8 ps-accuracy time information useful in case of time measurement), and even counter data. All can be displayed with RHB. The detail of the working principle of these two modules are given in the two next sections.

4.4.1.3 CRRC4-spectroscopy module working principle

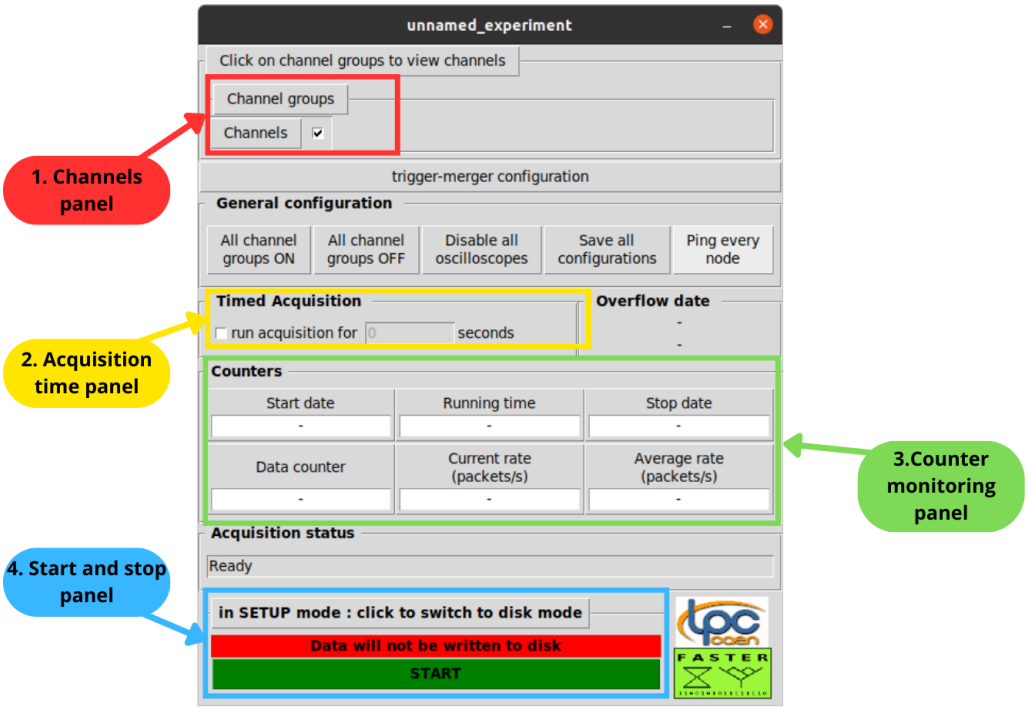

Figure 80: Command interface for FASTER.

The command interface for FASTER is composed of four main panels, as shown in Figure 80. The Channels panel is used to open the signal processing panel of Figure 81.

The time acquisition panel is used to set a given acquisition time. The counter monitoring panel allows the experimenter to visualize the running time (and remaining time in case of a timed acquisition), and the number and rate of data received by FASTER. Lastly, the start and stop panel can be used in two different modes : a SETUP mode in which the data is not recorded and can only be visualized with RHB in real time, and a DISK mode in which raw data are recorded in a file with a custom data format. In disk mode a file name must be specified before the acquisition is launched. The Channels panel

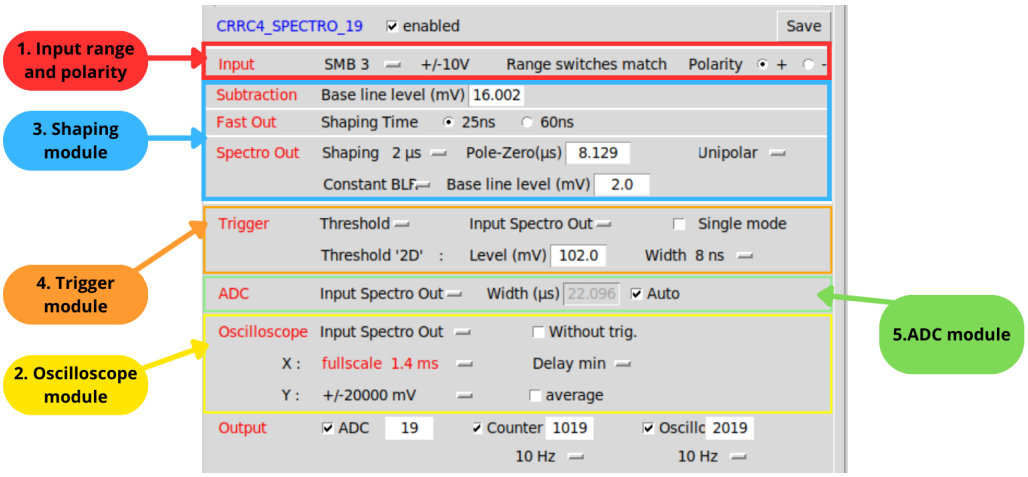

Figure 81: Channels panel for signal processing with the CRRC4 spectroscopy module.

is used to set the signal processing parameters for each entry channel on the FASTER cards. An example is shown on Figure 81 for the CRRC4 spectroscopy mode. It is made of 5 modules :

- *Input range and polarity module :* The input range in Volts can be selected to suit the signal amplitude. The available ranges depend on the kind of daughtercard used and are detailed in section 4.4.1.2. The signal polarity must be adjusted accordingly.

- *Oscilloscope module :* This module manages the FASTER oscilloscope. The X and Y scale (respectively in ms and mV) can be adjusted, the signal can be averaged and an external trigger can be used by checking the "Without trig" box. Otherwise internal trigger is used. The oscilloscope input is also chosen, so the signal can be monitored at different stages of optimization. An example of signal processing sequence is shown below in Figure 82.

- *Shaping module :* This module includes three shapers which operate in parallel. The "Subtraction" module is used to set the baseline to zero. The "Fast Out" module includes the CR-RC4 filter. Two shaping times parameters are available, 25 ns and 60 ns. They correspond to two different high cut-off frequencies. Most of the time the 25 ns shaping time is used, because the timestamp is better than with the 60 ns setting. The third module is the "Spectro Out" module. The shaping time of the signal can be adjusted between 60 ns and 32 µs. There is also the possibility to select whether the signal is unipolar or bipolar, and to adjust the Pole-Zero and the Baseline Restorer. All these parameters have to be adjusted to have a cleaner signal and therefore a better resolution of the spectrum.

Figure 82: Steps of signal processing for optimization with FASTER spectroscopy module, when X-rays from a ^{55}Fe source are recorded. The FASTER oscilloscope is shown at 4 different steps : Raw Signal (1), Subtraction (2), Shaping module (3) and after changing the Shaping time (4).

- *Trigger module :* The trigger module is used to set a trigger level on the signal for the spectrum reconstruction, to eliminate some of the background noise. It is used in the absence of an external trigger.

- *ADC module :* The Analog to Digital Converter module is the one that reconstructs the spectrum, it is possible to choose whether it is reconstructed from the raw signal, or after the signal has been optimized by the shaping module.

Signal processing starts with setting the subtraction level from the raw signal (120V in this case), and checking that the baseline is now closer to 0V. This ensures a more precise reconstruction of the signal, and therefore a better energy resolution. After the baseline is set, the signal after the Spectro Out module is checked (image 3 in Figure 82). In this case we can see that the overshoot is huge, and the shaping time and Pole-Zero need to be adjusted. After adjustment, the signal is checked and the spectrum can be recorded.

4.4.1.4 QDC-TDC module working principle

The QDC-TDC module has been used with the detector for ion spectroscopy depicted in section 4.3.4.1. The functioning principle of some of the modules is rather similar to the one described for the CRRC4 module. The channels panel for the QDC-TDC module when used with the ion spectroscopy detector is presented in Figure 83. Such

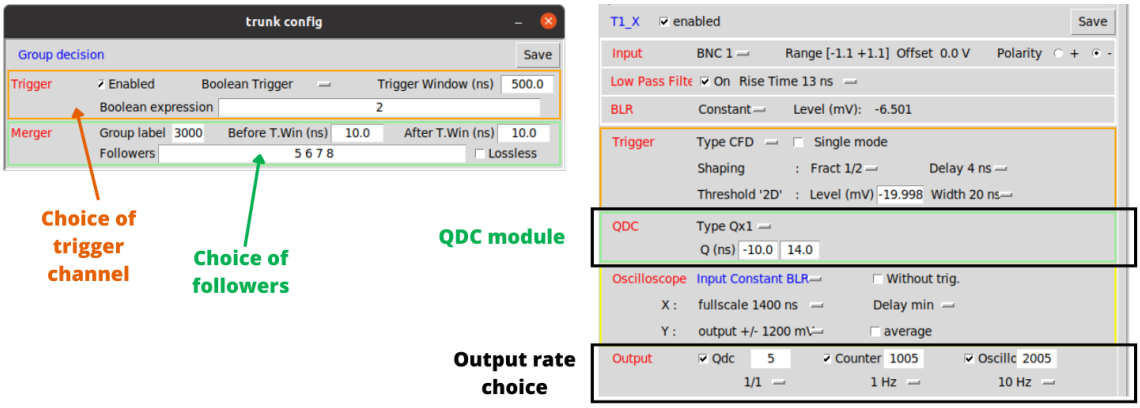

Figure 83: Channels panel for signal processing with the QDC-TDC module.

a detector gives 5 output signals. In the following, the signals are referred to as Tmcp (originating from the MCP), and Ttop, Tbottom, Tleft and Tright (originating from the delay-line anode, see Figure 75). The Tmcp signal is used as a trigger signal for the other 4, signalling when a particle hits the detector. The QDC module computes the charges originating from all 5 signals. One event is therefore composed of 5 signals, and the hit position is reconstituted as illustrated on Figure 84 for the x direction. Since the

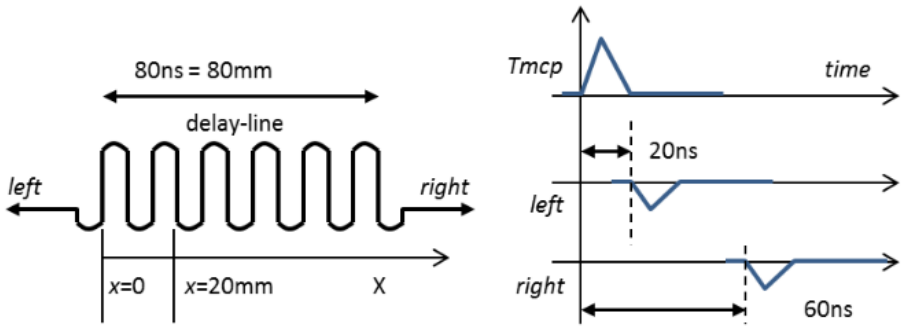

Figure 84: MCP and delay-line signals vs particle position.

arrival time of the particle at a position x is given by Tmcp, the Tleft and Tright pulse time are given by equations (115), where L is the total length of the anode wire and

Tp the time taken by an electric signal to travel a length L.

$$\begin{aligned} \text{Tleft} &= \text{Tp} \times \frac{x}{L} + \text{Tmcp} \\ \text{Tright} &= \text{Tp} \times \frac{L-x}{L} + \text{Tmcp} \end{aligned} \tag{115}$$

The incident particule position can then be estimated as $x = \frac{L}{\text{Tp}} \times (\text{Tp} + \text{Tleft} - \text{Tright})$. The same calculation can be made for the y position of the particule. Data analysis is made in this manner by the RHB and a hitmap is produced (see Figure 79 (d)).
While the RHB hitmap provides a good glimpse at the data, it cannot be used as such contrary to the spectra obtained with CRRC4 measurements. This is due to the fact that even after signal optimization, certain events are recorded with only 4 or even 3 signals instead of 5. Those events, despite being valid, are not being reconstructed by RHB. This leads to a discrepancy between the recorded MCP count rate signal and the count rate reconstructed in the hitmap data, sometimes up to 80% of missing events. No correlation between the ion charge state, the overall count rate of the acquisition time, the energy of the particles and the percentage of missing events have been found. In this case, additional data treatment is necessary. The events with only 4 signals constitute the majority of the "lost" events, and the missing signal arrival time can easily be reconstructed by considering the fact that the delay-line time propagation Tp is constant. Indeed, since $\text{Tleft} + \text{Tright} - 2 \times \text{Tmcp} = \text{Tp}$, it is easy to reconstruct the missing signal from the raw data as pictured in Figure 85.

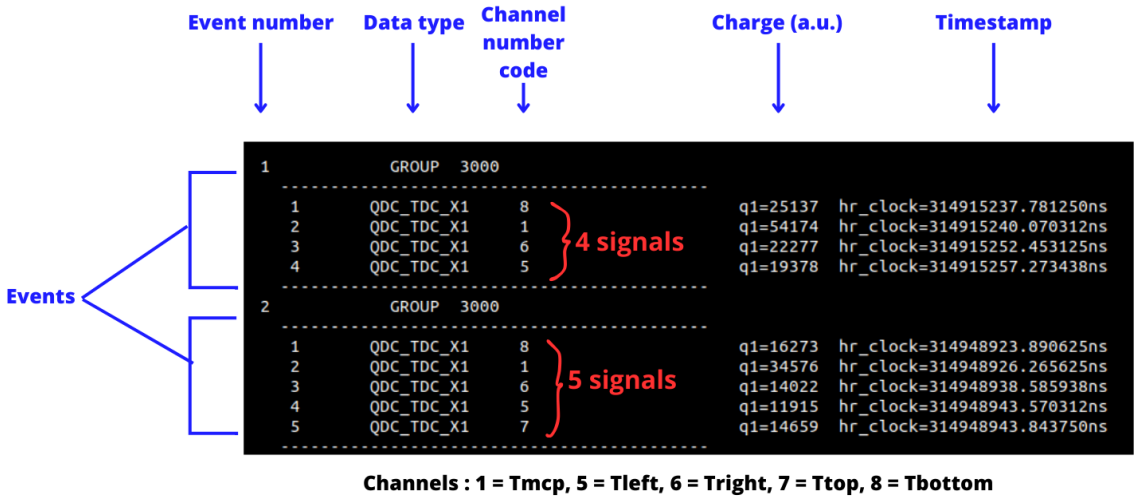

Figure 85: Raw data from a QDC-TDC showing an event with 5 signals and an event with 4 signals.

4.4.2 MAESTRO analog acquisition system

In order to properly characterize the resolution of our X-ray detection system (X-ray detector and FASTER acquisition system), we need to detect the signals with a reference acquisition system. The MAESTRO platform plays this role, since it has been used in the past with the X-ray detectors to determine their resolutions [138]. Maestro is a Multichannel Analyzer Emulation software platform developed by ORTEC [173], specifically designed for spectroscopy applications. Maestro offers a comprehensive suite of tools for

acquiring, analyzing, and visualizing data from various photon detectors. It is possible to adjust acquisition parameters such as acquisition time, detector settings, and trigger conditions through a graphic interface. Real-time monitoring of the acquisition process is possible. In terms of spectral analysis, Maestro provides powerful tools including energy calibration, peak identification, and region-of-interest (ROI) analysis. Visualization of acquired spectra is facilitated through Maestro, with options for displaying data in various formats such as histograms, spectra plots, and peak displays. The software offers tools for zooming, scaling, and overlaying spectra to aid in comparison and interpretation, as shown in Figure 86. Maestro comes equipped with built-in libraries of gamma-ray and X-ray spectra for reference and comparison purposes. Maestro can be easily used with any analog acquisition chain comprising a detector and several digital signal processing modules such as triggers, amplifiers, timing filters... Any analog to digital converter can then be used to feed the signal to a computer with the Maestro software installed. We used Maestro extensively for the calibration and characterization of the MOSAHR card of the FASTER system, with the ORTEC 927 ADC module. This module has a dead time of 2 µs per event and a maximum resolution of 16384 channels. The results are detailed in section 5.2.

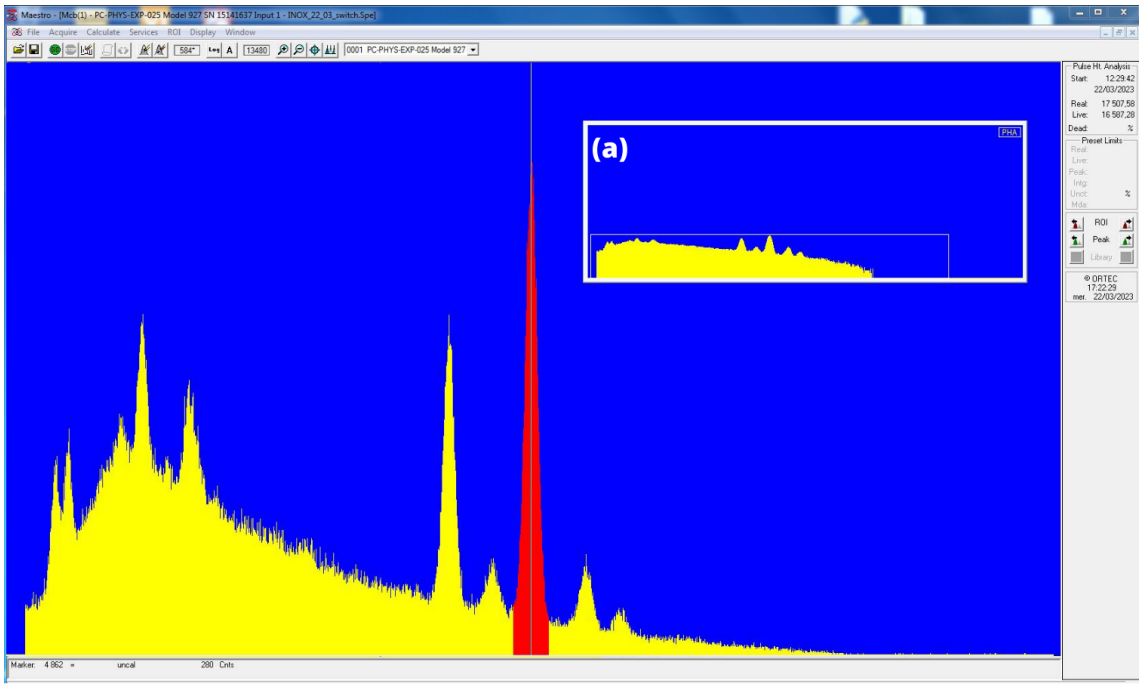

Figure 86: Maestro software window showing an X-ray spectrum of inox obtained with the LANCELOT X-ray detector. Panel (a) shows the full spectrum in logscale and the zoom featuring a selected peak in red is visible on the whole screen.

5 Tests performed on various parts of the experimental setup

To ensure a thorough understanding and precise characterization of each component of the experimental setup, comprehensive testing is essential. The production of C^{6+} ions using the SIMPA source and O^{q+} ions using the FISIC source has been evaluated in the laboratory, with detailed findings presented in the first section. Additionally, the resolution of the LANCELOT X-ray detector combined to the FASTER acquisition system has been measured, see the second section. Furthermore, the ion spectrometer, its associated detector, and the OMEGA charge state purificator have been rigorously tested at the ARIBE facility, with conclusions presented in the third section. These steps are vital to ensure the reliability and performance of the experimental setup.

5.1 Production of C^{6+} and O^{q+}

5.1.1 Production of C^{6+} with SIMPA

5.1.1.1 Motivations

As explained in Section 3.1, carbon ions are prevalent in astrophysical environments, and understanding the interactions between bare carbon ions and interstellar molecules is crucial for advancing our knowledge of interstellar plasmas. Therefore, it was interesting to test the capability of our ion sources to produce carbon ions for future ion-ion and ion-atom collisions, a task that had never been undertaken in our laboratory before. Additionally, carbon ions are employed in hadrontherapy to treat certain types of cancer, as discussed in Section 1.1.1. In this context, we had the opportunity to collaborate with Normandy Hadrontherapy (NHa) in Caen to evaluate the production of C^{6+} with ECR ion sources. The Normandy Hadrontherapy company is currently developing a new particle therapy system involving an isochronous cyclotron, C400 IONS [174], capable of accelerating Q/m=1/2 (charge over mass) ions up to 400 MeV/u. The first unit will be installed at the CYCLHAD hadrontherapy center [175] located in Caen, France and will supply proton, carbon and helium beams both for clinical purposes (cancer treatment) and physics research.
In the current existing facilities for carbon-therapy, C^{4+} or C^{5+} beams are extracted from an ECRIS [176, 177] then accelerated to a few MeV/u, usually by a cyclotron or a linac. Finally, the MeV/u beams are stripped to produce a C^{6+} beam which is then accelerated at the required energy for patient treatment (140-400 MeV/u [178]) by a synchrotron. The layout of three of these facilities, HIT (Heidelberg Ion Beam Therapy, Heidelberg, Germany) [179–182], HIMM (Heavy Ion Medical Machine, Lanzhou, China) [183–185] and GHM (Gunma University Heavy Ion Medical Center, Gunma, Japan) [186–188] is presented in Figure 87. For accelerating the carbon ions to an energy of about 7 MeV/u before stripping and injection into the synchrotron, HIT use a linac composed of a radio frequency quadrupole accelerator (RFQ) and an IH type drift type linac (IH-DTL, Interdigit H-mode Drift Tube Linac) [180, 189], GHM a linac composed also of a RFQ and an alternating phase focusing linac (APF linac) [187], whereas HIMM uses a cyclotron.

C^{4+} or C^{5+} beams are fully stripped using carbon-foil strippers with a thickness of a few tens of $\mu g/cm^2$ [181, 182, 185, 189, 190]. When an ion passes through the foil and

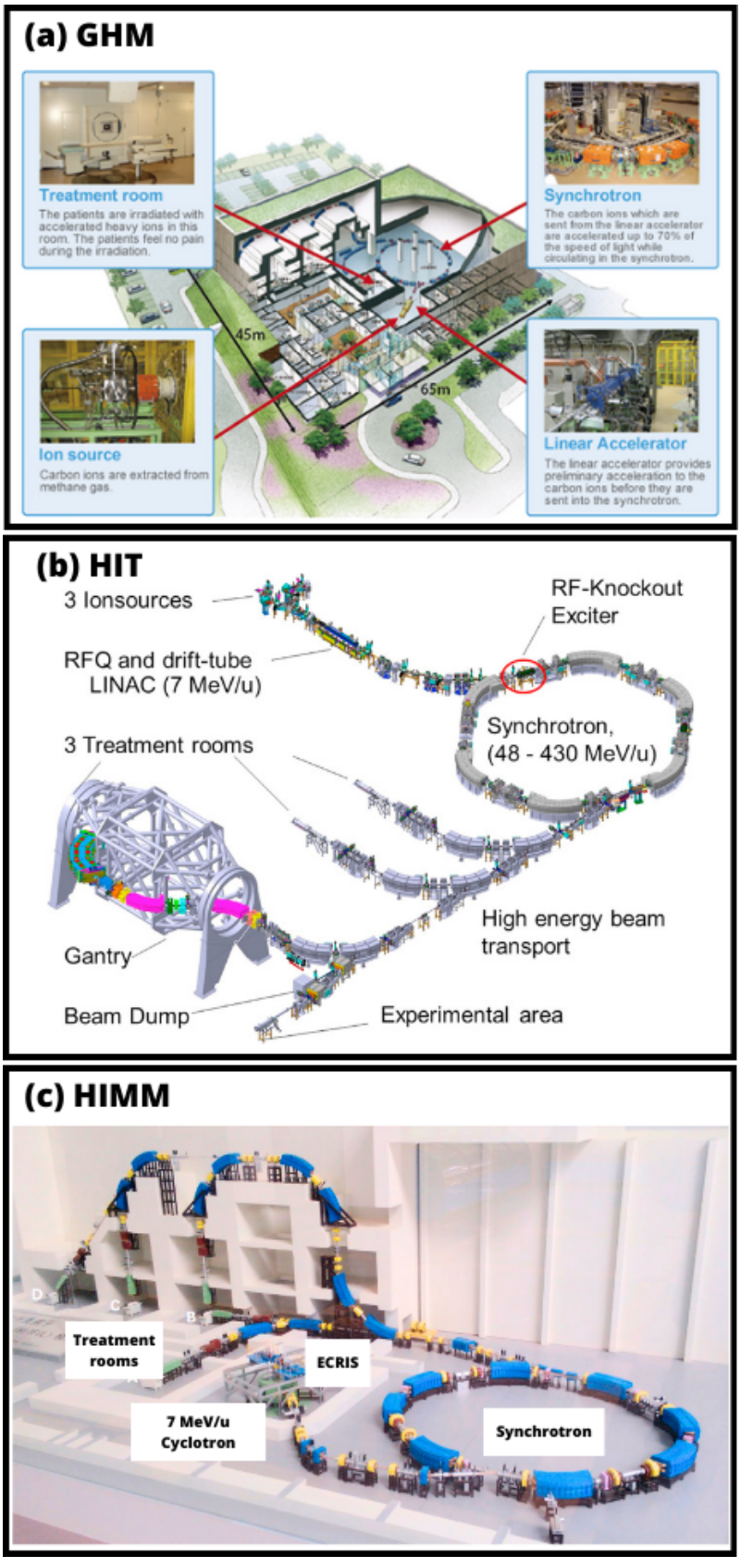

Figure 87: Layout of three carbon-therapy facilities : (a) GHM in Japan [186], (b) HIT in Germany [179], (c) HIMM in China [183].

collides with the atoms of the media, it can either gain or lose electrons. Simulations and calculations have found that the probability that a 7 MeV C^{5+} loses one electron and changes to C^{6+} is comprised between 70% and 90% [185, 191] for a 20 µg/cm^2 foil. The probability for a 6 MeV C^{4+} to strip to C^{6+} with a 60 µg/cm^2 foil [192] is 95%. The losses mainly originate from inelastic collisions with the atomic electrons of the foil and elastic scattering from the nuclei.
Different gas combinations and operation parameters have been tested for the ECRIS used for the HIT, HIMM and GHM facilities, and the optimal performance settings for the production of carbon ion beams are reported in Table 15. In addition to these three ECRIS, a fourth one is also reported. It was tested at the Korean Atomic Energy Research Institute (KAERI) for a prospective carbon facility therapy that has to be constructed.

	HIT			HIMM		GHM			KAERI		
Gas mixing	CH_4/He	CO_2/He		CH_4		CH_4		C_2H_2	CO_2	CH_4	CO_2/He
C^{q+} before stripping	C^{4+}	C^{4+}	C^{4+}	C^{4+}	C^{5+}	C^{4+}	C^{5+}	C^{4+}	C^{4+}	C^{4+}	C^{4+}
C^{q+} intensity (µA)	240	200		300	100	600	142	490	12	5	53
RF frequency (GHz)	14.5	14.5		14.5		10		10	14.5	14.5	14.5
RF power (W)	240	240		270	270	240	300-600	300-600	600	600	450
Ext. voltage (kV)	16	16	24	24	24	30	30	30	15	15	15

Table 15: Main settings for the optimal performance of various ECRIS for different pure gas, or with He as a support gas : HIT (Heidelberg Ion Beam Therapy) [193], KAERI (Korea Atomic Energy Research Institute) [194], HIMM (Heavy Ion Medical Machine) [195] and GHM (Gunma University Heavy Ion Medical Center) [190, 196].

In the case of C400 the carbon beams are accelerated to 400 MeV/u in one step by an isochronous cyclotron. Prior to their acceleration up to 400 MeV/u, C^{6+} ions must be produced, transported and injected into the cyclotron. According to the estimated beam transmission of the different stages of the beam transport system, it was determined that the ion source has to provide a C^{6+} beam current of at least 3-4 µA to fulfill the clinical dose rate requirement at the patient level.
However, generating a C^{6+} beam directly from the ion source, rather than through the stripping of C^{4+} or C^{5+} beams, presents a challenge. The pre-requisite for the validation of the C400 ION system are the following : achieving an intensity of C^{6+} beam of a few µA, a beam purity greater than 99 %, a long term (6h) stability without breakdowns and 98% of usable rate for clinical use.
As already described in section 4.1.3, our facility comprises two SUPERNANOGAN-type Electron Cyclotron Resonance (ECR) ion sources, SIMPA and FISIC that have the main features to fullfill the above requirements. When the production of C^{6+} was tested, only one ion source, SIMPA, was present in the lab, as the FISIC ion source was still under construction. The setup used for testing the C^{6+} production consisted of the SIMPA source connected to the FISIC beamline as presented in Figure 88. In the following, the motivations behind the choice of gas (5.1.1.2) and the results (5.1.1.3) are presented.

5.1.1.2 Choice of gas

The choice of gases to produce the plasma and ultimately extract the carbon beams is crucial to optimize current yield, as reported during the commissioning phase of the

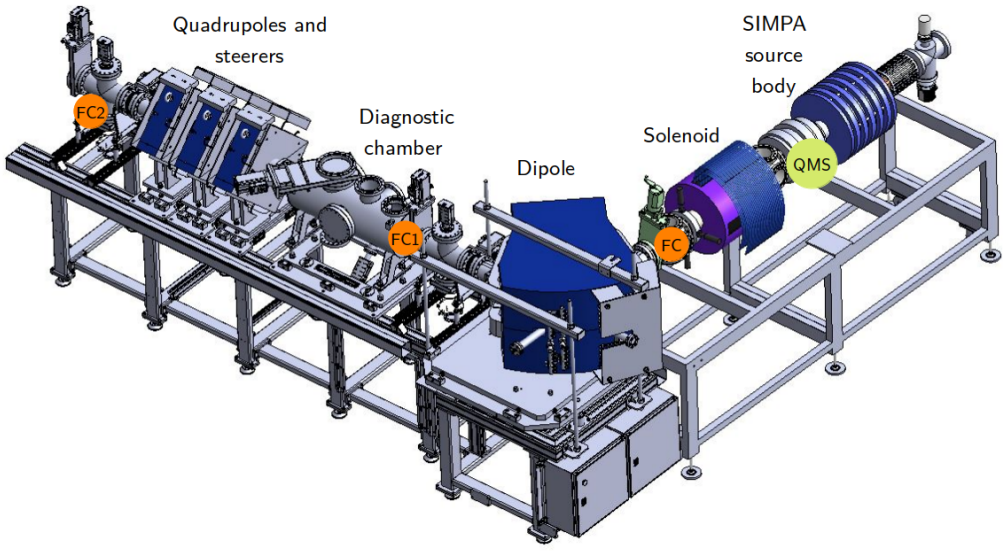

Figure 88: The SIMPA ion source connected to the FISIC beamline.

previously mentioned facilities. Isotopic gases are relevant since the magnetic dipole selects the charge states based on their Q/m ratio. $^{12}C^{6+}$ has a Q/m ratio of 1/2, making it indistinguishable from other ions with the same ratio that are inevitably present in the plasma. In Table 16 different Q/m ratio for He, C, N and O ions are reported. Since water and nitrogen are often present as contaminants, the 1/2 ratio may include

Charge state	Q/m	B (Gauss)
O^{3+}	0.19	1025.6
$^{13}C^{3+}$	0.23	932.2
He^{+}, $^{12}C^{3+}$, O^{4+}	0.25	894.1
N^{4+}	0.29	830.2
$^{13}C^{4+}$, O^{5+}	0.31	802.9
$^{12}C^{4+}$	0.33	778.2
N^{5+}	0.36	745.1
$^{13}C^{5+}$, O^{6+}	0.38	725.2
$^{12}C^{5+}$	0.42	689.8
N^{6+}, O^{7+}	0.43	681.7
$^{13}\mathbf{C}^{6+}$	**0.46**	**659.1**
$\mathbf{He}^{2+}$, $^{12}\mathbf{C}^{6+}$, $\mathbf{N}^{7+}$, $\mathbf{O}^{8+}$, $(\mathbf{H_2})^{+}$	**0.50**	**632.2**
H^{+}	1.00	447.1

Table 16: Q/m for different charge states of the main gases present in the plasma, as well as the corresponding B value (in Gauss) for our dipole. Some charge states with very close Q/m are put together under a mean value of their Q/m because the resolution of our scan does not allow their separation.

several ion species ($^{12}C^{6+}$, O^{8+}, N^{7+}, $^{4}He^{2+}$). However, our magnetic dipole resolution ($\sim$ 10 Gauss at 660 Gauss) is sufficiently good to unequivocally isolate the $^{13}C^{6+}$ charge state. As a result, in our study, $^{13}CO_2$ and $^{13}CH_4$, which are isotopic gases, have been used. We also tested carbon ion production with $^{12}C_2H_2$ for which we did not have an

isotopic version. These three gases have been the most frequently chosen as mentioned in the previous section. In addition to the main gas, a "support" gas can be used. It helps to produce multicharged ions with higher charge states by providing more electrons to the plasma. These additional electrons increase the ionization probability to obtain multi-charged ions and stabilize the plasma by reducing the temperature of the ions issued from the main gas via collisions with lighter ions from the support gas. We used He as a support gas for CO_2. The use of O_2 as a support gas for CH_4 has been reported previously, but did not yield the best results. However, since we are accustomed to using O_2 with the SIMPA source, we have decided to test the $CH_4 + O_2$ combination. The main dissociation channel for the three gases are [197]

- $C_2H_2 + e^- \rightarrow C_2^+ + H_2$
- $CH_4 + e^- \rightarrow C^+ + 2H_2$
- $CO_2 + e^- \rightarrow C + O + O^+$

As a result, H_2 molecules and oxygen atoms are produced, playing also the role of a support gas. In order to produce carbon ions, the ignition process is the production of C^+ ions by electron impact ionization. The electron impact ionization rate W_{EI} can be written in this general form as

$$W_{EI}(s^{-1}) = n_e(m^{-3}) \times \sigma_{EI}(m^2) \times V_e(m.s^{-1}) \tag{116}$$

where n_e is the electronic density, V_e the velocity of the electrons and σ_{EI} the electron impact ionization cross section. Figure 89 shows the cross sections for the total production of C^+ for the three different main gases as a function of the energy of the electrons. The three curves exhibit a cut-off for electron energies below 30 eV, and a maximum reached around 100 eV for all three gases. We can see that the CO_2 gas is the one that has the highest cross sections for C^+ production, and that the cross sections for CH_4 are notably below the other two gases. Consequently the highest carbon ion currents are expected for CO_2.

For C400 IONS, a beam with $Q/m = 1/2$ is required, but our results obtained for $^{13}C^{6+}$ can be extrapolated to $^{12}C^{6+}$ since both isotopes have the same ionization energy. However, a cleaner beam must be achieved by substantially reducing the contaminants. It would be also necessary to substitute ^{4}He to ^{3}He as a support gas in order to separate the $^{12}C^{6+}$ peak from the He^{2+} peak.

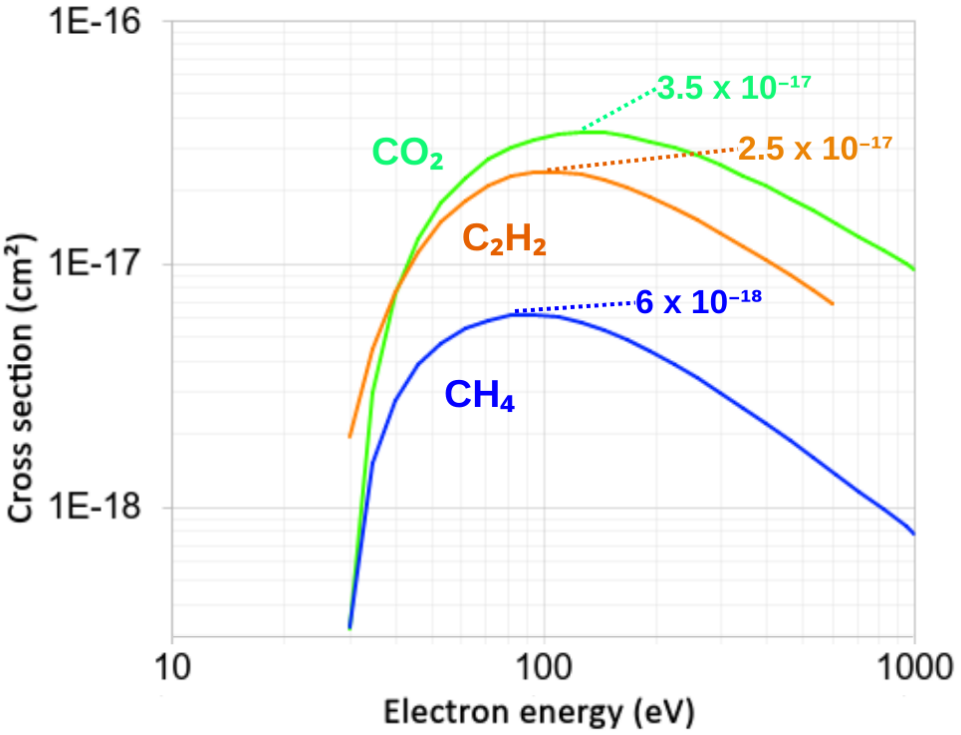

Figure 89: Cross sections for the total production of C^+ by electron impact for the three main gases used in the study [197, 198].

5.1.1.3 Results and discussion

A usual method for optimization of a given charge state is the optimization of lower charge states of the same ion species until the desired charge state can be detected by FC1 (see Figure 88). Therefore as a first step towards the optimization of C^{6+} beam current, C^{3+} was optimized to reach a current of about 20 µA before tuning the dipole to select the C^{6+} or C^{5+} charge state, depending on whether isotopic or regular carbon molecules are injected. Figure 90 shows the evolution of the ionization potential as a function of the final charge state q of the ion. For the C^{3+} charge state (with the electronic configuration $1s^2 2s^1$), the ionization potential of the electron remaining in the L shell is 64.5 eV. To strip the ion above the C^{4+} charge state, one must ionize the K shell. The ionization potential of the first electron in the K shell is 392 eV. Ionizing this shell requires hotter electrons in the plasma, which can be achieved by increasing the RF power, and adjusting the other source parameters consequently (in particular the bias voltage).
For each gas combination, Table 17 summarizes the maximal current output and the corresponding optimal parameters of the source (RF power, primary gas pressure at injection, and polarization electrode voltage (Bias)). Figures 91 and 92 exhibit the extracted current as a function of the dipole magnetic field obtained for the three different gases, and the comparison with and without support gas when one was used. Figure 92 is a zoom around the region of interest for each plot. It is worth noting when optimizing the current of a chosen charge state, the solenoid magnetic field is manually adjusted to maximize the measured current. During dipole sweep the solenoid value is then not changed. As a result, only the current of the intended charge state and neighbouring Q/m is optimal on the charge state distribution spectra, and the other peaks are enlarged.

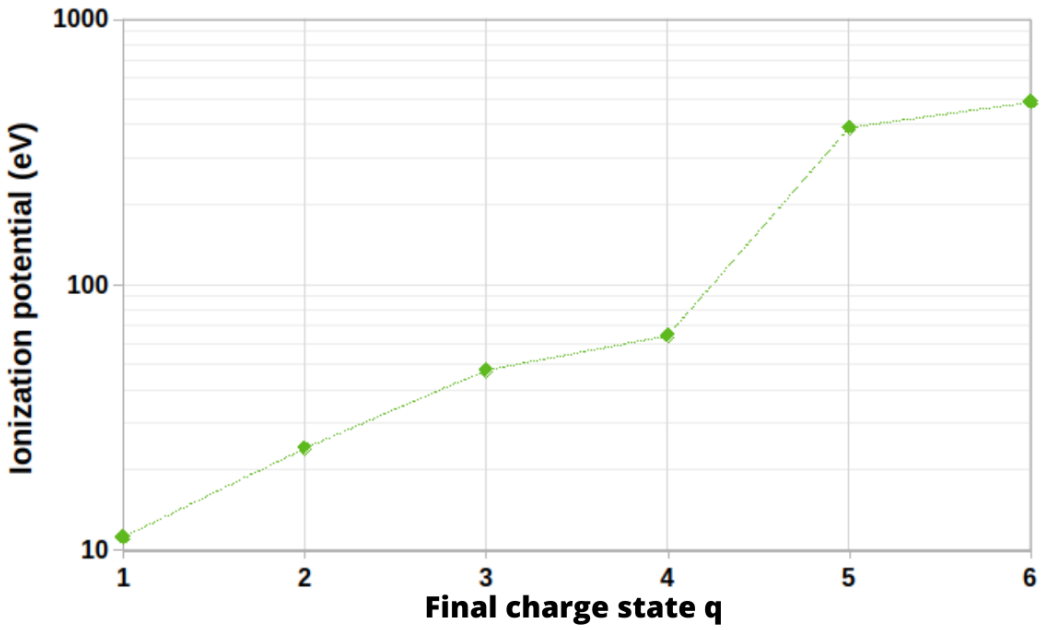

Figure 90: Ionization potential for carbon ions [199].

Gas	I($^{13}C^{6+}$) (µA)	P RF (W)	P_{inj} (mbar)	Bias(V)
$^{12}C_2H_2$	5.4 ($^{12}C^{5+}$)	100	5×10^{-5}	174
$^{13}CH_4$	2.3	106	6.7×10^{-5}	220
$^{13}CH_4$ + O_2	1.9	107	-	220
$^{13}CO_2$	1.1	130	5.1×10^{-5}	161
$^{13}CO_2$ + He	2.7	150	5.8×10^{-5}	137

Table 17: Measured currents extracted from SIMPA and source parameters for the different gas combinations.

On Figures 91 and 92, besides the peaks corresponding to the species present in the main and support gases (C, O, H, He, H_2), other peaks are visible, mainly nitrogen (labeled in red on the plots) and oxygen. Outgassing decreases gradually with operation time hence we can see the intensity of the nitrogen peaks diminishing from the plot (a) to the plot (c). In plot (b), the oxygen peaks come from dioxygen that was used as a support gas, but in plots (a) and (c) the oxygen peaks come from the water contaminant.

- For the case of C_2H_2 only $^{12}C^{5+}$ can be measured since $^{12}C^{6+}$ is drowned among other ion species. The measure is not very conclusive since the plasma presented a lot of instabilities. Nitrogen is also highly present as a polluant since the source was opened just prior to the experiments, which prevents us from drawing conclusions regarding the possible $^{12}C^{6+}$ current yield with this gas.

- For the CH_4 gas we remark that when O_2 is added as a support gas in a proportion of 1:3 no improvement is noticed in the current of the $^{13}C^{6+}$ peak, in fact the addition of support gas diminishes the maximum current observed (see Figure 92). Moreover instabilities in the plasma appear. Indeed the other facilities that had

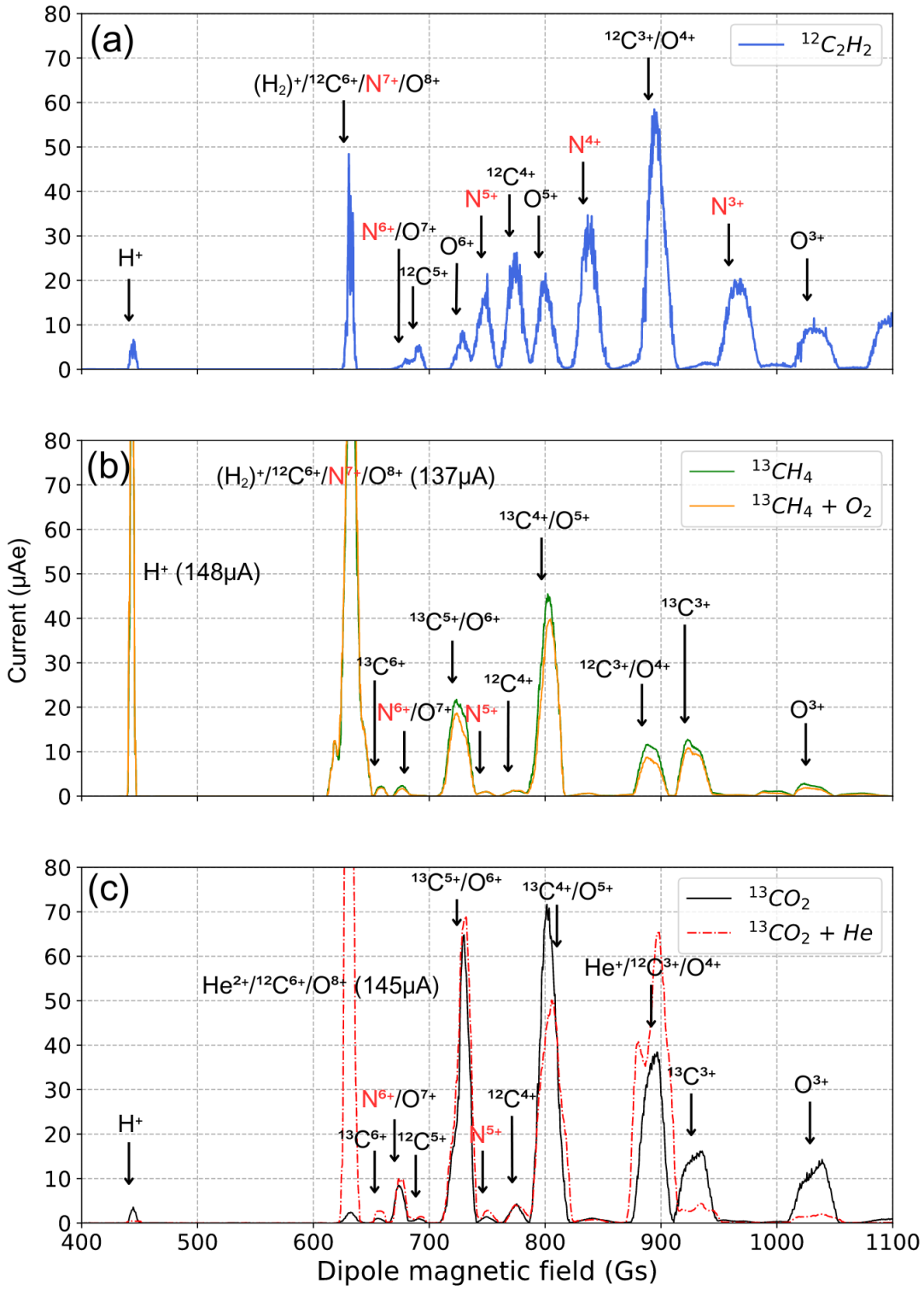

Figure 91: Measured currents extracted from SIMPA as a function of the dipole magnetic field for (a) C_2H_2, (b) CH_4, and (c) CO_2. The charge state(s) corresponding to each peak are indicated. When the peak is not entirely visible, its current is reported in parenthesis.

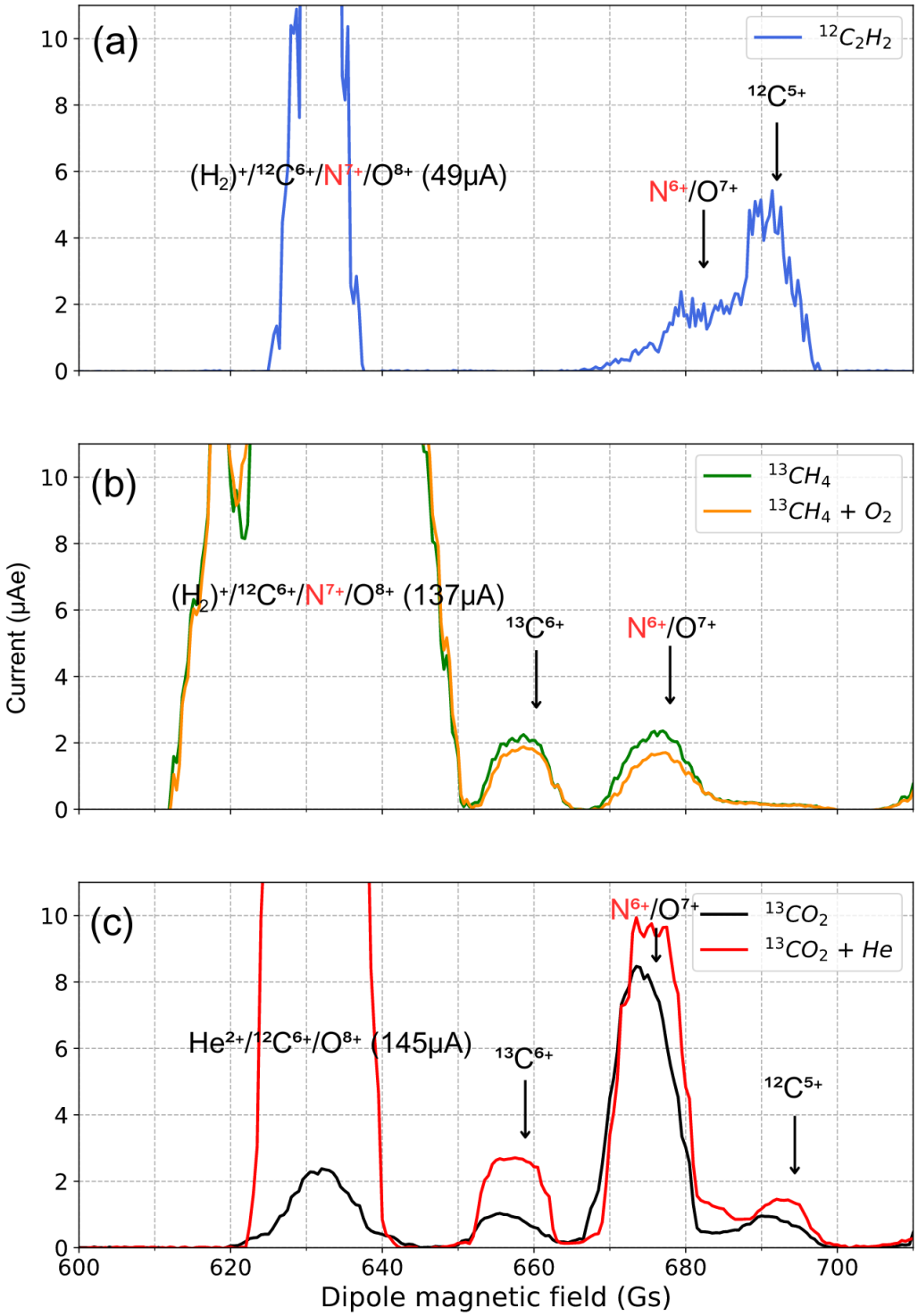

Figure 92: Measured currents extracted from SIMPA as a function of the dipole magnetic field (a) C_2H_2, (b) CH_4, and (c) CO_2, zoomed to the area of interest corresponding to the $^{12}C^{5+}$ and $^{13}C^{6+}$ peaks. When the peak is not entirely visible, its current is reported in parenthesis.

optimal results with CH_4 gas did not use any support gas (see Table 15).

- The last combination tested was $^{13}CO_2$ with and without helium as a support gas. We found that the addition of the support gas allowed to nearly triple the current yield for the $^{13}C^{6+}$ peak, as shown in Table 17 and Figure 92 (c). The fact that the highest current is obtained with CO_2 gas is coherent with the total C^+ production cross section shown in Figure 89. A measure of stability of the source was conducted and revealed a stability of the order of 1% for an acquisition time of 15 minutes. However the current from the $Q/m = 1/2$ peak is greatly enhanced by the addition of the support gas that forms He^{2+} ions, resulting in a total current too important to be injected in C400. The use of ^{3}He instead of ^{4}He gas could substantially reduce the magnitude of the $Q/m = 1/2$ peak and should be seriously considered, despite its unit cost than can exceed 10 times the cost of other gases.

For SIMPA the most efficient gas combination is $^{13}CO_2$ +He, and a $^{13}C^{6+}$ current of 2.7 µA was obtained after 1 day of use for an RF power of 150 W. Despite having proven that C^{6+} could be produced in our lab with sufficient intensities for use in ion-ion experiments, it was decided not to proceed with carbon ions. The clean-up time of the ion source after ion production was greater than anticipated (of the order of several weeks of continuous exploitation) and is not compatible with the general needs for ion production, which for example include frequent changes between argon and oxygen ions production.
However, the conducted tests have lead to the conclusion that a source system based on the SuperNanogan design should be able to achieve the required levels of carbon ion production, specifically C^{6+}, as mandated by the C400 facility. The aspired threshold is a beam current of 3-4 µA, a level that was almost reached with this setup. We are confident that with a longer runtime, such a current can be achieved. The requirement for the stability of the source is 2.5% for over 6 hours. However we did not perform stability measurements over runtimes this long. Overall even though the requirements for current and stability were not met during our week-long trial, we are confident that this benchmark can be reached with a similar setup that would be both more recent and dedicated only to the production of carbon beams.

5.1.2 Production of O^{q+} with FISIC

For the needs of the ion-ion and ion-atom collisions experiments, highly charged ions must be produced. Since it was observed that even though the SIMPA source is capable of producing enough C^{6+} ions for the experiments, it is not reasonable to use carbon ions because of source pollution considerations. Argon ions have been produced regularly with both SIMPA and FISIC sources (see section 4.1.3) but very high charge states are hard to obtain and necessitate very long runtimes. As a result, it was decided to use oxygen ions for collision experiments. The results presented in the following have been obtained with the FISIC ion source connected to the FISIC beamline (see descriptions in sections 4.1.3 and 4.2.2) in June-July 2024.

The ionization cross sections by electron impact for oxygen are presented in Figure 93, and the ionization potential as a function of the final charge state is shown in Figure 94. To generate low charge states, as shown in Figure 93, electrons with energies ranging from 10-30 eV are required. However, to produce higher charge states, such as O^{7+}

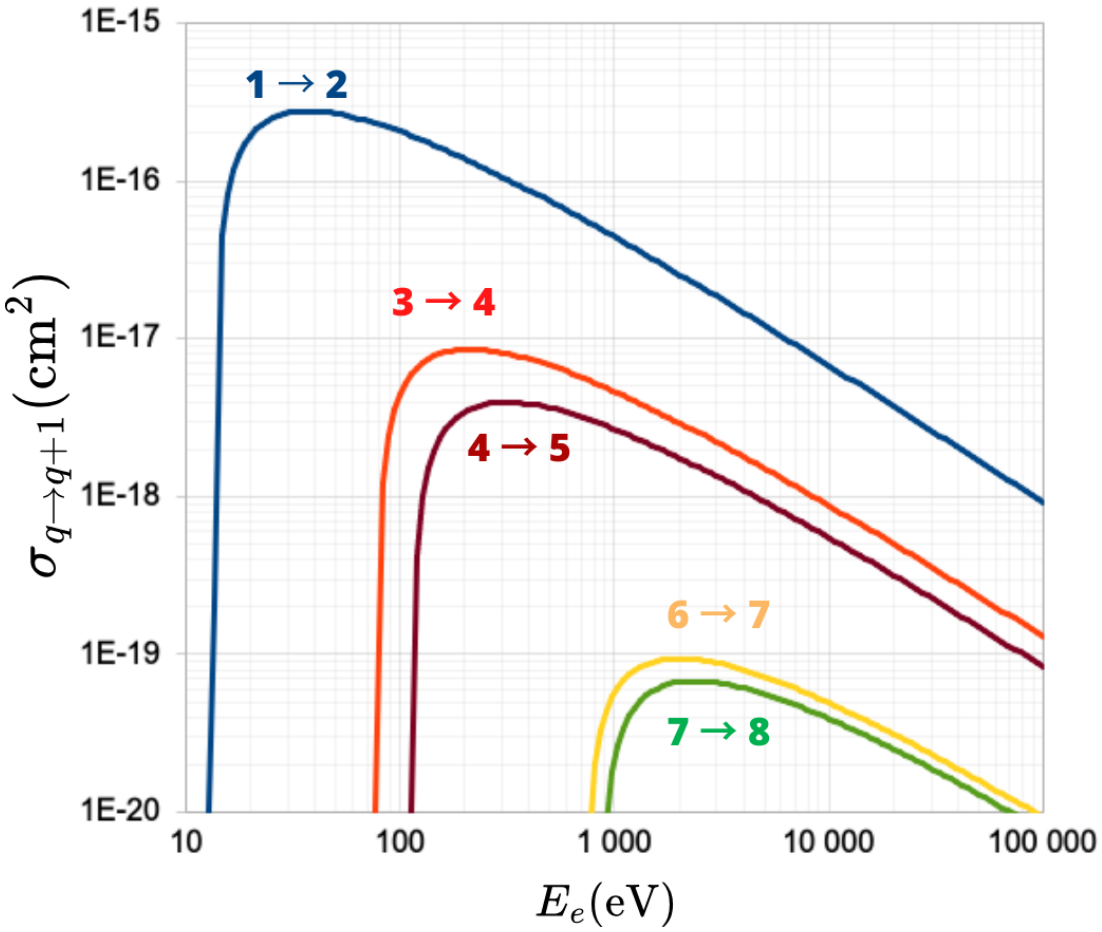

Figure 93: Cross sections for ionization by electron impact of oxygen as a function of the electron energy. Curves were computed with the Müller formula [135].

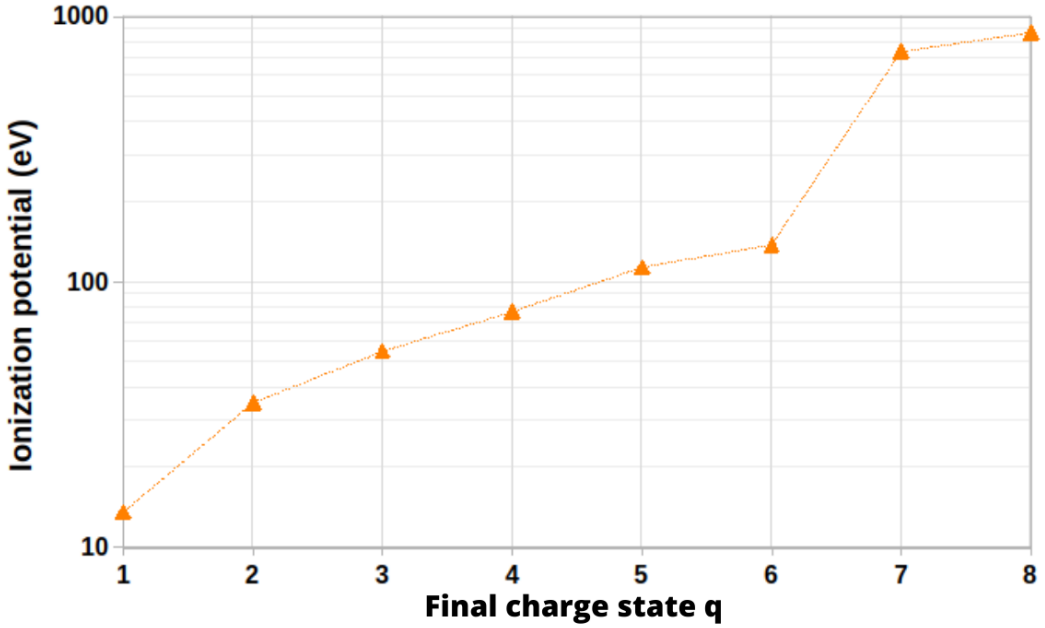

Figure 94: Ionization potential for oxygen ions [200].

or O^{8+}, the electron energy in the plasma must be raised above 1 keV. Additionally,

since the cross section for producing O^{8+} is more than three orders of magnitude smaller than that for O^{2+}, a greater quantity of electrons is necessary in the plasma. This is achieved, among other methods, by increasing the bias voltage. As visible on Figure 94, for producing charge states 7+ and 8+, the K shell needs to be ionized, and the ionization potential of K shell electrons is comprised between 700 and 900 eV, when the last L-shell electron has an ionization potential of 138 eV. For this reason, most of the time, optimization of the oxygen ion beam starts by optimizing the O^{6+} charge states, and then moves on to higher charge states. After only a few weeks of operation we were able to optimize the O^{7+} charge state directly after source start up. Beams of O^{7+} and O^{8+} have been obtained on multiple occasions. A good beam stability over several hours was reached, and a good reproductibility in terms of extraction and beamline parameters was observed over the course of a few weeks. A transmission of 100% was reached up to the collision chamber, with the ion beam passing through the FISIC beamline and OMEGA charge state purificator prior to reaching the collision chamber. On Figure 95, two charge state spectra are presented, both obtained with the FISIC source when the O^{7+} charge state is optimized. Spectrum (b) was taken three weeks after spectrum (a), with nearly daily operation during that time. Between the two, it can be noticed that the charge state distribution was shifted towards higher charge states. Around 1 µA of O^{8+} was obtained after optimization. The source parameters for the two spectra presented in Figure 95 are reported in Table 18.

	Figure 95 (a)	Figure 95 (b)
O^{7+} current (µA)	1	5.6
P_{RF}(W)	71.2	116
F_{RF}(GHz)	13.888	13.888
Main gas (O)	58 %	57%
Injection (mbar)	2.88×10^{-5}	1.71×10^{-5}
V_{BIAS}(V)	200	280
Puller(V)	−60	−200
Focus(V)	350	310
Quadrupole(A)	2.0	3.0

Table 18: Optimization parameters of the ion sources for generating an O^{7+} beam with a 10 kV extraction voltage, for the two spectra of Figure 95.

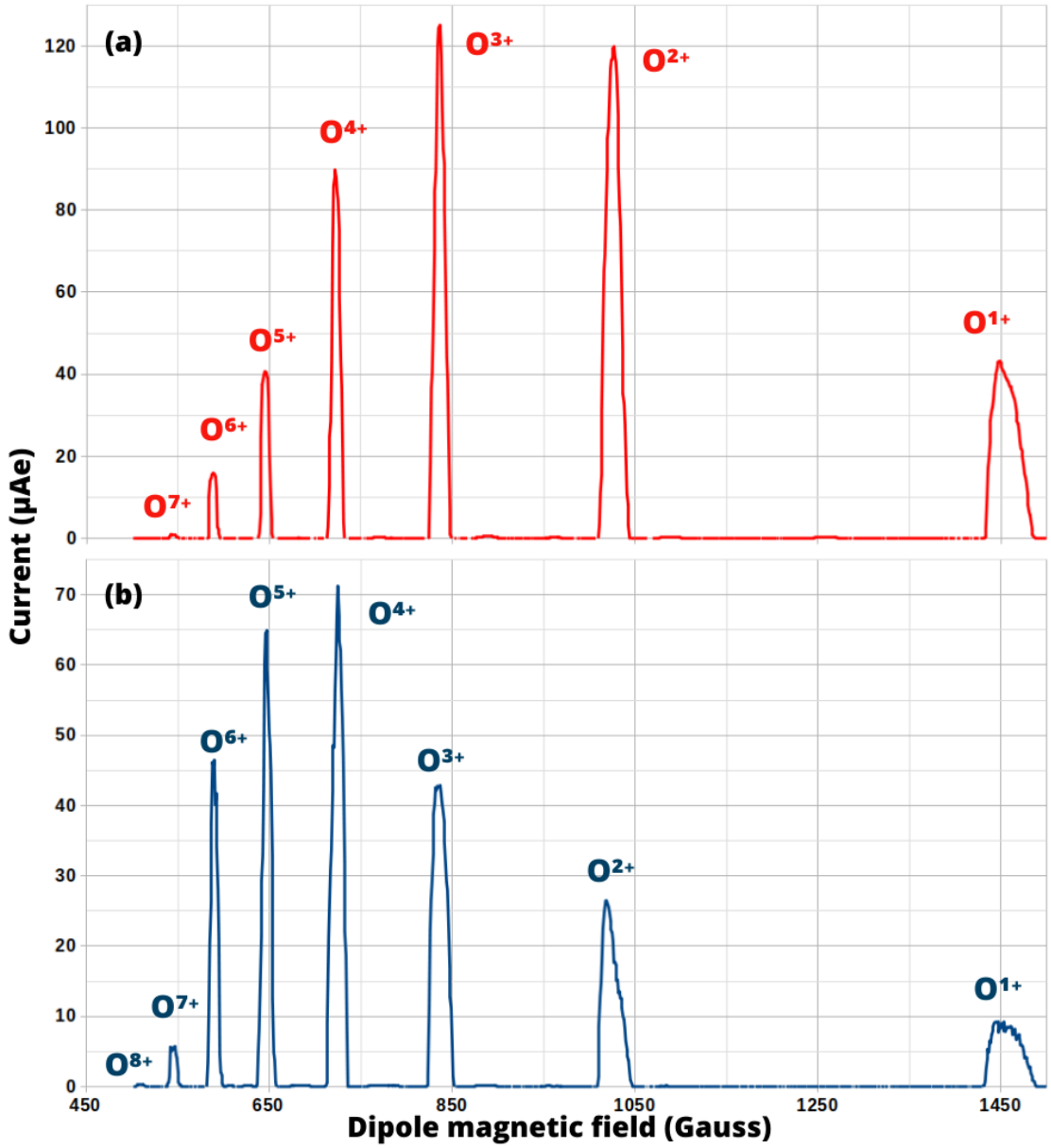

Figure 95: Currents of oxygen ion beams obtained with the FISIC source when the O^{7+} charge state is optimized. Spectrum (a) was obtained after a few days of operation with an O^{7+} current of 1 µA, and spectrum (b) was obtained three weeks later with an O^{7+} current of 5.6 µA.

5.2 Characterization of the X-ray detection setup

5.2.1 Objectives

The resolution of a SSD detector can be separated in two contributions: one from the acquisition chain, and a second one intrinsic to the detector itself, governed by the crystal size, cooling type, and preamplifier. It is important to measure the resolution of the detection system to know if it will be suitable for measuring low-energy X-rays less than 1 keV from transitions expected when performing collisions with oxygen ions for instance. The resolution of LANCELOT itself has been measured in a previous thesis and has proved to be satisfactory [138]. However, these measurements were made using an all analog acquisition chain called Maestro (see section 4.4.2), and we aim to determine if

the same resolution can be achieved with the digital setup FASTER (see section 4.4.1). To investigate this, we employ two different setups: one with GALA and FASTER, and another with LANCELOT and FASTER. We still need the ORTEC amplifier even with FASTER because the signal from the preamplifier have an amplitude in the mV range which is not high enough for FASTER. The setup with GALA was tested with X-rays from radioactive sources of ^{55}Fe and ^{241}Am, and the LANCELOT setup with X-rays obtained by inner shell vacancy produced by keV electron impact.
Additionally, as presented in section 4.4.1.2, we initially had only one acquisition card (CARAS) and specifically purchased another card (MOSAHR) for spectroscopy measurements. Tests made to compare between the two cards will be presented first, followed by the tests with GALA and LANCELOT and the measurement of LANCELOT's resolution under experimental conditions similar to the ones expected during ion-ion experiments.

5.2.2 Comparison between CARAS and MOSAHR

In section 4.4.1.2, we have explained the specificities of the two daughterboards and their respective purposes. To further illustrate these differences, we have recorded three X-ray spectra obtained with a $NaNO_3$ sample shown on Figure 96 : one with the MOSAHR daughterboard dedicated to X-ray spectroscopy and two with the CARAS daughterboard. For the spectra recorded with CARAS we used two settings of the ORTEC amplifier gain : 1k like for the MOSAHR daughterboard and 100 to have a signal of smaller amplitude. The parameters of the ORTEC amplifier and FASTER system for the spectrum obtained

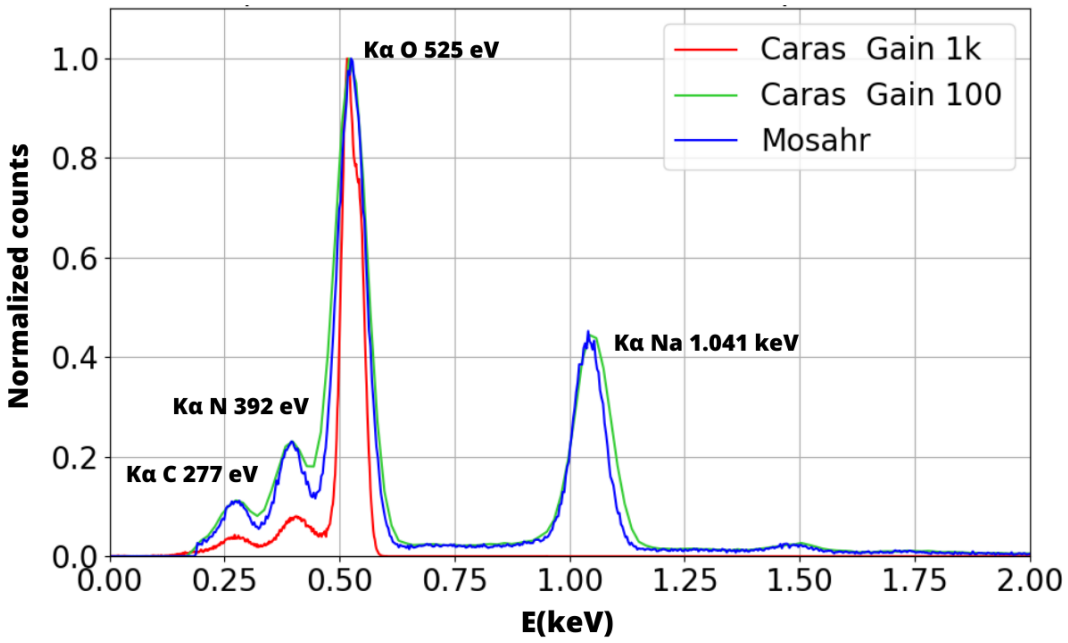

Figure 96: X-ray spectra obtained when 10 keV electrons hit the $NaNO_3$ target in parallel with the MOSAHR and CARAS daughterboards of FASTER for an acquisition time of 10 minutes.

with the MOSAHR daughterboard are the same as the ones described above in Table 22. Since the CARAS daughterboard can only take signals of an amplitude inferior to 2.3 V, the amplitude of the signal amplified with the 1k gain was too high and the spectrum is cut above 0.6 keV, explaining why the K_αNa peak is not visible. Moreover counts at lower energies are lost with the 1k gain, as shown by the ratio $K_\alpha N/K_\alpha O$ which is

very different from the two other curves. The spectrum reconstructed from the signal amplified with the 100 gain is complete but its resolution is deteriorated compared to the one with the MOSAHR daughterboard. This illustrates the necessity of two different daughterboards for the ion and X-ray spectroscopy.

5.2.3 Tests using GALA

As shown on Figure 97, a radioactive source is placed in front of the GALA detector. The signal from the detector pre-amplifier is then fed to an analog amplifier ORTEC 572, before being duplicated. One of the amplified signals passes through an external ADC module ORTEC 927 and is then sent to the Maestro acquisition system, while the other amplified signal is directly sent to the FASTER detection system. Table 19 gives the energies of the main transitions for the two radioactive sources.

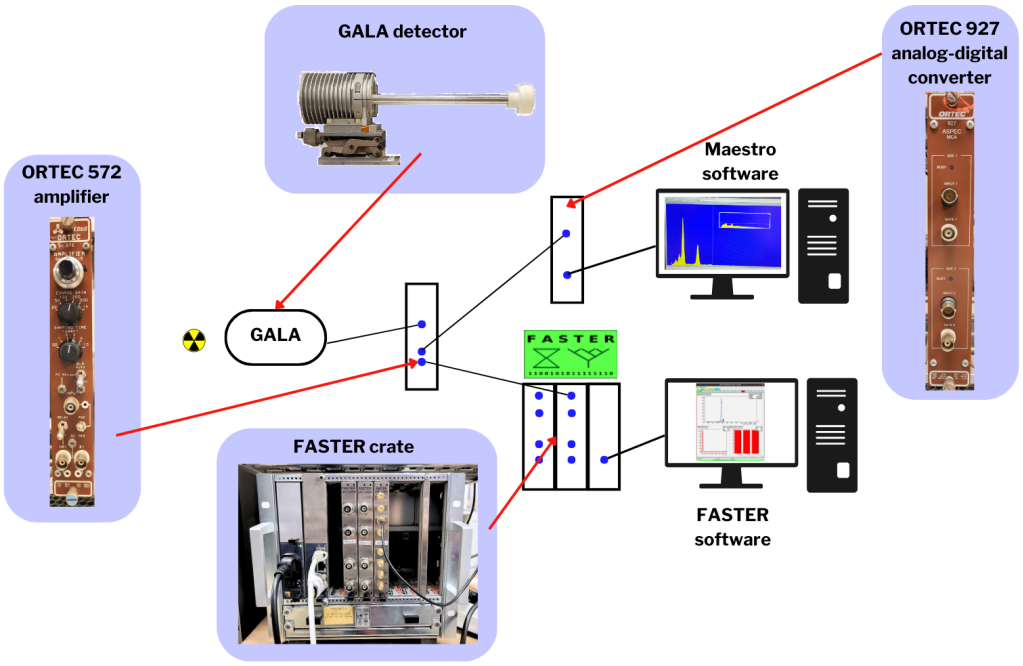

Figure 97: Set up used to compare the Maestro and FASTER acquisition systems with GALA.

Radioactive source	^{55}Fe		^{241}Am		
X-ray	K_α Mn	K_β Mn	L_α Np	L_β Np	L_γ Np
Energy (keV)	5.89	6.50	13.9	17.8	20.8

Table 19: X-ray energies from the radioactive sources used ([201]) with the setup described in Figure 97.

For each spectrum, the gain and shaping time are first set on the ORTEC amplifier and the shape and amplitude of the signal are checked using an external oscilloscope. The channel of the MOSAHR daughterboard of the FASTER system is then chosen accordingly depending on the amplitude of the amplified signal. The gain used on the ORTEC amplifier as well as the baseline and the shaping time on the FASTER software

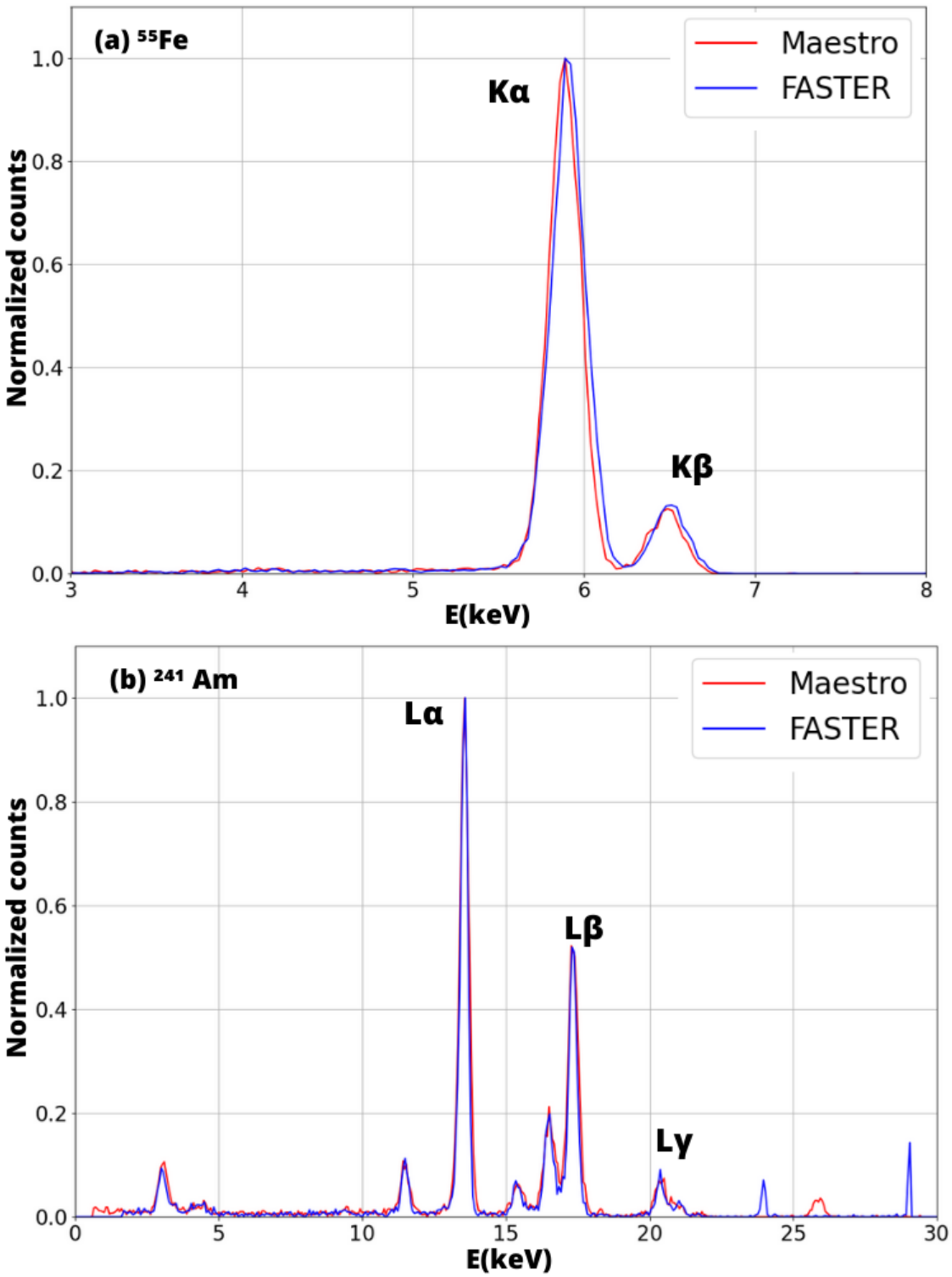

Figure 98: X-ray spectra obtained with GALA for (a) ^{55}Fe and (b) ^{241}Am sources in parallel with Maestro and FASTER with an acquisition time of 10 minutes.

are specified in Table 20. The necessity to use different shaping times for ^{55}Fe and ^{241}Am comes from the fact that the X-ray energies are lower for the ^{55}Fe source. For both sources the most appropriate channel on the MOSAHR daughterboard was the $\pm 10\,\mathrm{V}$ channel. As can be seen on Figure 98, the resolution of the spectra obtained

Parameter	^{55}Fe	^{241}Am
ORTEC Gain	50	20
FASTER Shaping time (µs)	2	2
FASTER Baseline (mV)	-50	100

Table 20: Main settings of the ORTEC amplifier and the FASTER acquisition system used for the ^{55}Fe and ^{241}Am sources.

with the Maestro and FASTER acquisition systems are very similar, ranging from 230 eV at 6 keV to 590 eV at 18 kev. This study has allowed us to gain a better understanding of the parameters of the FASTER acquisition system while using convenient X-ray sources (very low background noise, well-defined peaks). The next step is to perform resolution measurements with the LANCELOT detector and FASTER to fully characterize the X-ray detection system.

5.2.4 Tests using LANCELOT

The electronics chain used to test the LANCELOT detector with FASTER, shown on Figure 99 is very similar to the one used for GALA, except that the origin of the X-rays is not a radioactive source. Indeed, LANCELOT is a detector that cannot work at atmospheric pressure because of its polymer window. Instead we used an electron gun and solid targets to produce X-rays. A solid target in the form of a metal foil or crystal is placed in a sample holder in a vacuum chamber at $\sim 1 \times 10^{-7}\mathrm{mbar}$. An electron gun is positioned facing it, and the X-ray detector is placed at a 30° angle relative to the electron beam. When the electrons collide with the atoms of the target, vacancies in the inner electronic shells (K and/or L shells) may appear. These excited states de-excite by emitting X-rays, which are detected by LANCELOT. The X-ray energies from the targets used (Scandium, Vanadium and $NaNO_3$) are given in Table 21. The energy of the K_α transition from the carbon is also given in this table. This is because carbon is present as a polluant on the $NaNO_3$ target and this transition can therefore be seen on the spectrum.

	Scandium		Vanadium		$NaNO_3$ crystal			
X-ray	K_α	K_β	K_α	K_β	K_α C	K_α N	K_α O	K_α Na
Energy (keV)	4.09	4.46	4.95	5.42	0.277	0.392	0.525	1.04

Table 21: Typical X-ray energies [202] from the solid targets employed.

As described in the previous section the optimal channel of the MOSAHR daughterboard is chosen depending on the amplitude of the signal. Here for all three targets the

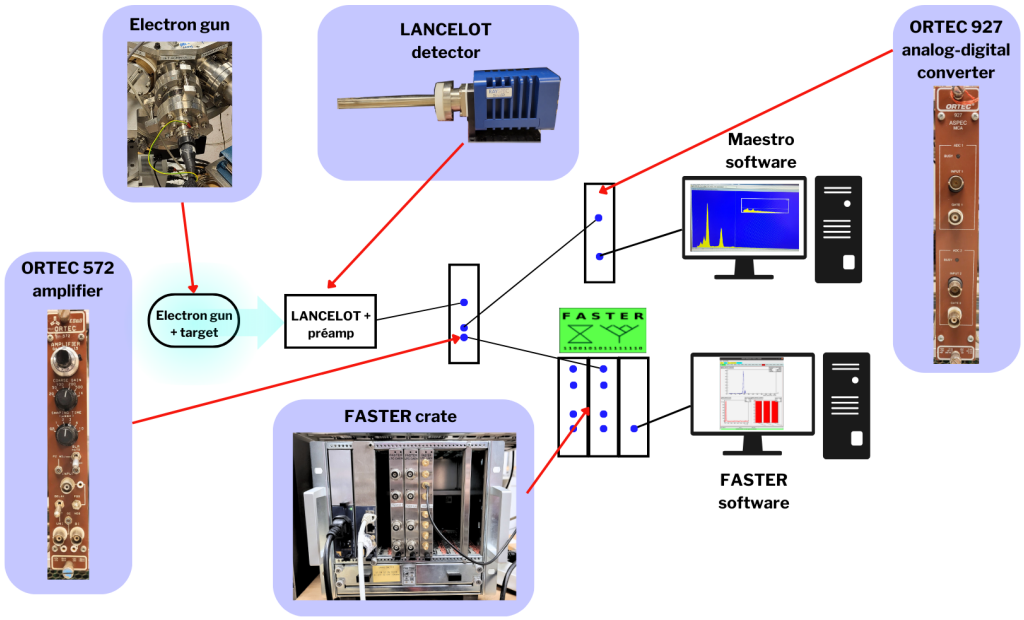

Figure 99: Set up used to compare the Maestro and FASTER acquisition systems with LANCELOT.

$\pm 10\,\mathrm{V}$ channel is chosen. The gain and shaping time used on the ORTEC amplifier as well as the baseline and the shaping time on the FASTER software are specified for each spectrum in Table. 22.

Parameter	Scandium	Vanadium	$NaNO_3$
ORTEC Gain	500	500	1000
FASTER Shaping time (µs)	4	4	2
FASTER Baseline (mV)	0.816	0.816	16

Table 22: Main settings of the ORTEC amplifier and the FASTER acquisition system used for the Scandium, Vanadium and $NaNO_3$ targets.

On Figure 100 and Table 23 we can see that the resolutions obtained with the FASTER and Maestro systems are similar. The resolution curve obtained with LANCELOT and the FASTER acquisition system is given in section 5.2.5.

Energy (eV)	277	392	525	1041	4088	4460	4948	5427
Meastro	29 ± 3	34 ± 3	36±3	40± 2	92± 2	93±2	100±2	107±3
FASTER	30 ± 4	35 ± 3	34±2	39± 2	95± 2	95±3	100±2	106±3

Table 23: Resolutions (Half Width at Half Maximum) in eV for the Maestro and FASTER systems.

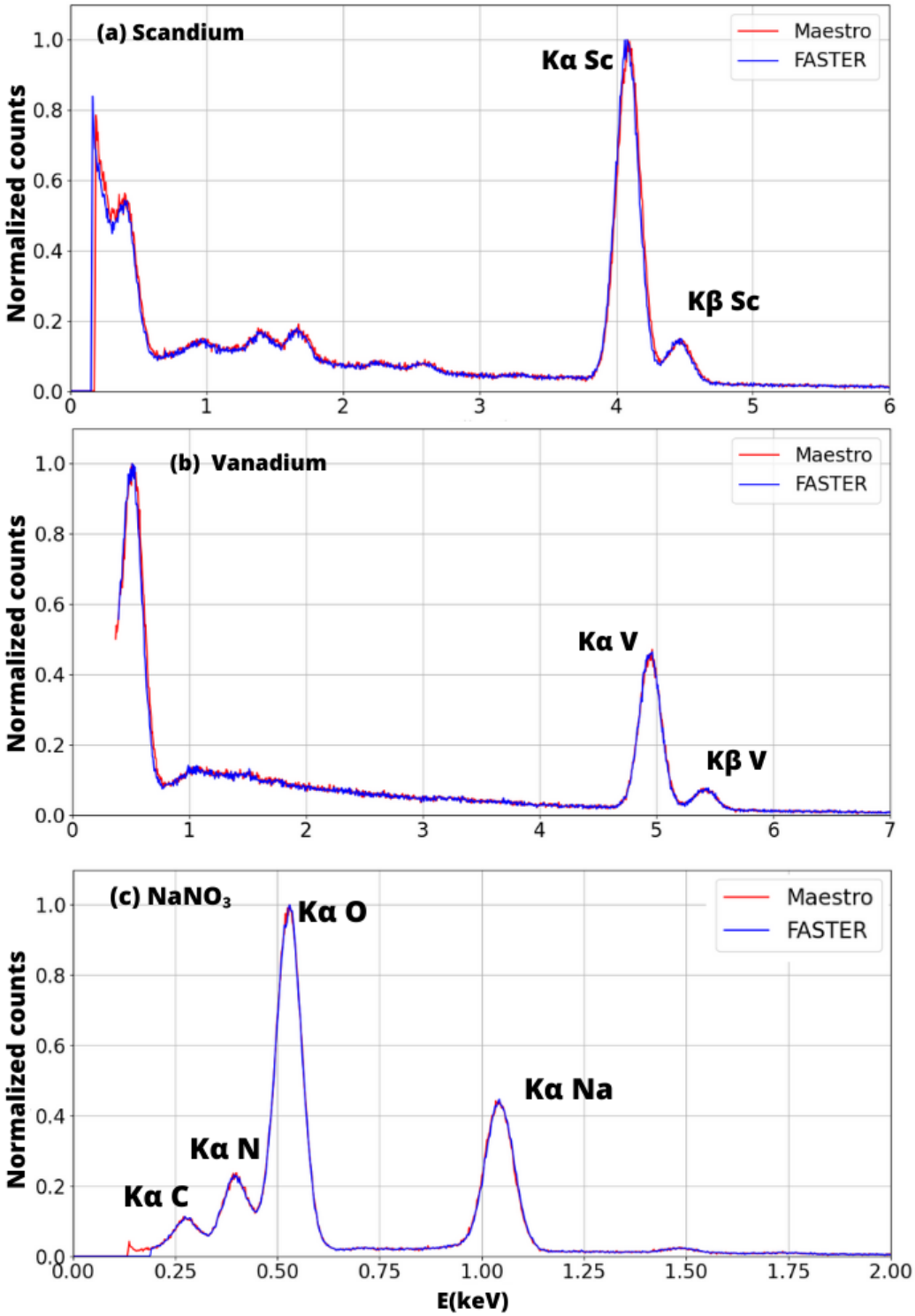

Figure 100: X-ray spectra obtained with LANCELOT for a. Scandium, b. Vanadium and c. $NaNO_3$ targets impacted by an electron beam of 10 keV in parallel with Maestro and FASTER with an acquisition time of 10 minutes.

5.2.5 Resolution of the LANCELOT detector with FASTER

The resolution of the LANCELOT detector with FASTER was measured as a function of the photon energy using the spectra obtained with the vanadium, scandium and $NaNO_3$ targets. The Half-Width at Half-Maximum (HWHM) was used as a measure of the res-

olution. Figure 101 summarizes the data from these three targets. A simple background extraction was performed on the spectra before fitting the peaks with a combination of gaussians using the "curve_fit" function from the Python package "scipy.optimize" (Figure 102). Below 1 keV, the resolution is about 30-35 eV. This low resolution is directly visible in the $NaNO_3$ spectrum where the capability of the acquisition chain to separate the peaks in that energy range is clear. During the collision experiments, oxygen and argon ion beams will be used. These ions capture electrons in higher electronic shells from atoms of the residual gas all along the beamline, and when these electrons de-excite they emit X-rays. These X-rays will be detected by LANCELOT. Therefore we need to be able to distinguish between peaks separated by a few tens of eV for energies below 1 keV for oxygen. Overall the performance of the acquisition chain (LANCELOT detector and FASTER acquisition system) in terms of resolution has been found to be perfectly suited for the planned measurements.

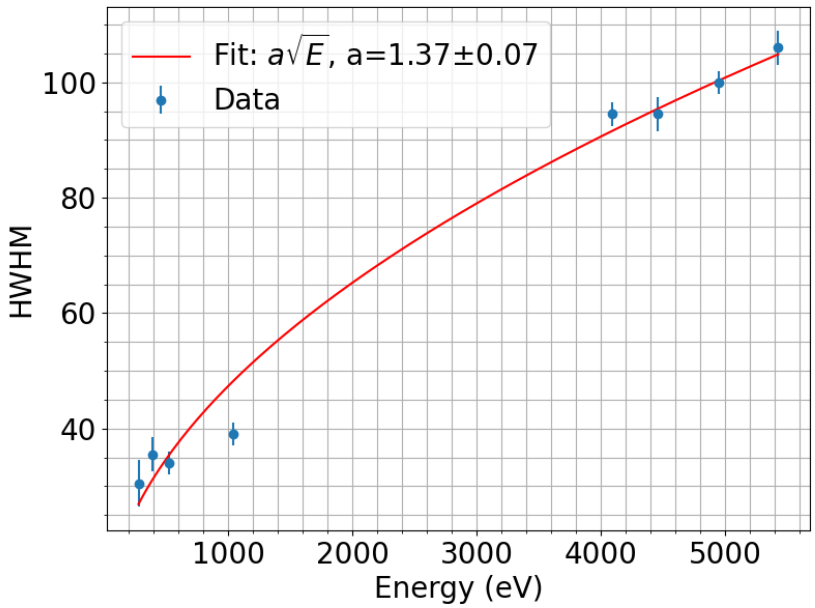

Figure 101: Experimental determination of the half width at half maximum (HWHM) as a function of the photon energy for the acquisition system composed of the LANCELOT detector and FASTER with the MOSAHR daughterboard.

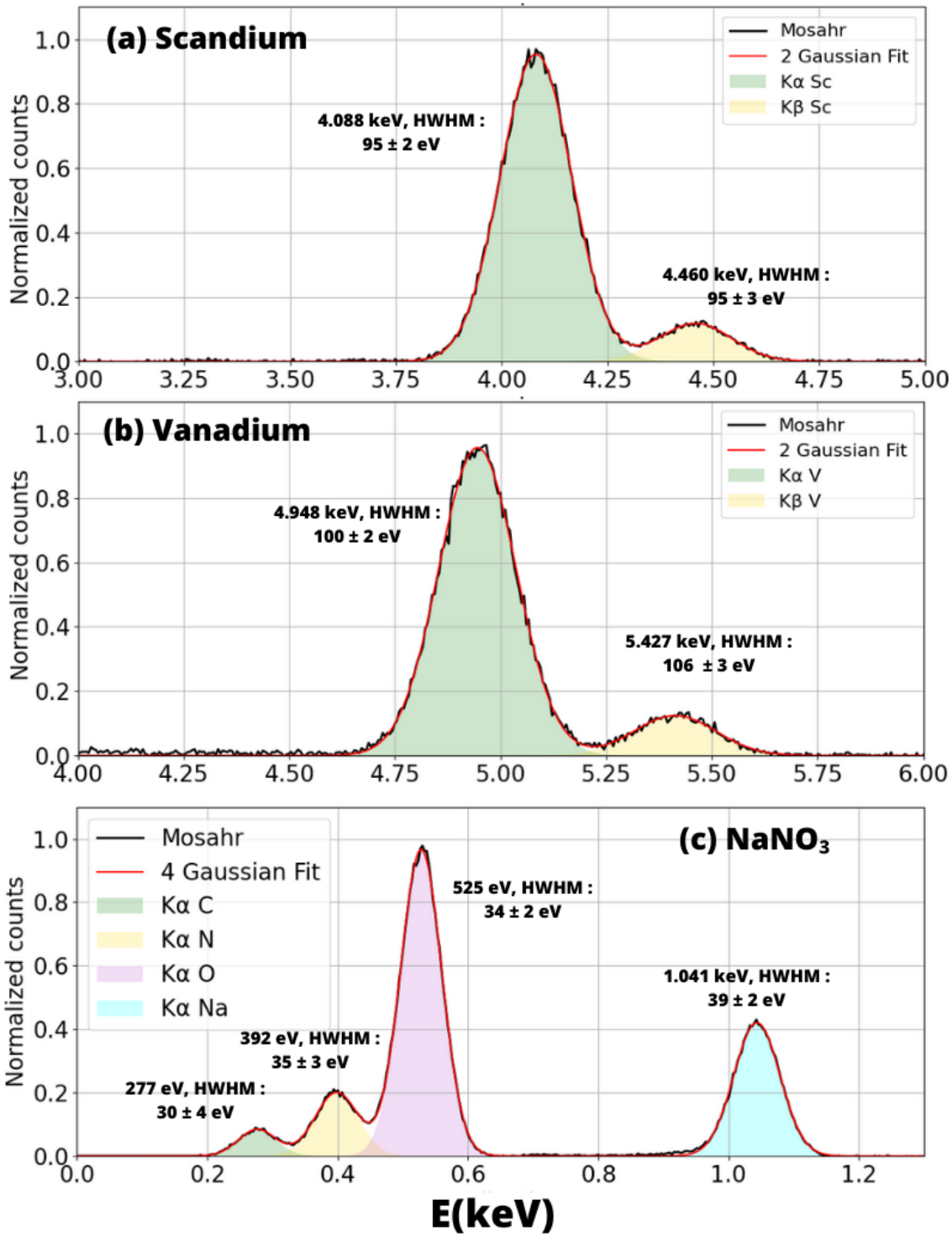

Figure 102: Spectra after background subtraction for a. Scandium, b. Vanadium and c. $NaNO_3$, fitted with a 2-gaussian (Sc and V) or 4-gaussian function ($NaNO_3$). The colored areas show the individual gaussians used in the final fit.

5.3 Tests performed at the ARIBE facility

5.3.1 Objectives and description of experiments

Two testing campaigns were conducted at ARIBE (see sections 4.1.4 and 4.2.4) for two elements of the collision zone presented in 4.3 : the ion spectrometer (4.3.3) and the OMEGA charge-state purificator (4.3.1) to ensure that their working principles and characteristics are well known and understood. Initially in 2021, the ion spectrometer was tested alone, and its design was modified based on the results obtained [160]. During a second campaign in 2023, the OMEGA and the modified spectrometer were tested together. The measurements were recorded with the custom detector for ion spectroscopy whose working principles are described in section 4.3.4.1 coupled to the FASTER acquisition system. The motivations for this study were the necessity to characterize the separating power and resolution of the spectrometer and the effect of the OMEGA when connected to the spectrometer, and to identify any possible background sources. The ARIBE facility was chosen to perform these tests because, unlike our setup, a set of three slits is present on the ARIBE beamline allowing to considerably reduce the emittance of the beam and its intensity if necessary. A small emittance may be needed to properly test the performances of the ion spectrometer. The reduced intensity is important in an effort to avoid any damage on the MCPs.

For both experimental configurations (namely the ion spectrometer alone or the OMEGA

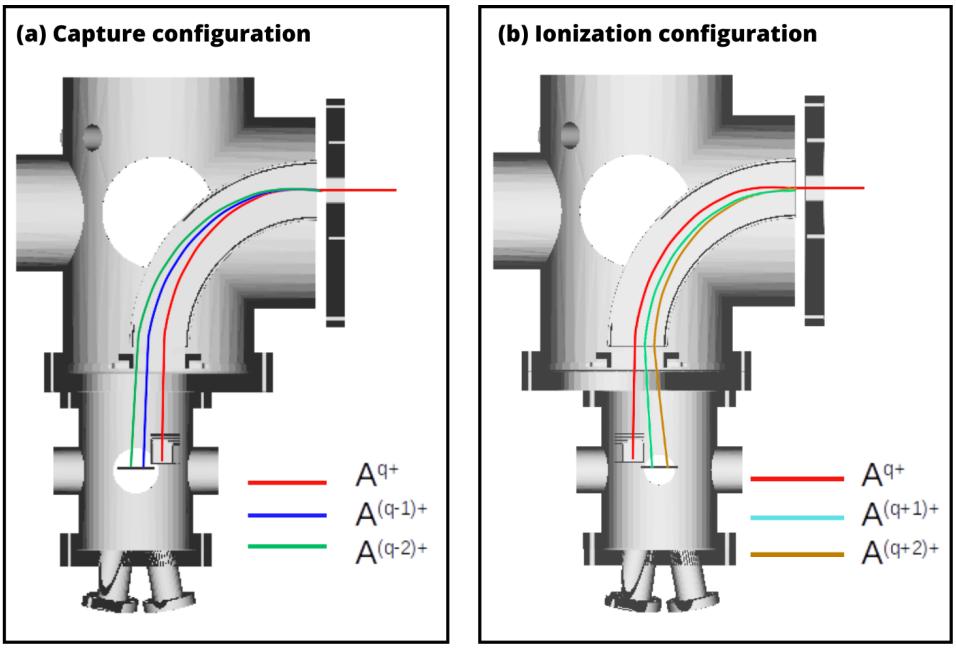

Figure 103: Typical trajectories of primary and secondary ion beams in the a. capture configuration and b. ionization configuration.

- ion spectrometer together) the chambers were connected to the L4 line at the ARIBE facility as depicted in the previous chapter on the Figure 61. Four different ion beams were used : Ar^{12+}, Ar^{9+} and O^{3+} with an extraction voltage of 10 kV. Their intensity was comprised between 1 pA and 10 nA, resulting in no more than a few thousand hits per second on the MCPs. For all the duration of the experiments, the pressure inside the ARIBE beamline, the OMEGA and the spectrometer was of the order of 10^{-8} mbar. The principle of the tests is the following : all along the last straight part of the ARIBE

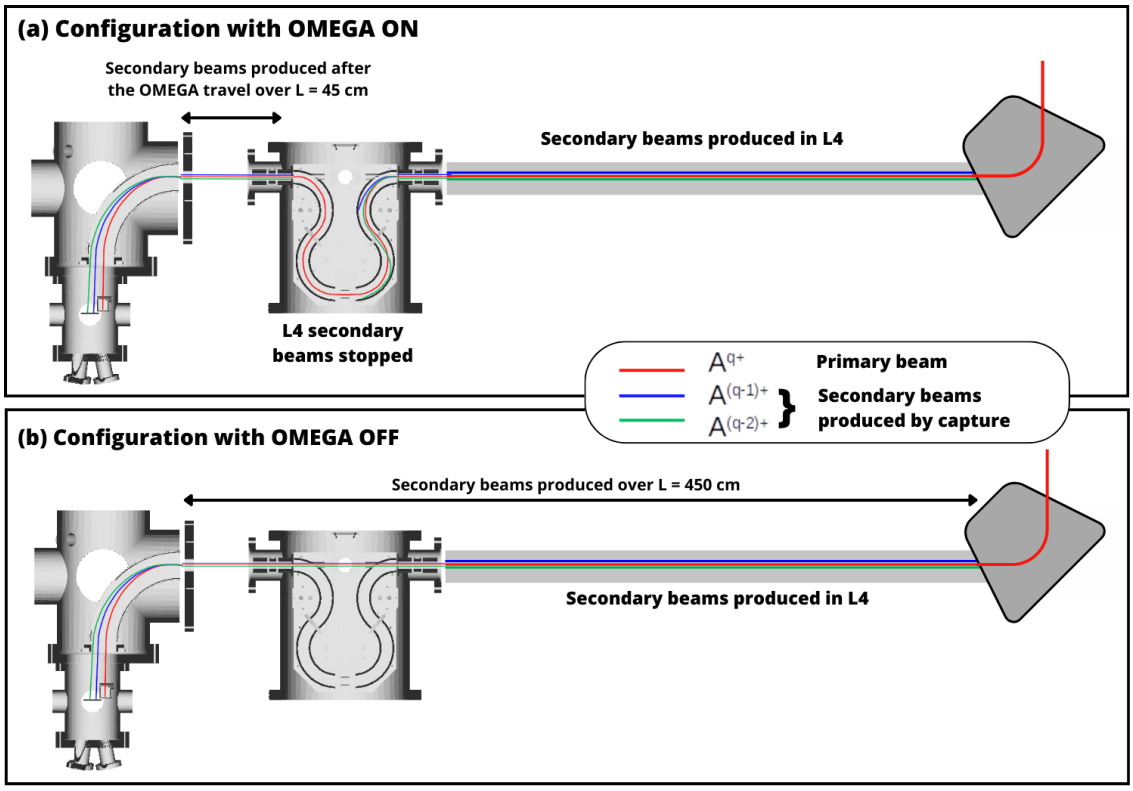

Figure 104: Typical trajectories of primary and secondary ion beams in the case the OMEGA is turned on (a) turned off (b). In the first case, secondary beams detected on the MCPs come from collisions with the residual gas occurring after the primary beam exits the OMEGA (L = 45 cm), whereas in the second case they occur along a greater distance (L = 450 cm).

beamline (having a 4.5 m length) starting from the last dipole, ions from the primary beam may collide with the residual gas present inside the beampipe. As a consequence, electron capture and ionization processes may occur, leading to the production of secondary beams of respectively lower or higher charge states. Therefore, ions with the same kinetic energy but different charge states enter the experimental setup. Secondary beams are separated from the primary beams inside the spectrometer and detected on the MCP. The detector can be rotated 180° as shown on Figure 103 : if placed in the *capture configuration* only ions of lower charge states than the primary beam can be detected, and if placed in the *ionization configuration* only higher charge states are measured. While the primary beam is driven all the way into the detector Faraday Cup, the secondary beams are supposed to be stopped inside the OMEGA if it is turned on as shown on Figure 104 for the case of capture beams. The measurements and conclusions obtained during those two test campaigns are detailed in the following sections.

5.3.2 Measurements in the capture configuration

In this section we detail the results of the measurements made in the capture configuration. The SIMION 3D suite [203, 204] was used to perform ion trajectories simulations throughout this analysis. In the first part, we present qualitative analyses of the results, and in the second part, we provide more quantitative results on the effect of OMEGA and give estimates of cross sections.

5.3.2.1 Qualitative comparison between measurements and simulations

Several tests were carried out for each primary ion charge state, where the voltages were changed on the inner and outer plate of the spectrometer as well as on the Matsuda plates. For all A^{q+} primary beams, a transmission of 100% through the OMEGA and ion spectrometer was reached. On Figure 105 the SIMION simulations for the expected ion trajectories inside the spectrometer are represented along with the typical images recorded by the MCPs for the corresponding measurements. Given the low intensity of the beams used and the cut in emittance made with the slits along the beamline, the simulations were carried out using an estimated beam emittance of 5π mmmrad, a beam diameter of 2 mm and a gaussian distribution for the positions and velocities of the ions in the beam. Table 24 summarizes the voltages on the spectrometer, the count rate and the version of the spectrometer that was used for each of the images and measurements presented.

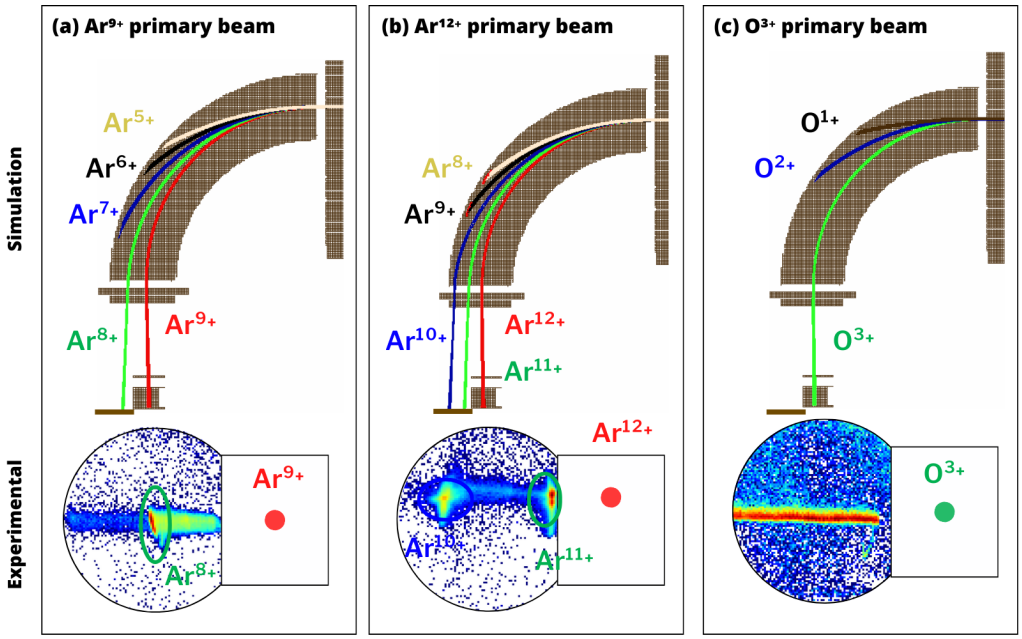

Figure 105: SIMION simulations of ion trajectories and corresponding experimental image on the MCPs obtained for Ar^{9+} (a), Ar^{12+} (b) and O^{3+} (c) as primary beams extracted at 10 kV.

Ion (figure)	Beam Current (pA)	Left Matsuda (V)	Right Matsuda (V)	Inner Plate Voltage (V)	Outer Plate Voltage (V)	Spectrometer version	Count Rate (ct/s)
Ar^{9+} (106)	4.7	1000	1500	-3380	3380	Second	450
Ar^{12+} (107 a)	1.5	1000	2000	-3380	3380	Second	2200
Ar^{12+} (107 b)	6	1500	1000	-3380	3500	First	525
O^{3+} (109)	10	1000	1000	-3333	3333	Second	450

Table 24: Summary of voltages and count rates recorded by the MCP for four different charge states for which the current measured by the Faraday Cup of the detector is given.

We detail the observations for each charge state, for which the most visually representative of the results are selected :

- Ar^{9+} : The result presented in Figure 106 was made with the OMEGA and with the second version of the spectrometer but all images obtained without the OMEGA or with the first version of the spectrometer show similar results in terms of overall peak shape. According to simulations shown on Figure 105 (a), only one spot on the MCP detector is expected. It corresponds to a secondary Ar^{8+} originating from stabilized electron capture on the residual gas that occurs all along the beamline. Beams of lower charge states are not expected to be seen on the MCPs. We do measure one main spot corresponding to the Ar^{8+} ions at their expected position on the MCPs, but a tail above is also visible, extending towards the position of the Faraday Cup. The intensity of this tail is low compared to the main peak and represents less than 10% of the main peak intensity in average in all runs. Further simulations (Figure 106) show that the tail results from electron capture occurring along the trajectory of the main Ar^{9+} beam inside the ion spectrometer. For these

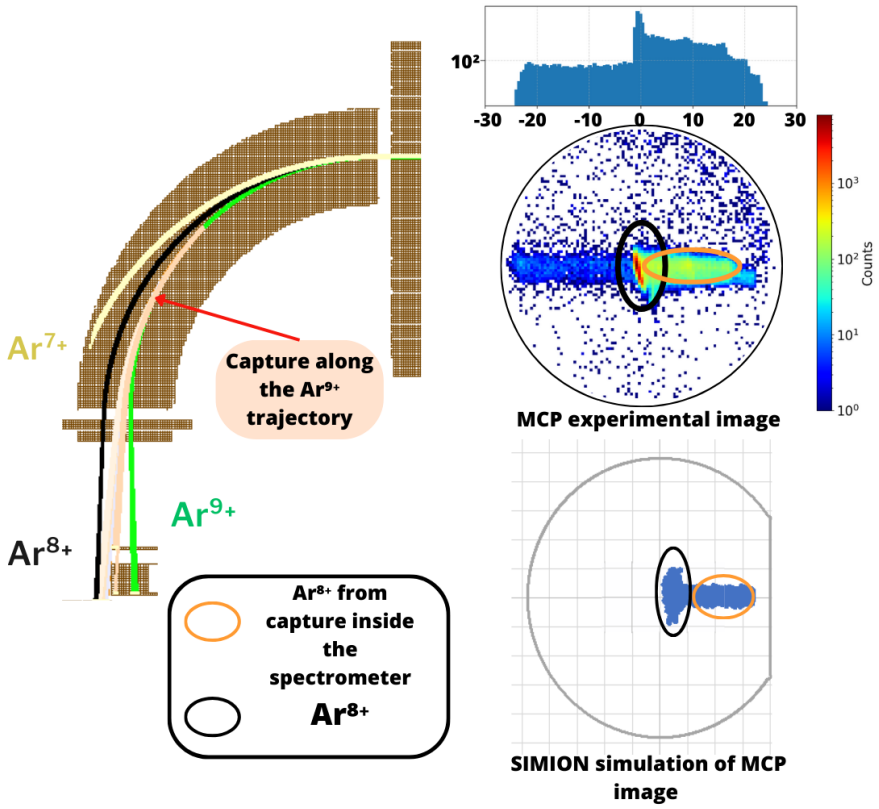

Figure 106: Experimental MCP images and SIMION simulations of ion trajectories for an Ar^{9+} primary beam with added ion beams to account for capture inside the spectrometer and comparison with the MCP experimental image. Gaussian distributions for the position and velocity of the particles as well as a beam diameter of 2 mm were used for the SIMION simulations. The profile histogram of the MCP image is also shown in logscale above the MCP image.

simulations, the position of the capture process is chosen randomly along the trajectory of the primary ions. The closer the capture occurs from the entrance of the spectrometer, the more the trajectory of the capture ions is close to the Ar^{8+} beam. On the other hand when the capture occurs further along the primary beam trajectory, the resulting capture beam is less submitted to the electrostatic field and therefore less deviated. This results in an uniform tail feature on the MCP image. A second, fainter tail is also visible under the Ar^{8+} peak. It represents around

2% of the main peak intensity in average. Both these tails are visible clearly on the logscale profile histogram shown on Figure 106. In the same manner this tail originates from capture along the Ar^{8+} beam trajectory and corresponds to Ar^{7+} ions. This full tail background originating from capture inside the spectrometer can unfortunately only be reduced by reducing the pressure inside the spectrometer itself.

- Ar^{12+} : The results presented in Figure 107 (a) and (b) were obtained respectively with the first and second version of the ion spectrometer. The simulations on Figure 105 b) show than two spots corresponding to simple and/or double electron capture are expected on the MCP. These peaks are visible on the MCPs in Figure 107 a), along with a third "parasitic" peak. The Ar^{11+} and Ar^{10+} peaks (expected signals) have been discriminated from the "parasitic" peak (background) with certitude by comparing the simulated and measured positions of the peaks when varying the outer and inner plates voltages, as shown on Figure 108 (a). The agreement between data and simulations is very good, leaving no doubt as

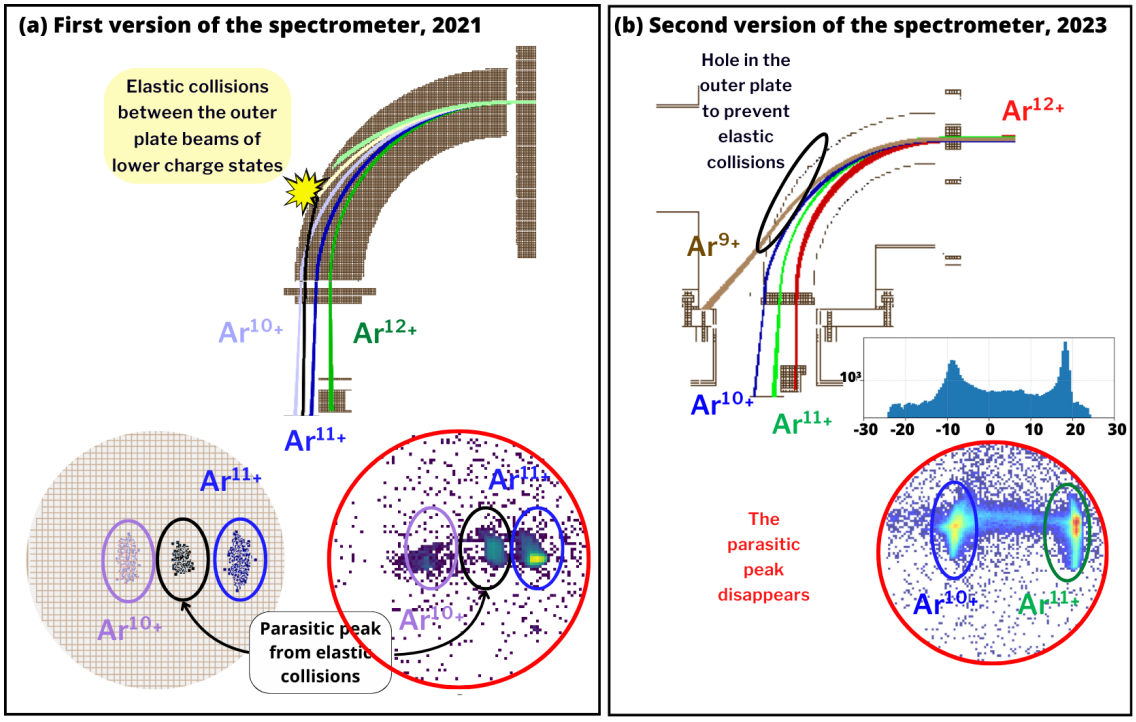

Figure 107: Experimental MCP images and SIMION simulations of ion trajectories for an Ar^{12+} primary beam in the first spectrometer version (a) and second version (b) showing the origin of the parasitic peak and its absence in the second version. Gaussian distributions for the position and velocity of the particles as well as a beam diameter of 2 mm were used for the SIMION simulations.

to our correct identification of the peaks. Figure 108 (b) shows the same kind of comparison for the second version of the ion spectrometer. Since it is not possible on SIMION to accurately represent the grid, due to discretization issues, we simulated the runs for a case with a hole in the outer plate but no grid, and for a case with no hole. We expect the real case to be an intermediate between the two in terms of distance between the peaks. That is indeed what we observe on Figure 108 (b), therefore confirming once again our correct identification of the peaks. For both cases represented on Figure 108, the error bars mainly originate

from the uncertainty on the active diameter of the MCP. The manufacturer gives the information that the diameter of the active surface is greater than 45 mm, and the ceramic ring that holds the MCPs has an internal diameter of 48 mm, therefore we used these extreme values as bounds when reconstructing the images and measuring the distances.

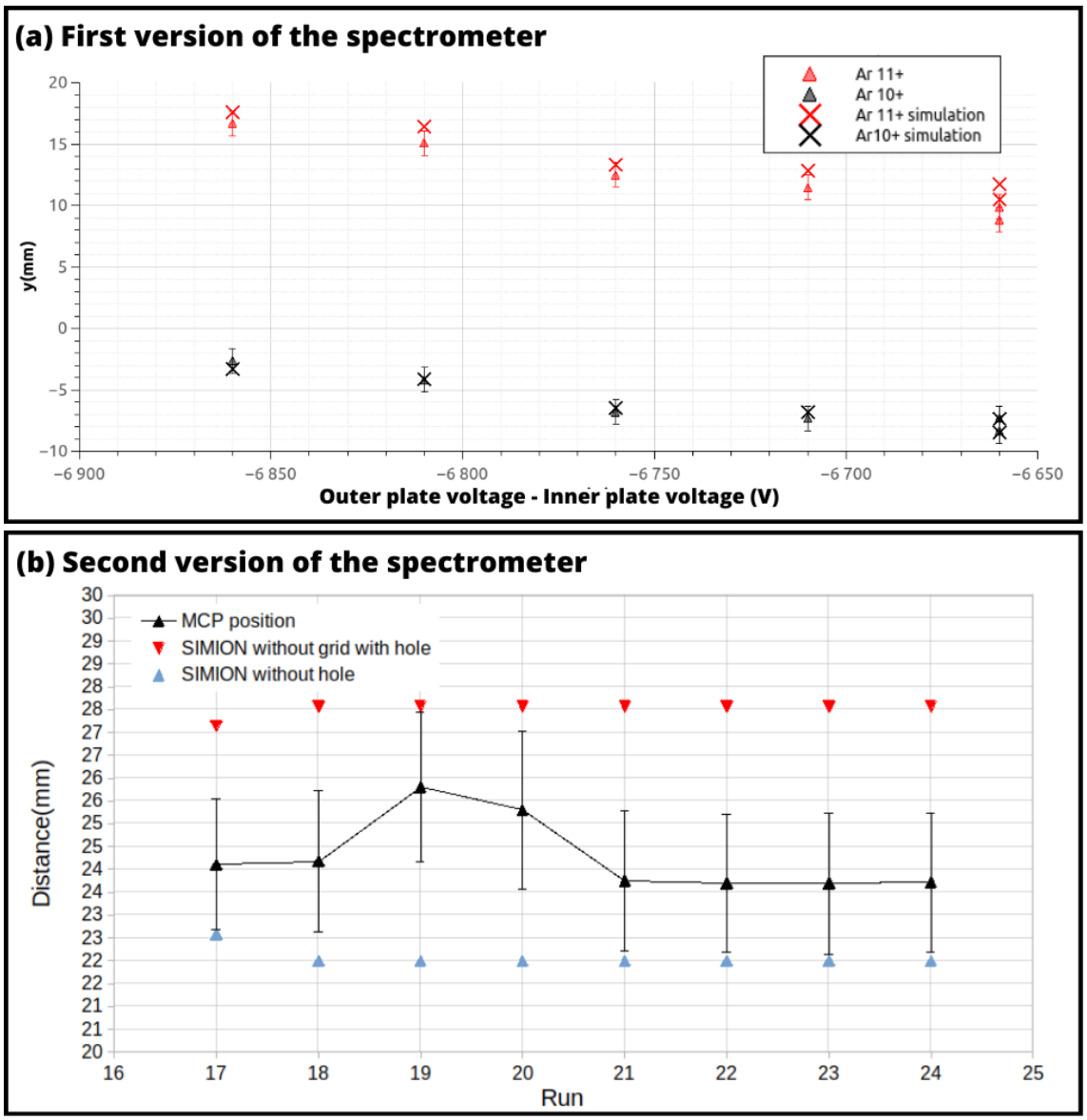

Figure 108: (a) Detected and simulated position of the Ar^{11+} and Ar^{10+} peaks as a function of the voltage difference between the outer and inner plate for the first version of the spectrometer. The voltages on the left and right Matsuda plates are respectively $1000\,V$ and $1500\,V$. (b) Detected and simulated distances between the Ar^{11+} and Ar^{10+} peaks for each run. Since SIMION cannot accurately simulate the grid, two "extreme" simulations are shown, one with the hole (without the grid) and one with the full plate (without the hole).

On Figure 107 a), to explain the presence of a "parasitic" peak, we simulated the possibility that the Ar^{9+} beam hits the outer plate and undergoes elastic collision [205, 206] giving rise to a peak that is recorded by the MCP. The simulated position of this parasitic beam on the MCP corresponds to the experimental position. Trying to reduce this background was the main motivation behind the

modification of the ion spectrometer (see section 4.3.3). On Figure 107 b) the SIMION simulation of the ion trajectories in the second version of the spectrometer is shown, and it is clearly visible that the Ar^{9+} beam no longer hits the outer plate, but is instead directed inside the ion spectrometer chamber. As shown on the corresponding MCP image, the parasitic peak is no longer visible, therefore confirming our suppositions on the origin of this peak.

- O^{3+} : The MCP image shown on Figure 109 was made with the OMEGA and with the second version of the spectrometer but all images obtained without the OMEGA show similar results, no matter which version of the spectrometer is used. It is clearly visible in Figure 105 c) that no secondary beams from stabilized electron capture hit the detector. However a horizontal line is visible on the MCPs. The position of this line changes when asymmetric Mastuda voltages are applied,

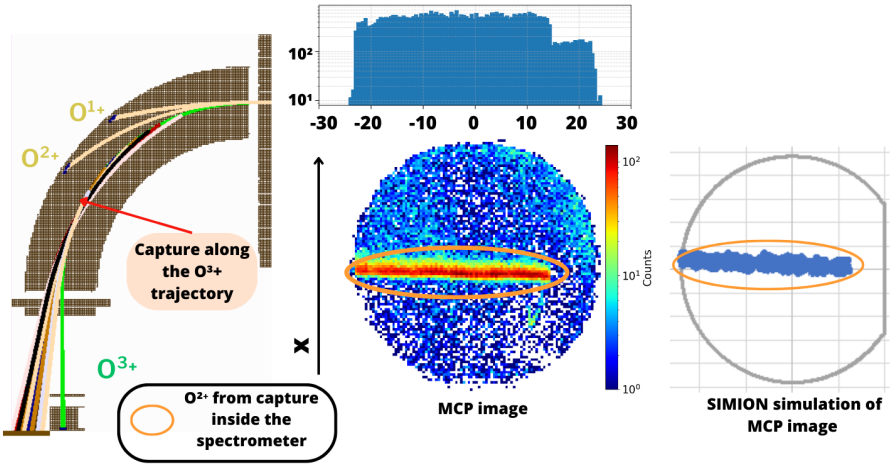

Figure 109: Experimental MCP image and SIMION simulations of ion trajectories for an O^{3+} primary beam extracted at 10 kV with added ion beams to account for capture inside the spectrometer and comparison with the MCP image. Gaussian distributions for the position and velocity of the particles as well as a beam diameter of 2 mm were used for the SIMION simulations.

and its width changes as a function of the Matsuda voltage difference. Just like for the case of the tail visible in the case of an Ar^{9+} primary beam, this "line" comes from capture along the O^{3+} trajectory inside the spectrometer. SIMION simulations, Figure 109, confirmed this, and also allowed to correctly simulate the small tilt of the horizontal line. The capture beams originating from random points in the primary beam trajectory are more or less subjected to the field induced by the outer and inner plate and have consequently different trajectories. The same thing is true for the effect of the Matsuda voltage difference. The beams created closer to the spectrometer entrance are more subjected to the influence of this voltage difference than those created closer to the exit. In consequence some ions are more deviated in the x-axis than others, resulting in a slightly tilted line. This background contribution is only dependent on the pressure inside the spectrometer, and cannot be reduced by other means.

5.3.2.2 Growth rate simulations and cross section estimations

As explained in section 1.3.4.1, the cross sections for simple and double electron capture on residual gas can be approximated using the Müller-Salzborn scaling law [90]. We simulate the evolution of populations of the different charge states in the case of Ar^{9+} and Ar^{12+} using the growth-rate method described in section 1.3.4.2 [91], and compare with the recorded counts. In order to investigate the effect of the OMEGA we used data from 2023 with and without the OMEGA. The residual gas for capture was approximated to be N_2. The 1st ionization potential for N_2 is 15.6 eV. The estimated cross sections are reported in Table 25. Figure 110 shows the growth-rate graphs for

Process	Ar^{9+}, q = 9	Ar^{12+}, q = 12
$\sigma_{q,q-1}$	$(10 \pm 7) \times 10^{-15}$	$(2 \pm 1) \times 10^{-14}$
$\sigma_{q-1,q-2}$	$(8 \pm 6) \times 10^{-15}$	$(2 \pm 1) \times 10^{-14}$
$\sigma_{q-2,q-3}$	$(7 \pm 5) \times 10^{-15}$	$(2 \pm 1) \times 10^{-14}$
$\sigma_{q,q-2}$	$(3 \pm 2) \times 10^{-15}$	$(3 \pm 2) \times 10^{-15}$
$\sigma_{q-1,q-3}$	$(3 \pm 2) \times 10^{-15}$	$(4 \pm 3) \times 10^{-15}$

Table 25: Estimated cross sections using Müller-Salzborn scaling law [90] for different charge states q of 10 qkeV argon ions colliding with N_2. The cross sections are given in cm^2.

Ar^{12+} and Ar^{9+} as initial charge states. Several paths are available for the formation of each secondary charge states. For instance, Ar^{11+} can be formed either through stabilized simple capture from Ar^{12+} or from autoionization following double capture from Ar^{12+}, with a probability reflected by the autoionization coefficient a_{10}. Ar^{10+} is formed following stabilized double capture from Ar^{12+}, stabilized simple capture from Ar^{11+} or from autoionization following double capture from Ar^{11+}. All those paths are shown on Figure 110 for Ar^{12+} (a) and Ar^{9+} (b) as initial charge states, with corresponding probabilities. Equation (117) is the resulting system of coupled equations describing the evolution of the charge state distributions for Ar^{12+} as a function of the distance inside the beamlines. The corresponding system for Ar^{9+} can be directly derived in the same manner.

$$
\begin{aligned}
\frac{\mathrm{d}N_{12}}{\mathrm{d}\ell} &= -n \times N_{12} \times (\sigma_{1211} + \sigma_{1210}) \\
\frac{\mathrm{d}N_{11}}{\mathrm{d}\ell} &= n \times [N_{12} \times (\sigma_{1211} + \sigma_{1210} \times a_{10}) - N_{11} \times (\sigma_{1109} + \sigma_{1110})] \\
\frac{\mathrm{d}N_{10}}{\mathrm{d}\ell} &= n \times [N_{12} \times \sigma_{1210} \times (1 - a_{10}) + N_{11} \times (\sigma_{1110} + \sigma_{1109} \times a_{09}) - N_{10} \times \sigma_{1009}] \\
\frac{\mathrm{d}N_{09}}{\mathrm{d}\ell} &= n \times [N_{10} \times \sigma_{1009} + N_{11} \times \sigma_{1109} \times (1 - a_{09})]
\end{aligned}
\tag{117}
$$

where n is the number of residual gas target atoms per cm^3, and ℓ the distance traveled by the beam. A python program was created to model the population evolution using these equations. As shown on Figure 104, the length is 450 cm when the OMEGA is turned off and the beam travels all the way from the last dipole to the ion spectrometer detector. When the OMEGA is on, the length used is 45 cm , corresponding roughly to

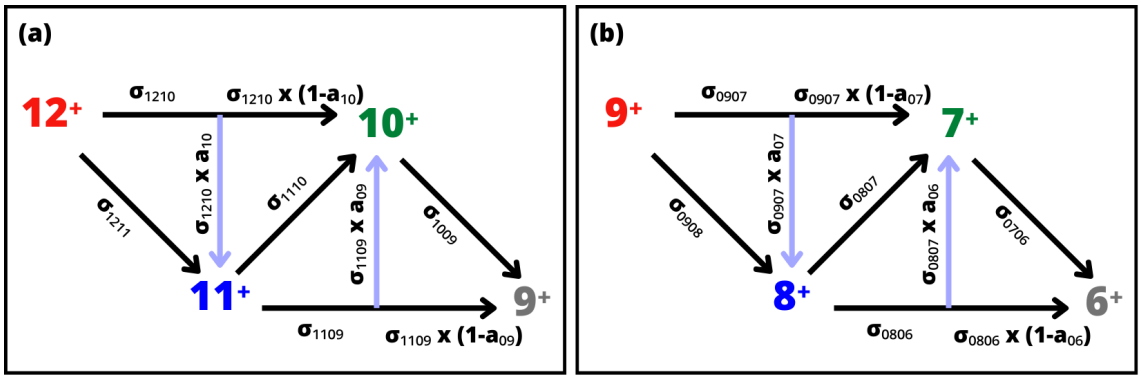

Figure 110: Pathways leading to a given charge state for Ar^{12+} (a) and Ar^{9+} (b) as initial charge state. Direct one- and two-electron capture are considered, as well as autoionization of excited states formed in two-electron capture with probability a_q.

the distance between the exit of the OMEGA and the detector. The average pressure inside the beamline was around 1×10^{-8} mbar.

The evolution of the population, and more precisely the ratio of the populations is simulated for several values of the autoionization coefficient as presented in Figure 111. The experimental points (squares) have been placed at the value of the autoionization coefficient that fit the best. In the case of Ar^{12+}, the best fit is for $a_{10} = 0.4$ and in the Ar^{9+} case, $a_{07} = 0.1$. The autoionization coefficient is higher for Ar^{12+} than for Ar^{9+} since the $2p$ shell of Ar^{12+} has less electrons (2) than that of Ar^{9+}. The outer shell electrons of Ar^{9+} are therefore less likely to be ejected since the shell is almost full. Table 26 gives a comparison between the simulated and measured population ratios for both Ar^{9+} and Ar^{12+} measurements, with the autoionization coefficients determined before. The measured populations are the average over several runs and the error is the standard deviation. For both Ar^{12+} and Ar^{9+}, the proportion of the q-2 population that comes from stabilized double electron capture (and not from two one-electron captures) is more than 97%.

		Ar^{12+}			Ar^{9+}
		N_{12}/N_{11}	N_{12}/N_{10}	N_{11}/N_{10}	N_{09}/N_{08}
$\ell = 45$ cm	With OMEGA, measured	$(7 \pm 1) \times 10^3$	$(5 \pm 1) \times 10^4$	6 ± 2	$(1 \pm 0.1) \times 10^4$
	With OMEGA, simulated	6×10^3	5×10^4	8	1×10^4
$\ell = 450$ cm	Without OMEGA, measured	$(7 \pm 1) \times 10^2$	$(6 \pm 1) \times 10^3$	8 ± 1	$(1 \pm 0.5) \times 10^3$
	Without OMEGA, simulated	6×10^2	5×10^3	8	1×10^3

Table 26: Simulated and measured population ratios for both Ar^{12+} and Ar^{9+} cases, with and without the OMEGA.

This is illustrated in Figure 112 where the general tendency for the evolution of the ratio of different charge state populations along the length of the beamline $\ell = 450$ cm is represented. The N_{q-1}/N and N_{q-2}/N ratios evolve linearly with ℓ, whereas the N_{q-3}/N ratio has a more complex evolution (see Figure 112 (a)), following a cubic law. This indicates that we are in a single collision regime for the production of $q-1$ and $q-2$ charge states. The ratio between N_{12}/N_{11}, N_{12}/N_{10} and N_{09}/N_{08} with and without the OMEGA is always of the order of 10, which corresponds to the ratio between the

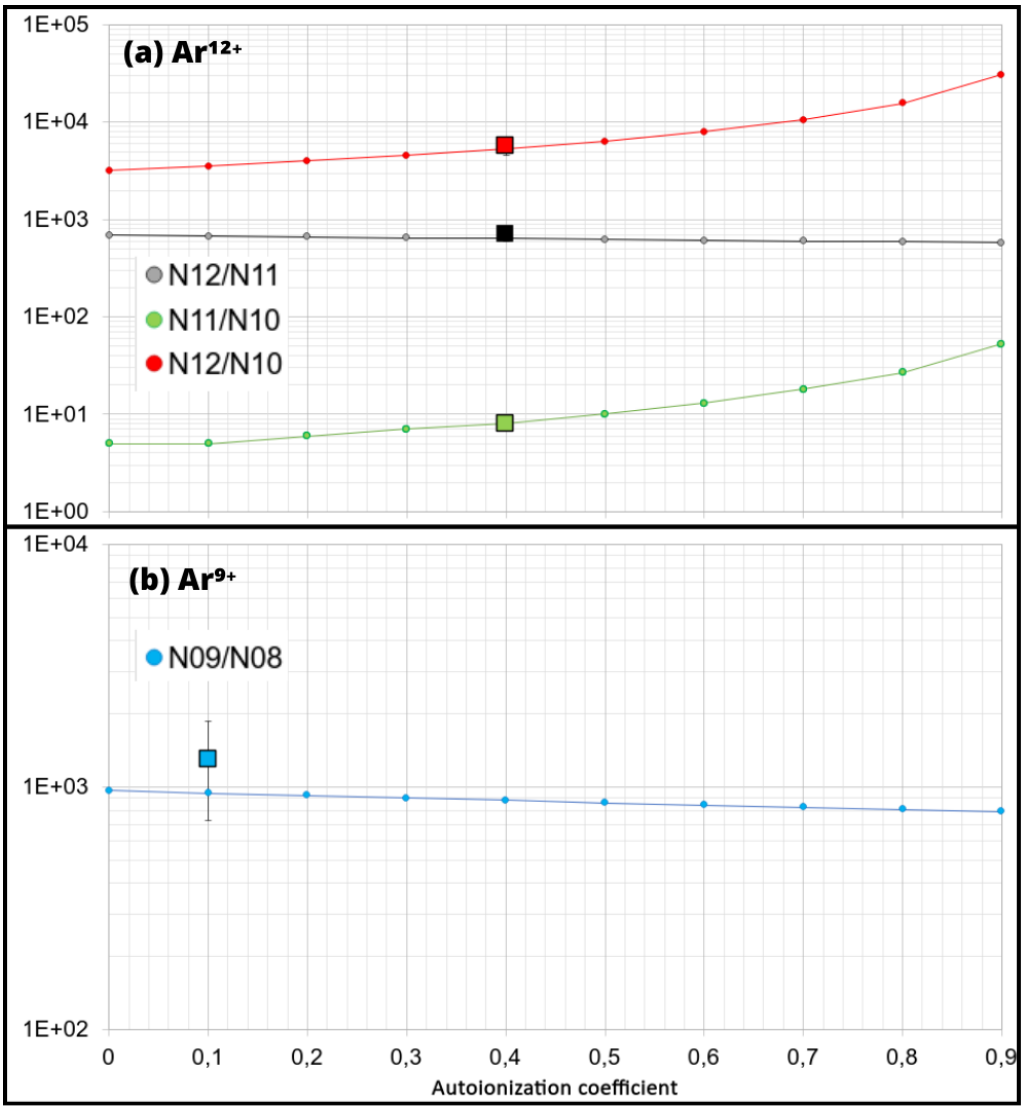

Figure 111: Ratios of different populations for autoionization coefficients a_q ranging from 0 to 0.9. The primary charge states are Ar^{12+} (a) and Ar^{9+} (b). The circles with full lines are simulated values and the squares are experimental values positioned at $a_{10} = 0.4$ for Ar^{12+} and $a_{07} = 0.1$ for Ar^{9+}. Both are for the case where the OMEGA is off.

length of the beamline with and without the OMEGA (450cm/45cm). This means that the OMEGA serves its purpose of cleaning the primary beam of secondary charge states as desired. For the case of the N_{11}/N_{10} ratio, no difference is found between the measurements with and without OMEGA. When the OMEGA is ON, the secondary charge states created along the length of the beamline are stopped inside the OMEGA and the Ar^{11+} and Ar^{10+} ions that are detected have been created along the same length, 45 cm. When the OMEGA is OFF, both secondary charge states are created along a total length of 450 cm. Since both secondary charge states travel the same length, their population ratio does not change whether the OMEGA is on or off. This is clearly visible in Figure 112 (b) showing that the ratio between the N_{q-2} and N_{q-1} populations is constant along the length of the beamline.

The cross sections for one- and two-electron capture can be extracted from the data using equation (118). For calculating n, equation (119) is used, where P is the pressure inside the beamline (an average of 1×10^{-8} mbar is used), k_B is the well-known Boltzmann

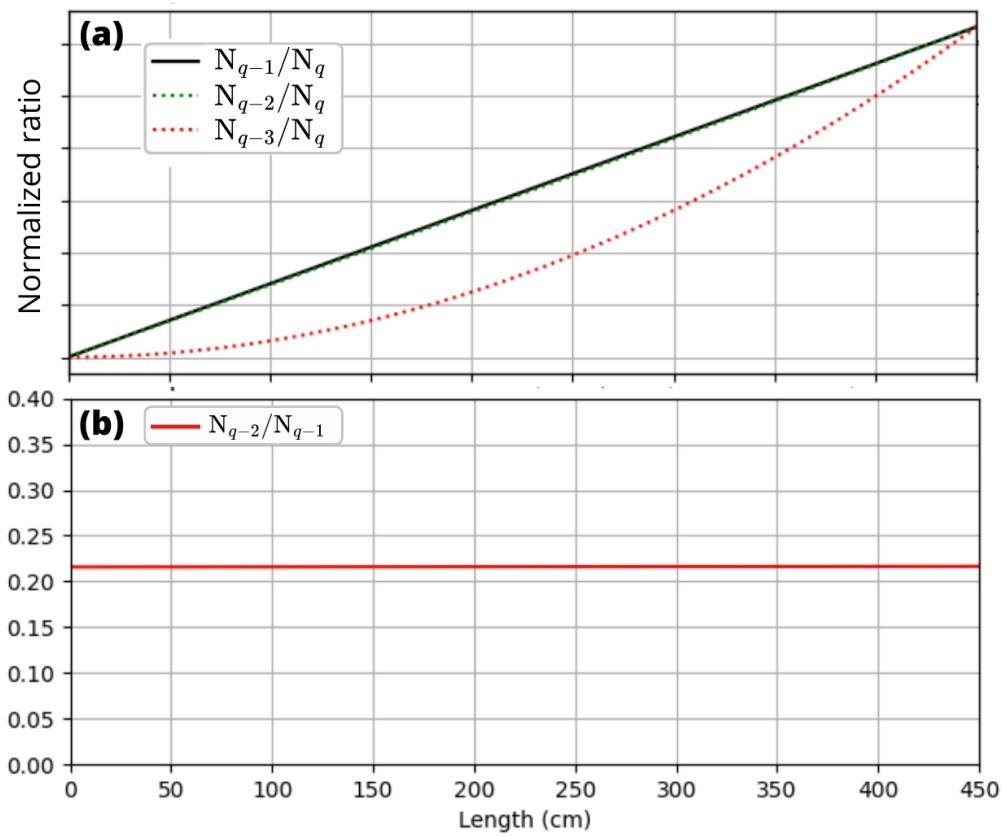

Figure 112: General tendency for the evolution of the ratio of different charge state populations along the length of the beamline ℓ = 450 cm, with an autoionization coefficient of 0.4. The ratios between the primary charge state N_q and secondary charge states are presented in (a) where all curves are normalized to the same y-scale for readability purposes. The ratio between the N_{q-2} and N_{q-1} populations is shown in (b).

constant and T the temperature $(300\,\mathrm{K})$. Table 27 summarizes the estimated cross

Process	Calculations from measurements	Müller-Salzborn cross sections
$Ar^{12+} \rightarrow Ar^{11+}$	$(1 \pm 0.7) \times 10^{-14}$	$(2 \pm 1) \times 10^{-14}$
$Ar^{12+} \rightarrow Ar^{10+}$	$(2 \pm 1) \times 10^{-15}$	$(3 \pm 2) \times 10^{-15}$
$Ar^{9+} \rightarrow Ar^{8+}$	$(8 \pm 6) \times 10^{-15}$	$(10 \pm 7) \times 10^{-15}$

Table 27: Cross sections extracted from the measurements and the corresponding ones calculated using the Müller-Salzborn scaling law. The cross sections are given in cm^2.

sections and their uncertainties. We can see that the agreement between the cross sections extracted from our measurements and the ones calculated with the Müller-Saltzborn laws is rather very good.

$$\sigma_{q,q-1} = \frac{N_{q-1}}{N_q} \times \frac{q}{q-1} \times \frac{1}{n\ell} \tag{118}$$

$$n = \frac{P(\mathrm{mbar}) \times 10^{-4}}{k_B T} = 2.41 \times 10^{8}\ \mathrm{cm}^{-3} \tag{119}$$

5.3.3 Measurements in the ionization configuration

For this configuration only two charge states were used : Ar^{9+} and O^{3+} at 10 kV. As shown on Figure 113, in the case of Ar^{9+}, the single ionization beam of Ar^{10+} hits the MCP detector, and no other beam is expected. In the case of O^{3+}, no beam hits the MCP detector, as the ionization beam O^{4+} hits the inner plate of the spectrometer. Since the typical ionization cross section is much smaller than the capture cross section, the primary beam intensity can be augmented by at least one order of magnitude without any risk of damaging the MCP detector. This allows us to much better characterize the background noise on the MCP. All of these measurements have been performed with the second version of the spectrometer. Table 28 summarizes all the information about the primary ion beam, the voltages used for the spectrometer and the counting rates recorded by the ion spectrometer detector.

Ion (figure)	Beam Current (nA)	Spectrometer Left Matsuda (V)	Spectrometer Right Matsuda (V)	Inner Plate Voltage (V)	Outer Plate Voltage (V)	Count Rate (counts/s)
Ar^{9+} 117 (a)	1.5	1500	1000	-3295	3315	664
Ar^{9+} 117 (b)	1.5	1500	1000	-3295	3315	4221
O^{3+} 114	1.6	850	1050	-3350	3350	783
O^{3+} 116	12	0	0	0	0	223

Table 28: Summary of experimental conditions, voltages used, and recorded count rates in the ionization configurations. 114, 116 and 117 refer to the experimental figures.

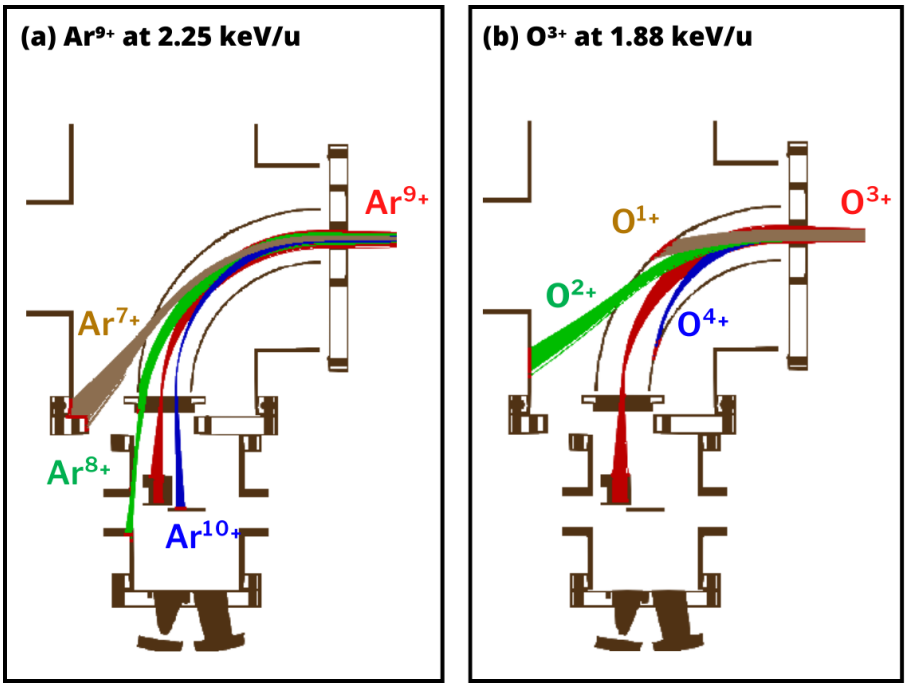

Figure 113: SIMION simulated trajectories in the ion spectrometer of 2.25 keV/u Ar^{9+} (a) and 1.88 keV/u O^{3+} (b) primary beams together with ionization and capture secondary beams, using a gaussian distribution for the position and velocity of the particles, and a beam diameter of 3 mm with an emittance of 10 π mm mrad. The voltages used in the simulation are those used to produce the images 117 (a) and 114.

- O^{3+} : On Figure 114, a semi-circular shaped background is visible. As expected

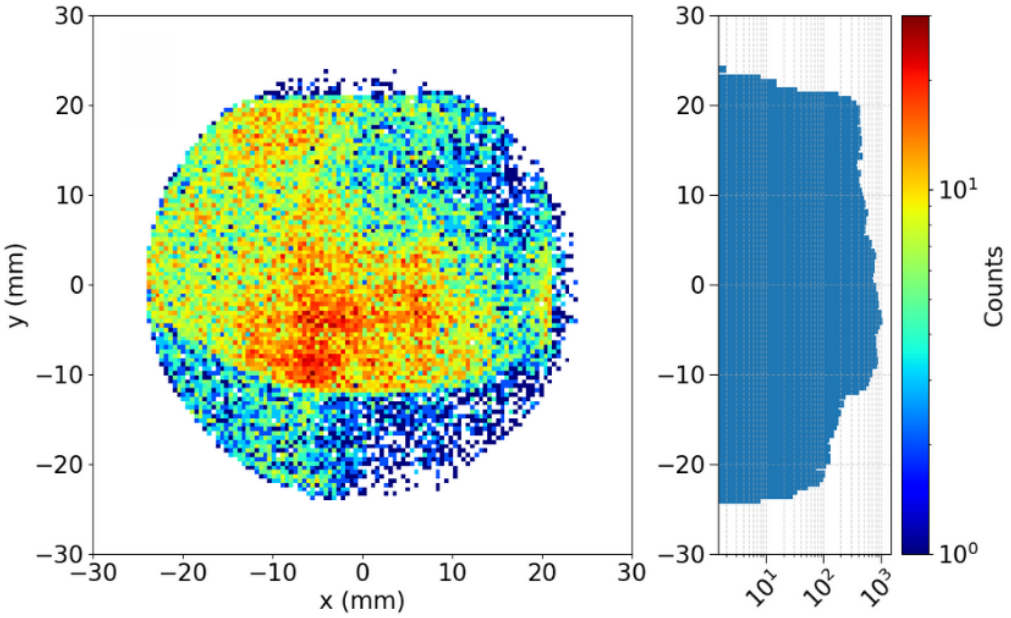

Figure 114: Experimental MCP image for an O^{3+} primary beam with the OMEGA on. The horizontal projection shows the shape of the background.

from the simulations in Figure 113, no spot is present. The SIMION simulations of Figure 115 made for this run shows that while the beam originating from simple capture (O^{2+}) passes entirely through the aperture in the outer plate of the spectrometer, a major portion of the O^{1+} beam from double capture collides on the outer plate between the aperture for the in-axis Faraday Cup and the hole present for this second version ion spectrometer. The trajectory of the ions from elastic collisions is simulated and the position at which they hit the MCPs is reconstructed with SIMION and the result shows a similarly shaped background as the one visible in Figure 114. It is therefore possible that, not unlike the "parasitic" peak seen for the case of Ar^{12+} in the previous section, this circular shaped background originates from elastic collisions on the outer plate above the hole. Another investigation was carried out to characterize the background noise without the contributions from internal collisions on the spectrometer. With all voltages on the spectrometer set to zero and the OMEGA turned on, a 12 nA O^{3+} beam was directed through both chambers to the spectrometer Faraday Cup in the beam axis. The resulting MCP image is shown on Figure 116. The horizontal logscale projection shows that the background is uniform over the surface of the MCPs. This further confirms our hypothesis that the background seen on Figure 114 stems from secondary beams being reflected by elastic collisions inside the spectrometer.

- Ar^{9+} : The MCP images shown on Figure 117 have been taken with the OMEGA on (a) and off (b). On both, a spot is visible and attributed to the Ar^{10+} ions from ionization. Like in the O^{3+} images, a semi-circular background is seen. However it could not be reproduced as accurately with the simulations, so it cannot be certain that it also originates from collisions inside the spectrometer. The Matsuda voltages and the inner and outer plates voltages have been changed to confirm that the observed Ar^{10+} spot moved in a consistent way compared to simulations. It is important to note that even though the y-direction position variations of the

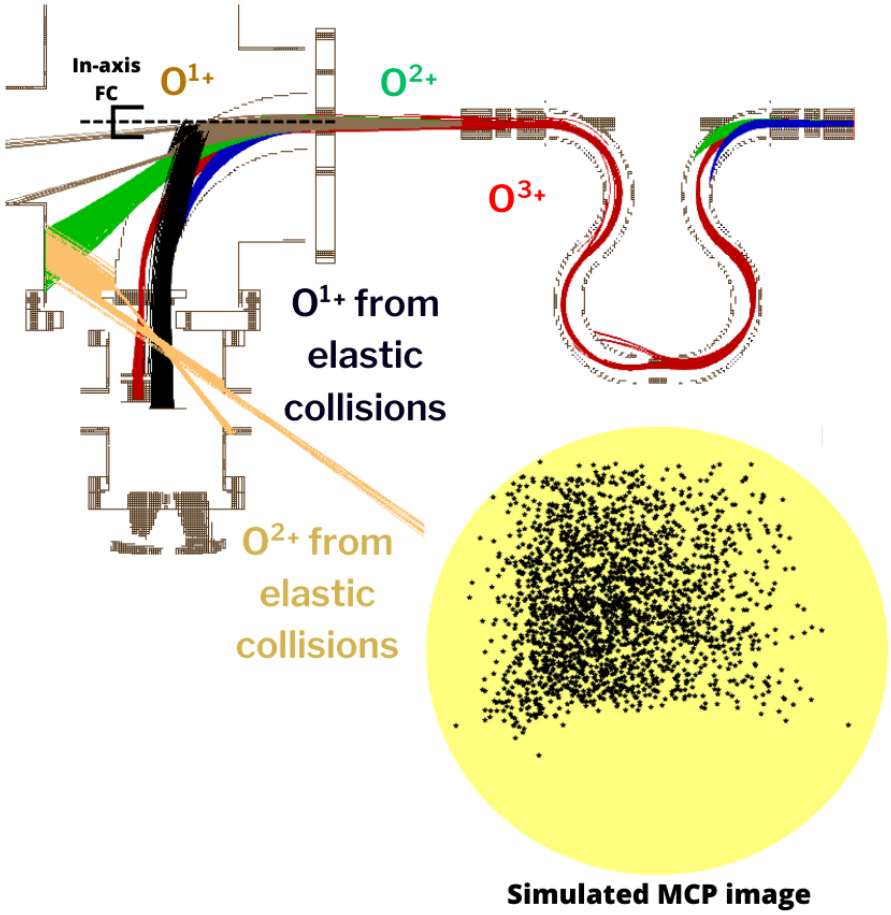

Figure 115: SIMION simulation for an O^{3+} primary beam with the OMEGA on, using a gaussian distribution for the position and velocity of the particles, and a beam diameter of 3 mm with an emittance of 10 π mm mrad. The corresponding simulated MCP image is shown under the simulation.

Ar^{10+} spot can be accurately reproduced with SIMION, the exact position of the spot is not the same. This is due to the fact that the spatial discretization in the SIMION software does not allow to correctly model the grid covering the aperture in the outer plate of the spectrometer as already mentioned in section 5.3.2. No grid is used in the simulations and consequently the field is slightly different than in the real spectrometer. The intensity ratio of Ar^{9+} to Ar^{10+} varied by a factor of 12 ± 5 between the runs without and with the OMEGA. This is consistent with the remarks in the previous section about the reduction of a factor 10 in the ratios between the number of primary and secondary ions due to the length traveled by the primary beam when the OMEGA is off or on (450cm/45cm).
The ionization cross section, both with and without the OMEGA, was estimated using

$$\sigma_{q,q+1} = \frac{N_{q+1}}{N_q} \times \frac{q+1}{q} \times \frac{1}{n\ell} \tag{120}$$

With the OMEGA turned on, the ionization cross section is found to be $(3 \pm 2) \times 10^{-17}$ cm^2, and $(4 \pm 2) \times 10^{-17}$ cm^2 with the OMEGA turned off. No direct comparison was found in the literature. In our experiments, a difference of 3 orders of magnitude is observed between cross sections for $Ar^{9+} + N_2 \rightarrow Ar^{10+}$ and Ar^{9+}

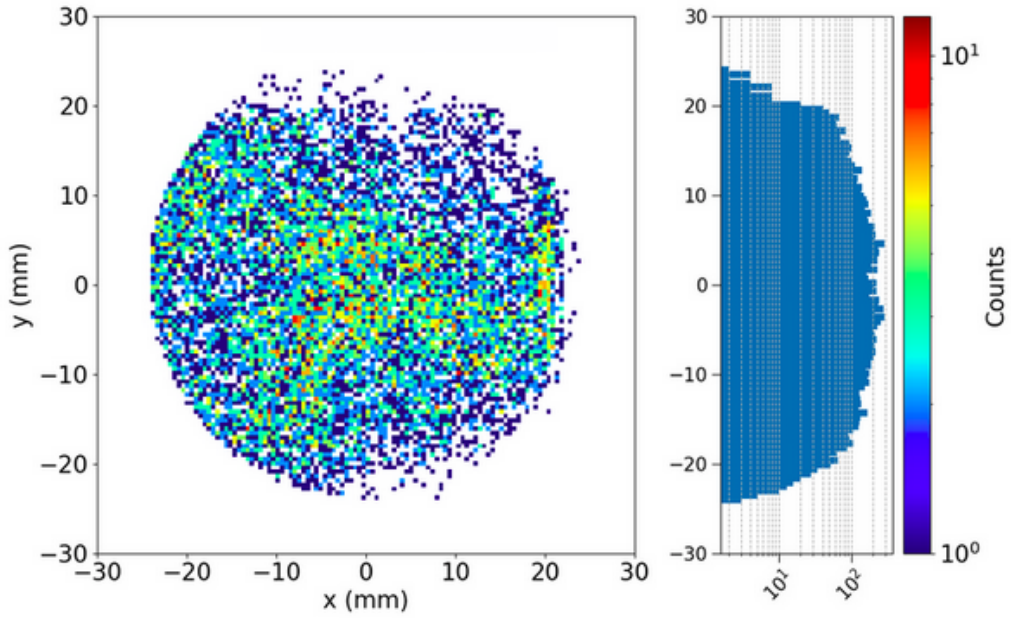

Figure 116: MCP experimental image for an O^{3+} primary beam with no voltages on the spectrometer. The primary beam is detected by the spectrometer Faraday Cup. On the right the horizontal projection is shown in logscale.

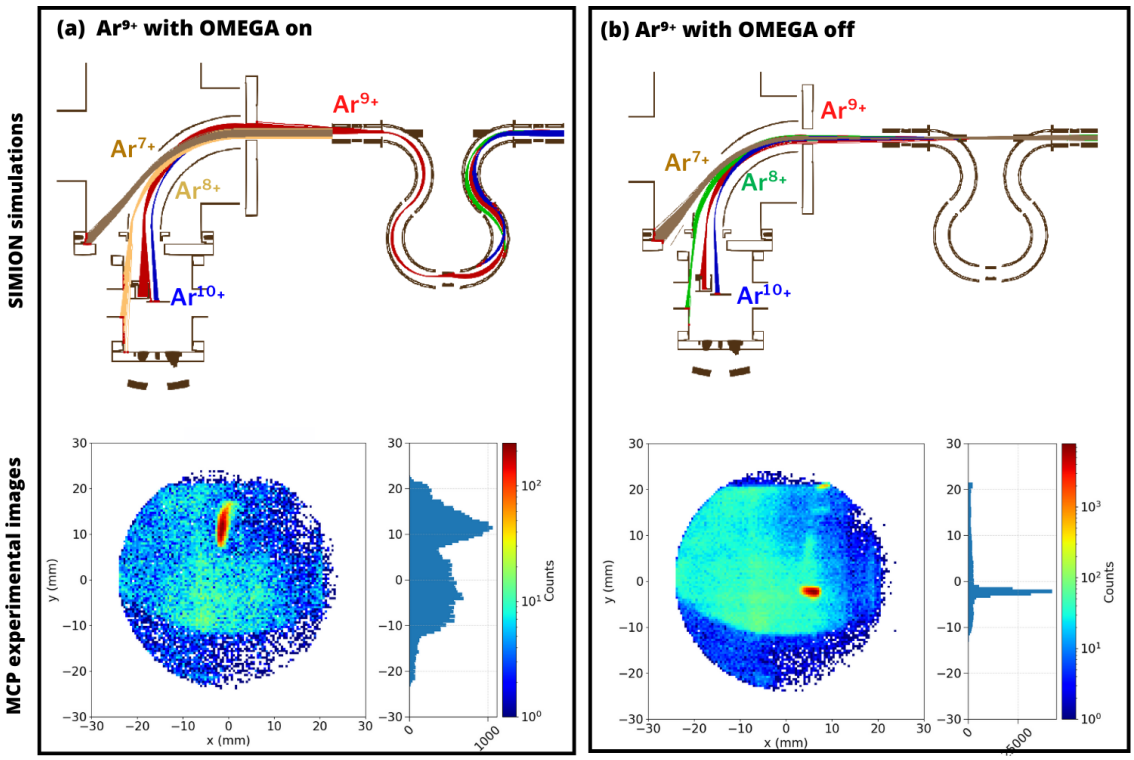

Figure 117: SIMION simulations and MCP experimental images of trajectories for an Ar^{9+} primary beam with the OMEGA on (a) and and turned OFF (b). A gaussian distribution for the position and velocity of the particles was used, as well as and a beam diameter of 3 mm with an emittance of 10 π mm mrad. The horizontal linear scale projections show the shape of the Ar^{10+} peak and the ratio between the background and the signal.

$+ N_2 \rightarrow Ar^{8+}$.

To further study the in-line ionization we performed a scan using the OMEGA as described in section 4.3.1 with a 9.6 µA beam of O^{7+} extracted at 10 kV with the FISIC source. The scan of poor quality is presented Figure 118, and shows the O^{8+} charge state, corresponding to in-line ionization of the O^{7+} primary ions. A difference of three orders of magnitude is measured between the O^{8+} charge state and the O^{6+} charge state resulting from in-line capture. This order of magnitude is coherent with the difference between capture and ionization cross sections measured at ARIBE, and it further highlights the need for more precise experiments to measure ionization cross section for systems and energy domains where data are scarce.

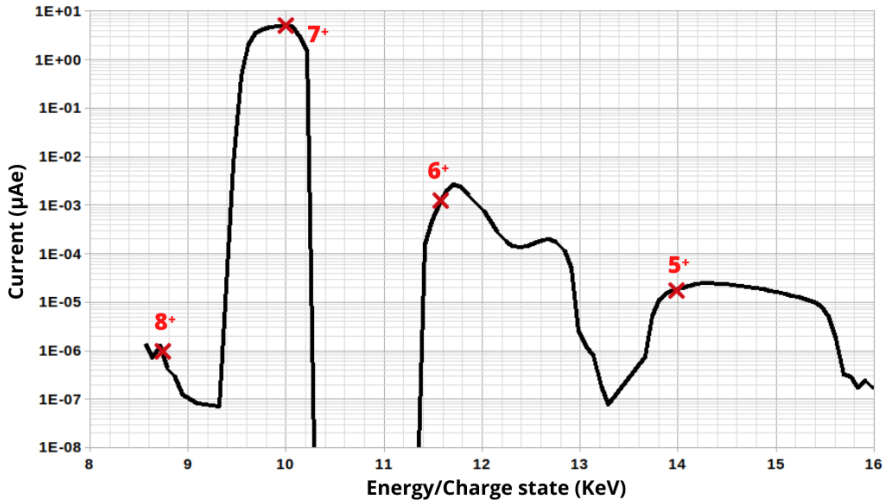

Figure 118: Energy scan of a 4.4 keV/u 9.6 µA O^{7+} primary beam performed with the FISIC source.

5.3.4 Conclusion and future prospects

The performance of a setup composed of the ion spectrometer and the OMEGA purificator installed upstream has been investigated through experimental measurements conducted at the ARIBE facility. Two arrangements were tested, allowing for the observation of capture and ionization processes between the ion beam and the residual gas. Simulations and analysis of background signals were conducted afterward. The primary focus was on testing the consecutive versions of the spectrometer and its ability to accurately separate the ion charge states while characterizing background noise.
The ion spectrometer proved efficient in separating the secondary charge states as intended, and the spectrometer modification allowed to suppress the parasitic peaks originating from elastic collisions inside the spectrometer in the capture configuration. The implementation of the OMEGA was successful in reducing the secondary peaks intensity by a factor of 10 proportional to the reduction in travel distance for secondary ions. Additionally, a transmission of 100% through the OMEGA and the spectrometer was obtained, as well as very good conservation of beam parameters. Capture cross sections were evaluated for Ar^{12+} and Ar^{9+} primary beams, and a very good agreement was found with estimations using the Müller-Salzborn scaling law and the growth-rate method. For the first time an ionization cross section was estimated for the Ar^{9+} primary beam, and comparisons with more recent measures made with the FISIC source indicate that this estimation is coherent. The beams used for the ARIBE experiments had a low emittance of around 5π mmmrad, but simulations conducted with the SIMION software suggest that achieving similar results with a higher emittance (up to 60π mmmrad) is doable with the current setup. Figure 119 shows SIMION simulation of the position and spread of an Ar^{12+} primary beam and secondary Ar^{11+} and Ar^{10+} in the detector Faraday Cup and MCPs for an emittance of 5π mmmrad and 60π mmmrad. The loss of particules due to the higher spread of the beam at an emittance of 60π mmmrad is of the order of 10 %.

In terms of beam intensity, the modifications of the spectrometer allowed to go from beams of a few pA (with the first version of the spectrometer) to beams of a few nA (with the second version). Ultimately our goal is to be able to use primary beams with intensities in the µA range, and these test campaigns have proven that the current setup is not adapted for such intensities. The background coming either from reflections inside the spectrometer or the detector chamber, and from secondary ions and electrons emitted from the Faraday Cup results in a high counting rate on the MCP. The intensity cannot be higher with the current setup without risking damages on the MCPs. The design of the detection system has to be modified to permit the use of µA beams.
The current design of the detector had the advantage of being compact, but given the conclusions from the tests that showed the limitations of the system, the need to decouple the detection of the primary and secondary beams is becoming clear. Several possible design changes of the detector can be contemplated

- A deeper Faraday Cup could prevent secondary electrons from escaping and reaching the MCPs.
- Having movable MCPs and a movable Faraday Cup placed further down in the detector chamber and away from the MCPs (to avoid parasitic charged particles being emitted close to the MCPs) as shown on Figure 120 could permit the detection of secondary and primary beams spread further apart while limiting the background on the MCPs.

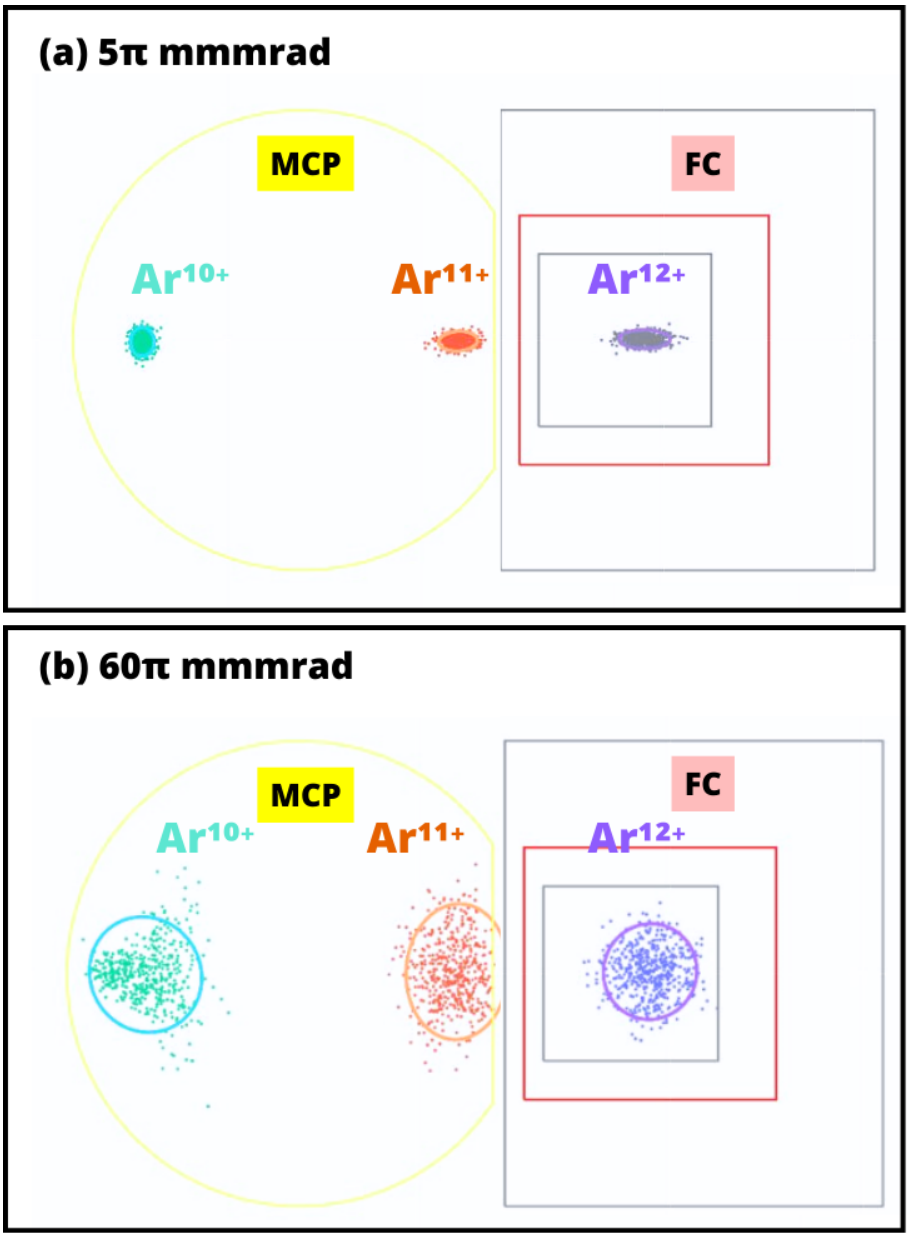

Figure 119: SIMION simulation of the position and spread of an Ar^{12+} primary beam in the detector Faraday Cup and secondary Ar^{11+} and Ar^{10+} on MCPs for an emittance of (a) 5π mmmrad and (b) 60π mmmrad. Simulations were made using 2 mm gaussian beams at the entrance of the ion spectrometer.

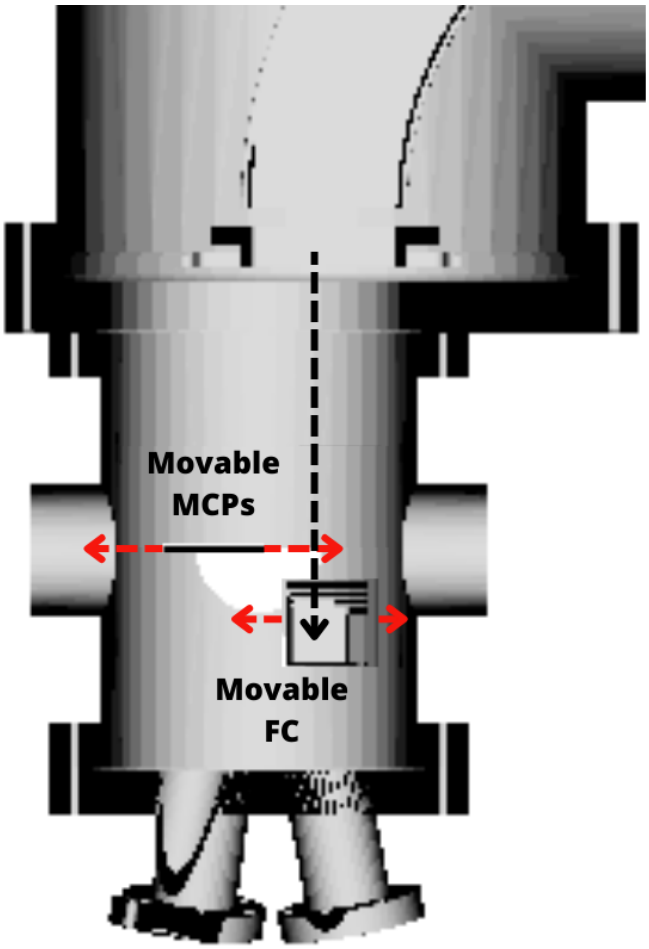

Figure 120: Sketch of possible modifications of the ion detection system, with movable MCPs and movable Faraday Cup.

- The MCPs could also be replaced by a movable channeltron based detector as already done by the Giessen team for ion-ion collision experiments [87, 89].

These changes, along with an improvement in the vacuum, could potentially yield a better signal-to-noise ratio.

6 Preliminary measures for collisions at INSP

In July 2024, a three-week measurement campaign was launched at INSP with the objectives of manipulating the ion beams of SIMPA and FISIC for ion-ion collisions and testing the gas jet for ion-atom. The setup used is depicted in Figure 121. Compared to the collision zone described in section 4.3, the ion spectrometer was not installed due to detector issues mentioned in 5.3. Only the X-ray detector LANCELOT was used, together with two Faraday Cups (FC_{SIMPA} and FC_{FISIC}). Additionally magnetic steerers for precise beam adjustments were installed on the SIMPA beamline, just before the collision chamber, as the steering elements on the beamline were far upstream on SIMPA. Oxygen and argon beams were produced, along with helium and argon gas jets. The following sections present the energy calibration of the X-ray detector, tests with the gas jet, tests with both beams, and a first measurement of the production of metastable states generated by both sources. Brief conclusions are given and evolution of the setup is suggested.

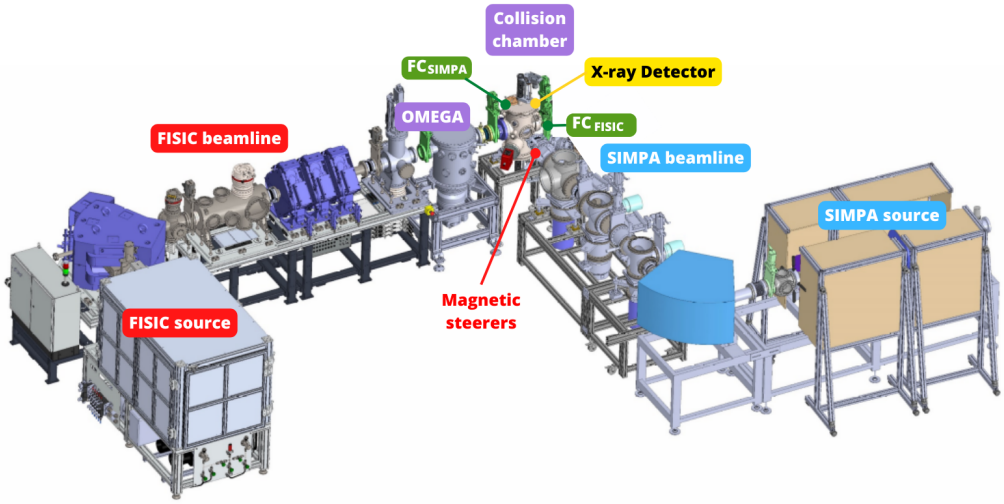

Figure 121: Experimental setup used at INSP for ion-ion and ion-atom collisions.

6.1 Energy calibration of LANCELOT

To accurately analyze the X-ray spectra obtained during collisions, an energy calibration of the system is necessary. For this purpose, three fluorescence X-ray spectra (see Figure 122) were recorded using the electron gun installed in the collision chamber and solid samples of stainless steel, silicon, and ceramic (Al_2O_3). These spectra were recorded over 40 minutes to ensure sufficient accuracy. After a week and a half of measurements, a new stainless steel spectrum was recorded to check for any energy shift. It was found that the energy calibration remained valid, with no shift observed. The spectra were fitted with a Python program using gaussian functions, and the background modeled by a fourth-degree polynomial.

The peak energies are computed using X-ray transition values from the X-ray Data Booklet [207] and the relative weights of the different lines are taken from [208]. Figure 122 presents the X-ray spectra obtained for (a) stainless steel and (b) ceramic samples. In the stainless steel spectrum (a), one can see that six gaussians are necessary to correctly fit the spectrum, while three are used for the ceramic spectrum. The composition of

stainless steel includes Cr, Fe, and Ni elements but contaminants such as C and O are often present. The ceramic sample contains Al and O elements. In Table 29, photon energies of the $K_{\alpha,\beta}$ and L transition lines are given. The peaks corresponding to C, Fe and Ni in the stainless steel sample were used for calibration, and the energies of the latter two were calculated using the barycenter of the Balmer L_α and L_β peak energies, as indicated in Table 29. The peaks modeled by three gaussians between channels 2000 and 2500 originate from Balmer Cr, Fe and Lyman O transition lines, and have not been used in the calibration.

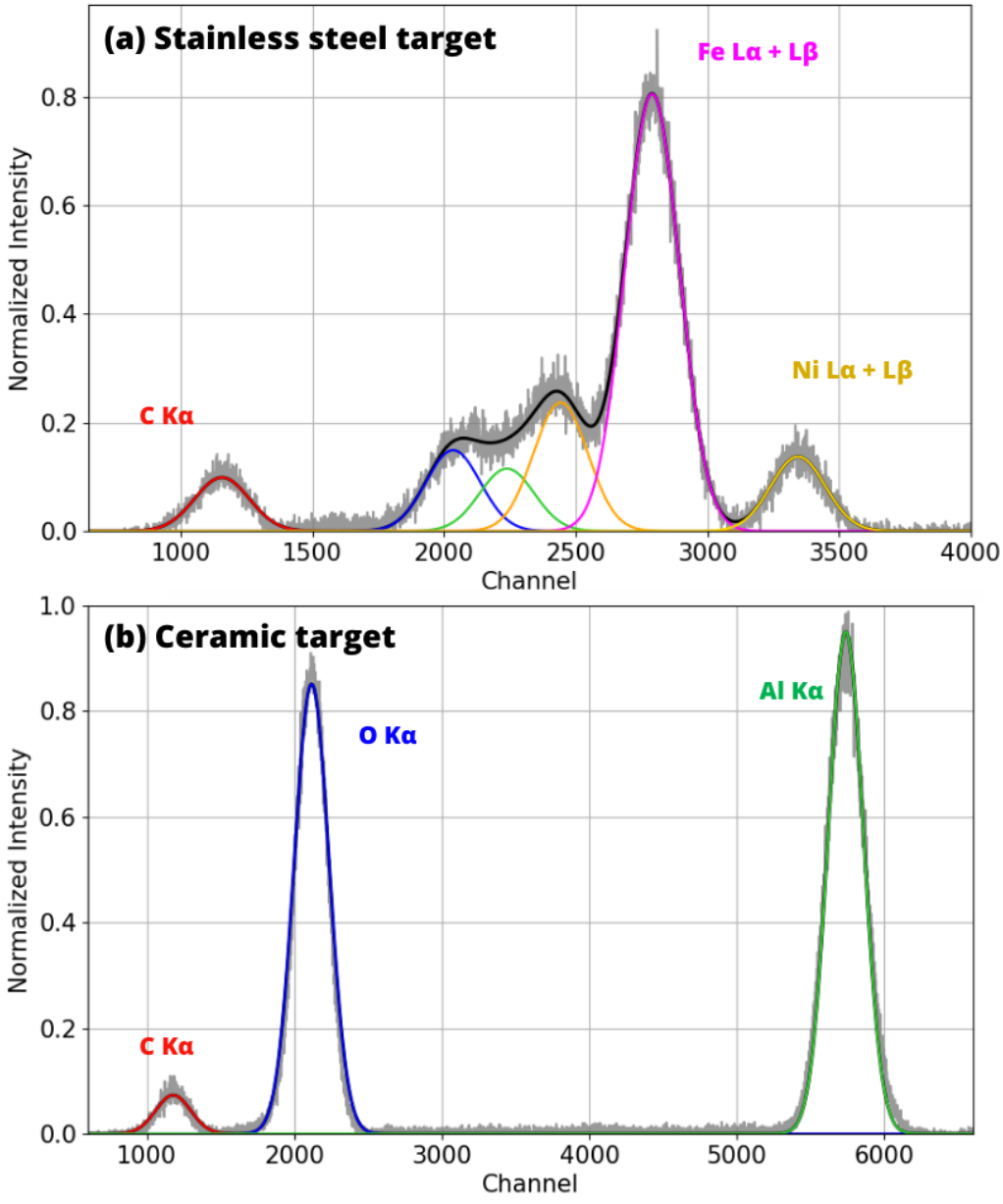

Figure 122: Experimental X-ray fluorescence spectra obtained when 10 keV electrons hit (a) the stainless steel sample and (b) the ceramic sample. Gaussian functions used to fit the peaks are plotted, with the black line being the sum of all gaussians. The background has been removed from the data.

Figure 122 (b) shows the spectrum obtained with the ceramic sample composed of Al and O. Carbon is also present as a contaminant. The peaks are easily identifiable,

and three gaussians were used for the fit. The energy of the Al peak is the barycenter of the Lyman $K_{\alpha 1}$ and $K_{\alpha 2}$ transitions, as indicated in Table 29.
The channel-energy calibration curve obtained from these measurements is presented in Figure 123. This calibration is used for all the X-ray spectra presented in the remainder of this chapter.

Sample	Element	Energy (eV)	Weight	Barycenter (eV)
	C Kα	277		
Stainless Steel	Cr Lℓ	500.3	17	
	Cr Lα	572.8	100	577.2
	Cr Lβ	582.8	79	
	Fe Lℓ	615.2	14	
	Fe Lα	705	100	708.6
	Fe Lβ	718.5	12	
	Ni Lα	851.5	100	853.4
	Ni Lβ	868.8	12	
Ceramic	Al Kα_2	1486.3	50	
	Al Kα_1	1486.7	100	1486.6
	O Kα	524.9		
Silicon	Si Kα_1	1740	100	1739.8
	Si Kα_2	1739.4	50	
	Si Kβ_1	1835.9	2	

Table 29: Energies and barycenter values of the solid targets used for detector calibration. X-ray energies taken from [207] and weights taken from [208].

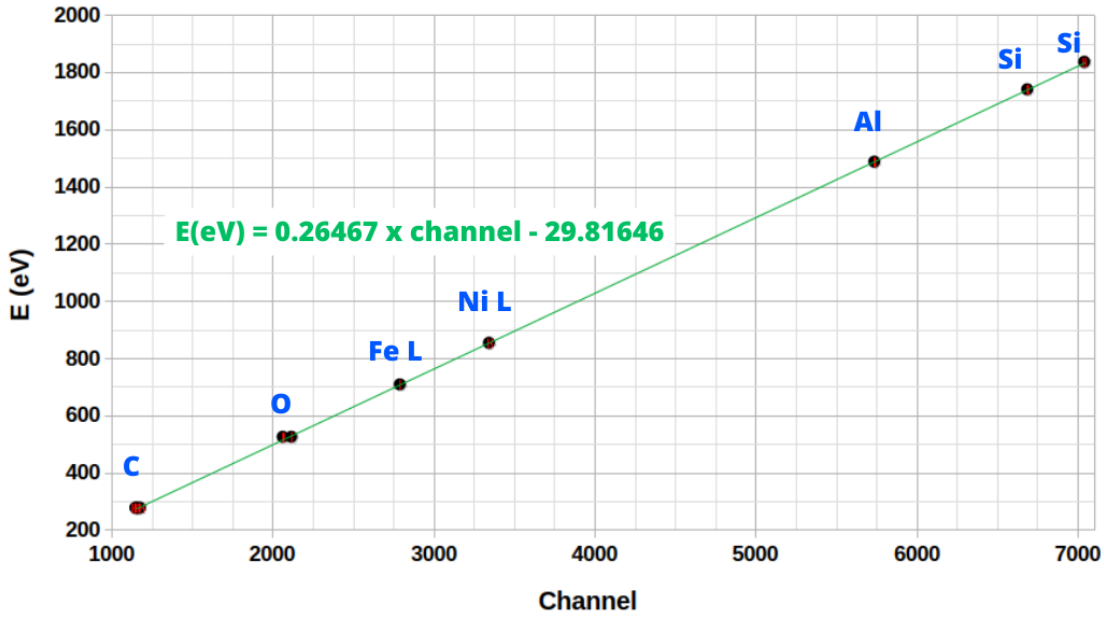

Figure 123: Channel-energy calibration curve for the LANCELOT detector.

6.2 Tests with the effusive jet

The gas jet, whose characteristics are detailed in section 4.3, was tested with argon and helium. The pressure in the collision chamber as a function of the backing pressure was measured. X-ray counting rates were measured as a function of the pressure in the chamber and the capillary distance. $^{16}O^{7+}$ beams from both sources and a ^{40}Ar gas jet were used. These results are presented in the following.

6.2.1 Requirements

In order to achieve reliable detection during ion-atom collisions, a signal-to-noise ratio of approximately 100 is required. In order to meet this criterion, given the effusive jet characteristics, two key conditions must be satisfied:

- The backing pressure must be maintained around 1.5 mbar to achieve an atomic density of a few 10^{12} atoms/cm^3 in the jet.
- The residual pressure within the chamber must remain below 10^{-6} mbar, corresponding to a residual atomic density of approximately 10^{10} atoms/cm^3.

Measurements of the residual pressure as a function of backing pressure for a helium and argon gas jet are presented in the following section.

6.2.2 Pressure tests

The pumping system of the collision chamber consisted of a turbomolecular pump located beneath the chamber. Since we did not have the correct adapter flange, a different one was used, and as a result, the pump is slightly off-center with respect to the jet. The best vacuum obtained with this pumping system in the absence of beam or gas jet was about 1×10^{-8} mbar.
The pressure in the collision chamber was measured as a function of the jet backing pressure to check the efficiency of the pumping system. After each change in the jet pressure, a waiting time of 30 seconds was observed to allow the pressure in the chamber to reach equilibrium. This procedure was first carried out with helium and then with argon. In Figure 124, the evolution is shown for both gases. For helium (a), three separate measurement series, each approximately 30 minutes apart, were conducted, and the jet was turned off between series. It was observed that after each series, the pressure in the collision chamber did not return to its initial value. This indicates that the pumping was insufficient, as the gas was not removed quickly enough, leading to the decision not to proceed with this gas. Test with argon is shown in Figure 124 (b), with a comparison to the first measurement series with helium. For a backing pressure of 1.5 mbar, the pressure in the chamber was 8×10^{-5} mbar with a helium jet and 2×10^{-5} mbar with an argon jet. This is more than an order of magnitude above the requirements given earlier. Moreover the pressure in the jet for a backing pressure of 1.5 mbar is of the order of 10^{-5} mbar, meaning that no jet was formed and the jet only increased the pressure inside the chamber. In conclusion, the pumping system is not sufficient for the size and shape of the collision chamber to meet the pressure requirements for ion-atom collision experiments.

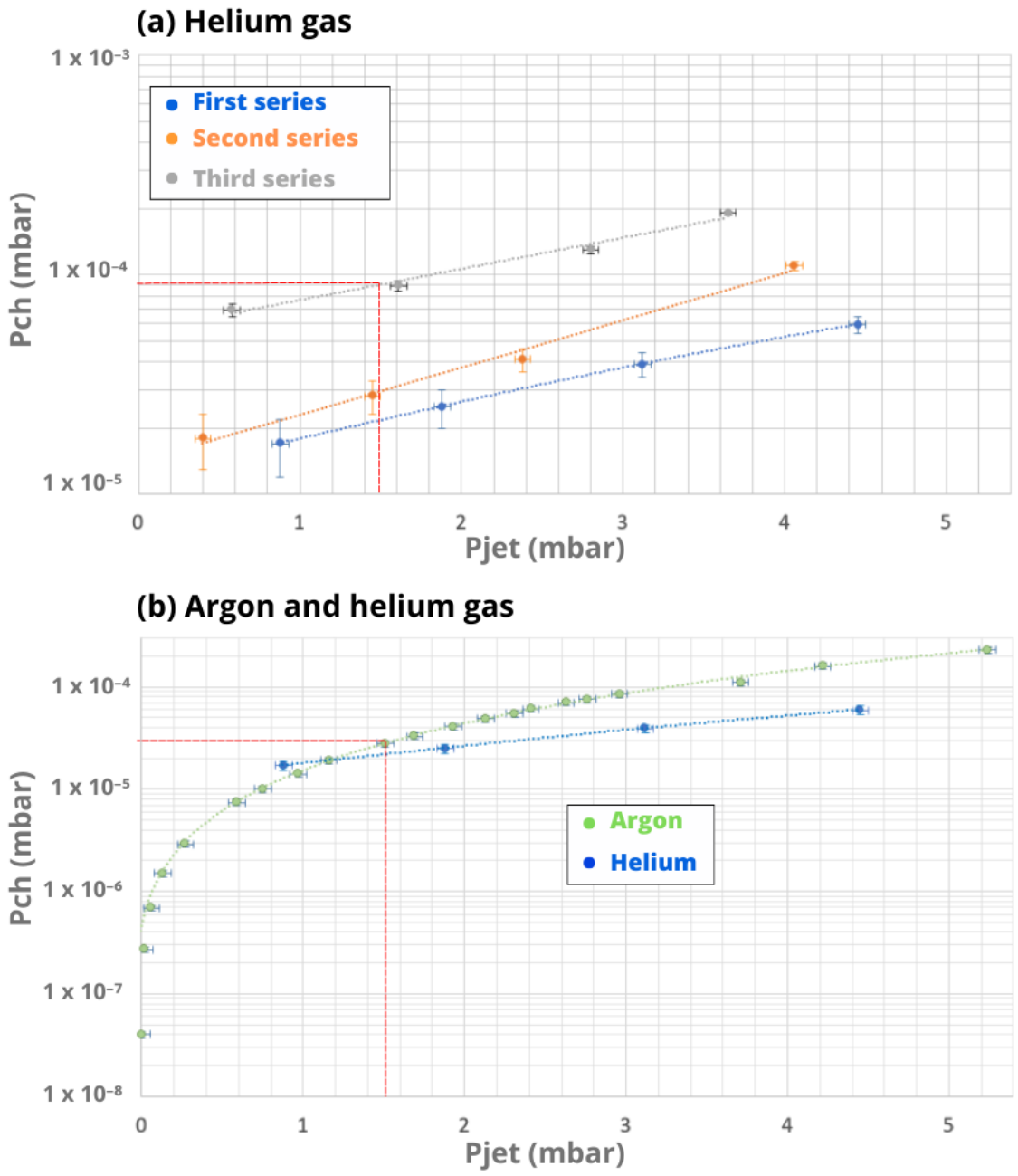

Figure 124: Evolution of the pressure inside the collision chamber as a function of the backing pressure of the gas jet, (a) for three series of measurements with helium, separated by 30 minutes, and (b) for argon compared with the first series of helium.

6.2.3 X-ray yield with residual pressure

The X-ray yield was measured as a function of the residual pressure in the chamber. An O^{7+} beam from SIMPA or FISIC was sent into the collision chamber with an argon jet at a backing pressure between 0.07 and 0.26 mbar. In this range of backing pressure, no jet is formed and the X-ray originate from charge-changing collisions between O^{7+} ions and residual gas in the chamber (mostly argon). The pressure in the chamber ranged therefore from 1×10^{-8} mbar to 4.5×10^{-6} mbar. The number of counts per second on the X-ray detector was normalized to the average current of the beam during each measurement. Figure 125 shows the evolution of the X-ray count rate as a function of

the pressure in the chamber. The rate increases linearly with pressure for both sources,

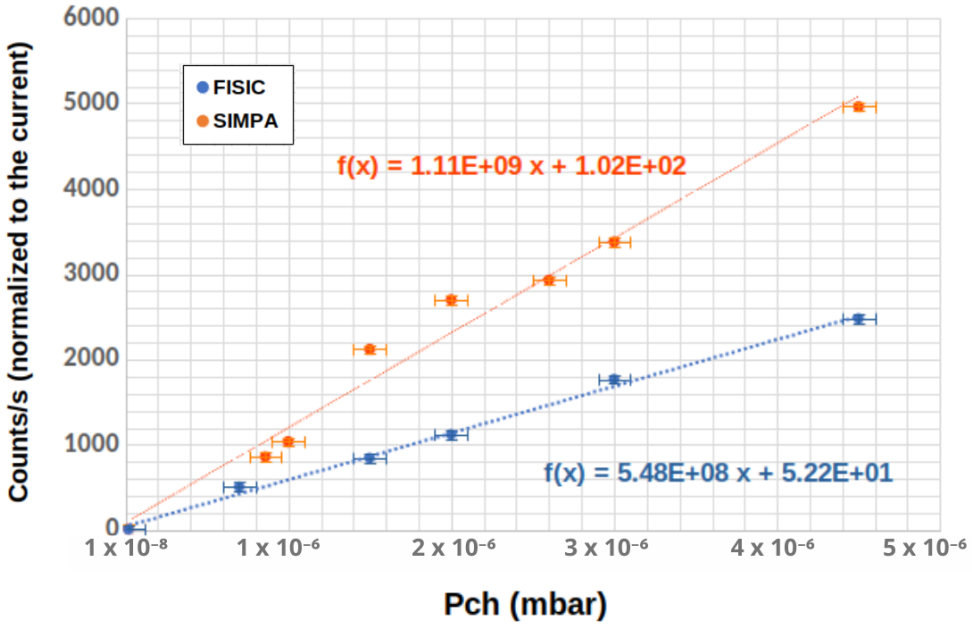

Figure 125: Evolution of the number of counts per second recorded by the X-ray detector as a function of the pressure inside the collision chamber, with 4.4 keV/u O^{7+} beams from FISIC ($\langle I \rangle$ = 2.6 µA) and SIMPA ($\langle I \rangle$ = 2.9 µA).

indicating that we are in the single-collision regime. A factor of two difference is noted between the number of counts recorded on SIMPA and FISIC. This difference could be attributed to the possibility that the SIMPA beam could be larger and not exactly perpendicular to the FISIC beam. Indeed, since the direction and size of the SIMPA beam cannot be adjusted with the same precision just before the collision zone as in the case of FISIC (the magnetic steerers and Einzel lens of SIMPA are further downstream the collision chamber than those of FISIC), differences in the portion of the beam that is in the viewed zone (as presented in the section 4.3.2) could explain the observed difference in the counting rate. The X-ray yield is greater than 10000 counts per second (with a current of 2.9 µA on SIMPA) with a pressure of 3×10^{-6} mbar (backing pressure of 0.3 mbar), which exceeds the detection limit of the detector. From approximately 8000 counts per second, pileup effects begin to appear, which greatly deteriorates the signal and makes the interpretation of the results impossible.
Figure 126[1] shows a typical X-ray spectrum obtained during these measurements. The spectrum is fitted with the sum of three gaussian functions after background removal, and the intensity is normalized to the current of the SIMPA beam. In Table 30 the energies are given for the corresponding transitions, calculated from the Screened Hydrogenic Model [209] [2].

[1]This spectrum (and all spectra presented in this chapter) is not corrected for the efficiency of the X-ray detector, which varies almost linearly between 0.44 for the main peak and 0.6 for the highest energy peak.

[2]Transition energies are spin averaged in the following manner : E(np) = (2 × E(np1/2) + 4 × E(np3/2))/6.

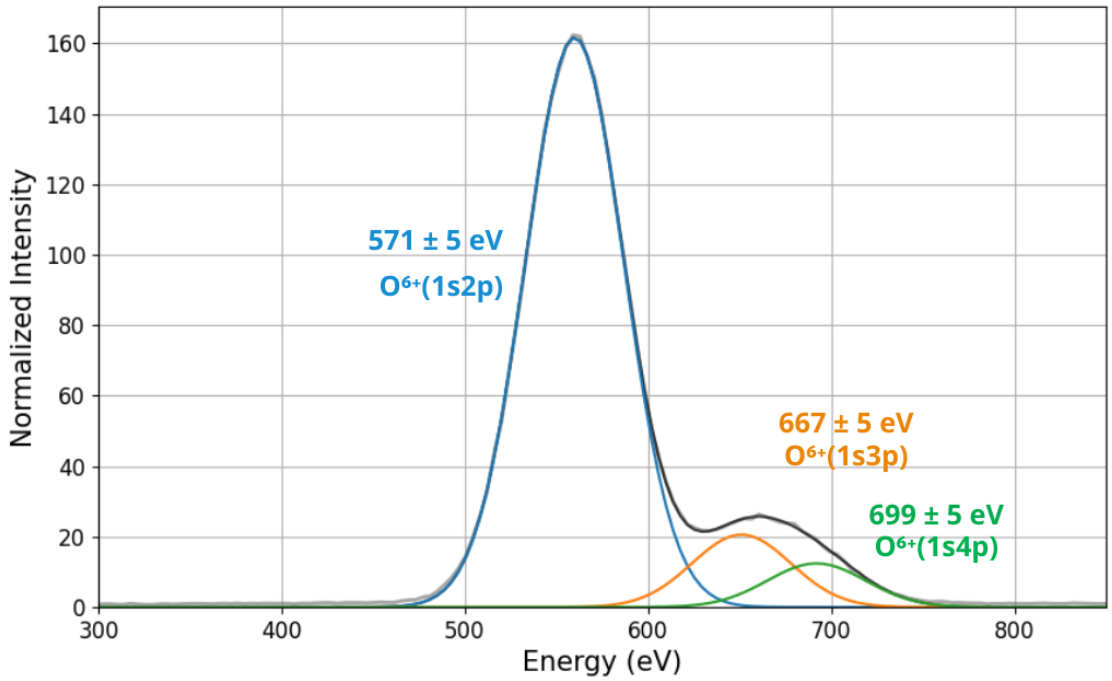

Figure 126: Experimental spectrum obtained with a 4.4 keV/u O^{7+} beam from SIMPA on argon residual gas, with a collision chamber pressure of 2×10^{-6} mbar and a backing pressure of 0.13 mbar. The transitions are between the states indicated and the O^{6+} ($1s^2$).

Initial State	Final State	Energy (eV)
O^{6+}(1s2p)	O^{6+}($1s^2$)	569.8
O^{6+}(1s3p)	O^{6+}($1s^2$)	663.7
O^{6+}(1s4p)	O^{6+}($1s^2$)	696.8

Table 30: Energy transitions in O^{6+} ions, calculated from the screening constants found in Mendoza *et al* [209]

6.2.4 X-ray yield with the position of the capillary

The evolution of the X-ray count rate was measured as a function of the position of the gas jet capillary. Beams of 4.4 keV/u O^{7+} from both FISIC and SIMPA were used, along with argon gas for the jet. The principle of the measurements is shown in Figure 127. The distance h_{jet} between the capillary and the beam varied from 7 mm to 42 mm. Figure 128 shows the X-ray yield as a function of the jet capillary position relative to the interaction point. It should be noted that for a comparison between FISIC and SIMPA, the calibration of the counts per second as a function of pressure determined previously was used. The pressure was 2.0×10^{-6} mbar with FISIC and 2.5×10^{-6} mbar with SIMPA, for a backing pressure of 0.13 mbar. Even with this low pressure, and in a single collision regime, the count rate is still too high (around 4300 counts per second (cps) per µA for a beam-capillary distance under 8 mm, corresponding to more then 10000 cps for beams of more than 2.3 µA).

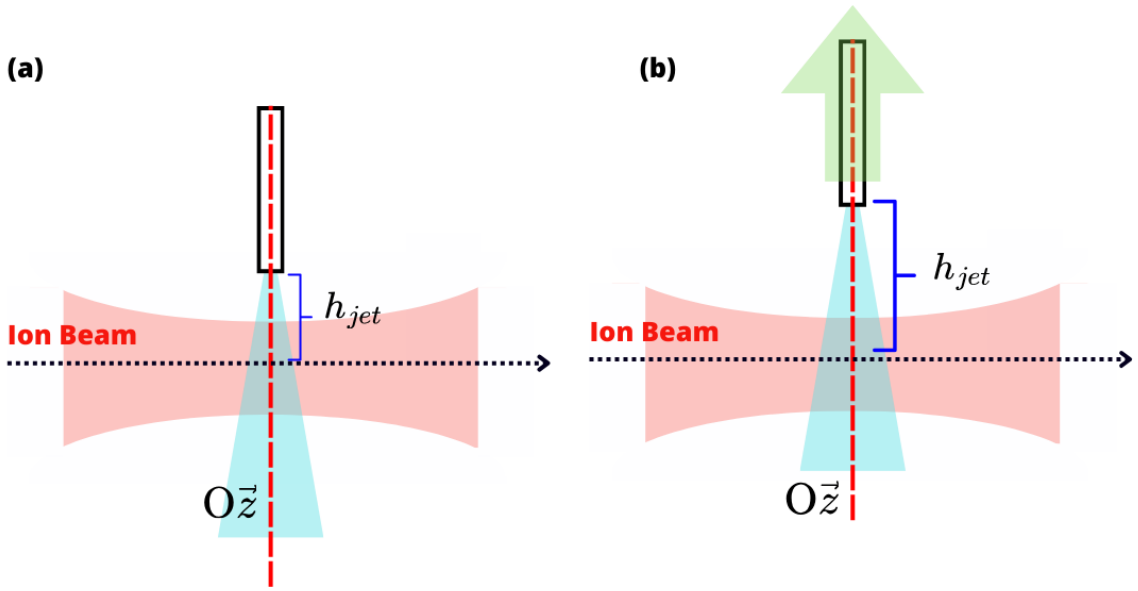

Figure 127: Schematic representation of the measurements principle. (a) Initial position of the jet. (b) The capillary is moved upwards from the beam axis.

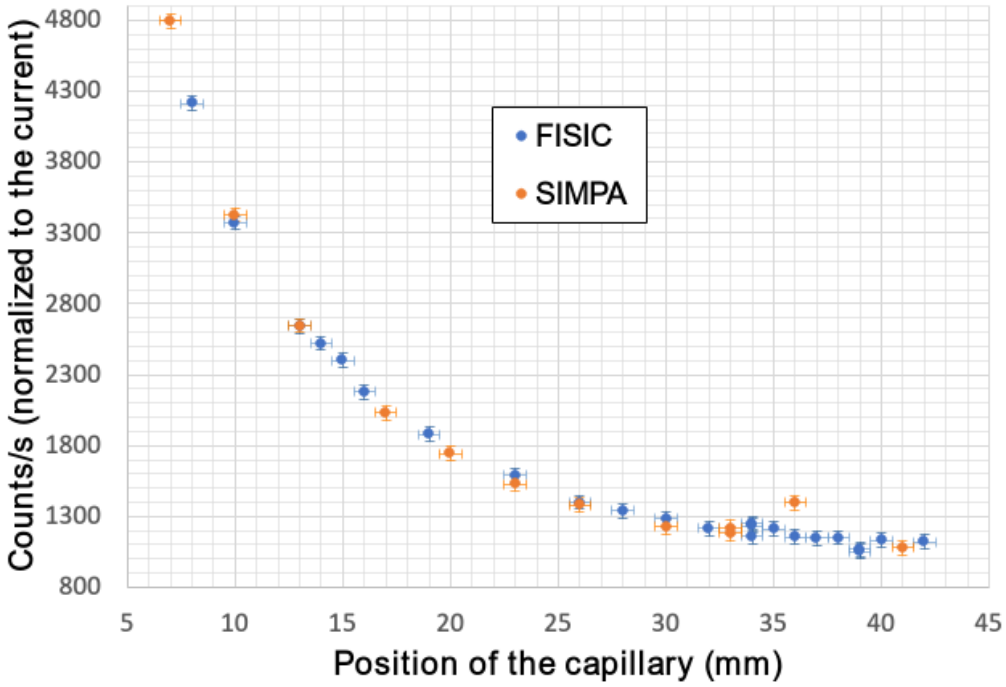

Figure 128: Evolution of the number of counts per second recorded by the X-ray detector as a function of the position of the jet capillary, with 4.4 keV/u O^{7+} beams from FISIC ($\langle I \rangle$ = 2.4 µA) and SIMPA ($\langle I \rangle$ = 1 µA). Collision chamber pressure is 2 $\times 10^{-6}$ mbar with the FISIC beam and 2.5$\times 10^{-6}$ with the SIMPA beam.

6.2.5 Viewed zone of the X-ray detector

Measurements were performed by sweeping the viewed zone with a 3.75 keV/u O^{6+} beam from FISIC (using the pre-collision steerers) and the X-ray yield was recorded. No gas jet was used and the residual pressure inside the collision chamber was 1.8 $\times$ 10^{-8}. The principle of the measurements is represented in Figure 129. The X-ray detector collimator is placed 47 mm from the interaction point. Figure 130 illustrates

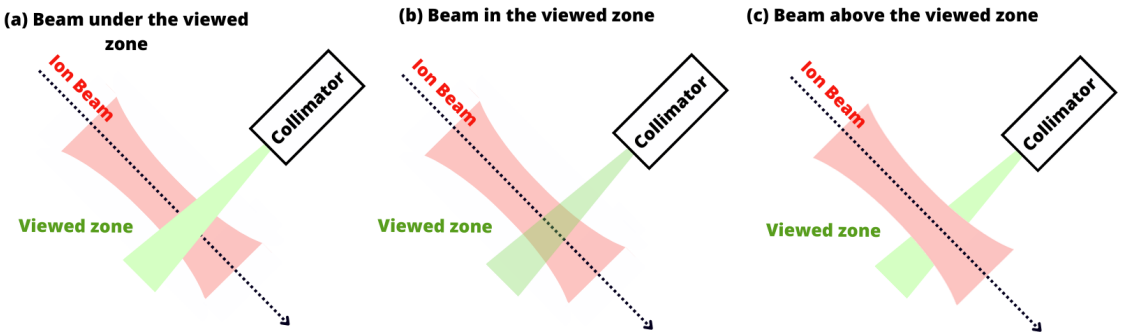

Figure 129: Schematic representation of the measurements principle. (a) Beam under the viewed zone. (b) Maximal overlap between the beam and the viewed zone. (c) Beam above the viewed zone.

the evolution of the X-ray counting rate as a function of the voltage on the steerer (and thus the beam position). The X-ray yield increases until a maximum is reached at 450 V, then decreases almost symmetrically to the rise. This behavior is understandable as the beam "scans" the area observed by the detector, with the maximum counting rate corresponding to the maximum beam in the viewed zone. To sweep the entirety of the viewed zone, a 700 V differential is needed on the steerer to cover the $\sim$ 13 mm as shown in section 4.3.2. Reducing the size of the collimator would reduce the viewed zone, and at the same time the X-ray count rate.

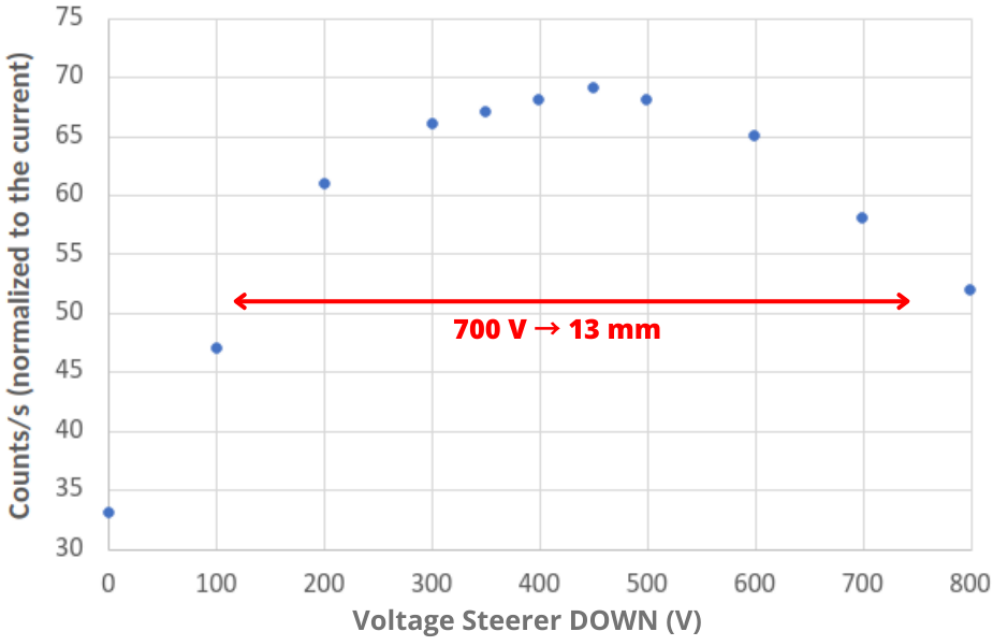

Figure 130: Evolution of the number of counts per second recorded by the X-ray detector as a function of the voltage applied on the pre-collision steerer for two positions of the detector collimator. Measurements made with a a 3.75 keV/u O^{6+} beam from the FISIC beamline with a current of 16 µA.

6.3 Manipulations of both ion beams

In this section, we present the commissioning of the setup for the manipulation of both beams simultaneously. First, the remote control elements are discussed, followed by the manipulation of the ion beam positions. Next, the production of low-charge argon beams is presented, and finally, the methodology for measurements with two simultaneous beams is provided.

6.3.1 Commissioning

For the first time, two ion beams were produced simultaneously by SIMPA and FISIC. The two sources, as well as the various components of the two beamlines, such as dipoles, quadrupoles, steerers, emittancemeter, Einzel lenses, OMEGA... are remotely controlled via various LabView programs. All computers controlling the different parts of the setup are located in a single "command control" corner of the experimental room, allowing for a full access to all elements at once. Figure 131 shows, as an example, three remote control programs used to manage (a) the ion production by the FISIC source, (b) the program used to control the voltages on the OMEGA as well as the current detected by the FC_{FISIC}, and (c) the various elements of the FISIC beamline and the program allowing charge state scans.

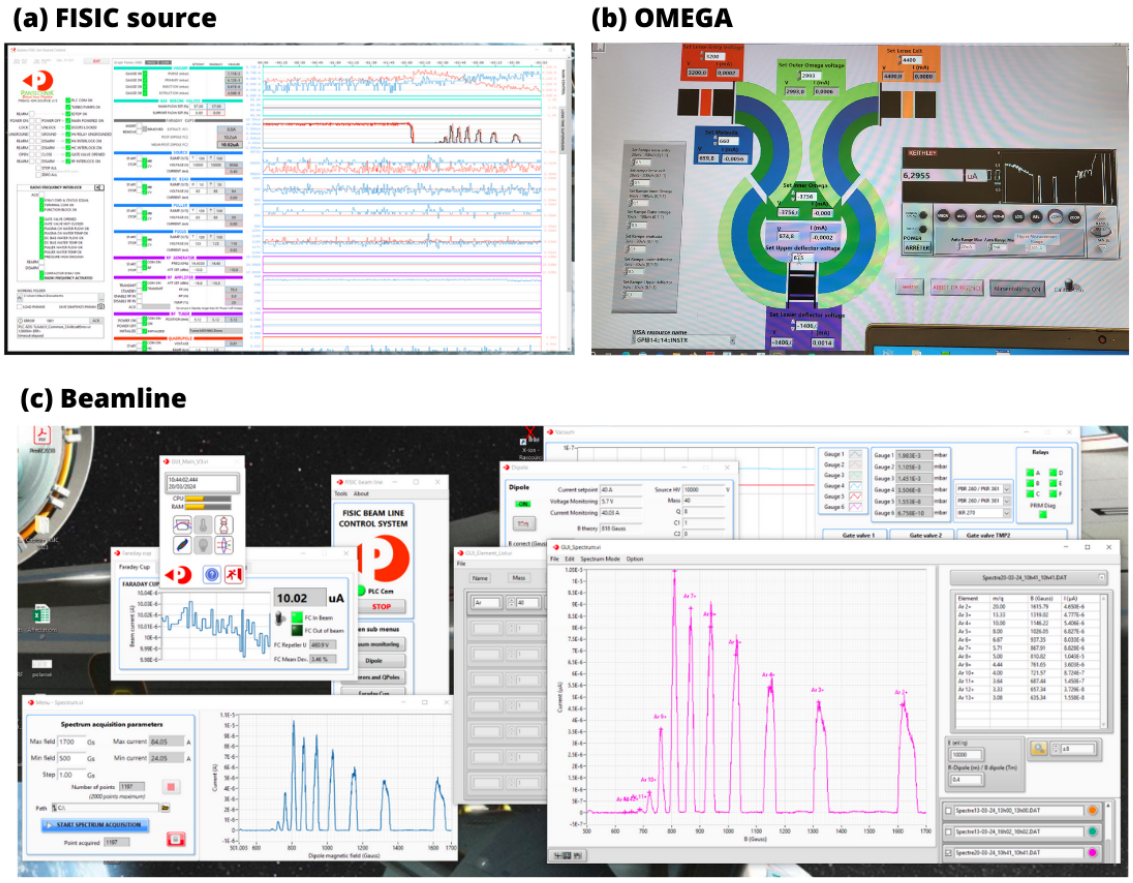

Figure 131: Screenshots of three remote control programs used to manage (a) the ion production by the FISIC source, (b) the voltages on the OMEGA and (c) the various elements of the FISIC beamline and the program allowing charge state scans.

6.3.2 Position control of the beams

To perform collision experiments between two ion beams, it is necessary to control the beam positions to ensure their alignment and proper overlap. The beam position is controlled by steerers, and particularly, the steerers located just upstream of the collision chamber on the FISIC beamline allow for a more precise control of the beam position. As an example, in Figure 132, the image of an O^{5+} beam SIMPA (center) on the stainless steel target and the images of an O^{7+} FISIC beam in four different configurations (left and right) can be seen. The position of the FISIC beam was controlled by adjusting the voltages on the left and bottom steerers, allowing for movement in both vertical and horizontal directions. This study showed that we are able to precisely control the

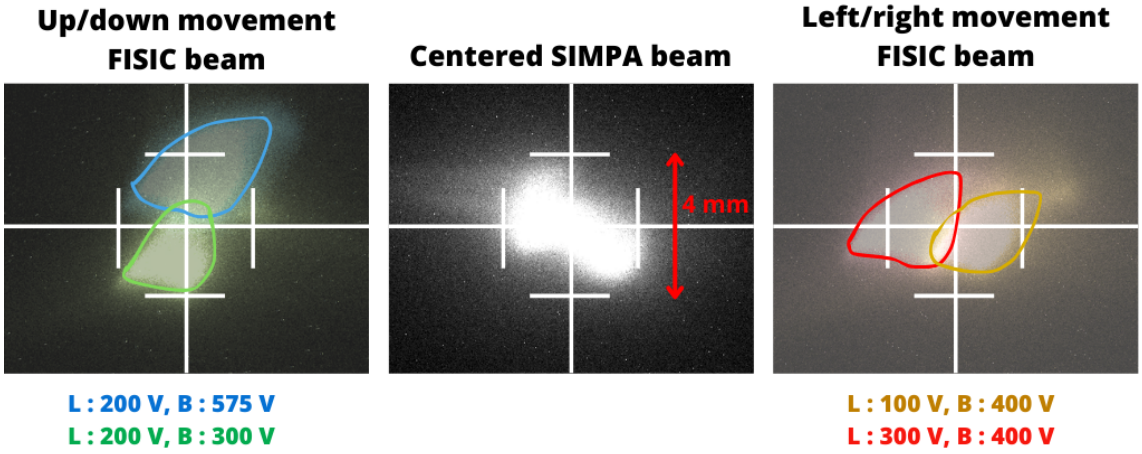

Figure 132: Position of the O^{5+} beam from SIMPA (center) and the O^{7+} beam from FISIC (left and right) for four different steerer settings. Beam current for SIMPA is 7.4 µA and 6.2 µA for FISIC.

position of the FISIC beam to ensure maximal overlap with the SIMPA beam.

6.3.3 Production of low-charged argon

Low-charged argon ions, down to Ar^{2+}, were produced using the SIMPA source. The limitations of our magnetic dipole for charge state selection did not allow us to produce Ar^{1+}. In Figure 133, a charge state spectrum obtained with the SIMPA source when Ar^{4+} is optimized is shown. In Table 31, the currents obtained for each charge state and the corresponding RF power are provided.

Charge state	**I(µA)**	RF power (W)
Ar^{6+}	6.2	50
Ar^{5+}	4.7	44
Ar^{4+}	3.8	34
Ar^{3+}	5.7	30
Ar^{2+}	5.4	0

Table 31: Currents obtained for different charge states of argon ions with the SIMPA source, and the corresponding RF power.

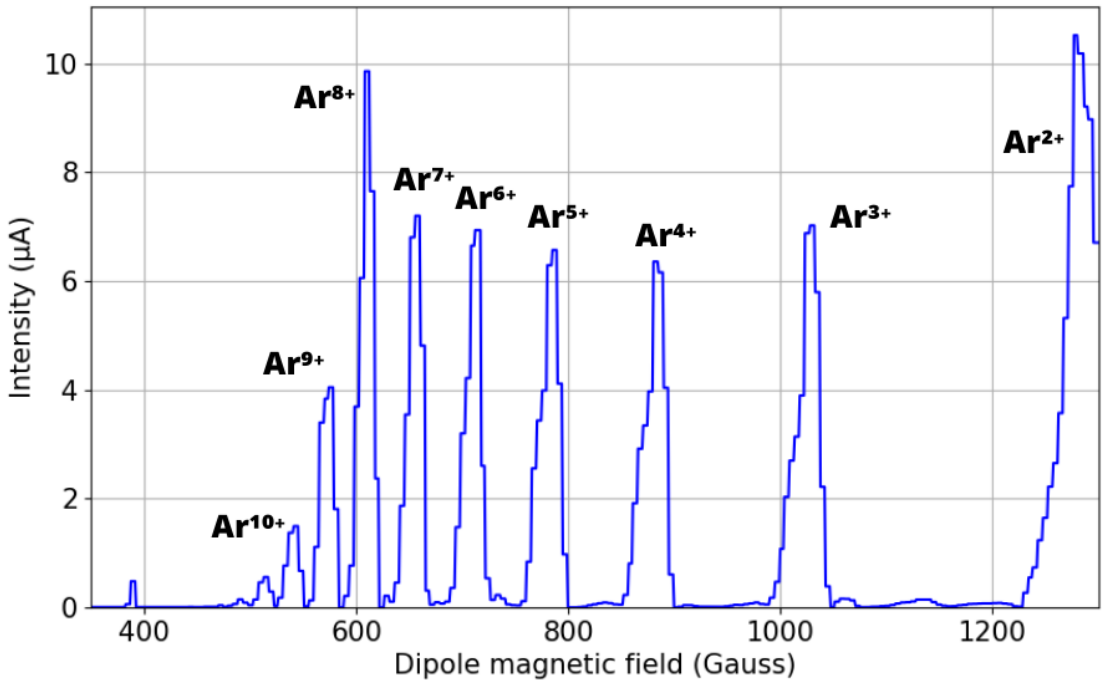

Figure 133: Currents of argon ion beams obtained with the SIMPA source when the Ar^{4+} charge state is optimized.

6.3.4 Methodology

To obtain the most reliable results possible and interpret them correctly, a protocol was established when using both beams:

- First, the beams from both sources are optimized separately. When sufficient current and good stability are achieved, they are driven to the collision chamber.
- The FISIC beam is passed through the OMEGA, and for both beams, care is taken to ensure nearly 100% transmission from the exit of the dipole to the collision chamber.
- The images of the two beams on the solid target (silicon, ceramic or stainless steel, selected based on the incident beam current) are examined separately, and the position of each beam is adjusted with steerers to center it on the target, and focalized with Einzel lenses. The correct overlap of the two beams is then verified.
- An X-ray spectrum of the separated beams in the collision chamber is recorded to ensure, among other things, that the counting rate is not too high and that no X-rays from ion-surface interactions are detected. This reference spectrum can also be used for background subtraction.
- The spectrum is then recorded with both beams simultaneously. During this time, the current of both beams, detected in the Faraday Cups located after the collision chamber in the beam alignment, is recorded, with a measurement taken every 10 seconds. This allows for the calculation of an average current to normalize the counting rate. The pressure inside the collision chamber is also recorded for normalization.

6.4 Tests with both ion beams

In this section we first give an estimate of the counting rates for ion-ion collisions, compared to the counting rates for ion-residual gas collisions. Then the X-ray spectra obtained are presented for several ion species.

6.4.1 Estimation of counting rates for ion-ion collisions

Table 32 shows the expected number of interactions per second originating from ion-ion collisions for 3 selected collision systems, compared for each system to the number of interactions per second expected from residual gas collisions N using

$$N = (P_S \times \frac{I_S}{q_S \times e} + P_F \times \frac{I_F}{q_F \times e}) \tag{121}$$

where I_i $(i = S, F)$ is the current of the beam from SIMPA or FISIC and q_i is the charge of the ions. P_i is the probability of interaction given by

$$P_i = \sigma_i \times n \times 2 \times \ell \tag{122}$$

where σ_i is the cross section of the change exchange process on residual gas, ℓ the length traveled in the viewed zone of the detector and n the number of residual gas targets (multiplied by two because the residual gas is mostly composed of N_2), expressed as

$$n = \frac{P(\text{mbar}) \times 10^{-4}}{k_B T} \tag{123}$$

The charge exchange processes of the oxygen and argon ions considered have cross sections of the order of 10^{-15} cm^2, so this value is the one used in these estimations. A current of 1 µA for both beams is assumed as well as a collision chamber pressure of 1 $\times$ 10^{-8} mbar. One can see that the expected count rate for ion-residual gas collisions

System	Ion-ion (cps)	Ion-residual gas (cps)	Ratio
O^{7+} - O^{8+}	20.8	4.8×10^5	4.2×10^{-5}
O^{7+} - O^{7+}	24.5	5.2×10^5	4.7×10^{-5}
O^{7+} - Ar^{6+}	40.1	5.6×10^5	7.2×10^{-5}

Table 32: Comparison of expected interaction rates for different collision systems, and the ratio between ion-ion and ion/residual gas interactions.

is about 5 orders of magnitude larger than the expected count rate for ion-ion collisions for each system. This means that with the pressure conditions in our current setup, as well as the absence of coincidence measurements, it is not possible to detect the signal from ion-ion collisions above the background originating from collisions with the residual gas. The X-ray spectra showed in the following only represent the interaction between the ions and the residual gas.

6.4.2 X-ray spectra

We present here a selection of X-ray spectra originating from ion-residual gas interactions taken in ion-ion collision conditions (with beams from SIMPA and FISIC overlapping in the collision zone) for several collision systems.

- **O^{7+} (FISIC) and O^{q+} (q = 5, 7), Ar^{q+} (q = 2, 3, 4, 5, 6) (SIMPA)** : The X-ray spectra recorded for all these collision systems have the exact same shape as the spectrum presented in Figure 126 (O^{7+} on argon residual gas). No X-ray is produced by O^{5+} and Ar^{2+} to Ar^{6+}, therefore all detected X-ray when both SIMPA and FISIC beams are in the collision chamber originate from interactions between the O^{7+} ions and the residual gas. In Figure 134, we illustrate the fact that all spectra are nearly identical by showing the superposition of X-ray spectra obtained for O^{7+} - Ar^{q+} systems. The intensity has been normalized to the current of the O^{7+} beam and the collision chamber pressure. For the case of the O^{7+} - O^{7+} system, X-rays from FISIC and SIMPA are detected. To separate the peaks, the O^{7+} - O^{8+} system has been studied. For the case of the O^{7+} - O^{7+} system,

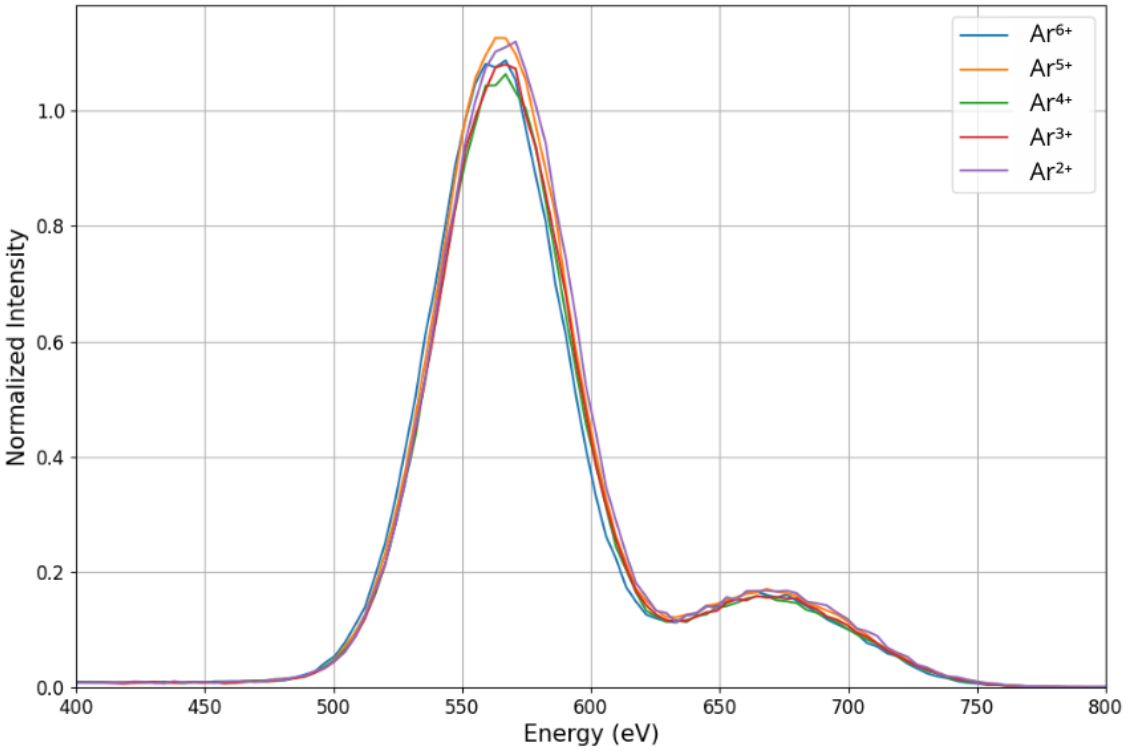

Figure 134: Experimental X-ray spectra for collisions of O^{7+} and Ar^{q+} (q = 2, 3, 4, 5, 6) at E_{cm} ranging from 4.4 keV/u to 5.5 keV/u on residual gas, with the intensity normalized to the current and pressure in the collision chamber.

X-rays from FISIC and SIMPA are detected. To separate the peaks, the O^{7+} - O^{8+} system has been studied.

- **O^{7+} - O^{8+}** : The methodology of the measurements given earlier in section 6.3.4 is illustrated with this collision system : the individual X-ray spectra from the interaction of each beam with the residual gas are shown, followed by the spectrum recorded with both beams simultaneously. Figure 135 presents the spectra obtained separately when (a) a 3.6 µA O^{7+} beam from SIMPA and (b) a 0.8 µA O^{8+} beam from FISIC capture on residual gas. The spectrum from O^{7+} is identical to the one presented in Figure 126 and has been fitted with the sum of three gaussians. The O^{8+} beam captures on residual gas in the collision chamber, resulting in the spectrum (b). It has been fitted with the sum of four gaussians. The O^{8+} ions can also capture on the residual gas of the beamline downstream

the viewed zone, and the resulting O^{7+} ions can in turn capture on residual gas in the collision chamber into O^{6+}. This results in a fourth peak at 570 ± 5 eV on the O^{8+} spectrum corresponding to $O^{6+}(1s2p) \rightarrow O^{6+}(1s^2)$. The energy of each peak is given on Figure 135, along with the corresponding transition. The energies of these transitions calculated from the Screened Hydrogenic Model with screening constants from [209] are given in Table 33.

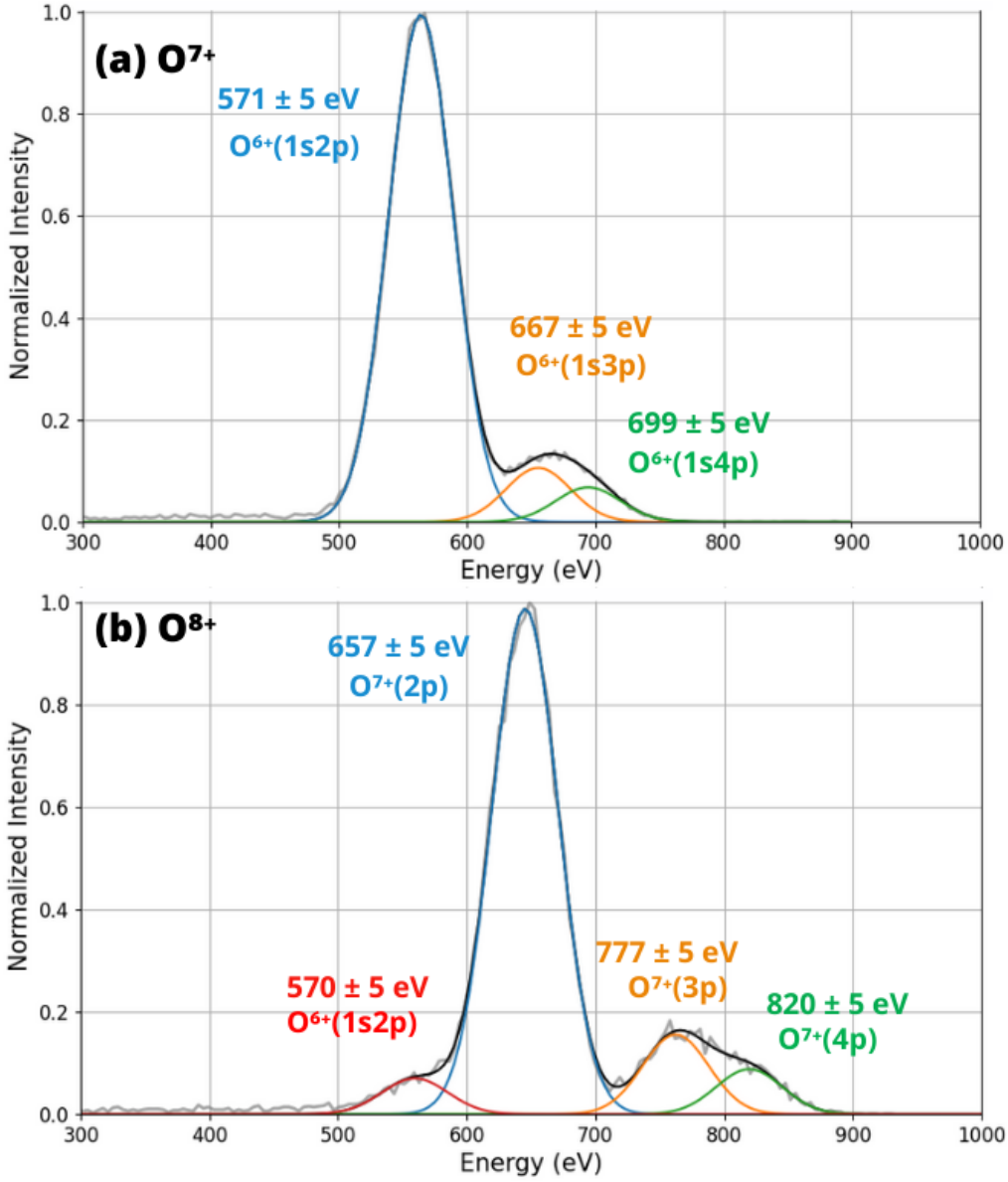

Figure 135: Experimental spectra obtained with (a) a 4.4 keV/u 3.6 µA O^{7+} beam from SIMPA and (b) a 5 keV/u 0.8 µA O^{8+} beam from FISIC colliding on residual gas. Fits made using 3 gaussian functions, with energies and corresponding transitions indicated.

Figure 136 shows the spectrum obtained when both beams are in the collision chamber. The fit has been made with a sum of 6 gaussians. The energy values taken as the center of the gaussians are the energies previously determined from the fits of the individual spectra in Figure 135. The resulting gaussians give a very satisfactory fit of the data. In addition, the ratios between the main and the two secondary peaks have been computed for the two spectra in Figure 135. The

Initial State	Final State	Energy (eV)
$O^{6+}(1s2p)$	$O^{6+}(1s^2)$	569.8
$O^{6+}(1s3p)$	$O^{6+}(1s^2)$	663.7
$O^{6+}(1s4p)$	$O^{6+}(1s^2)$	696.8
$O^{7+}(2p)$	$O^{7+}(1s)$	653.7
$O^{7+}(3p)$	$O^{7+}(1s)$	774.7
$O^{7+}(4p)$	$O^{7+}(1s)$	816.9

Table 33: Energy transitions in O^{6+} and O^{7+}, calculated from the screening constants found in [209].

ratios of the corresponding peaks in the spectrum obtained with the two beams in Figure 136 have been computed in the same way, and the comparison between the two is given in Table 34. The ratios are compatible between the individual spectra and the spectrum with both beams, further confirming the accuracy of the fit.

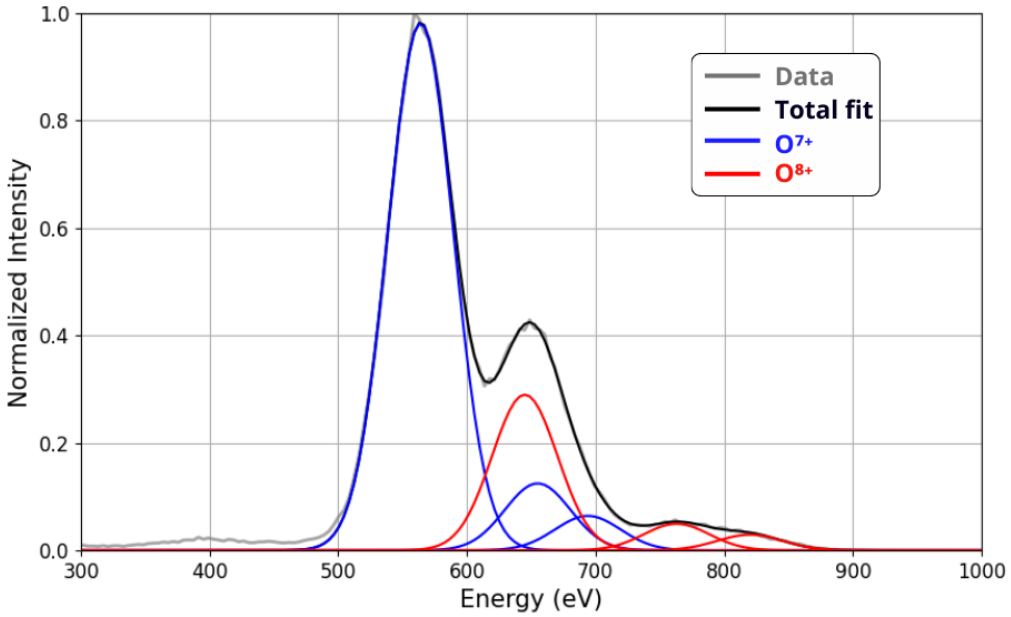

Figure 136: Experimental spectrum obtained with O^{7+} and O^{8+} beams at $E_{cm} \approx 9.61$ keV/u, with a 0.8 µA O^{8+} beam from FISIC and a 3.6 µA O^{7+} beam from SIMPA colliding on residual gas. Fit made using 6 gaussian functions, with energies from the fit of the individual spectra in Figure 135. Gaussians from O^{7+} in blue and from O^{8+} in red.

	O^{7+}	O^{8+}	O^{7+} + O^{8+}
$O^{6+}(1s3p)/O^{6+}(1s2p)$	9 ± 1		8 ± 1
$O^{6+}(1s4p)/O^{6+}(1s2p)$	14 ± 1		16 ± 1
$O^{7+}(3p)/O^{7+}(2p)$		6 ± 1	6 ± 1
$O^{7+}(4p)/O^{7+}(2p)$		12 ± 1	11 ± 1

Table 34: Comparison of peak ratios for the individual spectra of O^{7+} and O^{8+} and the spectrum with both beams.

6.5 Estimation of the metastable states fraction

In the case of a beam of O^{6+} in the ground state ($1s^2$), the capture process on the residual gas produces excited $O^{5+}(1s^2\ n'\ell')$ states. Consequently, no X-rays are observed. However, if states of O^{6+} with a K-shell vacancy are present, then X-ray emission can occur. Figure 137 shows a plot with two superimposed spectra, one obtained with an O^{6+} beam (blue) and the other one with an O^{7+} beam (red). Note that the intensities are normalized to 1. A peak around 557 ± 5 eV on the O^{6+} beam spectrum is present, with X-ray yield of the same order of magnitude (corrected to the beam current) than the main peak of the O^{7+} beam spectrum. The energy of the peak around 557 eV is

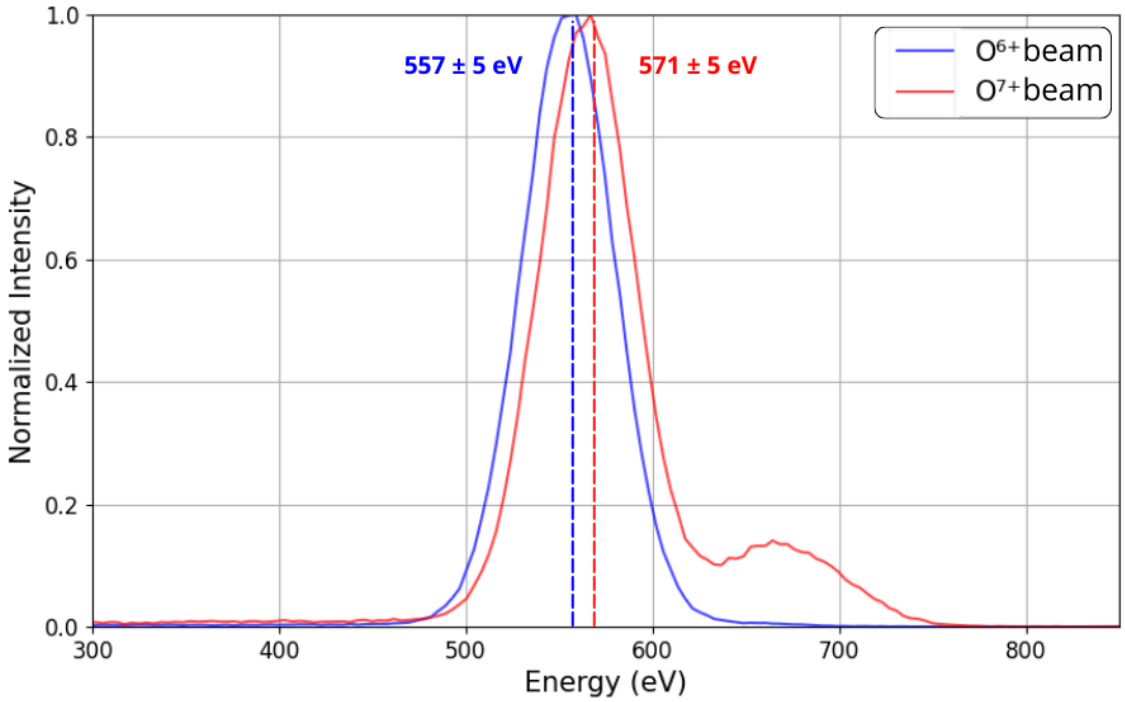

Figure 137: Comparison between experimental X-ray spectra obtained with a 3.75 keV/u O^{6+} beam from SIMPA (blue) and a 4.4 keV/u O^{7+} beam from FISIC (red) colliding on residual gas. Intensities have been normalized to 1.

inferior by 14 eV to the $O^{6+}(1s2p) \rightarrow O^{6+}(1s^2)$ transition seen in the spectrum from O^{7+} beam colliding with residual gas, as already studied. This shows a clear signature of the presence of additional electrons in the initial L-shell. This is attributed to the production of excited states of $O^{6+}(1sn\ell)$ by the source, which in turn capture electrons

to lead to the formation of excited $O^{5+}(1s n\ell n'\ell')$ decaying to $1s^2 n\ell$. The initial excited states of $O^{6+}(1s n\ell)$ that can be produced by the sources are as follows:

- **1s2p ^{1}P** : this singlet state decay via the resonance line (E1) with extremely short life (a lifetime of a few hundred femtoseconds [210]), and therefore no ions with this charge state are extracted from the source.
- **1s2p ^{3}P** : this triplet state which is metastable decays via the intercombination line and has a lifetime of 1.5 ns [210, 211], corresponding to traveled distances of a few millimeters with the typical kinetic energies of our ion beams, and therefore the ions in this state do not reach the dipole.
- **1s2s ^{1}S** : this singlet state decays by two-photon emission (2E1) with a lifetime of 0.4 µs [212], which corresponds to a traveled distance of 0.4 m at our energies. Therefore since the distance between the sources and the collision chamber is around 6 m, no ions in this state reach the X-ray detector viewed zone.
- **1s2s ^{3}S** : this triplet state which is a metastable decaying via (M1) transition has a very long lifetime of around 956 µs [213], corresponding to a distance of 900 m. In consequence, almost all these ions produced in the plasma chamber can reach the end of the beamline and consequently the viewed zone.

Therefore, the X-rays measured are the consequence of the presence of O^{6+} in the 1s2s ^{3}S configuration, giving rise to the formation of O^{5+}(1s2s (^{3}S) 2p)) by electron capture on the residual gas. This claim is supported by the energy of the transition as follows.
The NIST Atomic Data Booklet [214] gives the energies of this transition for the two spin configurations of O^{6+}(1s2s), e.g. 554.2 eV for triplet state and 568.2 eV for singlet state. Experimentally we have a transition energy of 557 $\pm$ 5 eV, which is closer to the value of the triplet state transition. Therefore the X-rays detected allow us to characterize the ion beam in terms of metastable states present at the collision point, but also to calculate the proportion of metastable O^{6+}(1s2s)^{3}S produced in the ion source via the counting rate.
Using the method previously described in section 6.4.1 to estimate the number of counts (taking into account the detector efficiency $\varepsilon = 0.4$ and solid angle $\Omega = 5.63 \times 10^{-5}$), we can compare the number of 1s2s ^{3}S metastable ions in the beam and the total number of ions calculated from the total current measured by the Faraday Cup, as shown in Table 35. For this we assume that all photons detected originate from metastable states, and that the fluorescence yield is 100 % whatever the charge state and the electronic configuration, which is a crude approximation. This can give an estimate for the percentage of metastable states in the beam of 25 % for the FISIC source and 40 % for the SIMPA source. These values are higher than anticipated.
However this study was conducted on a limited number of data, and more systematic measurements need to be conducted with different ion species and by varying the RF power on the source.

6.6 Evolution of the setup at INSP

We have demonstrated with the experimental data from these three weeks of experiments that the only detectable events are the collisions between the beams and the residual gas, both in ion-atom and ion-ion configurations. The pressure in the chamber

Source	RF power (W)	**Metastable (pps)**	**Total (pps)**	**% of metastable**
FISIC	83	6.2×10^{12}	2.4×10^{13}	25
SIMPA	91	5.3×10^{12}	1.6×10^{13}	40

Table 35: Estimation of the number of metastable ions (in particles per second), the total number of ions in the beam, and the percentage of metastable states.

being too high (of the order of 1×10^{-8} mbar) is the main cause, along with the area observed by the detector, which is too large. These two points represent significant opportunities for improvement, that can be achieved by changing the pumping system in the collision chamber to reduce the pressure by 2 orders of magnitude and by reducing the diameter of the LANCELOT collimator.
Even after a reduction in pressure and viewed zone, it appears that given the estimated difference in counting rates between the background from collisions with the residual gas and the signal from ion-ion/atom collisions, it is absolutely necessary fro future experiments to perform coincidence detections with the ion spectrometer to have a chance of observing anything meaningful. Additionally, placing the collision zone under high voltage could be considered to better separate the collision products.

Conclusions and perspectives

This thesis investigates ion-ion and ion-atom interactions with the aim of enhancing our understanding of the electronic dynamics during these collisions. Part of this project is a theoretical study and was conducted at LCPMR. The results presented in the thesis are based on a semiclassical non-perturbative approach called Asymptotic States Close-Coupling (ASCC) and on the use of the related computer codes developed by the team. In this approach, the relative motion between the projectile and target is described classically by straight-line, constant-velocity trajectories, while quantum mechanics is used for the electronic dynamics. The resulting time-dependent Schrödinger equation is solved by expanding the electronic wavefunction on sets of states of the target and projectile when infinitely separated. This approach is necessary to describe many coupled electronic channels in the intermediate energy domain. In the present computer implementation, the states can hold up to 4 active electrons and are expressed in terms of Gaussian Type Orbitals (GTOs) and their correctly antisymmetrized products. They describe precisely the ground and excited states of the collision partners (in different charge states) and also pseudostates, with energies below and above the ionization threshold(s), the latter modeling continuum states.
To construct the state basis for the description of the three collision systems investigated in this thesis, a Python code to optimize the GTOs to express the atomic states has been developed and used, with a strategy based on two criteria: obtaining precise energies for the states of importance in the dynamics while limiting the number of GTOs to have tractable computations for the dynamical stage of the program. With very large sets of states, which are very demanding in computational resources (CPU, RAM), cross sections for total and state-resolved single and double capture, excitation, and ionization channels have been obtained with controlled convergence.
During the thesis, three collision systems with one and two active electrons have been studied: C^{6+} + H(1s) for impact energies ranging from 0.1 to 100 keV/u, N^{6+}(1s) + He^{+}(1s) in the 0.25-25 keV/u range, and N^{7+} + He($1s^2$) within the 0.25-100 keV/u energy range. The first system was studied to develop the code for state optimization and to practice the use of the collision code. The results were compared to very intensive calculations recently published, performed with an alternative code based on the same approach: the comparison turned out to be excellent, showing the quality and versatility of the two codes. The two other systems are quite similar since they consist of the same nuclei and two electrons. Good agreement was found between our cross sections for the N^{7+} + He($1s^2$) system and results from the literature, both theoretical and experimental, demonstrating again the robustness of the computations performed during the thesis. New data was also obtained for the previously unstudied system N^{6+}(1s) + He^{+}(1s). For this system, molecular energy curves have been obtained in order to provide a better understanding of the capture mechanisms and the interpretation of the results. The cross section for single capture is on the order of magnitude of 10^{-16} cm^2, while for N^{7+} + He, it is around 10^{-15} cm^2. This suggests that, even with the same number of electrons present, the initial configuration plays a significant role in the value of the cross sections. Specifically, in the case of N^{6+}, the nucleus is screened by one electron, unlike for N^{7+}, and the ionization energy of the target is four times higher for He^{+} than for He. As a result, the capture cross sections are smaller, the transfer of electron being likely at much lower impact parameters.
These systems were chosen partly because they were initially planned to be conducted

at INSP and preliminary close-coupled calculations have already been performed for the systems presented in Chapter 6. The ASCC method is therefore very appropriate for accompanying experimental campaigns at INSP which will be run in the future.

On the experimental side, an investigation was conducted at INSP with the goal of performing ion-atom and ion-ion collisions in the laboratory. At the beginning of the PhD project, only one ion source (SIMPA) and beamline were operational at INSP. The second ion source (FISIC) was delivered at the end of 2022. Several separate studies were necessary to develop the experimental setup. The production of $^{13}C^{6+}$ using the SIMPA source was tested, in collaboration with colleagues from Normandy Hadrontherapy (NHa). A maximum current yield of 2.7 µA was obtained by using $^{13}CO_2$ gas along with He as a support gas. This study showed that a source system based on the SuperNanogan design is capable to achieve the required levels of carbon ion production required by NHa for the C400 hadrontherapy facility, and required for future ion-ion studies. However, it was decided not to proceed with carbon ions at INSP for the time being since the source clean-up time was not compatible with our needs of frequent changes between ion species for ion-ion/atom experiments. Systematic studies involving carbon ions are nonetheless considered for the future.
Two test campaigns at ARIBE (GANIL) were conducted to characterize the home-made ion spectrometer and its detector, alone at first, and then coupled for the first time to the OMEGA purification system. The spectrometer and its detection system were able to fully separate the single and double electron capture states (Ar^{11+} and Ar^{10+} resulting from in-line capture by a 3 keV/u Ar^{12+} beam on residual gas), thereby meeting all the requirements in terms of charge state separation. Once coupled to the OMEGA, a beam transmission of 100% was achieved, while retaining a satisfactory beam quality. The OMEGA and spectrometer were found to fulfill their roles as anticipated, however only beams with small currents of a few nA could be used, while intensities of a few µA are anticipated in ion-ion/atom collisions. A design modification of the spectrometer following the first test campaign had already allowed to go from intensities of a few pA to a few nA. Further improvements will be reached via modifications of the ion spectroscopy detector design. During these test campaigns based on growth-rate methods, estimates of single and double capture cross sections from ion-atom collisions between argon ions and residual gas, $Ar^{q+} \rightarrow Ar^{(q-k)+}$ (q = 9, 12, and k = 1,2, at collision energies of 3 and 2.3 keV/u respectively), were obtained. They showed excellent agreement with values calculated from the Müller and Salzborn scaling law. For the first time, an estimate of the ionization cross section $Ar^{9+} \rightarrow Ar^{10+}$ was obtained and gave an order of magnitude of a few 10^{-17} cm^2.
A comprehensive study of a novel X-ray detection chain composed of the previously characterized LANCELOT detector and the brand new FASTER fully numerical acquisition system was performed. This study aimed at using the FASTER system (already employed for ion spectroscopy) with the X-ray detector for future ion-X-ray coincidence detection. The study comprised testing (with X-rays from solid targets bombarded by 10 keV electrons) two different FASTER cards and exploring the different settings available (shaping time, ADC, pole-zero subtraction...) in order to fully characterize the acquisition chain.
Finally, a three-week test campaign was conducted at INSP in July 2024, which made use of most of the knowledge developed during the thesis work. For the first time in the laboratory, the FISIC and SIMPA beamlines were connected, with full remote

control of all elements up to the collision chamber. Oxygen and argon beams were produced by the two sources at the same time. The position of the two beams could be carefully controlled to obtain a full overlap at the interaction point in the collision chamber, and thanks to this, the SIMPA beam can by fully scanned by the FISIC beam. Experiments involving oxygen beam and an effusive argon jet were carried out, as well as others involving 4.4 keV/u O^{7+} on 10 keV/q O^{q+} (q = 5, 6, 7) and 10 keV/q Ar^{q+} (q = 2, 3, 4, 5, 6). A study of the gas jet allowed us to know the range of pressure needed in the collision chamber to be in the single-collision regime. Although cross sections could not be evaluated due to bad vacuum conditions from this test campaign, X-ray background measurements from collisions on residual gas were obtained. These tests allowed for an estimation of the proportion of metastable O^{6+}(1s2s) produced by the two sources, which was around 25% for the FISIC source and 40% for SIMPA. However those percentages are rough estimates and systematic measurements while varying the source parameters are necessary. Important points of improvement for the setup were identified, particularly regarding the pumping system to reduce the pressure in the collision chamber, and the design of the X-ray detector collimator. Conducting ion-atom collisions with a helium effusive jet will be feasible in the short term, however performing ion-ion collisions to measure capture cross sections is a much bigger challenge, especially within the keV/u collision energy range available at INSP. Improvement of the vacuum conditions and coincidence measurements will be necessary, among other steps. Additionally, the collision zone could be placed at high voltage to temporally separate ion-ion collisions from ion-residual gas collisions.

The current experimental setup presented here is part of a broader project [215] aimed at connecting the low-energy FISIC plarform to the CRYRING storage ring (GSI, Germany) (as shown in Figure 138), which is capable of producing highly charged heavy ions (up to U) with energies in the MeV/u range. When ions with a few MeV/u collide with ions at a few keV/u, the intermediate velocity regime is reached. The ion energy transfer is at its maximum. In this regime, theoretical predictions are at their limit of validity, and no experiment has been performed. This is primarily due to various experimental challenges, including the need for extremely high-quality ion beams with precise charge state control, an effective management of the overlap between the ion beams, and a high-energy ion detector capable of handling high count rates (up to 1 MHz) while being radiation resistant. Additionally, the setup requires an efficient cross-beam configuration in ultra-high vacuum, with the ability to adjust the energy of the low-energy ions in the interaction zone to distinguish real events from those caused by residual gas collisions. To accurately get the charge exchange cross sections, coincidence measurements will be performed between the slow-energy ions recorded after the collision by the ion spectrometer presented here and the high-energy ions.
A comprehensive experimental program for ion-ion collisions is now clearly conceivable, involving a wide variety of collision systems with the possibility to tune both the projectile and target charge states across a wide range, down to bare ion on hydrogenic target (pure three-body system). The role of additional electron bound to the target and/or the projectile ions could be studied one by one and offer insights on screening / anti-screening effects or multi-electron processes. Theoretical investigations using the ASCC method will be also very valuable in parallel with these experimental campaigns.

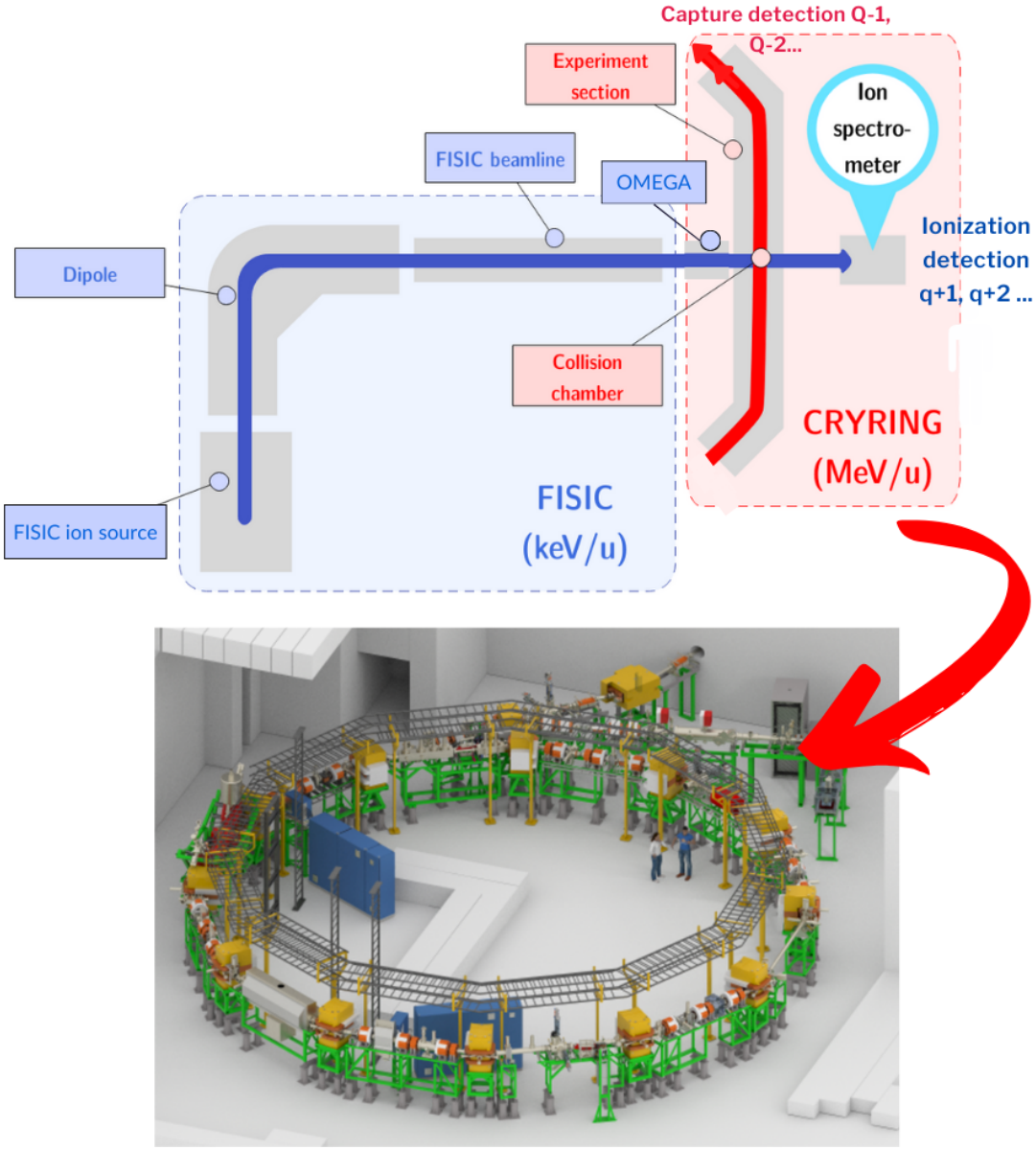

Figure 138: Setup of the FISIC platform on the CRYRING storage ring, and 3D model of CRYRING [216].

References

[1] A. Dalgarno and R. A. McCray. Heating and ionization of hi regions. *Annual Review of Astronomy and Astrophysics*, 10:375–426, 1972.

[2] Anil Bhardwaj, Ronald F Elsner, G Randall Gladstone, Thomas E Cravens, Carey M Lisse, Konrad Dennerl, Graziella Branduardi-Raymont, Bradford J Wargelin, J Hunter Waite Jr, Ina Robertson, et al. X-rays from solar system objects. *Planetary and Space Science*, 55(9):1135–1189, 2007.

[3] RT Zhang, T Liao, CJ Zhang, LP Zou, DL Guo, Y Gao, LY Gu, XL Zhu, SF Zhang, and X Ma. Charge exchange between highly charged ions and atomic h for modelling comet c/1999 s4 x-ray emission. *Monthly Notices of the Royal Astronomical Society*, 520(1):1417–1420, 2023.

[4] SJ Bromley, M Pindzola, D Bodewits, and MR Fogle. Time-dependent lattice cross sections and line ratios for solar wind charge exchange: Bare ne incident on atomic h and he. *The Astrophysical Journal Supplement Series*, 262(2):47, 2022.

[5] Rudy Delaunay, Michael Gatchell, Patrick Rousseau, Alicja Domaracka, Sylvain Maclot, Yang Wang, Mark H Stockett, Tao Chen, Lamri Adoui, Manuel Alcamí, et al. Molecular growth inside of polycyclic aromatic hydrocarbon clusters induced by ion collisions. *The journal of physical chemistry letters*, 6(9):1536–1542, 2015.

[6] Garry McCracken and Peter Stott. *Fusion: the energy of the universe*. Academic Press, 2013.

[7] BE Peigney, O Larroche, and V Tikhonchuk. Ion kinetic effects on the ignition and burn of inertial confinement fusion targets: A multi-scale approach. *Physics of Plasmas*, 21(12), 2014.

[8] RL Berger, W Arrighi, T Chapman, A Dimits, JW Banks, and S Brunner. The competing effects of wave amplitude and collisions on multi-ion species suppression of stimulated brillouin scattering in inertial confinement fusion hohlraums. *Physics of Plasmas*, 30(4), 2023.

[9] Arijit Bose. *Direct Drive Inertial Confinement Fusion: Analysis of the Implosion Core*. PhD thesis, 10 2017.

[10] Guozhuang Li, Jingren Gu, Zhihong Jiao, Sheng Zhang, and Xinxia Li. Impact ionization of highly charged ion-atom collisions considering strong magnetic field and plasma screening effect. *Nuclear Instruments and Methods in Physics Research Section B: Beam Interactions with Materials and Atoms*, 541:289–297, 2023.

[11] Arnold Pompos, Marco Durante, and Hak Choy. Heavy ions in cancer therapy. *JAMA oncology*, 2(12):1539–1540, 2016.

[12] Walter Tinganelli and Marco Durante. Carbon ion radiobiology. *Cancers*, 12(10), 2020.

[13] Herman Suit, Thomas DeLaney, Saveli Goldberg, Harald Paganetti, Ben Clasie, Leo Gerweck, Andrzej Niemierko, Eric Hall, Jacob Flanz, Josh Hallman, and Alexei Trofimov. Proton vs carbon ion beams in the definitive radiation treatment of cancer patients. *Radiotherapy and Oncology*, 95(1):3–22, 2010.

[14] William Henry Bragg and Richard Kleeman. Xxxix. on the α particles of radium, and their loss of range in passing through various atoms and molecules. *The London, Edinburgh, and Dublin Philosophical Magazine and Journal of Science*, 10(57):318–340, 1905.

[15] Saverio Braccini. Photons and hadrons for health. *ACTA PHYSICA POLONICA SERIES B*, 37(3):961, 2006.

[16] S Cervera, M Lobue, E Fontana, M Eddrief, VH Etgens, E Lamour, S Macé, M Marangolo, E Plouet, C Prigent, et al. Mastering disorder in a first-order transition by ion irradiation. *Physical Review Materials*, 8(2):024406, 2024.

[17] Mandeep Kaur, Sanjeev Gautam, and Navdeep Goyal. Ion-implantation and photovoltaics efficiency: A review. *Materials Letters*, 309:131356, 2022.

[18] Yu N Osetsky, Andrew F Calder, and Roger E Stoller. How do energetic ions damage metallic surfaces? *Current Opinion in Solid State and Materials Science*, 19(5):277–286, 2015.

[19] Dominique Vernhet, JP Rozet, K Wohrer, L Adoui, C Stephan, A Cassimi, and JM Ramillon. Excitation in swift heavy ion-atom collisions. *Nuclear Instruments and Methods in Physics Research Section B: Beam Interactions with Materials and Atoms*, 107(1-4):71–78, 1996.

[20] PD Fainstein, VH Ponce, and RD Rivarola. Single-electron ionisation of helium by anti-proton and proton impact. *Journal of Physics B: Atomic, Molecular and Optical Physics*, 22(19):L559, 1989.

[21] DSF Crothers and M McCartney. Ion—a program to evaluate cross-sections for ionisation in ion-atom collisions. *Computer physics communications*, 72(2-3):288–294, 1992.

[22] Dž Belkić, R Gayet, and A Salin. Computation of total cross-sections for electron capture in high energy collisions. iii. *Computer Physics Communications*, 32(4):385–397, 1984.

[23] WE Meyerhof, R Anholt, J Eichler, H Gould, Ch Munger, J Alonso, P Thieberger, and HE Wegner. Atomic collisions with relativistic heavy ions. iii. electron capture. *Physical Review A*, 32(6):3291, 1985.

[24] PD Fainstein, Victor H Ponce, and Roberto D Rivarola. Two-centre effects in ionization by ion impact. *Journal of Physics B: Atomic, Molecular and Optical Physics*, 24(14):3091, 1991.

[25] LF Errea, C Harel, H Jouin, L Méndez, B Pons, and A Riera. Quantal and semiclassical calculations of charge transfer cross sections in+ h collisions for impact energies of. *Journal of Physics B: Atomic, Molecular and Optical Physics*, 31(16):3527, 1998.

[26] David Robert Bates and R McCarroll. Electron capture in slow collisions. *Proceedings of the Royal Society of London. Series A. Mathematical and Physical Sciences*, 245(1241):175–183, 1958.

[27] David Robert Bates, Harrie Stewart Wilson Massey, and AL Stewart. Inelastic collisions between atoms i. general theoretical considerations. *Proceedings of the Royal Society of London. Series A. Mathematical and Physical Sciences*, 216(1127):437–458, 1953.

[28] A Dalgarno and HN Yadav. Eletcron capture ii: Resonance capture from hydrogen atoms by slow protons. *Proceedings of the Physical Society. Section A*, 66(2):173, 1953.

[29] Xiao-Xia Wang, Kun Wang, Yi-Geng Peng, Chun-Hua Liu, Ling Liu, Yong Wu, Heinz-Peter Liebermann, Robert J Buenker, and Yi-Zhi Qu. Charge transfer and excitation processes in low energy collisions of he+ ions with li atoms. *Research in Astronomy and Astrophysics*, 21(8):210, 2021.

[30] Yu Wang, Feng Wang, Xiaohe Lin, Ling Liu, Yong Wu, and Jianguo Wang. Elastic and electron capture processes in slow he+–he collision. *Astronomy & Astrophysics*, 674:A201, 2023.

[31] BH Bransden, AM Ermolaev, and R Shingal. One-and two-electron models for electron capture by he+ ions from li0 at intermediate energies. *Journal of Physics B: Atomic and Molecular Physics*, 17(22):4515, 1984.

[32] L Liu, JG Wang, and RK Janev. Spin-resolved electron capture and excitation processes in he+-li collisions. *Journal of Physics B: Atomic, Molecular and Optical Physics*, 49(10):105201, 2016.

[33] RD DuBois and LH Toburen. Electron capture by protons and helium ions from lithium, sodium, and magnesium. *Physical Review A*, 31(6):3603, 1985.

[34] SL Varghese, W Waggoner, and CL Cocke. Electron capture from lithium by protons and helium ions. *Physical Review A*, 29(5):2453, 1984.

[35] Friedrich Aumayr and Hannspeter Winter. Total single-electron-capture cross sections for impact of H^+, H^{2+}, He^+, and Ne^+(2–20 kev) on Li. *Physical Review A*, 31(1):67, 1985.

[36] RW McCullough, TV Goffe, MB Shah, M Lennon, and HB Gilbody. Electron capture by he2+ and he+ ions in lithium vapour. *Journal of Physics B: Atomic and Molecular Physics*, 15(1):111, 1982.

[37] Wolfgang Fritsch and Chii Dong Lin. The semiclassical close-coupling description of atomic collisions: Recent developments and results. *Physics Reports*, 202(1-2):1–97, 1991.

[38] Steven Knoop, Daniel Fischer, Yingli Xue, Myroslav Zapukhlyak, CJ Osborne, Th Ergler, T Ferger, J Braun, Gunter Brenner, Hjalmar Bruhns, et al. Single-electron capture in kev ar15+... 18++ he collisions. *Journal of Physics B: Atomic, Molecular and Optical Physics*, 41(19):195203, 2008.

[39] Wolfgang Fritsch and Chii Dong Lin. The semiclassical close-coupling description of atomic collisions: Recent developments and results. *Physics Reports*, 202(1-2):1–97, 1991.

[40] Ronald McCarroll. Charge exchange and ionization in ion-atom collisions. In *Atomic and Molecular Collision Theory*, pages 165–231. Springer, 1982.

[41] David Robert Bates and R McCarroll. Electron capture in slow collisions. *Proceedings of the Royal Society of London. Series A. Mathematical and Physical Sciences*, 245(1241):175–183, 1958.

[42] A Dubois and JP Hansen. Interpretation of the structures observed for excitation cross-sections in c 2+/he 2+-li collisions. *The European Physical Journal D-Atomic, Molecular, Optical and Plasma Physics*, 13:207–212, 2001.

[43] Nicolas Sisourat, Ingjald Pilskog, and Alain Dubois. Nonperturbative treatment of multielectron processes in ion-molecule scattering: Application to he 2+-h 2 collisions. *Physical Review A*, 84(5):052722, 2011.

[44] Thomas G Winter. Electron transfer and ionization in collisions between protons and the ions he+, li 2+, be 3+, b 4+, and c 5+ studied with the use of a sturmian basis. *Physical Review A*, 35(9):3799, 1987.

[45] Christian Harel, Herve Jouin, and Bernard Pons. Cross sections for electron capture from atomic hydrogen by fully stripped ions in the 0.05–1.00 au impact velocity range. *Atomic Data and Nuclear Data Tables*, 68(2):279–302, 1998.

[46] T Kirchner, M Horbatsch, HJ Lüdde, and RM Dreizler. Time-dependent screening effects in ion-atom collisions with many active electrons. *Physical Review A*, 62(4):042704, 2000.

[47] Arash Salehzadeh and Tom Kirchner. Strong multiple-capture effect in slow ar17+–ar collisions: a quantum mechanical analysis. *Journal of Physics B: Atomic, Molecular and Optical Physics*, 46(2):025201, 2013.

[48] Vida Maruhn-Rezwani, Norbert Grün, and Werner Scheid. Numerical solution of the time-dependent schrödinger equation and application to h+-h. *Physical Review Letters*, 43(7):512, 1979.

[49] Christopher Bottcher. Accurate quantal studies of ion-atom collisions using finite-element techniques. *Physical Review Letters*, 48(2):85, 1982.

[50] Merle E Riley and A Burke Ritchie. Excitation and ionization in h (1s)-h (1s) collisions: Ii. inclusion of electron exchange. *Journal of Physics B: Atomic, Molecular and Optical Physics*, 33(22):5177, 2000.

[51] L Sælen, T Birkeland, N Sisourat, A Dubois, and JP Hansen. Nonperturbative treatment of single ionization of h 2 by fast highly-charged-ion impact. *Physical Review A—Atomic, Molecular, and Optical Physics*, 81(2):022718, 2010.

[52] C Hill, K Heinola, A Dubois, N Sisourat, A Taoutioui, H Agueny, K Tőkési, I Ziaeian, C Illescas, A Jorge, et al. Atomic collisional data for neutral beam modeling in fusion plasmas. *Nuclear Fusion*, 63(12):125001, 2023.

[53] R Abrines and IC Percival. Classical theory of charge transfer and ionization of hydrogen atoms by protons. *Proceedings of the Physical Society*, 88(4):861, 1966.

[54] Sebastian Otranto, Ronald E Olson, and Peter Beiersdorfer. X-ray emission cross sections following charge exchange by multiply charged ions of astrophysical interest. *Physical Review A—Atomic, Molecular, and Optical Physics*, 73(2):022723, 2006.

[55] Sebastián Otranto and RE Olson. X-ray emission cross sections following ar 18+ charge-exchange collisions on neutral argon: The role of the multiple electron capture. *Physical Review A—Atomic, Molecular, and Optical Physics*, 83(3):032710, 2011.

[56] F Brouillard and W Claeys. On the measurement of ion (atom)-ion (atom) charge exchange. In *Physics of Ion-Ion and Electron-Ion Collisions*, pages 415–459. Springer, 1983.

[57] Pierre Defrance, F Brouillard, W Claeys, and G Van Wassenhove. Crossed beam measurement of absolute cross sections: An alternative method and its application to the electron impact ionisation of he+. *Journal of Physics B: Atomic and Molecular Physics*, 14(1):103, 1981.

[58] K Rinn, F Melchert, and E Salzborn. Measurements of charge transfer in h+-he+ collisions. *Journal of Physics B: Atomic and Molecular Physics*, 18(18):3783, 1985.

[59] K Wohrer, M Chabot, R Fossé, and D Gardès. A method for "on-line" determination of beam-jet overlaps; application to cluster fragmentation studies. *Review of Scientific Instruments*, 71(5):2025–2032, 2000.

[60] RA Phaneuf, CC Havener, GH Dunn, and A Müller. Merged-beams experiments in atomic and molecular physics. *Reports on Progress in Physics*, 62(7):1143, 1999.

[61] Robert Moshammer, M Unverzagt, W Schmitt, J Ullrich, and H Schmidt-Böcking. A 4π recoil-ion electron momentum analyzer: a high-resolution "microscope" for the investigation of the dynamics of atomic, molecular and nuclear reactions. *Nuclear Instruments and Methods in Physics Research Section B: Beam Interactions with Materials and Atoms*, 108(4):425–445, 1996.

[62] RT Zhang, DG Seely, VM Andrianarijaona, IN Draganić, and CC Havener. Measurement of the charge exchange cross section for n7+, o7+ ions in collision with atomic h. *The Astrophysical Journal*, 931(1):1, 2022.

[63] R Ali, CL Cocke, MLA Raphaelian, and M Stockli. Multielectron processes in 10-kev/u ar q+(5 q 17) on ar collisions. *Physical Review A*, 49(5):3586, 1994.

[64] A Niehaus. A classical model for multiple-electron capture in slow collisions of highly charged ions with atoms. *Journal of Physics B: Atomic and Molecular Physics*, 19(18):2925, 1986.

[65] J Burgdörfer, R Morgenstern, and A Niehaus. Angular momentum of captured electrons: The classical over-barrier model and its limitations. *Nuclear Instruments*

and Methods in Physics Research Section B: Beam Interactions with Materials and Atoms, 23(1-2):120–122, 1987.

[66] Ratko K Janev and Hannspeter Winter. State-selective electron capture in atom-highly charged ion collisions. *Physics Reports*, 117(5-6):265–387, 1985.

[67] Joachim Ullrich, Robert Moshammer, Reinhard Dörner, Ottmar Jagutzki, Volker Mergel, Horst Schmidt-Böcking, and Lutz Spielberger. Recoil-ion momentum spectroscopy. *Journal of Physics B: Atomic, Molecular and Optical Physics*, 30(13):2917, 1997.

[68] Reinhard Dörner, Volker Mergel, Ottmar Jagutzki, Lutz Spielberger, Joachim Ullrich, Robert Moshammer, and Horst Schmidt-Böcking. Cold target recoil ion momentum spectroscopy: a 'momentum microscope'to view atomic collision dynamics. *Physics Reports*, 330(2-3):95–192, 2000.

[69] Reinhard Dörner, Volker Mergel, Ottmar Jagutzki, Lutz Spielberger, Joachim Ullrich, Robert Moshammer, and Horst Schmidt-Böcking. Cold target recoil ion momentum spectroscopy: a 'momentum microscope'to view atomic collision dynamics. *Physics Reports*, 330(2-3):95–192, 2000.

[70] A Cassimi, S Duponchel, X Flechard, P Jardin, P Sortais, D Hennecart, and Ronald E Olson. State-selective electron capture in low velocity multiply charged ion, helium collisions. *Physical review letters*, 76(20):3679, 1996.

[71] A Cassimi. Recoil ion momentum spectroscopy: A microscope for hci-atom or molecule collisions. *Physica Scripta*, 1999(T80A):98, 1999.

[72] RT Zhang, JW Gao, YW Zhang, DL Guo, Y Gao, XL Zhu, JW Xu, DM Zhao, S Yan, S Xu, et al. Strongly perturbed state-selective charge exchange between slow ar 8+ and he. *Physical Review Research*, 5(2):023123, 2023.

[73] Hiro Tawara, Endre Takács, Tibor Suta, Károly Makónyi, Laura P Ratliff, and John D Gillaspy. K x rays produced in collisions of bare ions with atoms: Contribution of multiple-electron transfer in kr 36+, ar 18+, and ne 10++ ar collisions. *Physical Review A—Atomic, Molecular, and Optical Physics*, 73(1):012704, 2006.

[74] H Tawara, P Richard, UI Safronova, and PC Stancil. K x-ray production in h-like si 1 3+, s 1 5+, and ar 1 7+ ions colliding with various atom and molecule gas targets at low collision energies. *Physical Review A*, 64(4):042712, 2001.

[75] Peter Beiersdorfer, H Chen, KR Boyce, GV Brown, RL Kelley, CA Kilbourne, FS Porter, and SM Kahn. Laboratory simulation of cometary x-rays using a high-resolution microcalorimeter. *Nuclear Instruments and Methods in Physics Research Section B: Beam Interactions with Materials and Atoms*, 235(1-4):116–119, 2005.

[76] M. Trassinelli. Investigation of slow collisions for (quasi) symmetric heavy systems: what can be extracted from high resolution x-ray spectra. *Journal of Physics B: Atomic, Molecular and Optical Physics*, 45(8):085202, 2012.

[77] He Klinger, A Muller, and E Salzborn. Electron capture processes of multiply charged argon ions in argon at energies from 10 to 90 kev. *Journal of Physics B: Atomic and Molecular Physics*, 8(2):230, 1975.

[78] M Druetta, S Martin, T Bouchama, C Harel, and H Jouin. Spectroscopic study of the charge-exchange collision between ar 8+ and he or h 2 at beam energies of 80, 40, and 8 kev. *Physical Review A*, 36(7):3071, 1987.

[79] MA Abdallah, W Wolff, HE Wolf, E Sidky, EY Kamber, M Stöckli, CD Lin, and CL Cocke. Cold-target recoil-ion-momentum spectroscopy study of single electron capture from he by slow ar 8+ ions. *Physical Review A*, 57(6):4373, 1998.

[80] B Peart, RA Forrest, and K Dolder. Measurements of inelastic collisions between cs+ ions. *Journal of Physics B: Atomic and Molecular Physics*, 14(10):1655, 1981.

[81] B Peart, RA Forrest, and K Dolder. Measurements of inelastic collisions between homonuclear ions: Na+, k+ and rb+. *Journal of Physics B: Atomic and Molecular Physics*, 14(19):L603, 1981.

[82] B Peart, RA Forrest, and K Dolder. Measurements of cross sections for the formation of 7li2+ by collisions between 7li+ ions. *Journal of Physics B: Atomic and Molecular Physics*, 14(18):3457, 1981.

[83] HJ Kim and RK Janev. Electron-loss cross sections in symmetric multicharged-ion collisions. *Physical review letters*, 58(18):1837, 1987.

[84] CY Chen, CL Cocke, JP Giese, F Melchert, I Reiser, M Stöckli, E Sidky, and CD Lin. Studies of charge exchange in symmetric ion-ion collisions. *Journal of Physics B: Atomic, Molecular and Optical Physics*, 34(3):469, 2001.

[85] D Skiera, R Trassl, K Huber, H Bräuning, E Salzborn, M Keim, A Achenbach, T Kirchner, HJ Lüdde, and RM Dreizler. Charge-changing processes in collisions between li-like ions and he2+. *Physica Scripta*, 2001(T92):423, 2001.

[86] H Bräuning, A Diehl, A Theiß, R Traßl, and E Salzborn. Ionisation in collisions between multiply charged ions. https://citeseerx.ist.psu.edu/document?repid=rep1&type=pdf&doi=9a99ce5f3f45fe6e98a855cad28470b3435bff56.

[87] A Diehl, H Bräuning, R Trassl, D Hathiramani, A Theiß, H Kern, E Salzborn, and I Hofmann. Charge transfer and ionization in collisions between multiply charged noble gas ions. *Journal of Physics B: Atomic, Molecular and Optical Physics*, 34(20):4073, 2001.

[88] H Bräuning, A Diehl, and E Salzborn. Charge transfer in homonuclear collisions of heavy ions. *Journal of Physics B: Atomic, Molecular and Optical Physics*, 39(16):3255, 2006.

[89] S Meuser, F Melchert, S Krüdener, A Pfeiffer, K Von Diemar, and E Salzborn. Crossed-beams arrangement for the investigation of charge-changing collisions between multiply charged ions. *Review of scientific instruments*, 67(8):2752–2759, 1996.

[90] Alfred Müller and Erhard Salzborn. Scaling of cross sections for multiple electron transfer to highly charged ions colliding with atoms and molecules. *Physics Letters A*, 62(6):391–394, 1977.

[91] J Vancura, VJ Marchetti, JJ Perotti, and VO Kostroun. Absolute total and one- and two-electron transfer cross sections for ar q+(8 q 16) on he and h 2 at 2.3q kev. *Physical Review A*, 47(5):3758, 1993.

[92] Erhard Salzborn and Alfred Müller. Transfer ionization in collisions of multiply charged ions with atoms. In *Atomic Processes in Electron-Ion and Ion-Ion Collisions*, pages 357–402. Springer, 1986.

[93] H Tawara and A Russek. Charge changing processes in hydrogen beams. *Reviews of modern physics*, 45(2):178, 1973.

[94] Brian Harold Bransden and Martin Rastall Coulter McDowell. *Charge exchange and the theory of ion-atom collisions*. Oxford University Press, 1992.

[95] Gabriel Labaigt. *Etude théorique de processus multi-électroniques au cours de collisions atomiques et moléculaires*. PhD thesis, Université Pierre et Marie Curie-Paris VI, 2014.

[96] Nicolas Sisourat. *Etude théorique de phénomènes d'interférences au cours de collisions atomiques et moléculaires*. PhD thesis, Paris 6, 2008.

[97] Stylianos Passalidis. *Modelling of multi-electronic processes occurring during atomic collisions*. PhD thesis, Sorbonne Université, 2022.

[98] Lawrence F Shampine. *Numerical solution of ordinary differential equations*. Routledge, 2018.

[99] S Francis Boys. Electronic wave functions-i. a general method of calculation for the stationary states of any molecular system. *Proceedings of the Royal Society of London. Series A. Mathematical and Physical Sciences*, 200(1063):542–554, 1950.

[100] CM Reeves and MC Harrison. Use of gaussian functions in the calculation of wavefunctions for small molecules. ii. the ammonia molecule. *The Journal of Chemical Physics*, 39(1):11–17, 1963.

[101] Richard C Raffenetti. Even-tempered atomic orbitals. ii. atomic scf wavefunctions in terms of even-tempered exponential bases. *The Journal of Chemical Physics*, 59(11):5936–5949, 1973.

[102] Jérémie Caillat. *Etude théorique des processus électroniques au cours de collisions ion-atome et ion-molécule*. PhD thesis, Paris 6, 2003.

[103] SE Nielsen, JP Hansen, and A Dubois. Propensity rules for orientation in singly-charged ion-atom collisions. *Journal of Physics B: Atomic, Molecular and Optical Physics*, 23(15):2595, 1990.

[104] Junwen Gao. *Two-electron processes and correlation effects in ion-atom collisions: a close-coupling approach at intermediate energies*. PhD thesis, Sorbonne université, 2019.

[105] Jérémie Caillat, Alain Dubois, and Jan Petter Hansen. On the discrepancies of the calculated C^{5+} (n= 5) capture cross sections in C^{+}-H collisions. *Journal of Physics B: Atomic, Molecular and Optical Physics*, 33(20):L715, 2000.

[106] IB Abdurakhmanov, K Massen-Hane, Sh U Alladustov, JJ Bailey, AS Kadyrov, and Igor Bray. Ionization and electron capture in collisions of bare carbon ions with hydrogen. *Physical Review A*, 98(6):062710, 2018.

[107] Katharin Igenbergs, Josef Schweinzer, Alexander Veiter, Lukas Perneczky, Edwin Frühwirth, Markus Wallerberger, Ronald E Olson, and Friedrich Aumayr. Charge exchange and ionization in N^{7+}-, N^{6+}-, C^{6+}-H (n= 1, 2) collisions studied systematically by theoretical approaches. *Journal of Physics B: Atomic, Molecular and Optical Physics*, 45(6):065203, 2012.

[108] Hiroya Suno and Takako Kato. Cross section database for carbon atoms and ions: Electron-impact ionization, excitation, and charge exchange in collisions with hydrogen atoms. *Atomic Data and Nuclear Data Tables*, 92(4):407–455, 2006.

[109] HW van der Hart and JE Hansen. Energies and autoionization widths of doubly-excited 3lnl'states in N^{5+}. *Journal of Physics B: Atomic, Molecular and Optical Physics*, 25(10):2267, 1992.

[110] C Harel and H Jouin. Autoionizing double capture in N^{7+} on helium collisions at low energies. *Europhysics Letters*, 11(2):121, 1990.

[111] W Wu, JP Giese, Z Chen, R Ali, CL Cocke, P Richard, and M Stöckli. Evidence for population of highly asymmetric states in double-electron capture by O^{7+}, O^{8+} and N^{7+} colliding with he at low to intermediate velocities. *Physical Review A*, 50(1):502, 1994.

[112] NIST. Nist atomic spectra database for N VI. https://physics.nist.gov/cgi-bin/ASD/energy1.pl?de=0&spectrum=N+VI&units=3&format=0&output=0&page_size=15&multiplet_ordered=0&conf_out=on&term_out=on&level_out=on&unc_out=1&j_out=on&lande_out=on&perc_out=on&biblio=on&temp=&submit=Retrieve+Data. Accessed: 2024-07-12.

[113] NIST. Nist atomic spectra database for He I. https://physics.nist.gov/cgi-bin/ASD/energy1.pl?de=0&spectrum=He+I&units=3&format=0&output=0&page_size=15&multiplet_ordered=0&conf_out=on&term_out=on&level_out=on&unc_out=1&j_out=on&lande_out=on&perc_out=on&biblio=on&temp=&submit=Retrieve+Data. Accessed: 2024-07-12.

[114] ECG Stueckelberg. Theory of continuous absorption of oxygen at 1450a. *Physical Review*, 42(4):518, 1932.

[115] T Iwai, Y Kaneko, M Kimura, N Kobayashi, S Ohtani, K Okuno, S Takagi, H Tawara, and S Tsurubuchi. Cross sections for one-electron capture by highly stripped ions of B, C, N, O, F, Ne, and S from He below 1 kev/amu. *Physical Review A*, 26(1):105, 1982.

[116] Hiroyuki Daido, Mamiko Nishiuchi, and Alexander S Pirozhkov. Review of laser-driven ion sources and their applications. *Reports on progress in physics*, 75(5):056401, 2012.

[117] Evgeni D Donets. Historical review of electron beam ion sources. *Review of Scientific Instruments*, 69(2):614–619, 1998.

[118] Joshua L Rovey, Brandon P Ruzic, and Thomas J Houlahan. Simple penning ion source for laboratory research and development applications. *Review of Scientific Instruments*, 78(10), 2007.

[119] Korea Basic Science Institute. Low energy heavy-ion beam facility at korea basic science institute. https://www.slideserve.com/chico/low-energy-heavy-ion-beam-facility-at-korea-basic-science-institute. Accessed: 2024-04-16.

[120] R. Geller. Electron cyclotron resonance multiply charged ion sources. *IEEE Transactions on Nuclear Science*, 23(2):904–912, 1976.

[121] P Ludwig, F Bourg, P Briand, A Girard, G Melin, D Guillaume, P Seyfert, A La Grassa, G Ciavola, S Gammino, et al. Summary of the performances of the superconducting electron cyclotron resonance ion source at 14 ghz. *Review of scientific instruments*, 69(12):4082–4085, 1998.

[122] G Douysset, H Khodja, A Girard, and JP Briand. Highly charged ion densities and ion confinement properties in an electron-cyclotron-resonance ion source. *Physical Review E*, 61(3):3015, 2000.

[123] ZQ Xie. Production of highly charged ion beams from electron cyclotron resonance ion sources. *Review of Scientific instruments*, 69(2):625–630, 1998.

[124] https://www.pantechnik.com/. Accessed: 2023-04-28.

[125] A Girard, P Briand, G Gaudart, JP Klein, F Bourg, J Debernardi, JM Mathonnet, G Melin, and Y Su. The quadrumafios electron cyclotron resonance ion source: Presentation and analysis of the resultsa. *Review of scientific instruments*, 65(5):1714–1717, 1994.

[126] C Bieth, JL Bouly, JC Curdy, S Kantas, P Sortais, P Sole, and JL Vieux-Rochaz. Electron cyclotron resonance ion source for high currents of mono-and multicharged ion and general purpose unlimited lifetime application on implantation devices. *Review of Scientific Instruments*, 71(2):899–901, 2000.

[127] Alexander Gumberidze, Martino Trassinelli, Nacer Adrouche, CI Szabo, Paul Indelicato, F Haranger, J-M Isac, Emily Lamour, E-O Le Bigot, Jacques Merot, et al. Electronic temperatures, densities, and plasma x-ray emission of a 14.5 ghz electron-cyclotron resonance ion source. *Review of Scientific Instruments*, 81(3):033303, 2010.

[128] Nacer Adrouche. *Diagnostic du plasma de la source d'ions ECR SIMPA par spectroscopie X, Collision d'ions néon hydrogenoïdes avec des agrégats d'argon*. Theses, Université Pierre et Marie Curie - Paris VI, September 2006.

[129] S Biri, L Kenez, A Valek, M Kidera, T Nakagawa, and Y Yano. Highly charged ion production using an electrode in biased and floating modes. Technical report, nstitute of Physical and Chemical Research (RIKEN), 1999.

[130] Hans-Juergen Schlueter. Quadrupole mass spectrometer, April 3 2018. US Patent 9,934,954.

[131] mks. Mks e-vision 2. https://www.mks.com/f/e-vision-2-residual-gas-analyzer?q=:ranking-desc:isObsolete:false:-excludeCountries:FR:npCategory:residual-gas-analyzers:suppress:false. Accessed: 2024-04-22.

[132] G Melin, F Bourg, P Briand, M Delaunay, G Gaudart, A Girard, D Hitz, JP Klein, P Ludwig, TK Nguyen, et al. Status of development of ecr ion sources at grenoble. *Review of scientific instruments*, 65(4):1051–1056, 1994.

[133] A Muller, E Salzborn, R Frodl, R Becker, H Klein, and H Winter. Absolute ionisation cross sections for electrons incident on o+, ne+, xe+ and ari+ (i= 1,..., 5) ions. *Journal of Physics B: Atomic and Molecular Physics*, 13(9):1877, 1980.

[134] Christophe Prigent. *L'émission X: un outil et une sonde pour l'interaction laser-agrégats*. PhD thesis, Université Pierre et Marie Curie-Paris VI, 2004.

[135] A Muller, K Huber, K Tinschert, R Becker, and E Salzborn. An improved crossed-beams technique for the measurement of absolute cross sections for electron impact ionisations of ions and its application to ar+ ions. *Journal of Physics B: Atomic and Molecular Physics*, 18(14):2993, jul 1985.

[136] H Zhang, S Cherkani-Hassani, C Bélenger, M Duponchelle, M Khouilid, E M Oualim, and P Defrance. Electron impact ionization of argon ions (q = 4–11). *Journal of Physics B: Atomic, Molecular and Optical Physics*, 35(18):3829, sep 2002.

[137] NIST. Nist atomic spectra database ionization energies data for argon. https://physics.nist.gov/cgi-bin/ASD/ie.pl?spectra=Ar&units=1&at_num_out=on&el_name_out=on&seq_out=on&shells_out=on&level_out=on&e_out=0&unc_out=on&biblio=on. Accessed: 2024-05-29.

[138] Perla Dergham. *Probing Surface Magnetism with Highly Charged Ions*. PhD thesis, Sorbonne université, 2023.

[139] GANIL. Aribe@ganil. https://indico.in2p3.fr/event/31693/contributions/133356/attachments/82156/122437/ARIBE_activities.pdf#Navigation1. Accessed: 2024-04-22.

[140] V Toivanen, C Barué, C Feierstein, P Jardin, F Lemagnen, L Maunoury, F Noury, and P Rousseau. Upgrade of the gts electron cyclotron resonance ion source at ganil. In *AIP Conference Proceedings*, volume 2011. AIP Publishing, 2018.

[141] D Hitz, A Girard, K Serebrennikov, G Melin, D Cormier, JM Mathonnet, J Chartier, L Sun, JP Briand, and M Benhachoum. Production of highly charged ion beams with the grenoble test electron cyclotron resonance ion source (plenary). *Review of scientific instruments*, 75(5):1403–1406, 2004.

[142] D Hitz, D Cormier, and JM Mathonnet. A new room temperature ecr ion source for accelerator facilities. In *Proceedings EPAC*, volume 1718, 2002.

[143] SS Vybin, IV Izotov, VA Skalyga, L Maunoury, Patrick Rousseau, and C Feierstein. A very low energy ion beam extraction system design of the gts ecr ion source at ganil. *Nuclear Instruments and Methods in Physics Research Section A: Accelerators, Spectrometers, Detectors and Associated Equipment*, 1061:169109, 2024.

[144] A.J.H. Boerboom. Ion optics of multipoles. *Nuclear Instruments and Methods in Physics Research Section A: Accelerators, Spectrometers, Detectors and Associated Equipment*, 258(3):426–430, 1987.

[145] IW Drummond. The ion optics of low-energy ion beams. *Vacuum*, 34(1):51–61, 1984. Vacuum Special Issue: Proceedings of the 3rd International Conference on Low Energy Ion Beams Loughborough University of Technology, UK.

[146] Peter Strehl. *Beam instrumentation and diagnostics*, volume 120. Springer, 2006.

[147] Jakub Serych. Jakub serych, magnet types in particle accelerators. http://demonstrations.wolfram.com/MagnetTypesInParticleAccelerators/WolframDemonstrationsProject. Accessed: 2024-04-26.

[148] Bohumila Lencová. Electrostatic lenses. In *Handbook of charged particle optics*, pages 161–208. CRC Press, 2017.

[149] A Adams and FH Read. Electrostatic cylinder lenses ii: Three element einzel lenses. *Journal of Physics E: Scientific Instruments*, 5(2):150, 1972.

[150] William H Aberth, Rafael Schnitzer, and Ferdinand C Engesser. Construction of an einzel lens capable of high voltage operation. *Review of Scientific Instruments*, 45(10):1289–1290, 1974.

[151] Esteban Daniel Cantero, A Sosa, W Andreazza, E Bravin, D Lanaia, D Voulot, and CP Welsch. Design of a compact faraday cup for low energy, low intensity ion beams. *Nuclear Instruments and Methods in Physics Research Section A: Accelerators, Spectrometers, Detectors and Associated Equipment*, 807:86–93, 2016.

[152] R Anne, JL Vignet, Y Georget, R Hue, and C Tribouillard. Beam profile and beam time structure monitors for the extracted beams from the ganil cyclotrons. In *15th International Conference on Cyclotrons and their Applications*, pages 293–296. IOP Publishing, 1998.

[153] Enrico Bravin. Transverse emittance. *arXiv: Accelerator Physics*, 2020.

[154] HR Kremers, JPM Beijers, and S Brandenburg. A pepper-pot emittance meter for low-energy heavy-ion beams. *Review of Scientific Instruments*, 84(2), 2013.

[155] Paul W Allison, Joseph D Sherman, and David B Holtkamp. An emittance scanner for intense low-energy ion beams. *IEEE Transactions on Nuclear Science*, 30(4):2204–2206, 1983.

[156] F Zocca, F Roncarolo, GJ Focker, U Raich, E Bravin, D Gerard, and M Duraffourg. Profile and emittance measurements at the cern linac4 3 mev test stand. Technical report, 2013.

[157] Lauri Panitzsch, Michael Stalder, and Robert F Wimmer-Schweingruber. Direct high-resolution ion beam-profile imaging using a position-sensitive faraday cup array. *Review of Scientific Instruments*, 80(11), 2009.

[158] Sophie Cervera. *Manipulation des propriétés magnétiques de matériaux à effet magnétocalorique géant par impact d'ions lourds*. PhD thesis, Université Pierre et Marie Curie-Paris VI, 2017.

[159] Daniel Schury, Ajit Kumar, Alain Méry, Jean-Yves Chesnel, Anna Lévy, Stéphane Macé, Christophe Prigent, Jean-Marc Ramillon, Jimmy Rangama, Patrick Rousseau, et al. An electrostatic in-line charge-state purification system for multi-charged ions in the kiloelectronvolt energy range. *Review of Scientific Instruments*, 90(8), 2019.

[160] Mariette Jolly, Spyridon Voikopoulos, Emily Lamour, Alain Méry, Angela Bräuning-Demian, Jean-Yves Chesnel, Alexandre Gumberidze, Michael Lestinsky, Stéphane Macé, Christophe Prigent, et al. Performance of a kev/u ion spectrometer for the fisic platform. *Atoms*, 10(4):146, 2022.

[161] Mikhail Yavor. Chapter 6 electrostatic energy analyzers. In *Optics of Charged Particle Analyzers*, volume 157 of *Advances in Imaging and Electron Physics*, pages 213–258. Elsevier, 2009.

[162] Hisashi Matsuda. Electrostatic analyzer with variable focal length. *Journal of the Mass Spectrometry Society of Japan*, 9(17):8–14, 1961.

[163] LA Baranova and FH Read. Electrostatic electron-optical crossed lens with controlled astigmatism. *Review of scientific instruments*, 65(6):1993–1997, 1994.

[164] M Szilagyi and J Szep. Optimum design of electrostatic lenses. *Journal of Vacuum Science & Technology B: Microelectronics Processing and Phenomena*, 6(3):953–957, 1988.

[165] Bernhard J Holzer. 6.1 beam optics and lattice design in high energy particle accelerators: Design and principles of synchrotrons and circular colliders. *Accelerators and Colliders*, pages 119–123, 2013.

[166] DOMINIQUE VERNHERT. *Distribution et anisotropie de moments cinetiques de capture pour des collisions d'ions multicharges de basse vitesse*. PhD thesis, UPMC, 1990. Thèse de doctorat dirigée par Chetioui, Annie Physique Paris 6 1990.

[167] Takahiro Yuyama, Yosuke Yuri, Tomohisa Ishizaka, Ikuo Ishibori, and Susumu Okumura. Real-time beam profile measuremnt system using fluorescent screens. *Proceedings of IBIC2012, Tsukuba, Japan*, 2012.

[168] basler. Basler ace 2r. https://www.baslerweb.com/en/shop/a2a1920-51gmpro/?creative=588959982218&keyword=%2Ba2a1920-51gmpro&matchtype=b&network=g&device=c&gad=1&gclid=Cj0KCQjwyLGjBhDKARIsAFRNgW8LISYJ-7XNd7OWt57wuOtFjUWYUNzuOGbDNUjdcGjRIigSIVTQmjQ wcB#specs. Accessed: 2024-04-22.

[169] hamamatsu. Mcp. https://www.hamamatsu.com/eu/en/product/optical-sensors/electron_ion-sensor/mcp/catalog.html. Accessed: 2024-04-26.

[170] L Strüder, P Lechner, and P Leutenegger. Silicon drift detector–the key to new experiments. *The Science of Nature*, 85(11):539–543, 1998.

[171] Emily Lamour, Christophe Prigent, Benjamin Eberhardt, Jean Pierre Rozet, and Dominique Vernhet. 2e1 ar17+ decay and conventional radioactive sources to determine efficiency of semiconductor detectors. *Review of Scientific Instruments*, 80(2), 2009.

[172] https://faster.in2p3.fr/. Accessed: 2024-03-21.

[173] ORTEC. Maestro - ortec. https://www.ortec-online.com/products/software/maestro-mca. Accessed: 2024-04-26.

[174] Jerome Mandrillon, Michel Abs, Philippe Cailliau, S Deprez, X Donzel, G Goose, Y Jongen, W Kleeven, L Koffel, VE Nuttens, et al. Status on nha c400 cyclotron for hadrontherapy. *JACoW*, pages 264–268, 2022.

[175] François Chevalier, P Lesueur, and G Gaubert. Cyclhad: A french facility dedicated for research and treatment in hadrontherapy. *Nuclear Physics News*, 32(2):27–31, 2022.

[176] Santo Gammino. Ion sources for medical applications. *arXiv preprint arXiv:1804.08516*, 2018.

[177] K Tinschert, R Iannucci, and R Lang. Electron cyclotron resonance ion sources in use for heavy ion cancer therapy. *Review of scientific instruments*, 79(2), 2008.

[178] M Muramatsu and A Kitagawa. A review of ion sources for medical accelerators. *Review of Scientific Instruments*, 83(2), 2012.

[179] Christian Schoemers, Eike Feldmeier, Jakob Naumann, Ralf Panse, Andreas Peters, and Thomas Haberer. The intensity feedback system at heidelberg ion-beam therapy centre. *Nuclear Instruments and Methods in Physics Research Section A: Accelerators, Spectrometers, Detectors and Associated Equipment*, 795:92–99, 2015.

[180] Tanja Eichkorn, Laila König, Thomas Held, Patrick Naumann, Semi Harrabi, Malte Ellerbrock, Klaus Herfarth, Thomas Haberer, and Jürgen Debus. Carbon ion radiation therapy: One decade of research and clinical experience at heidelberg ion beam therapy center, 2021.

[181] EC Cortés García, E Feldmeier, M Galonska, C Schömers, M Hun, S Brons, R Cee, S Scheloske, A Peters, and Th Haberer. Optimization of the spill quality for the hadron therapy at the heidelberg ion-beam therapy centre. *Nuclear Instruments and Methods in Physics Research Section A: Accelerators, Spectrometers, Detectors and Associated Equipment*, 1040:167137, 2022.

[182] Tim Winkelmann, Rainer Cee, Thomas Haberer, Bernd Naas, Andreas Peters, and Jochen Schreiner. Improvements for extending the time between maintenance periods for the heidelberg ion beam therapy center (hit) ion sources. *Review of Scientific Instruments*, 85(2), 2014.

[183] J Shi, JC Yang, JW Xia, RS Mao, and LR Zhou. Heavy ion medical machine (himm) slow extraction commissioning. *Nuclear Instruments and Methods in Physics Research Section A: Accelerators, Spectrometers, Detectors and Associated Equipment*, 918:76–81, 2019.

[184] JC Yang, J Shi, WP Chai, JW Xia, YJ Yuan, and Y Li. Design of a compact structure cancer therapy synchrotron. *Nuclear Instruments and Methods in Physics Research Section A: Accelerators, Spectrometers, Detectors and Associated Equipment*, 756:19–22, 2014.

[185] Weiping Chai, Jiancheng Yang, Jiawen Xia, Youjin Yuan, Jian Shi, Dayu Yin, Peng Li, Guodong Shen, Guofeng Qu, and Xiang Gao. Stripping accumulation and optimization of himm synchrotron. *Nuclear Instruments and Methods in Physics Research Section A: Accelerators, Spectrometers, Detectors and Associated Equipment*, 763:272–277, 2014.

[186] https://heavy-ion.showa.gunma-u.ac.jp/research/facility_en.html. Accessed: 2024-03-21.

[187] Tatsuya Ohno, Tatsuaki Kanai, Satoru Yamada, Ken Yusa, Mutsumi Tashiro, Hirofumi Shimada, Kota Torikai, Yukari Yoshida, Yoko Kitada, Hiroyuki Katoh, et al. Carbon ion radiotherapy at the gunma university heavy ion medical center: new facility set-up. *Cancers*, 3(4):4046–4060, 2011.

[188] H Souda, S Yamada, T Kanai, E Takeshita, M Muramatsu, A Kitagawa, M Kanazawa, H Izumiya, and Y Kano. Operation status of the electron cyclotron resonance ion source at gunma university. *Review of Scientific Instruments*, 85(2), 2014.

[189] Yuanrong Lu. *Development of an IH-DTL injector for the Heidelberg cancer therapy project*. PhD thesis, Frankfurt (Main), Univ., Diss., 2005, 2005.

[190] M Muramatsu, A Kitagawa, AG Drentje, S Hojo, T Ueda, H Miyazaki, K Yusa, M Tashiro, K Torikai, M Sakama, et al. The compact electron cyclotron resonance ion source keigm for the carbon ion therapy facility at gunma university. *Review of Scientific Instruments*, 81(2):02A327, 2010.

[191] Xiu-Cui Xie, Ming-Tao Song, and Xiao-Hu Zhang. Simulation of stripping injection into hitfil with carbon ion. *Chinese Physics C*, 37(9):097004, 2013.

[192] SY Lee, WM Tam, and Z Liu. Strip injection for carbon ion synchrotrons. *Review of Scientific Instruments*, 78(9):096104, 2007.

[193] K Tinschert, R Iannucci, and R Lang. Electron cyclotron resonance ion sources in use for heavy ion cancer therapy. *Review of scientific instruments*, 79(2):02C505, 2008.

[194] Cheol Ho Lee, Byung-Hoon Oh, Dae-Sik Chang, and Sun-Chan Jeong. Carbon beam extraction with 14.5 ghz electron cyclotron resonance ion source at korea atomic energy research institute. *Review of Scientific Instruments*, 85(2):02A903, 2014.

[195] JQ Li, Y Cao, LT Sun, XZ Zhang, JW Guo, X Fang, H Wang, and HW Zhao. Intense carbon beams production with an all permanent magnet electron cyclotron resonance ion source for heavy ion medical machine. *Review of Scientific Instruments*, 91(1):013307, 2020.

[196] AG Drentje, A Kitagawa, and M Muramatsu. Isotopic anomaly for carbon ions in an electron cyclotron resonance ion source. *Review of Scientific Instruments*, 81(2), 2010.

[197] NIFS. Nifs database. https://dbshino.nifs.ac.jp/nifsdb/amol/top. Accessed: 2024-05-29.

[198] K Li, SX Peng, TH Ma, YX Jiang, BJ Cui, WB Wu, AL Zhang, ZY Guo, and JE Chen. New progress of a 2.45 ghz ecr ion source for carbon positive ion mass spectrometry. *Vacuum*, 219:112670, 2024.

[199] NIST. Nist atomic spectra database ionization energies data for carbon. https://physics.nist.gov/cgi-bin/ASD/ie.pl?spectra=C&units=1&format=0&order=0&at_num_out=on&sp_name_out=on&ion_charge_out=on&el_name_out=on&seq_out=on&shells_out=on&level_out=on&ion_conf_out=on&e_out=0&unc_out=on&biblio=on&submit=Retrieve+Data. Accessed: 2024-05-29.

[200] NIST. Nist atomic spectra database ionization energies data for oxygen. https://physics.nist.gov/cgi-bin/ASD/ie.pl?spectra=O&units=1&format=0&order=0&at_num_out=on&sp_name_out=on&ion_charge_out=on&el_name_out=on&seq_out=on&shells_out=on&level_out=on&ion_conf_out=on&e_out=0&unc_out=on&biblio=on&submit=Retrieve+Data. Accessed: 2024-04-26.

[201] lnhb. Données atomiques et nucléaires, laboratoire national henri becquerel. http://www.lnhb.fr/accueil/donnees-nucleaires/donnees-nucleaires-tableau/. Accessed: 2024-03-28.

[202] Gwyn P Williams. X-ray data booklet. *X-ray data booklet*, 35:52, 2001.

[203] SIMION. Simion 3d suite. https://simion.com/. Accessed: 2024-04-02.

[204] David A Dahl. Simion for the personal computer in reflection. *International Journal of Mass Spectrometry*, 200(1):3–25, 2000. Volume 200: The state of the field as we move into a new millenium.

[205] WF Van der Weg and DJ Bierman. Collisions of ar+ ions with surface cu atoms and charge exchange of scattered ions near the metal surface. *Physica*, 44(2):177–205, 1969.

[206] Hannspeter Winter. Collisions of atoms and ions with surfaces under grazing incidence. *Physics Reports*, 367(5):387–582, 2002.

[207] X-ray data booklet. https://xdb.lbl.gov/Section1/Sec_1-2.html. Accessed: 2024-08-26.

[208] Andrea Aßmann, Jan Dellith, and Michael Wendt. Electron excited l x-ray spectra of the elements 24 z 33. *Microchimica Acta*, 155:87–89, 2006.

[209] MA Mendoza, JG Rubiano, JM Gil, Rafael Rodríguez, Ricardo Florido, Pablo Martel, and E Mínguez. A new set of relativistic screening constants for the screened hydrogenic model. *High Energy Density Physics*, 7(3):169–179, 2011.

[210] CF Moore, WJ Braithwaite, and Dennis L Matthews. Lifetime measurements of helium-like and lithium-like oxygen. *Physics Letters A*, 44(3):199–200, 1973.

[211] Patrick Richard, Robert L Kauffman, Forrest Hopkins, CW Woods, and KA Jamison. Oxygen metastable x-ray emitters. *Physical Review A*, 8(4):2187, 1973.

[212] Gordon WF Drake, GA Victor, and Alexander Dalgarno. Two-photon decay of the singlet and triplet metastable states of helium-like ions. *Physical Review*, 180(1):25, 1969.

[213] JR Crespo López-Urrutia, P Beiersdorfer, Daniel Wolf Savin, and K Widmann. Precision measurement of the lifetime of the 1 s 2 s 3 s 1 metastable level in heliumlike o 6+. *Physical Review A*, 58(1):238, 1998.

[214] Nist asd levels. https://physics.nist.gov/cgi-bin/ASD/energy1.pl?de=0&spectrum=0+Li-like&submit=Retrieve+Data&units=1&format=0&output=0&page_size=15&multiplet_ordered=0&conf_out=on&term_out=on&level_out=on&unc_out=1&j_out=on&lande_out=on&perc_out=on&biblio=on&temp=. Accessed: 2023-9-08.

[215] Friedrich Aumayr, Kiyoshi Ueda, Emma Sokell, Stefan Schippers, Hossein Sadeghpour, Frédéric Merkt, Thomas F Gallagher, F Barry Dunning, Paul Scheier, Olof Echt, et al. Roadmap on photonic, electronic and atomic collision physics: Iii. heavy particles: with zero to relativistic speeds. *Journal of Physics B: Atomic, Molecular and Optical Physics*, 52(17):171003, 2019.

[216] https://www.gsi.de/work/forschung/appamml/atomphysik/anlagen_und_experimente/cryringesr. Accessed: 2023-9-08.

Appendices

A Atomic system of units

The atomic system of units, by simplifying and streamlining the writing of equations and expressions characteristic of quantum mechanics, is particularly well-suited for the theoretical development of atomic and molecular collisions. By definition, in the atomic system, the numerical value of the following physical constants is set to one:

- the electron mass m_e,
- the absolute value of the electron charge e,
- the reduced Planck constant $\hbar$,
- $4\pi\varepsilon_0$, where ε_0 is the permittivity of free space.

From these constants, characteristic quantities (such as time, distance, energy, etc.) are constructed, each having a numerical value of 1. This collection of units forms the atomic unit system. Key constants in atomic physics and some characteristic quantities are presented in atomic units (a.u.) and in the International System (SI) in table A.1.

Electronic processes depend on the relative velocity v of the collision partners. However, cross-sections are preferably expressed in terms of the collision energy E, defined as the kinetic energy of the system in the center of mass divided by its reduced mass. The unit associated with E is keV/u: "kilo-electron-volt per atomic mass unit," which is related to v by the relation

$$E \approx 25v^2. \tag{124}$$

The usual unit for cross-sections is 10^{-16} cm^2, or 1 Å^2,

$$10^{-16}\ \text{cm}^2 = 3.57\ \text{a.u. of area}, \tag{125}$$

$$1\ \text{a.u. of area} = 0.28 \times 10^{-16}\ \text{cm}^2. \tag{126}$$

Quantity	**Atomic Units (a.u.)**	**SI Units**
Energy	1 Hartree (Ha)	$4.3597447222071 \times 10^{-18}$ J
Length	1 Bohr (a_0)	$5.29177210903 \times 10^{-11}$ m
Time	1 Atomic unit of time (τ)	$2.4188843265857 \times 10^{-17}$ s
Mass	1 Electron mass (m_e)	$9.10938356 \times 10^{-31}$ kg
Charge	1 Elementary charge (e)	$1.602176634 \times 10^{-19}$ C
Electric potential	1 Hartree/e	27.211386245988 V
Temperature	1 Hartree/k_B	3.1577513×10^{5} K
Momentum	1 $\hbar/a_0$	$1.99285191410 \times 10^{-24}$ kg·m/s
Velocity	1 Atomic unit of velocity (a.u.) = αc	$2.18769126379 \times 10^{6}$ m/s

Table A.1: Conversion table between atomic units and SI units

B Gaussian Type Orbitals basis set

B.1 C^{6+}+ H(1s) collision system

i	ℓ	α	i	ℓ	α
1	s	1.5998587196060572E-02	1	d	2.4420530945486497E-02
2	s	4.0287955080986732E-02	2	d	6.6277699855449512E-02
3	s	1.0145391619375455E-01	3	d	1.7987870566511724E-01
4	s	2.5548323538284878E-01	4	d	4.8819359788173849E-01
5	s	6.4336287854116592E-01	5	d	1.3249649986720748E+00
6	s	1.6201289797528617E+00	6	d	3.5959755624066094E+00
7	s	4.0798404735238343E+00			
8	s	1.0273934049338640E+01	1	f	3.2374575428176434E-02
9	s	2.5872021598675659E+01	2	f	9.3590709239878403E-02
10	s	6.5151430638726779E+01	3	f	2.7055863251260065E-01
			4	f	7.8215000422176106E-01
1	p	2.0417004905055654E-02			
2	p	5.0926657834239060E-02	1	g	4.2919342601287762E-02
3	p	1.2702766591996328E-01	2	g	1.0565749363404864E-01
4	p	3.1684835791885035E-01	3	g	2.6010430925598743E-01
5	p	7.9032296774725286E-01			
6	p	1.9713228039161794E+00	1	h	5.3131219437854815E-02
7	p	4.9171209187010900E+00	2	h	1.3220355112667587E-01
8	p	1.2264900543480911E+01			

Table B.2: GTO for C^{5+}

i	ℓ	α	i	ℓ	α
1	s	2.2229964825261957E-03	1	p	5.4693139323930846E-03
2	s	6.5328574704451936E-03	2	p	1.2213466712720720E-02
3	s	1.9198512937210019E-02	3	p	2.7273762484039517E-02
4	s	5.6419859252662227E-02	4	p	6.0904748629727633E-02
5	s	1.6580453540860574E-01	5	p	1.3600574573533905E-01
6	s	4.8726005924529842E-01	6	p	3.0371298280011344E-01
7	s	1.4319413202457485E+00	7	p	6.7821822837426260E-01
8	s	4.2081346618128741E+00	8	p	1.5145219050509131E+00
9	s	1.2366706010628896E+01			
10	s	3.6342805029780081E+01	1	d	5.7845637626698200E-03
			2	d	1.2684481056451917E-02
			3	d	2.7814726619458548E-02
			4	d	6.0992563548486409E-02
			5	d	1.3374543849061823E-01
			6	d	2.9327907004314874E-01

Table B.3: GTO for H

B.2 N^{7+}+ $He(1s^2)$ and N^{6+} (1s)+ $He^+(1s)$ collision system

i	ℓ	α	i	ℓ	α
1	s	1.0481131341546858E-01	1	p	1.2067926406393290E-01
2	s	2.9012492020268532E-01	2	p	2.6536601973498164E-01
3	s	8.0308572213915164E-01	3	p	5.8352298529663194E-01
4	s	2.2229964825261956E+00	4	p	1.2831299000133713E+00
5	s	6.1534070711166020E+00	5	p	2.8215209713999028E+00
6	s	1.7033053754470611E+01	6	p	6.2043450097815436E+00
7	s	4.7148663634573971E+01	7	p	1.3642959733629887E+01
8	s	1.3051074191219141E+02	8	p	2.9999999999999996E+01
9	s	3.6126270484536792E+02			
10	s	1.0000000000000000E+03	1	d	1.3579458100895739E-01
			2	d	2.9482971841698424E-01
			3	d	6.4011805343030914E-01
			4	d	1.3897890773273001E+00
			5	d	3.0174335329358972E+00
			6	d	6.5512855685955076E+00
			1	f	2.4373297485515866E-01
			2	f	7.2815455547697488E-01

Table B.4: GTO for N^{6+}+ and N^{5+}

i	ℓ	α	i	ℓ	α
1	s	5.4286754393238594E-03	1	p	2.4420530945486511E-02
2	s	2.3117750817470892E-02	2	p	5.8251367124689271E-02
3	s	9.8445819580114655E-02	3	p	1.3894954943731377E-01
4	s	4.1922674352369182E-01	4	p	3.3144247494664264E-01
5	s	1.7852567354823430E+00	5	p	7.9060432109077017E-01
6	s	7.6024291408426246E+00	6	p	1.8858632787726506E+00
7	s	3.2374575428176435E+01	7	p	4.4984326689694454E+00

Table B.5: GTO for He and He^+

C Emittance measurements with FISIC

C.1 Ar^{9+}

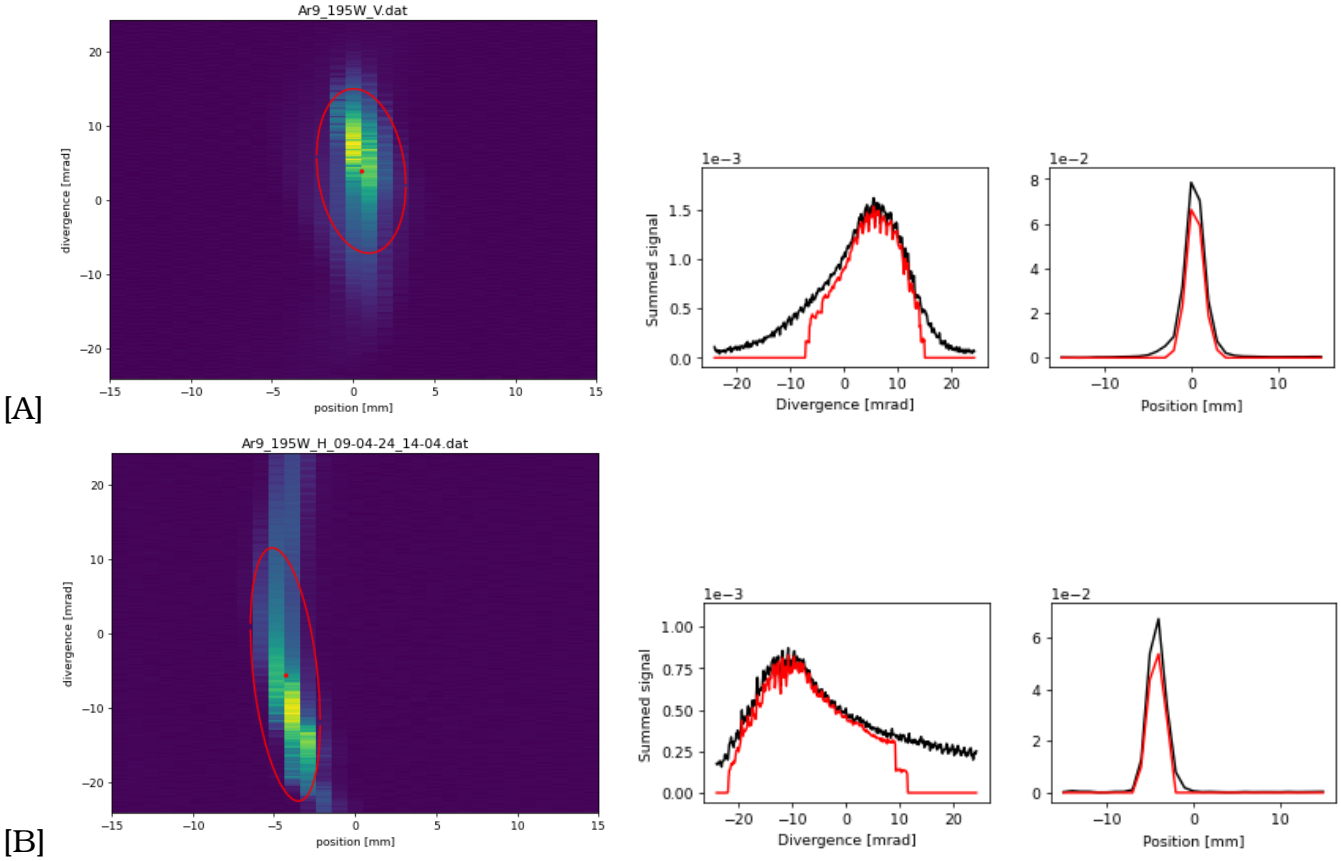

Figure C.1: (A) Vertical emittance and projection for Ar^{9+}. (B) Horizontal emittance and projection for Ar^{9+}. Extraction voltage : 10 kV, RF Power : 195 W

Results		
	Emittance π.mm.mrad	percentage $\%$
Horizontal	34	73
Vertical	30	72

C.2 Ar^{11+}

[A]

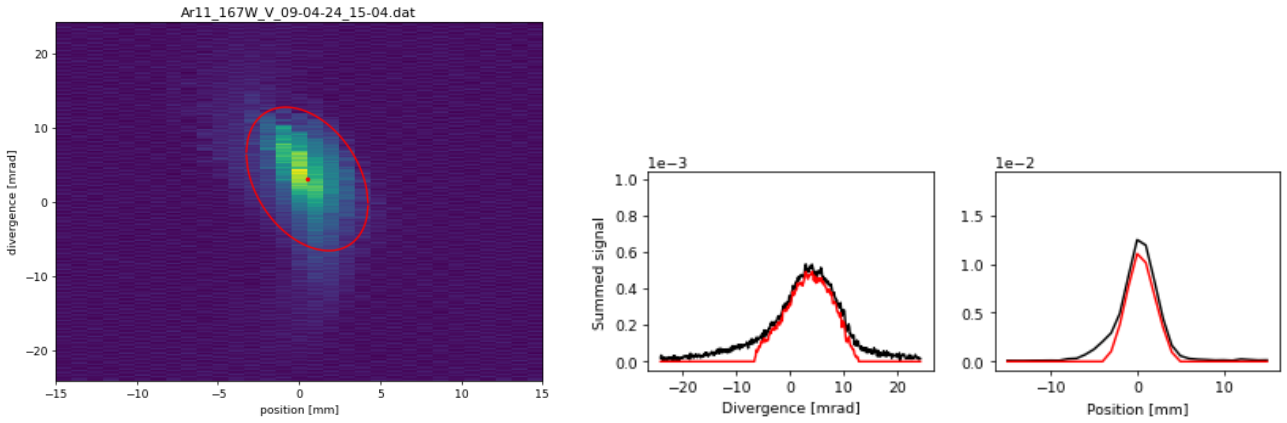

[B]

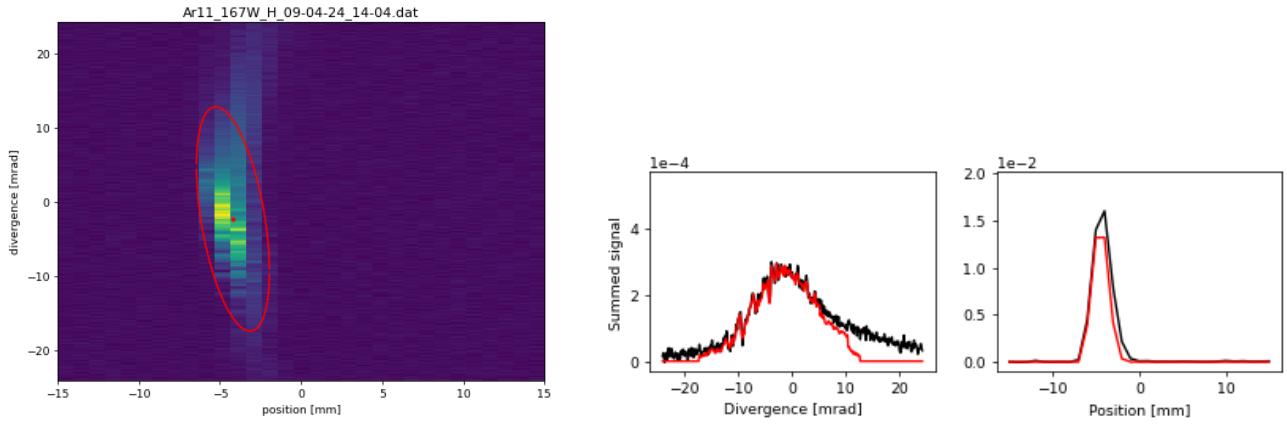

Figure C.2: (A) Vertical emittance and projection for Ar^{11+}. (B) Horizontal emittance and projection for Ar^{11+}. Extraction voltage : 10 kV, RF Power : 167 W

Results		
	Emittance π.mm.mrad	percentage %
Horizontal	30	76
Vertical	34	71

C.3 Ar^{13+}

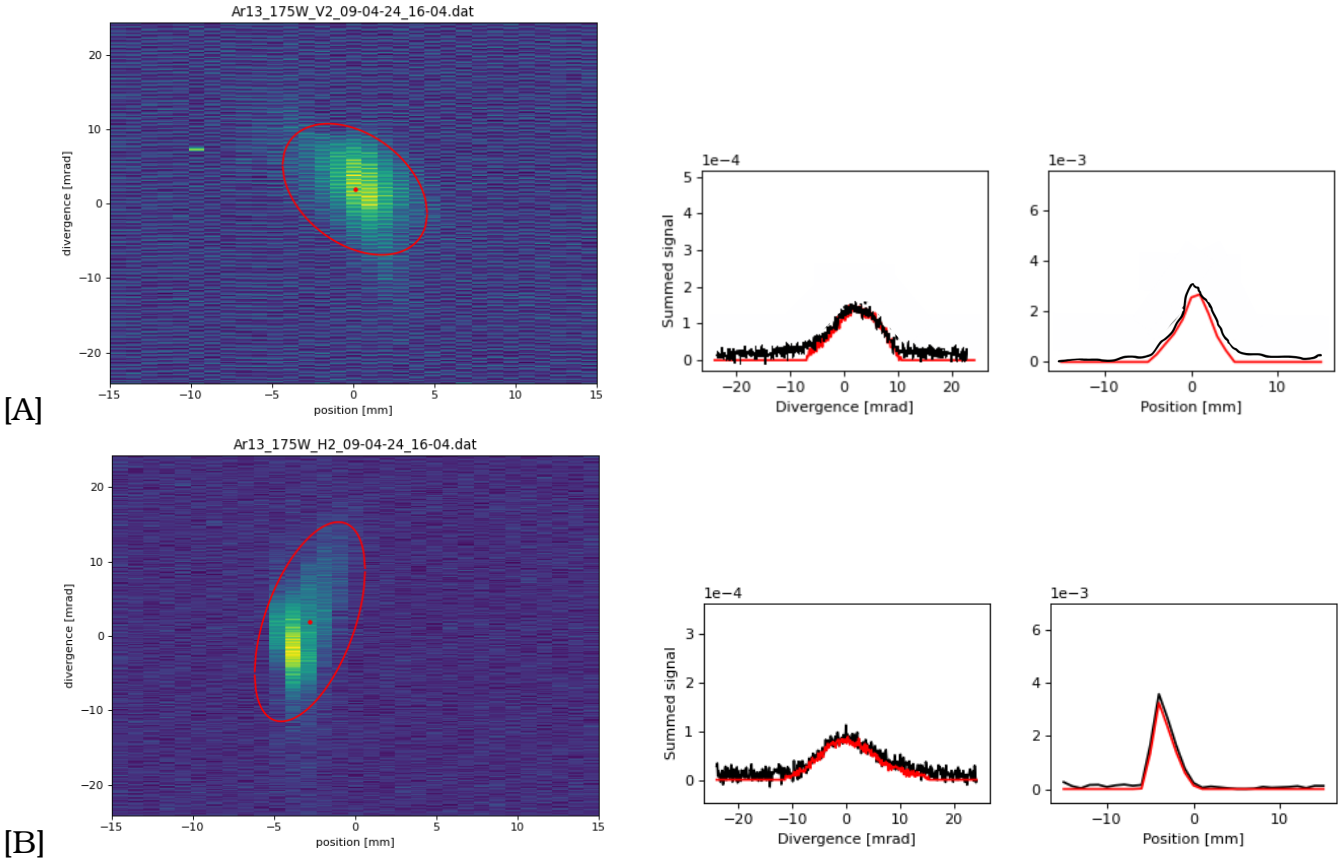

Figure C.3: (A) Vertical emittance and projection for Ar^{13+}. (B) Horizontal emittance and projection for Ar^{13+}. Extraction voltage : 10 kV, RF Power : 175 W

Results		
	Emittance π.mm.mrad	percentage %
Horizontal	38.96	70.43
Vertical	36.39	34.07

C.4 O^{5+}

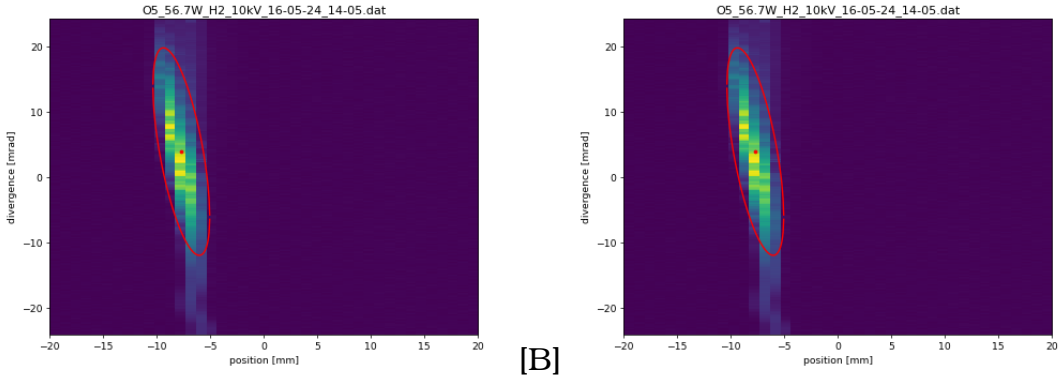

[A] [B]

Figure C.4: (A) Vertical emittance for O^{5+}. (B) Horizontal emittance for O^{7+}. Extraction voltage : 10 kV, RF Power : 56.7 W

Results		
	Emittance π.mm.mrad	percentage $\%$
Horizontal	33	76
Vertical	43	71

C.5 O^{7+}

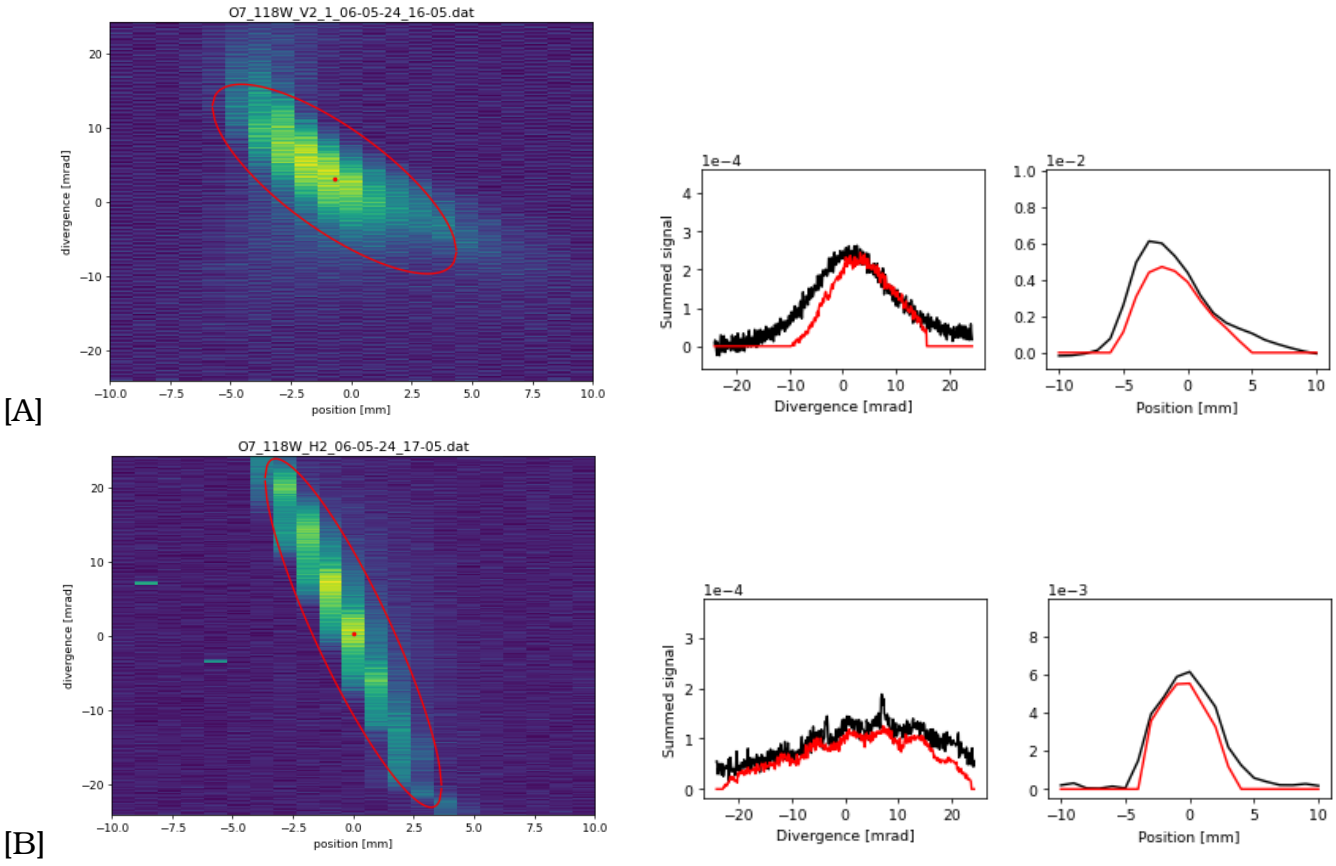

Figure C.5: (A) Vertical emittance and projection for O^{7+}. (B) Horizontal emittance and projection for O^{7+}. Extraction voltage : 10 kV, RF Power : 118 W

Results		
	Emittance π.mm.mrad	percentage %
Horizontal	40	74
Vertical	42	70

C.6 O8+

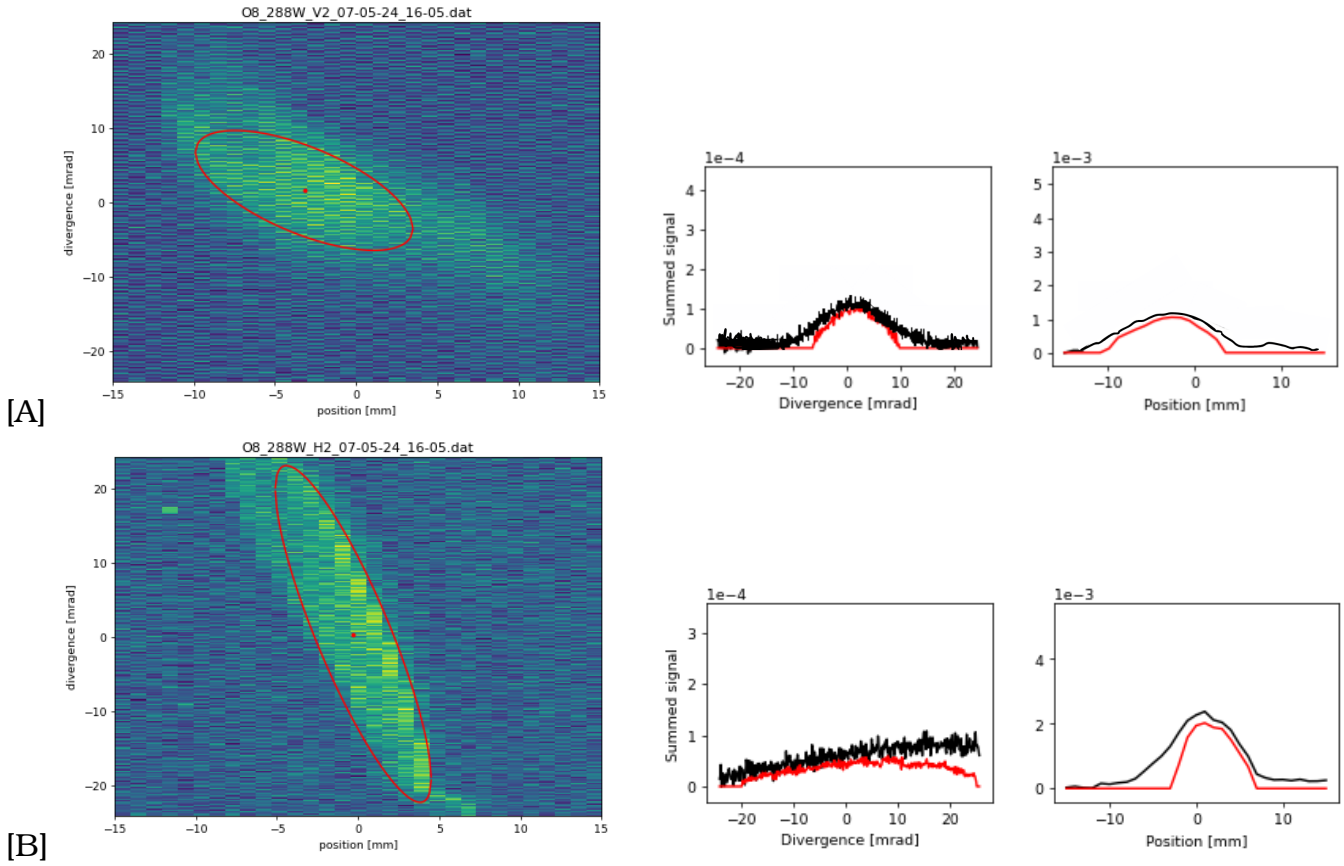

Figure C.6: (A) Vertical emittance and projection for O^{8+}. (B) Horizontal emittance and projection for O^{8+}. Extraction voltage : 10 kV, RF Power : 282 W

Results		
	Emittance π.mm.mrad	percentage $\%$
Horizontal	56	33
Vertical	42	38

D FCA measurements with SIMPA

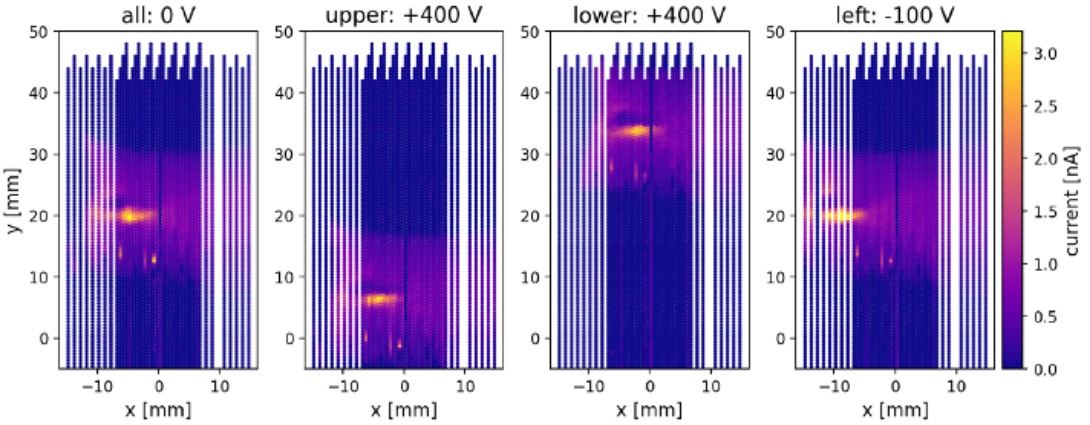

[A]

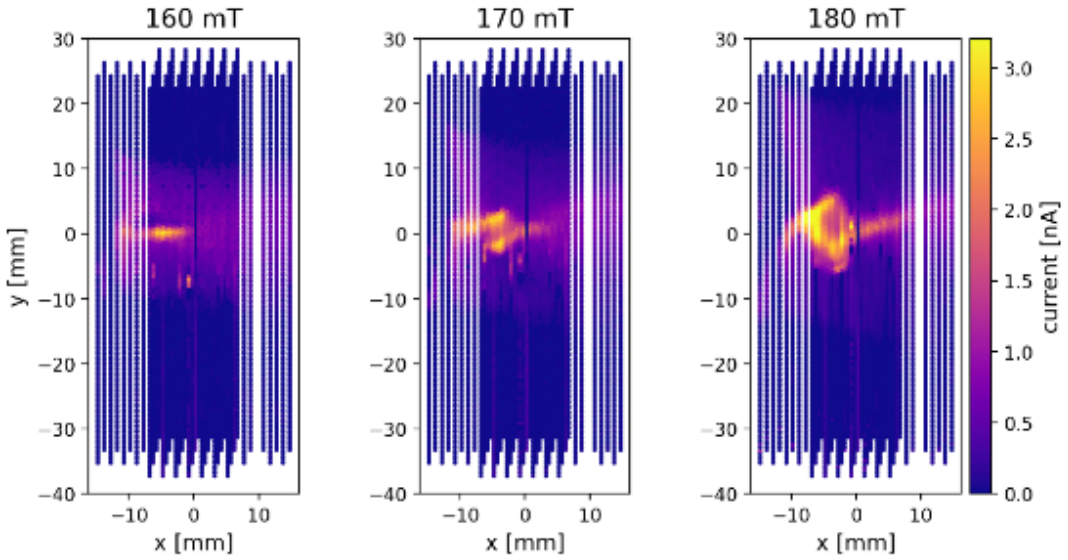

[B]

Figure D.1: (A) Displacement along the Y and X axes as a function of the steerers voltage. The displacement was found to be 3.5 mm per 100 V (B) Evolution of the shape of the beam as a function of the magnetic field (mT) of the solenoid.

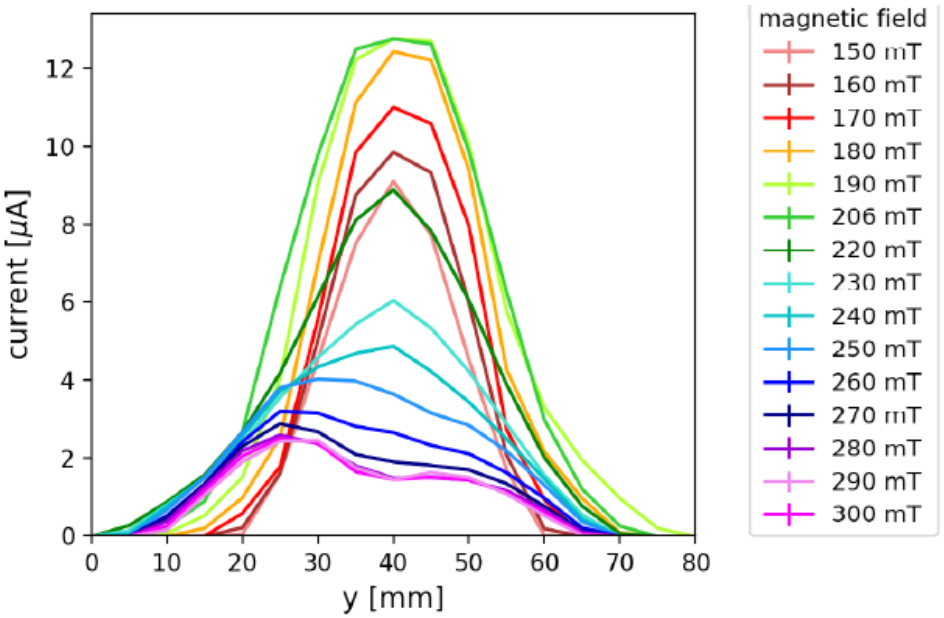

Figure D.2: Intensity (μA) as a function of the position (mm) on the Y axis for different solenoid magnetic field (mT), measured by the FCA Faraday Cup.